ASSESSING ALTERATIONS IN MYOCARDIAL MN^{2+} FLUXES FOLLOWING MYOCARDIAL INFARCTION IN A MURINE MODEL USING T_1-MAPPING MANGANESE-ENHANCED MRI

A Dissertation
Presented to
The Academic Faculty

by

Benjamin J Waghorn

In Partial Fulfillment
of the Requirements for the Degree
Doctorate of Philosophy in
Medical Physics

Georgia Institute of Technology

December 2009

Assessing Alterations in Myocardial Mn^{2+} Fluxes Following Myocardial Infarction in a Murine Model Using T_1-Mapping Manganese-Enhanced MRI

Approved by:

Dr. Tom C.-C. Hu, Co-advisor
Department of Radiology
Medical College of Georgia

Dr. Autumn Schumacher
School of Graduate Studies and School of Nursing
Medical College of Georgia

Dr. Farzad Rahnema, Co-advisor
Nuclear and Radiological Engineering and Medical Physics Programs
Georgia Institute of Technology

Dr. Chris Wang
Nuclear and Radiological Engineering and Medical Physics Programs
Georgia Institute of Technology

Dr. Sang Hyun Cho
Nuclear and Radiological Engineering and Medical Physics Programs
Georgia Institute of Technology

Dr. Nathan Yanasak
Department of Radiology
Medical College of Georgia

Date Approved: November 6, 2009

ACKNOWLEDGEMENTS

I am thankful to my supervisor, Tom Hu, whose enthusiasm, guidance and support from the initial to the final level enabled me to develop an understanding of the subject. Offering me guidance and timely encouragements throughout my graduate career, Nathan Yanasak has also provided support in many ways, for which I am extremely grateful. I am also indebted to Autumn Schumacher for her meticulous and invaluable advice on paper writing and the field of cardiovascular physiology.

My research was conducted as a unique collaboration between Georgia Institute of Technology and the Medical College of Georgia. There have been too many lab members, faculty members, friends and other supporting people throughout my graduate program to list and thank individually, but without all of these people this dissertation would not have been possible. I would, however, like to thank one of these people individually. Yidong Yang, a fellow class mate and lab member, has been working side-by-side with me over the past several years. Our discussions, both professional and personal, have aided me in reaching this point in my career.

Lastly, none of this would have been possible without the support of my entire family, most importantly my wife, Kristen, and daughter, Olivia. I often regard my graduate life as being like a roller-coaster ride. Having supported me throughout the entire ride I owe a special debt of gratitude to Kristen.

Ben Waghorn

TABLE OF CONTENTS

ACKNOWLEDGEMENTS iii

LIST OF TABLES vi

LIST OF FIGURES vii

LIST OF SYMBOLS AND ABBREVIATIONS xi

SUMMARY xiv

CHAPTER 1: INTRODUCTION 1
- 1.1 Calcium and Excitation Contraction Coupling 4
- 1.2 Myocardial Infarction 9
- 1.3 Magnetic Resonance Imaging (MRI) 21
- 1.4 Magnetic Resonance Imaging Contrast Agents 30
- 1.5 Manganese-Enhanced MRI (MEMRI) 34
- 1.6 Cardiac MEMRI 38
- 1.7 T_1-Mapping 41
- 1.8 Clinical Manganese Based Contrast Agents 46
- 1.9 Pharmaceutical Alterations of Ca^{2+} Handling 53

CHAPTER 2: PURPOSE OF DOCTORAL DISSERTATION 56
- 2.1 Background – Quantitative Cardiac Manganese-Enhanced MRI 57
- 2.2 Part I – Mn^{2+} Dose Dependent Cardiac Efflux 78
- 2.3 Part II – Pharmacologically and MI altered Mn^{2+} Efflux 78
- 2.4 Part III – Pharmacokinetic Modeling of Mn^{2+} Fluxes 79

CHAPTER 3: PART I - MN^{2+} DOSE DEPENDENT CARDIAC EFFLUX 81
- 3.1 Introduction 81
- 3.2 Materials and Methods 83
- 3.3 Results 88
- 3.4 Discussion 91
- 3.5 Conclusions 94

CHAPTER 4: PART II – PHARMACOLOGICALLY AND MYOCARDIAL INFARCTION ALTERED MN^{2+} EFFLUX 95
- 4.1 Introduction 95
- 4.2 Methods 98
- 4.3 Results 105
- 4.4 Discussion 123

CHAPTER 5: PART III – PHARMACOKINETIC MODELING OF MN^{2+} FLUXES 133
5.1 Introduction 133
5.2 Methods and Materials 136
5.3 Results 147
5.4 Discussion 157
5.4 Conclusions 161

CHAPTER 6: CONCLUSIONS AND FUTURE DIRECTIONS 162
6.1 Conclusions 162
6.2 Long-Term Goals 168

APPENDIX A: FLOW CHARTS 170

APPENDIX B: MODELING OUTPUT DATA 174

REFERENCES 199

LIST OF TABLES

Table 1.1 Clinical classification of different types of myocardial infarction (36)..... 10

Table 1.2 FDA approved clinical MRI contrast agents. 36

Table 2.1 Dose dependent T_1-map ΔR_1 values for the LV Wall are shown in columns 1 and 2. ICP-MS absolute blood and heart Mn values from mouse samples are displayed in columns 3-5. LV Wall ROI absolute Mn content from the calculated content maps are given in the final column. 62

Table 2.2 Temporal ΔR_1 signal attenuation post-$MnCl_2$ infusion in the LV Wall. 68

Table 2.3 Average ΔR_1 signal enhancement post-Mn^{2+} infusion for control, sham-operated and myocardial infarction groups. For the myocardial infarction group ROIs were defined both for the myocardial infarction peri-infarcted zone, surrounding the infarction site, and the infarcted site (MI)..... 74

Table 4.1 Group Characteristics 131

Table 5.1 Summarized raw input data 137

Table 5.2 Summary of the pharmacokinetic models 142

Table 5.3 Best fit parameters calculated by the three models..... 153

LIST OF FIGURES

Figure 2.1 Example short-axis heart images for a control mouse. (a) T_1-weighted pre-$MnCl_2$ infusion image; (b)T_1-weighted post- $MnCl_2$ infusion image; (c) pre-$MnCl_2$ infusion T_1-map; (d) post-$MnCl_2$ infusion T_1-map. (b) shows the locations of the interventricular septum (S), left ventricular free wall (LVWall), liver (L) and chest wall (CW)..... 59

Figure 2.2 Effect of altering the dose of infused Mn^{2+} on left ventricular free wall relaxivity (triangles). The x-axis shows the total dose of infused $MnCl_2$, normalized to the mouse BW. The y-axis shows the change in relaxation rate, ΔR_1, pre- vs. post- $MnCl_2$ infusion. As a function of dose, two linear dose uptake regions were noted, along with a plateau region above 197 nmoles g^{-1} BW. The least square fits are shown with total Mn^{2+} infusion dose, X [nmoles g^{-1} BW]. Comparison of this data to the total heart manganese content [μg g^{-1} dry], as determined by ICP-MS (squares) is also shown. This plot can be used to estimate the Mn content *in vivo*..... 61

Figure 2.3 Effect of $MnCl_2$ infusion dose on the total Mn content determined by ICP-MS for (a) the heart and (b) blood. The x-axis shows the total dose of $MnCl_2$ infused. The y-axis shows the absolute Mn content in μg g^{-1} dry weight for the heart and μg ml^{-1} for the blood. Both plots show the linear least square best fit to the data. 64

Figure 2.4 Temporal Mn^{2+} washout curve. The x-axis shows experimental time course post- $MnCl_2$ infusion, in hours. The y-axis shows the difference of relaxation rate, ΔR_1, pre- vs. post- $MnCl_2$ infusion. The insert plot shows the complete washout curve over an extended period of time. 69

Figure 2.5 Example short-axis post- $MnCl_2$ infusion T_1-map cardiac images for; (a) a sham-operated mouse, and (b) a myocardial infarction mouse. Significant LV Wall thinning can be seen for the MI mouse with a longer T_1 relaxation time relative to healthy myocardial tissue. (b) shows the interventricular septum (S), myocardial infarction peri-infarcted zone and myocardial infarction necrosed tissue site. 72

Figure 2.6 The effect of myocardial injury on the uptake of Mn^{2+}. Regions of interest were defined for the LV Wall in the control and sham-operated groups. ROIs for the MI model were also defined at the injury site contained within the LV Wall and in the peri-infarcted zone, immediately surrounding the injury site. Data is presented as the average ROI ΔR_1 (solid horizontal line, s^{-1}) ± SD (shaded box), with the data range shown (solid vertical line). 73

Figure 3.1 Example short-axis mouse heart T_1-maps (a) pre-$MnCl_2$ infusion (b) 0.2 hrs and (c) 5 hrs post-$MnCl_2$ infusion. Left and right ventricles are labeled as LV and RV respectively, with a sample LV Wall ROI also shown. 88

Figure 3.2 Dependence of the temporal changes in LV Wall ΔR_1 on the $MnCl_2$ infusion dose. (a) Binned data ± 1 standard deviation and first-order exponential fits using individual data points with 95% confidence intervals. (b) Corresponding dependence of the temporal LV Wall ΔR_1 washout half-life on the dose of $MnCl_2$. A first-order exponential was used to fit the half-life data. Sample sizes are shown for the mice (n_{mice}) and T_1 maps (n_{maps}). LV = left ventricle. 89

Figure 3.3 Elemental analysis data showing the temporal changes in Mn content for the control, 190 nmoles g^{-1} group, along with the first order exponential fit. Sample size (n) is also shown..... 91

Figure 4.1 Sample short-axis mouse heart T_1 maps from a healthy myocardium, acquired (a) pre-$MnCl_2$ infusion, (b) 1.3 h, (c) 4.1 h, and (d) 11.4 h post-190 nmoles g^{-1} $MnCl_2$ infusion. Left and right ventricles are labeled as LV and RV, respectively. A sample LV Wall region of interest (ROI) is also shown in (b). 106

Figure 4.2 Elemental analysis data showing; (a) the effect of the absolute heart Mn content on the *in vivo* LV Wall ΔR_1 for three experimental groups; control (square), 20 mg kg^{-1} (triangle) and 50mg kg^{-1} (open circle) SEA0400. A linear fit to all of the data, along with the 95% confidence band, is shown. Also shown is dose dependent data (x) from Waghorn et al, 2008, §2.1.2. Temporal changes in Mn content for each group are shown in (b), along with first order exponential fits for the control and 50 mg kg^{-1} SEA0400. Sample size (n) is also shown. 107

Figure 4.3 The effect of the NCX channel inhibitor SEA0400 on the temporal changes in ΔR_1, measured in the LV Wall. First order exponential fits using individual data points are shown along with the binned data ± 1SD and the 95% CI envelopes. Sample size, n, is also shown. 110

Figure 4.4 The dependence of the temporal LV Wall ΔR_1 washout half-life (a) and extrapolated ΔR_1 at the time of $MnCl_2$ infusion ($\Delta R_{1,0}$) (b) on the dose of NCX inhibitor SEA0400. Both values result from a first order exponential fit to the temporal ΔR_1 washout, starting at one hour post-Mn^{2+} infusion. Shown are the 95% CI values and resulting extra sum-of-squares F test comparing the individual SEA0400 groups to the control group..... 113

Figure 4.5 Effect of altering the SEA0400 dose (sodium calcium exchanger inhibitor) on the temporal changes in LV Wall ΔR_1. (a) Binned data ± 1standard deviation and first-order exponential fits using individual data points with 95% confidence intervals. (b) Corresponding dependence of the temporal LV Wall

ΔR_1 washout half-life (solid squares) and extrapolated $\Delta R_{1,0}$ (open circles) on the SEA0400 dose. LV = left ventricle. 116

Figure 4.6 The effect of dobutamine on the temporal changes in LV Wall ΔR_1 compared to the Control (190 nmoles g^{-1}) and 50 mg kg^{-1} SEA0400 groups. (a) Binned data ± 1standard deviation and first-order exponential fits using individual data points with 95% confidence intervals. (b) A comparison between the second-order fast (open circle) and slow (solid square) half-lives for the 190 nmoles g^{-1}, 50 mg kg^{-1} SEA0400 and Dobutamine groups. LV = left ventricle. 117

Figure 4.7 (a) Sample cardiac short-axis T_1 map for a myocardial infarction mouse after infusion of the manganese contrast agent ($MnCl_2$). The segmented myocardium is shown with the remaining tissue illustrated with increased opacity. (b) Demonstration of the sectoring orientation on the isolated myocardium. Temporal manganese ion efflux is demonstrated at (c) 1.6 h (d) 3.6 h and (e) 6.3 h post-190 nmoles g^{-1} $MnCl_2$ infusion. 118

Figure 4.8 Sample radial fitting for an infarcted myocardium at 1.6 h after infusion of the manganese contrast agent. The fitting algorithm optimizes average ΔR_1 values for the viable zone (A), and the necrosed zone (B), with the peri-infarcted zone linearly connecting these two regions. Also shown is a comparison of the *in vivo* ΔR_1 radial profile to histological staining, along with the correlating histological slice locations. 119

Figure 4.9 Sample temporal radial fitting of the segmented myocardium for the (a) Sham (thoracotomy only) and (b) MI (thoracotomy and coronary artery occlusion) groups. 121

Figure 4.10 (a) First-order exponential efflux curves for the Control (no surgery; 190 nmoles g^{-1} $MnCl_2$), Sham (thoracotomy only) and MI (thoracotomy and coronary artery occlusion) groups. Sample sizes are shown with corresponding 95% confidence intervals. (b) Radial Mn^{2+} efflux half-life data points calculated from first-order exponential curves on each sector of the myocardium. A radial fit is overlaid of the calculated average half-life values for the viable and necrosed zones. A line depicting the peri-infarcted zone linearly connects these two regions. A = Region A; B = Region B. 122

Figure 5.1 Schematic representations of pharmacokinetic Models 1 (a), 2 (b) and 3 (c). 140

Figure 5.2 Cardiac Mn^{2+} efflux data for the $MnCl_2$ dose dependent infusion groups (a), and the SEA0400 dose dependent groups (c). Overlaid are the least square best fit total heart model results from Model 2. Mn^{2+} content in the heart (compartments 2 + 3, solid line), compartment 2 (dashed line) and compartment 3 (dotted line) for the 190 nmoles g^{-1} $MnCl_2$ and 35 mg kg^{-1} SEA0400 groups are shown in (b) and (d) respectively. 148

Figure 5.3 Temporal Mn^{2+} efflux transfer rate, $k_{21}(t)$, predicted by Model 2 following inhibition of the NCX with varying does of SEA0400, injected 1 hour post-$MnCl_2$ infusion. Also shown are the corresponding SEA00400 elimination half-lives. 149

Figure 5.4 Model 2 total heart compartment (compartments 2 and 3) residuals for the control (a) and SEA0400 (b) dose dependent groups c) Model comparisons of the combined blood and heart sum of residuals squared for all the study groups, normalized to Model 1. * represents significance ($p < 0.05$)..... 150

Figure 5.5 Dose dependent trends for the transfer rate parameters (a) and pharmaceutical absorption and efflux half-lives (b) predicted by the best model (Model 1 for all groups except the 50 mg kg^{-1} SEA0400 group, which is improved with Model 2). Also shown are linear least square and exponential best fits for the transfer rate parameters (a) and half-lives (b) respectively. 154

Figure 5.6 Comparison of the MI efflux data to the modeled healthy efflux data. (a) shows an example output from the radial MI fitting algorithm, fitting constant ΔR_1 values for the remote (A) and necrosed (B) tissue, and linearly changing ΔR_1 in peri-infarcted zone between. The temporal efflux of regions A and B are illustrated in (b). The exponential efflux half-lives for these regions are compared to the healthy, dose dependent efflux in (c). The potentially salvageable peri-infarcted zone tissue is shaded in all three subplots. 156

Figure A.1 Automated myocardial isolation flow chart. Representation of the short axis cardiac slice orientation (top left) used to acquire a short axis T_1-map of a MI mouse post-$MnCl_2$ infusion (top right). Input of this T_1 map with an associated T_1-weighted image (not shown), an unbiased isolation program was used to isolate the myocardial tissue from image (bottom left and right), as described in §4. 170

Figure A.2 Myocardium segmentation flow chart. The orientation definition (defined in the top image) is used to create a position dependent T_1 profile (top graph). Data from both pre- and post-$MnCl_2$ infusion T_1 maps are input into the shown equation, with a resultant output for the radial ΔR_1, at a given time, shown (bottom graph). 171

Figure A.3 Flow chart of the process of data acquisition and absolute Mn content calculation for the efflux studies, leading to the modeling of Mn transport with either 2- 3- or 4-compartment models. 172

Figure A.4 Flow chart of the procedures involved with estimating the transfer rate and pharmaceutical parameters using pharmacokinetic modeling, as described in §5. 173

Figure B.1 Output model fits, residuals and parameters. 175

LIST OF SYMBOLS AND ABBREVIATIONS

ΔR_1 – Defined as (post-$MnCl_2$ infusion R_1) – (pre-$MnCl_2$ infusion R_1)

$\Delta R_{1,0}$ – The exponentially extrapolated ΔR_1 value at the time of $MnCl_2$ infusion

$[Ca^{2+}]_i$ – Intracellular calcium concentration

$[Ca^{2+}]_e$ – Extracellular calcium concentration

BW – "Body weight", referencing the entire body weight of the mouse subject

CHD – Coronary heart disease

CI – Confidence intervals

CNS – Central nervous system

CT – Computed tomography

DHP - Dihydropyridine

ECG – Electrocardiogram

FLASH – "Fast low-angle shot" pulse sequence

FOV – Field of view

GEFC – "Gradient echo flow compensation" pulse sequence

HCC – Hepatocellular carcinoma

ICP-MS – Inductively coupled plasma-mass spectrometry

Inter-TE – Echo time in Look-Locker sequence following small flip angle excitation

Inversion time/interval – Delay post adiabatic inversion before small flip angle excitation/ delay between subsequent excitations

LAD – "Left anterior descending" coronary artery

LL – “Look-Locker” pulse sequence

LV – Left ventricle

LV Wall – Left ventricular free wall

MEMRI – Manganese-enhanced magnetic resonance imaging

MI – Myocardial infarction

MnDPDP –Manganese-dipyridoxyl diphosphate

MnPLED – Manganese dipyridoxyl-ethyliamine

MPS – Myocardial perfusion scintigraphy

MRI – Magnetic resonance imaging

NCX – Sodium-calcium exchanger

NMR – Nuclear magnetic resonance

NSTEMI – Non-ST-elevation myocardial infarction

ODE – Ordinary differential equation

PET – Positron emission tomography

PMCA – Plasma membrane Ca^{2+} ATPase

r_1 – Longitudinal relaxivity

r_2 – Transverse relaxivity

R_1 – Longitudinal relaxation rate, defined as $1/T_1$

R_2 – Transverse relaxation rate, defined as $1/T_2$

RV – Right ventricle

ROI – Region of interest

RyR – Ryanodine receptors

SD – Standard deviation

SERCA – Sarco(endo)plasmic reticulum calcium pump ATPase

SPECT – Single photon emission computed tomography

SR – Sarcoplasmic reticulum

STEMI – ST-elevation myocardial infarction

T_1 – Spin-lattice relaxation time

T_2 – Spin-spin relaxation time

TE – Echo time

TR – Repetition time

SUMMARY

During cardiac ischemia, intracellular calcium (Ca^{2+}) overload occurs, which can result in cell death. MRI T_1 shortening contrast agent manganese (Mn^{2+}) acts as a surrogate marker for Ca^{2+}. Cardiac T_1-mapping manganese-enhanced MRI (MEMRI) techniques were applied to study the efflux of Mn^{2+} from both healthy mice and mice post-myocardial infarction (MI) surgery. Post-$MnCl_2$ infusion temporal changes in the myocardial relaxation rate, ΔR_1, were shown to be linearly correlated to the absolute Mn content. The relative importance of individual efflux mechanisms in healthy mice were investigated by inhibiting the sodium-calcium exchanger (NCX) with SEA0400, following infusion of $MnCl_2$, with SEA0400 reducing the rate of Mn^{2+} efflux. Regional alterations in Mn^{2+} uptake and efflux were also studied post-MI, allowing for the identification of potentially salvageable myocardium in the peri-infarcted zone surrounding the necrosed tissue. Application of pharmacokinetic models to *in vivo* and elemental analysis data from both the healthy and MI mice groups suggested that the NCX was more active in Mn^{2+} efflux than for Ca^{2+} and that there was an increase in Mn^{2+} uptake due to the disease condition, consistent with Ca^{2+} overloading. Studying Mn^{2+} efflux using these protocols could provide a pre-clinical model for examining alterations in relative Ca^{2+} fluxes and to potentially monitor disease progression.

CHAPTER 1: INTRODUCTION

Coronary heart disease remains the leading cause of death in the United States despite encouraging trends over the past three decades. Recent data from the American Heart Association reveals that 80 million American adults have one or more types of cardiovascular disease, of which 16.8 million have coronary heart disease (CHD) (1). Myocardial infarction (MI; heart attack) accounts for approximately 7.9 million of the total CHD cases. Despite being seen predominantly in developed countries, myocardial infarction is also becoming increasingly more common in developing countries. Recent advances in diagnostic techniques and therapeutic patient care have seen the number of deaths from heart disease in the US drop by approximately 36% between 1991 and 2006 (1). However, in 2006 at total of 631,636 US deaths (26% of the total number of US deaths) were still caused by heart disease, the largest cause of death ahead of cancer (with 559,888 deaths, 23.1% of the total US deaths) (1).

It has been demonstrated that the principle cause of diminished cardiac performance following a MI is due to abnormal intracellular Ca^{2+} handling impairing cardiomyocyte contractility (2). During ischemia the sodium-hydrogen exchange mechanism can lead to intracellular sodium overload. This in turn leads to reduced calcium efflux and increased calcium influx via the sodium-calcium exchanger (NCX) mechanism, resulting in intracellular calcium overload (2). The mitochondria act as a buffer to uptake this excess calcium from the cytosol, resulting in the expenditure of considerable energy (3). Energy starvation impairs calcium removal from the cytosol by inhibiting the sodium pump and the calcium pumps of the sarcoplasmic reticulum (SR)

and plasma membrane. All of these processes result in the increase of intracellular calcium that can inhibit actomyosin dissociation, impairing relaxation and therefore further increasing energy expenditure (4). These vicious cycles amplify the calcium overload, and cell death can result from one of several mechanisms following elevations in intracellular calcium concentration. Examples of these mechanisms include protease activation, membrane rupture, cell contracture, and gap junction dysfunction (2,5).

In spite of this established importance of calcium regulation in the heart both prior to, and following, myocardial injury, monitoring strategies to assess intracellular Ca^{2+} fluctuations across the plasma membrane in affected cardiac tissue are limited. In order to address the alterations in Ca^{2+} handling following MI, it is first necessary to consider calcium transport in the healthy heart. Section 1.1 introduces the calcium fluxes involved in cardiac myocyte contraction, looking at the excitation-contraction coupling process involving both intracellular and extracellular Ca^{2+} cycles. Alterations in calcium handling following MI are discussed in §1.2, along with a discussion into cellular viability and different techniques and modalities used to detect viable myocytes. One imaging modality used to detect myocardial viability in post-MI patients is magnetic resonance imaging (MRI). An introduction to the physics and principles of MRI is provided in §1.3. A number of MRI contrast agents are routinely used in the clinic to increase image contrast between different tissue types, or to act as a molecular marker. By altering the relaxation properties of tissue, the contrast agents can increase image contrast, allowing for enhanced tissue discrimination that can be used for a number of purposes including tumor delineation and viability studies. The general properties of MRI contrast agents are introduced in §1.4. Gadolinium (Gd^{3+}) is the most commonly used contrast agent and has

many applications, including the ability to diagnose hibernating myocardium. However, Gd^{3+} is limited as a viability agent, providing only perfusion information due to its extracellular properties. Manganese (Mn^{2+}), another MRI contrast agent, is an intracellular agent and has been shown to act analogously to Ca^{2+}. Section 1.5 therefore introduces the technique of manganese-enhanced MRI (MEMRI). MEMRI has many biological applications including studying brain neuroarchitecture (6), tracing neuronal connections (7), visualizing cerebral function and dysfunction (8), cell labeling (9) and cardiac viability (10). MEMRI has the potential to be used as a clinical viability agent in cardiovascular studies (11), offering molecular information not achievable with other modalities. The specific application of MEMRI to cardiac imaging is discussed in §1.6. Positive paramagnetic contrast agent Mn^{2+} is known to reduce the longitudinal relaxation time, T_1. Application of quantitative imaging techniques, such as T_1-mapping, with MEMRI can be used in viability studies (§1.7), and can be used to infer indirect changes in Ca^{2+} handling following MI. Mn^{2+} based contrast agent MnDPDP is clinically approved for liver imaging, and is discussed in (§1.8). Finally, in order to study the effect of altered Ca^{2+} handling on Mn^{2+} transport within the heart, different pharmaceutical agents such as dobutamine (an inotropic agent) and SEA0400 (a NCX inhibitor, NCX_i) can be administered. These pharmaceuticals have also demonstrated therapeutic properties and are described in §1.9. This introduction provides a framework for understanding how *in vivo* cardiac MEMRI T_1-mapping techniques can be applied to a mouse model to assess alterations in Mn^{2+} handling under various conditions, including post-MI surgery.

1.1 Calcium and Excitation Contraction Coupling

Intracellular calcium (Ca^{2+}) is the central regulator of cardiac contractility (12). Action potentials, traveling from the sinus node to the ventricular cells, travel along the transverse tubules (T-tubules) and induce the opening of L-type calcium channels within contractible myocytes (3). A majority of the calcium entering the cells initiate calcium-induced calcium release from the SR, with a smaller contribution leading to direct myofilament activation. The resultant increase in intracellular free calcium, $[Ca^{2+}]_i$, causes Ca^{2+} binding to multiple cytosolic Ca^{2+} buffers. The most important of these for contraction is the thin-filament protein troponin C. Binding of Ca^{2+} to troponin C induces a conformal change in the thin-filaments, resulting in contraction. More specifically, troponin C is activated by Ca^{2+} released from the SR, and binds to the inhibitory molecule troponin I. This enables interaction between the actin and myosin heads and induces contraction. A reduction in $[Ca^{2+}]_i$ leads to dissociation of Ca^{2+} from the troponin C, as well as the binding of troponin I to actin with a resultant loss in the binding between actin and myosin and ultimately relaxation (3). The third protein in the troponin complex, troponin T, binds the troponin complex to tropomyosin (4). Following relaxation Ca^{2+} is removed from the cytosol via one of four transporters (13): [1] SR Ca^{2+}-ATPase, [2] sarcolemmal sodium-calcium exchanger (NCX), [3] plasma membrane Ca^{2+}-ATPase (PMCA), and [4] mitochondrial Ca^{2+} uniporter. All of these processes, along with contributions from numerous other cellular structures, combine to form the excitation-contraction coupling process in cardiac muscle cells (14).

1.1.1 Calcium Influx Across the Plasma Membrane

There are three types of Ca channels; L, T and N type. Cardiac muscle contains both L and T type, with N channels being found in nervous tissue. L-type Ca channels are characterized with four properties; large conductance (~25 pS in 110 mM Ba), long lasting openings, sensitivity to 1,4-dihydropyridines (DHPs) and activation at larger depolarizations. In contrast, T type Ca channels are characterized by a small conductance (~8 pS), transient openings, insensitivity to DHPs and activation at smaller depolarizations (14). The L-type Ca channels are responsible for the vast majority of Ca entry in ventricular muscle, and are therefore of primary interest in the discussion of myocyte Ca influx.

L-type voltage-gated ion channels can be found in excitable cells (e.g., myocytes, glial cells, neurons, etc.) with a permeability to the Ca^{2+} ion (15,16). At physiological or resting membrane potential, voltage-gated calcium channels are normally closed. They are activated (i.e., opened) at depolarized membrane potentials, providing the name "voltage-dependent". Activation of particular voltage-gated calcium channels allows Ca^{2+} entry into the cell which, dependent on the cell type, can result in muscular contraction (17), excitation of neurons, up-regulation of gene expression, or release of hormones or neurotransmitters.

Voltage-gated calcium channels are formed as a complex of several different subunits: α_1, $\alpha_2\delta$, $\beta_{1\text{-}4}$, and γ. The α_1 subunit forms the ion conducting pore, and the associated subunits have several functions, including modulation of gating (18). At approximately 190 kDa the α_1 subunit pore is necessary for the Ca^{2+} channel functioning. The α_1 subunit consists of the characteristic four homologous I-IV domains containing

six transmembrane α-helices each. The α_1 subunit forms the Ca^{2+} selective pore, which contains voltage-sensing machinery and the drug/toxin-binding sites.

Calcium ions can also enter the cytosol by the reversal of the exchange mechanisms used for calcium efflux (13). In particular, the sodium-calcium exchanger (NCX), described in the following subsection as a mode for Ca^{2+} efflux, can reverse during depolarizing voltages to allow Ca^{2+} entry into the cell. Ca^{2+} entry via this mechanism can also act as an activator for the release of Ca^{2+} from the SR, thus enhancing the contractile process (3).

1.1.2 Calcium Efflux Across the Plasma Membrane

Calcium entry through L-type Ca^{2+} channels into cardiac myocytes is known to be the initiating event of the excitation-contraction coupling process (19,20). Calcium that enters cells via the L-type Ca^{2+} channels during each action potential must be pumped out of the cell to maintain composition of the cytosol at a steady state. There are two known mechanisms to remove Ca^{2+} from cardiac cells (21), either via the NCX, or via the PMCA (22). Attempts to estimate the relative contributions to Ca^{2+} efflux have shown that the NCX is the dominant efflux mechanism, with only between 9 and 32% (23,24) of the efflux occurring from non-NCX mechanisms (including the PMCA) in rats and 19% in mice (25).

First discovered in cardiac muscle in 1968, the NCX is a transmembrane protein expressed in the membrane of almost every cell (26). Even from this early date the quantitative importance of sodium-calcium exchange was known: approximately 80% of myocardial calcium efflux is known to occur via this mechanism. The NCX is an antiport

that carries Na^+ ions against Ca^{2+} ion (4). The stoichiometry was originally established at 3 Na^+ : 1 Ca^{2+} (27), but more recently it has been reported to be closer to a mean ration of 4 Na^+ : 1 Ca^{2+} with significant variation in this ratio (28). This discrepancy comes from the NCX having two modes, a Na^+-only mode and the major Na^+/Ca^{2+} co-transport mode at 3 Na^+ : 1 Ca^{2+}. This gives the overall stoichiometry as 3.2 Na^+ : 1 Ca^{2+} (29). The direction of the antiport is determined by electrochemical energies from the membrane potential and from the Na^+ and Ca^{2+} concentration gradients. The NCX Ca^{2+} flux during an action potential is an initial Ca^{2+} influx with outward current due to the strong depolarization at initially low intracellular Ca^{2+} concentrations (30). In the 'forward mode', the NCX extrudes Ca^{2+} from the cell in exchange for Na^+ entry into the cell, generating an inward current (31). This small current can be clinically important, especially in calcium-overloaded hearts, where the change in depolarizing current associated with increased calcium efflux can cause transient depolarizations and lethal arrhythmias.

Due to the dominance of the NCX mechanism in cellular Ca^{2+} efflux, the NCX has a large effect not only on the cytoplasmic Ca^{2+} concentration, but also indirectly on the amount of Ca^{2+} stored in the SR. The voltage dependence of the NCX may produce net Ca^{2+} entry into the cell at the start of the action potential and contribute a small amount to triggering Ca^{2+}-induced Ca^{2+} release from the SR (32). In steady state, the Ca^{2+} influx, largely occurring via the L-type voltage gated Ca^{2+} channel, must equal the efflux. Changes to either the influx or efflux, which results in increased cytoplasmic Ca^{2+} concentration, will require the SR to uptake more Ca^{2+} (33). In addition, the direction of

the NCX current is also influenced by transient increases in intracellular Na^+ concentrations due to Na^+ influx with the upstroke of the action potential (34,35).

The primary competing mechanism for intracellular Ca^{2+} efflux is the PMCA, which uses energy from the hydrolysis of ATP to expel Ca^{2+} ions from the cell. Unlike the NCX, the PMCA is an electroneutral pathway transporting 2 H^+ ions per Ca^{2+} ion (36). Energy in the form of ATP is required to transport the calcium ions against the large concentration gradients that exist between the relatively low cytosolic Ca^{2+} concentrations and the much higher concentrations in the extracellular space. With no specific inhibitor to study the PMCA, attempts have been made to study its function by inhibiting other Ca^{2+} removal processes.

1.1.3 Intracellular Calcium Cycles

The primary cytosolic Ca^{2+} store is the SR. Ca^{2+} ions entering the cell from the extracellular fluid alone are not sufficient to initiate cardiac contraction. Therefore Ca^{2+} needs to be released from the intracellular stores in order for contraction to occur. Following the influx of a relatively small concentration of Ca^{2+} from the extracellular space, the Ca^{2+} binds to ryanodine receptors (RyR, intracellular calcium release channels), initiating the release of larger amounts of Ca^{2+} from the SR. This process is called calcium-induced calcium release. Release of Ca^{2+} from the SR occurs via a passive flux due to SR Ca^{2+} concentrations several orders of magnitude greater that the corresponding intracellular concentrations. Within cardiac myocytes, Ca^{2+} released from the SR is insufficient to fully saturate the troponin C, allowing for the contractile

response to be controlled. This is in contrast to skeletal muscle where Ca^{2+} released from the SR binds to a majority of the troponin C resulting in maximum contractions.

Stores of Ca^{2+} within the SR are repopulated following release of Ca^{2+} from the contractile proteins. Uptake of Ca^{2+} into the SR requires the expenditure of energy and occurs via the sarco(endo)plasmic reticulum calcium pump ATPase (SERCA), a P-type ion pump. Ca^{2+} is then transported across the concentration gradient using energy derived from ATP, a similar process to that involved with Ca^{2+} efflux via the PMCA.

1.2 Myocardial Infarction

The existence of myocardial ischemia is owed to the severe reduction of coronary flow, leading to a supply of oxygen to the myocardium that is insufficient to meet the demands of the tissue (3). The major myocardial adaptation to the decrease in blood flow is reduced contraction. Following reperfusion, if the myocardium eventually undergoes a full recovery the tissue is defined to be stunned during the period of time required to achieve the fully recovered state of the myocardium. The negative inotropic effect of stunning is completely reversible as is does not result in cell death. This process can last many weeks. Hibernation, in contrast, is the return to function of myocardial tissue caused by revascularization. In regions of hibernating tissue, wall motion abnormalities are present.

Table 1.1 Clinical classification of different types of myocardial infarction (37)

Type 1
Spontaneous myocardial infarction related to ischemia due to a primary coronary event such as plaque erosion and/or rupture, fissuring, or dissection
Type 2
Myocardial infarction secondary to ischemia due to either increased oxygen demand or decreased supply, e.g. coronary artery spasm, coronary embolism, anemia, arrhythmias, hypertension, or hypotension
Type 3
Sudden unexpected cardiac death, including cardiac arrest, often with symptoms suggestive of myocardial ischemia, accompanied by presumably new ST elevation, or new left bundle branch block, or evidence of fresh thrombus in a coronary artery by angiography and/or autopsy, but death occurring before samples could be obtained, or at a time before the appearance of cardiac biomarkers in the blood
Type 4a
Myocardial infarction associated with percutaneous coronary interventions
Type 4b
Myocardial infarction associated with stent thrombosis as documented by angiography or at autopsy
Type 5
Myocardial infarction associated with coronary artery bypass grafting

Myocardial viability can be defined as the presence of living myocytes, with non-viability defined as the presence of necrotic myocytes, or the replacement of myocytes by fibrosis or scar tissue (38). Ischemic cell death, called myocardial infarction (MI), is a major cause of mortality and morbidity worldwide (39). More that 3 million people each year are estimated to have an acute ST-elevation MI (STEMI), with more than 4 million having a non-ST-elevation MI (NSTEMI).

Myocardial infarction (MI) is defined as the presence of necrosis (cell death of cardiac myocytes) resulting from prolonged ischemia due to a coronary perfusion imbalance between blood supply and demand (40). Along with the rise and fall of cardiac serum biomarkers (41), the clinical criteria for diagnosing a MI includes images showing new loss of viable myocardium. Clinically, the various types of MI can be classified as shown in Table 1.1 (37).

Acute MI occurs when coronary flow is reduced to levels so low as to cause myocardial cell death (4). During MI blood flow is reduced in occluded coronary arteries to such a low level that myocardial cell death occurs as a result of oxygen deprevation. The endocardial myocytes, which are especially vulnerable to decreased oxygen and perfusion pressure, die off quicker than those in the epicardium causing a thinning of the muscular cardiac wall. Myocardial cell death begins approximately 15 to 40 minutes after the heart's blood supply is cut off completely, with few viable cells remaining in the ischemic region approximately 6 hours later. The timescale is dependent on collateral flow in humans, but does not exist in a murine model. If irreversibly damaged ischemic tissue is reperfused, an infarct ensues that leads to contraction band necrosis. In these regions the cells literally tear themselves apart (4). Death of ischemic myocardial cells

can occur via either necrosis (a process leading to fibrosis following remodeling) or apoptosis (a regulated process not associated with inflammation, occurring after reperfusion of severely ischemic myocardium).

Necrosis is associated with the leaking into the bloodstream of intracellular proteins following plasma membrane damage. Myocardial cell death can therefore be recognized by the appearance in the blood of different proteins released into the circulation from the damaged myocytes: myoglobin, cardiac troponin T and I, creatine kinase (CK), lactate dehydrogenase (LDH), and many others (42,43). The preferred clinical biomarker for myocardial necrosis is cardiac troponin (I or T), which has nearly absolute myocardial tissue specificity as well as high clinical sensitivity, therefore allowing for even microscopic zones of myocardial necrosis to be identified. Apoptosis can also occur after reperfusion of severely ischemic myocardium (44). The release of cytochrome C from the mitochondria appears to be the apoptosis inducing mechanism (45).

Alterations in myocyte Ca^{2+} handling appear to be centrally involved in the dysfunctional characteristics of the failing heart (46). Abnormal intracellular Ca^{2+} handling leading to impaired cardiomyocyte contractility is the primary cause of diminished cardiac performance in the diseased heart (47,48). During ischemia the sodium-hydrogen exchange mechanism can lead to intracellular sodium overload. This in turn leads to reduced calcium efflux and/or increased calcium influx via the sodium-calcium exchanger mechanism, resulting in intracellular calcium overload (2). Cell death can result from one of several mechanisms following elevations in intracellular calcium

concentration. Examples of these mechanisms include protease activation, membrane rupture, cell contracture, and gap junction dysfunction (2,5).

Following MI there is progressive myocardial remodeling in the murine model, characterized by left ventricular dilation, contractile dysfunction and myocyte hypertrophy. There are also altered expressions of contractile, calcium-handling, and extracellular matrix proteins (49). Similarly, myocardial ischemia appears to have significant negative effects both on acute and chronic cardiac remodeling and on damage to other organs, likely due to decreased cardiac output, including the vascular endothelium (50,51), kidney (52), skeletal muscle (53,54), and brain (55).

Many clinical infarctions involve the left ventricle, specifically by way of occlusion of the left anterior descending coronary artery (LAD); however, the infarction may not affect the entire left ventricle. Successful treatment for injured myocardial tissue, both by pharmacological intervention and physical revascularization procedures, is heavily dependent on being able to salvage viable tissue in the peri-infarcted region bordering the ischemic area (56,57).

1.2.1 Detecting Myocardial Viability

In theory, all ischemic events that occur before cell death are reversible, and the further a diagnostic technique deviates from directly assessing whether myocytes are present or absent, the more imprecise the technique becomes in determining myocardial viability. Several imaging methods such as nuclear medicine (58), computerized tomography (59) and magnetic resonance imaging (MRI) (60,61) are clinically useful for detecting the location and size of newly infarcted tissue. However, current imaging

techniques primarily utilize extracellular techniques to study myocardial perfusion or metabolism, leading to an inadequate assessment of the peri-infarcted zone adjacent to the necrosed tissue, and no direct viability information. Kim et al. (62) demonstrated that MRI delayed enhancement methods using gadolinium (Gd) contrast could delineate regions of irreversible injury and viable tissue after a myocardial injury. Mechanisms underlying Gd concentration in the necrotic myocardium are most likely due to abnormal coronary perfusion and increased tissue edema (63). However, use of an intracellular viability tracer would allow for improved identification, quantification and evaluation of the potentially salvageable peri-infarcted tissue. Such an improved imaging technique and the more accurate determination of the peri-infarcted tissue may assist in developing new therapies for treating damaged tissue in the heart. These therapies could be directly or indirectly applied to the affected myocardium to ultimately enhance clinical outcomes for the post-MI patient (56).

Assessment of myocardial viability in patients with coronary artery disease and left ventricle dysfunction has been known to be of major importance for prognosis for over two decades (64-66). Dysfunctional but viable myocardium have the potential to recover after restoration of myocardial blood flow by either coronary artery bypass grafting or percutaneous transluminal coronary angioplasty (58). The extent of these peri-infarcted zones in patients with prior MI has been shown to provide a good noninvasive predictor of post-MI mortality (56). Left ventricular ejection fraction is currently the most robust clinical parameter for post-MI risk assessment, but the need for other accurate predictors of outcome, including molecular imaging, is apparent (67,68).

Electrocardiography

Electrocardiographic (ECG) techniques are routinely used in the diagnostic work-up of patients with suspected MI (69-72). The extent of myocardium at risk can be estimated by evaluating the acute or evolving changes in the ST-T waveforms and the Q-waves. During an MI, the ECG goes through a series of abnormalities. The initial abnormality, a hyperacute T wave, is a T wave with greater amplitude and reduced width relative to the normal T wave. This abnormality lasts for a very short time, and then elevation of the ST segment may occur, reflecting epicardial ischemia. During this period, ion pumps in the ischemic tissue fail, resulting in cells that are depolarized throughout the cardiac cycle. Due to differences in the charge of the positively charged normal tissue and the negatively charged depolarized tissue, during diastole a current will flow between the normal and ischemic tissue zones (3). Ultimately this leads to elevated ST segments, and is the hallmark abnormality of an acute MI. This elevation occurs when the heart muscle is being injured due to a lack of blood flow. An ECG can be used not only to indicate the presence of MI but can also show the approximate location of the heart attack, and often which artery is involved. Although ECG provides an indication for MI, the observed changes in ST or Q-waves can be caused by other conditions.

Nuclear Imaging

Nuclear imaging techniques play a major role in the assessment of myocardial viability and perfusion (66,73-75). Positron emission tomography (PET) imaging was first used clinically to identify myocardial viability in the mid 1980's (66), and has since been recognized as an accurate technique for the quantification of metabolism and

perfusion of the myocardium. Positron emitting radionuclides provide versatility for PET with their ability to be incorporated into important biochemical molecules. Uptake of these radionuclides can be imaged and quantified leading to assessment of myocardial perfusion, glucose utilization, fatty acid uptake and oxidation, oxygen consumption and contractile function (76). For metabolic FDG imaging, the preserved or increased glucose utilization, and subsequent FDG uptake in hypoperfused and dysfunctional myocardium, is regarded as a metabolic marker of cell viability. This can be differentiated from scar tissue where reductions in both blood flow and FDG uptake are detected. FDG (a glucose analogue) and ammonia (a perfusion tracer) studies are commonly combined to differentiate between different types of myocardium in the post-MI heart. Infarcted myocardium exhibit reduced uptake of both FDG and ammonia dependent on the extent of infarction, while stunned myocardium have normal uptake of both tracers and hibernating myocardium only have a reduction in uptake of ammonia (66,77).

Flow tracer radiopharmaceuticals such as ^{201}Thallium, ^{99m}Tc-sestamibi and ^{99m}Tc-tetrofosmin are all used for diagnosis of myocardium viability, with their active uptake by myocardial cells dependent on myocardial blood flow and active transport (78). Thallium, in association with single photon emission computed tomography (SPECT), has been extensively used for identifying myocardial viability and hibernation, and was the first tracer used for this purpose (79). ^{201}Thalium acts as a potassium analogue, with myocardial uptake dependent on both regional flow and intact sarcolemmal membranes (79). This technique therefore provides information regarding both cell perfusion and viability. However, simple stress-redistribution protocols using ^{201}Thalium can underestimate the amount of viable myocardium. Technetium-99m labeled tracers offer

lower radiation doses and a shorter half-life versus thallium. However, uptake of ^{99m}Tc is dependent on both perfusion and viability, leading to underestimates of viable tissue in areas of reduced perfusion. In addition to viability studies, another nuclear imaging technique, myocardial perfusion scintigraphy (MPS) SPECT, is well established as a diagnostic technique for detection of coronary artery disease (80-82).

Despite the application of nuclear medicine techniques to determine myocardial viability, in addition to the above mentioned shortcomings the modalities are limited by the achievable spatial resolution: an ultimate spatial resolution of approximately 2 mm for PET and a spatial resolution in the order of 4 to 6 mm for SPECT. This clearly limits the precise determination of necrotic of peri-infarcted tissue in the post-MI myocardium.

Computed Tomography

In recent years, cardiac computed tomography (CT) has also been shown to be able to accurately diagnose coronary artery disease, as well as having the potential to provide information on myocardial function, perfusion, structure and viability (59). Until recently CT was not commonly used to evaluate the myocardium; however improvements in whole-heart CT imaging from clinical multi-slice spiral CT (for example improved scan speed, gantry rotation times and spatial resolution along with improved post-processing facilitated single breath-hold) now permits assessment of cardiac function as well as myocardial viability using contrast-enhanced CT. Iodated contrast agents have similar kinetics as gadolinium-DTPA in infarcted and noninfarcted myocardium (83). Therefore, contrast-enhanced chest CT is able to detect initial acute MI as a focal area of decreased left ventricular myocardial enhancement in a specific coronal

artery distribution (83,84). Contrast-enhanced multidetector CT is able to determine and characterize acute and chronic MI via perfusion deficits but determination of cellular viability if only made indirectly.

Magnetic Resonance Imaging

Recent advances in cardiac MRI technology and availability have lead to increased use of the technique for identifying myocardial viability, with its role in cardiovascular imaging also providing information regarding anatomy, function and blood flow. Increased image resolution and the ability to measure sub-cellular metabolites of the myocardium using MR spectroscopy make MRI an attractive imaging modality for the detection and classification of myocardium viability *in vivo* (85).

One application of MRI is to use an extracellular paramagnetic contrast agent, such as gadolinium-DTPA. Gd-DTPA exchanges rapidly between the intravascular and extracellular interstitial space. However, Gd-DTPA does not pass through the membranes of cardiac myocytes so this technique cannot be used as a direct marker of viability. The value of delayed contrast hyper-enhancement imaging is an accurate identification of infarcted myocardium with resolution that allows the transmural extent of myocardial injury to be examined. In 2001, Saeed et al. attempted to use extracellular MRI contrast agent Gd-DTPA to identify the peri-infarcted zones of the reperfused MI rat heart (86). Their results indicated that Gd-DTPA-enhanced regions encompassed both the peri-infarcted and necrosed (non-viable) tissue collectively. This non-specific extracellular uptake was shown to overestimate the infarct zone. However, by subsequent administration of mesoporphyrin (a tumor seeking agent converted into necrotic

myocardium markers (87)), and Gd-DTPA, differences in the tissue enhancement allowed for more accurate estimations of the peri-infarcted tissue to be made. Other studies have suggested that delayed gadolinium-enhanced MRI under-predicts the extent of the necrosed tissue (88). As discussed previously, however, Kim et al. (62) have demonstrated that MRI delayed enhancement methods using Gd could delineate regions of irreversible injury and viable tissue after a myocardial injury. Hyper-enhancement during Gd-DTPA-enhanced cardiac MRI occurs due to the chelated gadolinium diffusing into the interstitial space between cells. However, as mentioned above, Gd-DTPA does not penetrate the cell membrane and can therefore only be used to indirectly infer viability.

Myocardial tagging is a well developed method for the evaluation of regional myocardial contraction (89), and, via indirect methods, viability. In MRI tagging studies, a set of saturation pulses placed in the tissue provide a spatially varying signal intensity pattern that is an intrinsic part of the tissue. The change in shape of this intensity pattern reflects changes in the shape of the underlying tissue (90). In coronary artery disease, regional heterogeneity of myocardial function is common under conditions of ischemia and infarction. The assessment of this heterogeneity can be used to determine the underlying myocardial viability. In acute infarction, normal systolic deformation may be diminished, abolished or reversed to systolic stretching (91). However, in tissue that has either been reperfused or not, the extent of the post-infarction dysfunction far exceeds the extent of necrosis, and even extends beyond the peri-infarct ischemic zone to affect the remote normally perfused myocardium (91,92). Additionally, tagging has demonstrated some residual active myocardial deformation in the center of the infarct regions,

presumably reflecting islands of viable myocardium and/or effects of cross-fiber shortening due to remote contraction (89). Regions of viable but stunned and dysfunctional myocardium adjacent to the necrotic infarct region that return to normal function a few months after infarction can be shown to have some residual contraction early after infarction (93).

Manganese-Enhanced MRI

Despite the number of techniques available for determining myocardial viability, a majority of the contrast agents and technique currently under clinical use and are only able to provide indirect viability estimates via extracellular perfusion, metabolism or contraction measurements. A number of cellular ionic changes, such as Ca^{2+} overload, occur in the ischemic heart that can lead to cellular necrosis (§1.2). The ability to monitor changes in the intracellular handling of these ions could provide a more direct assessment of viability that is not available to perfusion agents. One such example is the MRI molecular contrast agent manganese (Mn^{2+}), an intracellular agent known to act as a Ca^{2+} analogue. Manganese acts to shorten the T_1 relaxation time of tissue in which it is uptake, allowing it to serve as an MR contrast agent (94,95). Mn^{2+} has the potential to enter viable myocardium via voltage gated calcium channels (96-98), accumulating in the myocytes in an additive fashion (99,100). This accumulation in excitable cells, along with its T_1 shortening effect, makes Mn^{2+} a useful molecular contrast agent in the study of calcium flux and viability.

While Mn^{2+} has the potential to be used as a truly intracellular contrast agent, as well as taking advantage of the excellent soft-tissue contrast and high spatial resolution of

MRI, Mn^{2+} is known to be cardiotoxic. Care must therefore be taken in to minimize these toxicity concerns in both preclinical studies and in the clinic to realize the full potential of the technique of manganese-enhanced MRI (MEMRI). The properties and applications of Mn^{2+}, including the use of MEMRI in post-MI studies, are described in more detail in §1.5 and §1.6, following an introduction to MRI and contrast-enhanced MRI (§1.3 and §1.4).

1.3 Magnetic Resonance Imaging (MRI)

Magnetic resonance imaging (MRI) is a noninvasive, nonionizing, high resolution, high contrast cross-sectional (tomographic) imaging modality which provides excellent soft-tissue contrast. These properties have contributed to making MRI the fastest growing modality in recent years (101). MRI is made possible by the physical phenomenon of nuclear magnetic resonance (NMR). Nuclei are comprised of neutrons and protons, so therefore have positive charges. In addition, nuclei with either an odd atomic number or odd mass number have an associated angular momentum. MRI is based on the interaction of this nuclear spin with an external magnetic field, $\vec{B}_0$.

The dominant nucleus in a majority of MRI applications is the proton in hydrogen, ^1H (102). These protons are primarily found in water, with contributions also from lipids. Each nucleus with an intrinsic spin also possesses a microscopic magnetic field. This fact can be derived both quantum mechanically and using a classical approach, and has been demonstrated in many texts (102). Below is a description of how protons

interact within the large $\vec{B}_0$ field (typically 1.5 or 3T clinically, and 7T or 9.4T for small bore magnets) in order to create the MRI signal. The description provides a basic introduction to the topics of MRI, relevant to this dissertation, following the text of Webb (103), as well as texts by Haacke at al. (102), and Prince et al. (101).

1.3.1 Quantum Mechanical Description

Protons have an intrinsic angular momentum, $\overrightarrow{P}$, referred to as "spin", named as such because it can be conceptualized as the proton spinning around an internal axis of rotation (although this is not rigorously accurate). The positively charged proton therefore has a magnetic moment, $\vec{\mu}$, which produces an associated magnetic field, similar to a bar magnet. The angular momentum $\vec{P}$ is quantized, and is determined by the spin quantum number, *I*:

$$\left|\vec{P}\right| = \frac{h}{2\pi}[I(I+1)]^{1/2} \qquad \text{Equation 1.1}$$

where *h* is Planck's constant (6.63×10^{-34} J·s) ($\hbar = h/2\pi$). For protons $I = 1/2$, so the magnitude of $\vec{P}$ is given by

$$\left|\vec{P}\right| = \hbar\frac{\sqrt{3}}{2} \qquad \text{Equation 1.2}$$

The magnetic moment is related to the angular momentum of the proton by

$$|\vec{\mu}| = \gamma\left|\vec{P}\right| \qquad \text{Equation 1.3}$$

where γ is the gyromagnetic ratio. The hydrogen nucleus, ^{1}H, has a gyromagnetic ratio, $\gamma\!\!\!^{-}(= \gamma/2\pi)$ of 42.58 MHz T^{-1}, with other common nuclei for MRI ^{13}C, ^{19}F and ^{31}P having $\gamma\!\!\!^{-}$ values of 10.71, 40.05 and 11.26 MHz T^{-1} respectively. Because $\vec{P}$ is quantized, so too is the value of $|\vec{\mu}|$:

$$|\vec{\mu}| = \gamma\left|\vec{P}\right| = \gamma\hbar[I(I+1)]^{1/2} \qquad \text{Equation 1.4}$$

When placed in a strong external magnetic field $\vec{B}_0$, defined to lie along the z axis, the z component of the magnetic moment is restricted to values given by

$$\mu_z = \gamma P_z = \gamma\hbar m_I \qquad \text{Equation 1.5}$$

where m_I is the nuclear magnetic quantum number, defined to take values of I, I-1, …, −I. There are therefore two values of m_I for the proton, $+1/2$ and $-1/2$, leading to partial alignment with (parallel) or against (anti-parallel) $\vec{B}_0$ respectively.

Because the magnetic moment is discretized, the energy values are also quantized:

$$E = -\vec{\mu}\cdot\vec{B} = -\mu_z B_z = -\gamma m_I \hbar B_z \qquad \text{Equation 1.6}$$

There are therefore two possible interaction energies for the proton. The magnitude of energy absorbed or released by the proton spin system due to transitions between the higher and lower energy states is given by:

$$\begin{aligned}\Delta E &= E\left(m_I = -\frac{1}{2}\right) - E\left(m_I = +\frac{1}{2}\right) \\ &= \frac{1}{2}\gamma\hbar B_0 - \left(-\frac{1}{2}\gamma\hbar B_0\right) = \gamma\hbar B_0\end{aligned} \qquad \text{Equation 1.7}$$

This energy difference can be inserted into the Boltzmann equation to calculate the relative number of nuclei in each configuration:

$$\frac{N_{antiparallel}}{N_{parallel}} = exp\left(-\frac{\Delta E}{kT}\right) = exp\left(-\frac{\gamma\hbar\vec{B}_0}{kT}\right) \qquad \text{Equation 1.8}$$

Here k is the Boltzmann coefficient (= 1.38×10^{-23} J K^{-1}) and T is the temperature in kelvins. Using a first order approximation:

$$\frac{N_{antiparallel}}{N_{parallel}} = 1 - \frac{\gamma\hbar\vec{B}_0}{kT} \qquad \text{Equation 1.9}$$

The magnitude of the MRI signal is proportional to the differences in populations between the two energy levels:

$$N_{parallel} - N_{antiparallel} = N_s \frac{\gamma \hbar \vec{B}_0}{2kT} \qquad \text{Equation 1.10}$$

N_s is the total number of protons in the region of MRI signal generation. For typical clinical field strengths of 1.5 T, the excess of parallel versus anti-parallel oriented protons is approximately five per million.

1.3.2 Classical Description

Due to the fact that the magnetic moment $\vec{\mu}$ does not align itself along the *z*-axis (in fact it can be shown to align at an angle of 54.7°), the external magnetic field creates a torque, $\vec{C}$, while attempting to align $\vec{\mu}$ along $\hat{z}$.

$$\vec{C} = \vec{\mu} \times \vec{B}_0 = i_N |\mu| |B_0| \sin\theta \qquad \text{Equation 1.11}$$

Here i_N is a unit vector normal to both $\vec{\mu}$ and $\vec{B}_0$. The torque leads to precession of the proton around the magnetic field, which can be shown to have an angular precessional frequency, ω, of:

$$\omega = \gamma B_0 \qquad \text{Equation 1.12}$$

ω is known as the Larmor frequency.

Following the previous quantum mechanical description, the amount of energy absorbed or released from the proton spin system following energy state transition can be written as:

$$\Delta E = \hbar \omega \qquad \text{Equation 1.13}$$

The frequency associated with the emission or absorption of the quantum of energy (the photon) is exactly the Larmor precessional frequency. In order for transitions

to occur between parallel and antiparallel energy levels, electromagnetic energy of a given frequency ($f = \Delta E/h$) needs to be delivered to the system. Due to range of required frequencies within the electromagnetic spectrum (~63.9 MHz for a 1.5-T scanner), the applied electromagnetic energy is commonly referred to as radiofrequency (RF) pulses.

Considering the net effect of all the protons in the body, the net magnetization of the sample is defined as M_0:

$$M_0 = \sum_{n=1}^{N_s} \mu_{z,n} = \frac{\gamma h}{4\pi}\left(N_{parallel} - N_{antiparallel}\right) = \frac{\gamma^2 h^2 B_0 N_s}{16\pi^2 kT} \quad \text{Equation 1.14}$$

When placed in an external magnetic field, the random distributions of the magnetic moments as they rotate around $\hat{z}$ give zero contributions of the net magnetization to the x and y components of $\vec{M}$. The net magnetization therefore only has a z component, $M_z = M_0$. Application of a second magnetic field, B_1, oscillating at the Larmor frequency, creates non-zero components M_x and M_y. The resultant effect is that the net magnetization precesses around both the applied B_1 field ($\omega_1 = \gamma B_1$) and around the B_0 field ($\omega = \gamma B_0$). The tip angle, α, is defined as the nutation angle through which M_0 is rotated by the action of the B_1 field:

$$\alpha = \gamma B_1 \tau_{B1} \quad \text{Equation 1.15}$$

α is therefore dependent on the strength of the field, and the duration of the field, τ_{B1}.

Signal detection is achieved by placing an RF coil close to the excited tissue. The time-varying magnetic field produced by the precessing magnetization vectors cause a

current to flow in the coil, following Faraday's law. The current induces a voltage, E, across the ends of the loop that is proportional to change of magnetic flux;

$$E \propto -\frac{d\phi}{dt} \qquad \text{Equation 1.16}$$

Since the magnetization only precesses in the *xy* plane, it is only this plane of magnetization that contributes to the signal, and not the *z* component.

1.3.3 Imaging

MRI utilizes spatially varying gradients to create position dependent magnetic fields. This in turn leads to position dependent resonant frequencies of the proton. For example, for a linear gradient, G_z, applied along $\hat{z}$:

$$\omega_z = \gamma B_z = \gamma(B_0 + zG_z) \qquad \text{Equation 1.17}$$

A system of three separate gradient coils is required to encode the three spatial dimensions:

$$\frac{\partial B_z}{\partial z} = G_z; \frac{\partial B_z}{\partial x} = G_x; \frac{\partial B_z}{\partial y} = G_y \qquad \text{Equation 1.18}$$

A slice select gradient, G_{slice}, is used simultaneously with a frequency-selective RF pulse to select the required imaging slice. Slice select orientations are defined as coronal (*y*), axial (z) or sagittal (*x*), with oblique slices being achieved by the application of two gradients. For an RF pulse applied at a frequency of ω_s and with an excitation bandwidth of $\pm\Delta\omega_s$, only protons with precessional frequencies in the range $\omega_s \pm \Delta\omega_s$ are excited. The slice thickness, T, is determined by:

$$T = \frac{2\Delta\omega_s}{\gamma G_{slice}} \qquad \text{Equation 1.19}$$

Because the frequency response of an RF pulse can be reasonably approximated by its Fourier transform, a sinc-shaped RF pulse is often used to produce a square-shaped frequency excitation profile. The phase, φ_{sl}, accumulated by nuclei during the application of the RF pulse is position dependent:

$$\varphi_{sl}(z) = \gamma G_z z \frac{\tau}{2} \qquad \text{Equation 1.20}$$

where τ is the duration of the pulse, and z is the proton position within the slice. A rephasing gradient can be used to overcome this undesired loss of phase coherence.

A two-dimensional image requires encoding of the two dimensions following slice selection. This is achieved using phase- (G_{phase}) and frequency-encoding (G_{freq}) gradients. The former imposes a spatially dependent phase on the protons, while the latter creates a spatially dependent precessional frequency during signal acquisition. After the slice selection pulse, G_{phase} is applied for a period τ_{pe}. When applied in the direction y, G_{phase} introduces a spatially dependent phase shift;

$$\varphi(G_y, \tau_{pe}) = \omega_y \tau_{pe} = \gamma G_y y \tau_{pe} \qquad \text{Equation 1.21}$$

During data acquisition, G_{freq} is applied (assumed for this discussion to be applied along the x direction) in order to encode the frequency-encoding direction. The combined effects of the phase- and frequency-encoding gradients give a signal:

$$s(G_y, \tau_{pe}, G_x, t) \alpha \int_{slice} \int_{slice} \rho(x,y) e^{-j\gamma G_x x t} e^{-j\gamma G_y y \tau_{pe}} dx dy \qquad \text{Equation 1.22}$$

where $\rho(x,y)$, the proton density, is the number of protons at position (x,y).

To form a two dimensional dataset, the phase-encode gradient is repeated with different values N_p times, with N_r data points acquired during readout. *k-space* can be

used to model how the acquired $N_r \times N_p$ matrix can be transformed into the final image. Defining k_x and k_y as

$$k_x = \frac{\gamma}{2\pi} G_x t, \quad k_y = \frac{\gamma}{2\pi} G_y \tau_{pe} \qquad \text{Equation 1.23}$$

for the frequency- (x) and phase- (y) encoding direction respectively, the signal can be rewritten as:

$$s(k_x k_y) \alpha \int_{slice} \int_{slice} \rho(x,y) e^{-jk_x x} e^{-jk_y y} dx dy \qquad \text{Equation 1.24}$$

A two-dimensional inverse Fourier transform of the *k-space* data above provides an estimate of $\rho(x,y)$, and therefore an image of proton density. The image FOV can also be calculated using *k-space* formalism:

$$FOV_x = \frac{1}{\Delta k_x} = \frac{2\pi}{\gamma G_x t_{dw}}, \quad FOV_y = \frac{1}{\Delta k_y} = \frac{2\pi}{\gamma G_y t_{pe}} \qquad \text{Equation 1.25}$$

t_{dw} is the dwell time, the time between acquisition of successive data points in the frequency-encoding dimension.

1.3.4 Relaxometry

Following excitation of the protons with an RF pulse, the z component of the net magnetization, M_z, is reduced from its equilibrium value of M_0. Additionally, M_x and M_y become non-zero. With time post-excitation these components return to their equilibrium values, characterized by the Bloch differential equations:

$$\frac{dM_x}{dt} = \gamma M_y \left(B_0 - \frac{\omega}{\gamma}\right) - \frac{M_x}{T_2}$$
$$\frac{dM_y}{dt} = \gamma M_z B_1 - \gamma M_x \left(B_0 - \frac{\omega}{\gamma}\right) - \frac{M_y}{T_2} \qquad \text{Equation 1.26}$$

$$\frac{dM_z}{dt} = -\gamma M_y B_1 - \frac{M_z - M_0}{T_1}$$

The above equations contain characteristic relaxation times T_1 and T_2, the spin-lattice and spin-spin relaxation times respectively. The rate of return of M_z to the equilibrium M_0 is governed by T_1, while the return of M_x and M_y to their thermal equilibrium values of zero depend on T_2.

Following an excitation pulse α, the longitudinal magnetization, M_z, at time t is given by:

$$M_z(t) = M_0 \cos\alpha + (M_0 - M_0 \cos\alpha)\left(1 - e^{-t/T_1}\right) \qquad \text{Equation 1.27}$$

The spin-lattice relaxation occurs as protons lose their energy to the surrounding lattice. In contrast, spin-spin relaxation involves the loss of phase coherence between protons in the transverse plane. These two components of magnetization, M_x and M_y, relax back to the thermal equilibrium value of zero with a characteristic time T_2:

$$\frac{dM_x}{dt} = -\frac{M_x}{T_2}, \quad \frac{dM_y}{dt} = -\frac{M_y}{T_2} \qquad \text{Equation 1.28}$$

For example, following an RF pulse, α, along the x axis, the value of M_y is given by:

$$M_y(t) = M_0 \sin\alpha \, e^{-t/T_2} \qquad \text{Equation 1.29}$$

The loss of phase coherence is caused by two different mechanisms. The first, pure T_2, is caused by variations in proton precessional frequencies due to changing magnetic moments as protons interact with their neighboring nuclei. This effect occurs even in a perfectly homogeneous external magnetic field B_0. The second mechanism, termed T_2^+, is caused by variations in the local magnetic field strength at a given location in the body. This can be caused by imperfections in the magnet, or by differences in

tissue susceptibility. Combined, these processes lead to an overall relaxation time T_2^*, given by

$$\frac{1}{T_2^*} = \frac{1}{T_2^+} + \frac{1}{T_2} \qquad \text{Equation 1.30}$$

Different tissues types have inherently different T_1 and T_2 relaxation properties so pulse sequences designed to provide either T_1 or T_2 contrast can be used to gain anatomical of physiological information.

1.4 Magnetic Resonance Imaging Contrast Agents

The bulk of modern clinical radiological imaging relies on the existence of image contrast between tissue types. Before the field of MRI was realized, early experiments were conducted to assess alterations in the spin-lattice (T_1) and spin-spin (T_2) relaxation times in solutions containing paramagnetic ions. The significance of the alterations caused by the ions for the development of MRI was that differences in the local magnetic properties of substances could be probed according to their access to water. In particular, Damadian observed that the relaxation times for tumors in rats presented differently than normal tissue as a function of the decrease in water constrained in tumor tissue (104). Lauterbur shortly thereafter demonstrated the utility of relaxometry in imaging. His classic paper on "zeugmatography" in 1973, which laid the foundation for the frequency-domain MR techniques employed in the modern clinic, used two capillary tubes of water. One of the capillaries was doped with a solution of $MnSO_4$ in order to induce T_1-shortening (105). By varying the power of the RF transmission, two different images

("zeugmatograms") were acquired, which showed variation in the image intensity for the Mn-doped capillary and demonstrated the feasibility of using T_1 variation as an image contrast.

As illustrated in the example above, intrinsic relaxometric differences in tissue can serve as image contrast, and furthermore contrast can be enhanced by agents with different affinities for pathological and healthy tissue. Useful qualities of a contrast agent include: (a) physical properties that affect the local magnetic environment sensitively; and (b) chemical properties that allow the contrast agent to travel to the appropriate region of interest for imaging.

1.4.1 Magnetic Properties of Paramagnetic Agents

In ionic form, elements such as Mn and the lanthanide series exact a dramatic effect on the relaxation properties of water; this results from unpaired electrons in the *d* or *f* atomic shells, which give rise to a strong magnetic moment. Other elemental examples include: Cr^{3+} (3 unpaired electrons), Fe^{3+} (5 unpaired), Ni^{2+} (2 unpaired), Cu^{2+} (1 unpaired, with dipole contributions from the *d* shell), Eu^{3+} (6 unpaired), Gd^{3+} (7 unpaired) and Dy^{3+} (5 unpaired, with contributions from the *f* shell). Although the properties of each ion govern its utility in imaging, the strength of an ions effect on contrast will depend upon the strength of the magnetic moment.

The effect of these ions on the excited ^1H nuclei (which comprise the MRI signal) depends on multiple components. First, the dipoles of the ions may interact with nuclear ^1H dipole, which in turn stimulates spin-flip transitions and accelerates T_1 relaxation of ^1H. The strength of this interaction depends on the approach distance between ^1H and the

ion. If the ion is part of a larger molecule (e.g., deoxyHb), large distance leads to a small interaction. The effect magnitude of the dipole-dipole interaction is also modulated by the correlation time which determines the duration of the coupling between ^{1}H and ionic dipole. To increase coupling, the rotational rate of the ion or chelating molecule should be similar to the excitation frequency of ^{1}H. If the ion is not chelated, it will have a wide range of rotational velocities compared to the excitation frequency of ^{1}H. In this case, the dipole-dipole interaction is weaker. For suitable rotational rates, the correlation time will depend on the electron spin relaxation time of the agent, where slower electronic relaxation results in greater coupling of the dipoles. Ultimately, relaxation rates should be comparable to the ^{1}H Larmor frequency for an agent to be effective at increasing T_1 relaxation. Electron spin relaxation times for ionic Mn, and Gd are $\sim 10^{-8} - 10^{-10}$ seconds (106) and appropriate for the range of Larmor precessional frequencies in clinical scanners. Larmor precession, as described in the previous subsection, refers to the precession of the magnetic moments of electrons, atomic nuclei, and atoms about an external magnetic field. Those effects which lead to spin-flip transitions also result in randomization of ^{1}H phase after de-excitation and result in increased local T_2 relaxation. Finally, the presence of the paramagnetic dipoles around less mobile ^{1}H nuclei (e.g., tissue containing macromolecules) alters the local precessional frequency, which further increases T_2 relaxation.

Consideration of these effects determine the ratio of T_1 and T_2 relaxation rates for a given contrast agent concentration. Relaxation describes several processes where nuclear magnetization prepared in a non-equilibrium state return to the equilibrium distribution in the external magnetic field (107). Ions with longer spin relaxation time

(e.g., Mn^{2+}, Gd^{3+}) tend to stimulate spin-flip transitions effectively and are useful for enhancing contrast positively on T_1-weighted images. At higher concentrations, they are also useful for increasing T_2 relaxation. Typically, paramagnetic agents, such as chelated Gd, increase T_1 and T_2 relaxation at the same rate per mM (108). Since this rate is the same, the change of T_1 relaxation per mM is larger by proportion than the change in T_2 relaxation. On the other hand, ions with shorter spin relaxation times, such as dysprosium (Dy^{3+}), do not stimulate spin-flip transitions readily (108). These ions function primarily to vary the local Larmor frequency and to decrease the intensity on T_2-weighted images. While Mn^{2+} may not have as strong of a magnetic moment as other agents such as Gd^{3+}, the T_2 relaxation rate ($R_2 = 1/T_2$) of water containing Mn^{2+} ions at 1.5T grows at 10 times the rate per mM as compared to the T_1 relaxation rate ($R_1 = 1/T_1$). This makes Mn^{2+} a valuable agent for both T_2 and T_1 imaging.

Another avenue to increase T_1 relaxation is to chelate the paramagnetic ions to decrease their rotational velocity and increase the correlation time. An added benefit of using a chelate is that for less chemically-reactive but toxic metals, such as Gd and Mn, the chelated complex is excreted from the body within a short timescale (~ a few hours). This greatly decreases potential toxic side effects. Examples of chelates that have been used include: Gd-DTPA, Gd-DPDT, Gd-DOTA, and other macromolecules such as Mn-DPDP, Cr-EDTA, Dy-EDTA. Nonionic molecules have also been utilized to prevent the release of the ion and to decrease the rotational velocity.

Quantitatively, alterations in the relaxation rates (R_1 and R_2), can be described in terms of the relaxivities (r_1 and r_2) and the concentration C of the contrast agent within the region of interest (109):

$$\Delta R_1 = \frac{1}{T_{1,C}} - \frac{1}{T_{1,0}} = r_1 C \qquad \text{Equation 1.31}$$

Here, $T_{1,C}$ is the longitudinal relaxation time of the tissue containing a concentration C of contrast agent, and $T_{1,0}$ is the corresponding value without the contrast agent.

1.4.2 FDA Approved Clinical MRI Contrast Agents

A list of clinically approved contrast agents are listed in Table 1.2, along with some of their characteristics. At the time of writing there are 5 clinically approved Gd-based contrast agents, MultiHance® (110), Magnevist® (111), Omniscan™ (112), ProHance® (113) and OptiMARK™ (114). Additionally, there is one Mn-based contrast agent, TESLASCAN® (115), and one Fe-based contrast agent, Feridex I.V. ® (116).

1.5 Manganese-Enhanced MRI (MEMRI)

Ionic manganese in divalent form (Mn^{2+}) is a particularly useful contrast agent for its sensitivity, as well as its function as a calcium (Ca^{2+}) analogue. Consequently, the use of Mn^{2+} in imaging studies has increased dramatically as molecular medicine incorporates clinical imaging techniques (117). As a paramagnetic MRI contrast agent, manganese (Mn^{2+}) has been found to be particularly useful for cardiac research and research in the brain (117,118). The ability to monitor changes in the intracellular handling of Ca^{2+} ions in the heart could provide a more direct assessment of cardiac viability that is not available to other imaging modalities or MRI contrast agents (§1.2.1). Manganese-enhanced MRI (MEMRI), an intracellular molecular imaging technique, is

able to fill the gap left by the other imaging techniques, and has the potential to be used a true viability agent. Section 1.6 discusses the use of MEMRI in cardiac studies in detail.

Within the central nervous system (CNS), Mn^{2+} enters excitable cells via major routes of transport for Ca^{2+} and Na^{+}, such as voltage-gated Ca^{2+} channels, the NCX, the Na^{+}/Mg^{2+} antiporter, and the active Ca^{2+} uniporter in mitochondria (119,120). Once inside the cells, Mn^{2+} can bind with high affinity to Ca^{2+} and Mg^{2+} binding sites in proteins and nucleic acids, or it can be transported anterogradely in axonal tracts (121,122) and released into the synaptic cleft along with the neurotransmitter glutamate (123). Based on such properties, three major applications of neuronal MEMRI have been defined: (1) to enhance the cerebral neuroarchitecture; (2) to trace neuronal tracts in the living brain; and (3) to demarcate active regions of the brain. Mn^{2+} has also been used as a cell labeling MRI contrast agent (9).

Both the physical and chemical characteristics of Mn^{2+} are reviewed in the following subsections, with a thorough introduction to the use of MEMRI in cardiac studies presented in §1.6.

Table 1.2 FDA approved clinical MRI contrast agents.

	MultiHance® (110)	Magnevist® (111)	Omniscan™ (112)	ProHance® (113)	OptiMARK™ (114)	TESLASCAN® (115)	Feridex I.V.® (116)
Relaxivity, r_1/r_2 ($mM^{-1}s^{-1}$)	9.7/12.5	4.9/6.3	5.4/-	5.4/-	NR	NR	NR
Mean Distribution (min)	5.0±0.7 to 36.3±4.3	12±7.8	3.7±2.7	12±2.4	13.3±6.8	NR	NR
Elimination Half-life (min)	70.2±15.6 to 121.2±36	96±7.8	77.8±16	94.2±4.8	103.6±19.5	Plasma Half-life; 20 min	144±12 h
FDA Approved Indications and Usage	CNS	CNS, head & neck, body (excl. heart)	CNS, body (excl. heart)	CNS, head & neck	CNS, liver	Liver	Liver
Adult Dose (mmol kg^{-1})	0.1	0.1	0.1	0.1	0.1	5μmol kg^{-1}	0.05 mL kg^{-1}

1.5.1 Biochemical Properties of Mn^{2+}

Unlike the typically toxic heavy metals in the lanthanide series, transition elements such as Mn, Fe, and Cr are utilized to some degree by the human body. This property makes them useful as a contrast agent for labeling metabolic processes. Considering the normal human intake, 20 μg of Mn is retained in the body per day. The U.S. Federal Drug Administration currently recommends a daily intake of 5 mg day^{-1}, and the American Medical Association Nutrition Advisory Group recommends a dosage of 0.15-0.8 mg day^{-1}. A healthy human body is capable of tolerating a wide range of variation, and normal whole blood ranges have been listed as 0.4-1.4 ng mL^{-1} (124). One case study described a patient with a blood Mn^{2+} value of 3.7 ng mL^{-1} (125).

Manganese is normally eliminated via the biliary tract. Overload of manganese in the body may result from high intake of supplements (126), pathological conditions such as hepatobiliary disease, or environmental exposure in occupations such as welding (127). Manganese poisoning may present neurotoxic symptoms such as Parkinsonian-like behavior, psychological change, anxiety, or seizures (125,127). Cardiovascular effects include tachycardia or hypotension. The biological role of Mn in the body is for regulation of enzymes. Chemically, Mn^{2+} is similar to Ca^{2+} and Mg^{2+} and has a high affinity for protein sites where these elements may be present. The ionic radius of Mn^{2+} (0.08 nm) is intermediate between Ca^{2+} (0.1 nm) and Mg^{2+} (0.065 nm).

1.6 Cardiac MEMRI

A majority of calcium enters myocytes through voltage-gated calcium channels, initiating contraction. Calcium exits through the sarcolemma sodium calcium exchanger (NCX) and plasma membrane calcium pump ATPase (PMCA) for relaxation (§1.1). Inflowing calcium triggers the release of additional calcium from the sarcoplasmic reticulum (SR) by activation of the ryanodine receptors (RyR) in the SR membrane. Although intracellular calcium is a key regulator of myocardial contraction, there are only a few ways to assess this important factor. Fluorescent techniques have been widely used in isolated cardiac myocytes, but these techniques cannot be extended to *in vivo* studies. MRI calcium probes, such as fluoroBapta and DOPTA-Gd, have also not found widespread use.

1.6.1 Mn^{2+} Uptake by Myocardial L-Type Ca^{2+} Channels

One possible technique for assessing intracellular calcium is to use a paramagnetic agent that has physical properties similar to calcium, such as manganese ions (Mn^{2+}). Mn^{2+} has an ionic radius similar to that of Ca^{2+}, and is handled similarly in many biological systems. For example, Mn^{2+} is known to enter cardiac myocytes through voltage-gated calcium channels (99,128). Mn^{2+} is also an excellent T_1 contrast agent (94). These properties of Mn^{2+} were recently used to detect and visualize cell activity using MRI. The results of those studies indicate that Mn^{2+} might be a useful MRI agent for quantifying relative rates of calcium influx in the heart.

Infusion of Mn^{2+} via the mouse tail vein leads to significant signal enhancement in T_1-weighted images (99); an increase of approximately 40–50% in healthy hearts.

Dobutamine (increased inotropy) or diltiazem (decreased inotropy) have been used with MEMRI experiments to examine whether alterations in cardiac inotropy affect the MRI signal enhancements detected with Mn^{2+} infusion. Dobutamine has been shown to increase the steady-state signal enhancement in the left ventricular free wall (LV Wall) of mice, and diltiazem decreased the steady-state signal enhancement significantly when compared to control conditions (99). Both results lend themselves to the conclusion that Mn^{2+} is transported via the L-Type Ca^{2+} channel, and that the rate of Mn^{2+} enhancement is proportional to changes in Ca^{2+} influx.

At 14.0 nmoles min^{-1} g^{-1} BW infused Mn^{2+}, dobutamine increased the steady-state signal enhancement by 102% for both the interventricular septum and LV Wall compared to Mn^{2+} infusion alone. Similar increases in signal enhancements were detected following dobutamine administration in mice infused with 3.3 nmoles min^{-1} g^{-1} BW $MnCl_2$, relative to $MnCl_2$ infusion alone. Signal intensity decreases of 69% and 59% for diltiazem plus Mn^{2+} compared to Mn^{2+} infusion alone have been observed in the interventricular septum and LV wall respectively (99).

Unfortunately Mn^{2+} is known to be cardiotoxic at high doses (129). Indeed, it is the toxic properties of Mn^{2+} that have limited its development as an MRI contrast agent. However, Mn^{2+} is also an essential element for maintaining cell viability. With the increase in stability and sensitivity of MRI scanners it should be possible to use much lower doses of Mn^{2+} than have been used in early studies to determine the suitability of Mn^{2+} as an MRI contrast agent. Thus far, data in mice have indicated that subtoxic Mn^{2+} doses can cause significant enhancement of the heart without affecting left ventricular ejection fraction or heart rate after the MRI experiments (99). These mice then survived for at least one month

after the MRI experiments. However, the reliance of T_1 weighted images on short TRs rather than the inversion recovery pulse sequence means these protocols will not be optimally designed for MEMRI studies. For the same Mn^{2+} dose the dynamic enhancement range using an optimal pulse sequence may be increased by a factor of 2 over more traditional T_1 weighted protocols. Furthermore, signal enhancements detected in experiments to data have been relatively large, indicating that still lower doses of Mn^{2+} could be used.

1.6.2 Assessment of Myocardial Viability

Alterations in myocyte Ca^{2+} regulation may be critical for both the mechanical dysfunction and the arrhythmogenesis associated with congestive heart failure (12,130). Recent advances have improved the feasibility of studying ischemic heart disease with MRI (131). MR contrast agents can be applied in a variety of ways to improve MRI sensitivity for detecting and assessing ischemically injured myocardium. Contrast-enhanced perfusion MRI has been used to explore disturbances in large (angiography) (132) and small coronary arteries (myocardial perfusion) (133). It is known that the size of the abnormal signal area on Gd-enhanced T_1-weighted MRI correlates relatively well with infarct area (62). However, the size of the nonperfused area on first-pass perfusion images is often smaller than the final infarct area. Therefore, there is a need to obtain intracellular measures of cell viability not achievable with perfusion agents.

The application of Mn^{2+} contrast enhancement to cardiac MRI, either in the form of paramagnetic free manganese ($MnCl_2$) or in a chelated form (manganese dipyridoxyl diphosphate, MnDPDP), allows for the potential monitoring of calcium dynamics. This is

of particular importance in studies of the infarcted heart. MEMRI has previously been used to detect cell viability in the ischemic heart (134,135). A study to assess whether viable myocardium can be distinguished from necrosed tissue using MnDPDP-enhanced MRI has been conducted in rats (136). Infusion of various doses of the chelated Mn contrast agent demonstrated that Mn was retained in the viable myocardium, but was shown to have rapid clearance from the infarcted region. This demonstrated the ability of the contrast agent to differentiate infarcted tissue from viable tissue. In its free paramagnetic form, $MnCl_2$ has similarly been shown to demarcate infarcted zones in mice (137) and dogs (10).

To date there is some inconsistency between *in vitro* and *in vivo* results. *In vivo* manganese-enhanced MRI has observed signal attenuations in the affected myocardium of mice (137), rats (138) and larger mammalian species (139). However, *in vitro* studies have shown enhanced Ca^{2+} influx as a compensatory process (140). Camelliti, et al. (141) have presented *ex vivo* results demonstrating small islands of viable myocytes in ischemic regions, with potentially reduced perfusion. These islands could potentially be used to explain the non-zero Mn^{2+} uptake in the ischemic regions. Additionally, limited perfusion in the affected tissue could also explain the disparity. Clearly, there is a need for ongoing MEMRI research to address this inconsistency.

1.7 T_1-Mapping

Divalent manganese (Mn^{2+}) has been used as a molecular MR contrast agent in many biological applications due to it T_1 shortening effect. Indeed, T_1 weighted images

have been shown to provide contrast following uptake of Mn^{2+}. In many MEMRI experiments there are a large range of T_1 values, such as those experienced in the mouse brain following systemic administration of $MnCl_2$ (142). T_1 weighted images need to be optimized in order to detect a specific range of T_1 values. However, it is not typically possible to detect the complete range of T_1 values using just one protocol, and acquisition of multiple images is required. Similarly, small changes in T_1 values can provide important information that might not be detectable with T_1 weighted protocols. Utilization of a quantitative technique would provide a greater sensitivity to a wide range of T_1 changes, and would also allow for reduced doses of Mn^{2+} to be administered. By reducing the dose, potential cardiotoxic and neurotoxic effects caused by high levels of Mn^{2+} can be minimized.

The use of Mn^{2+} to produce shortening of the spin-lattice relaxation time, T_1, was proposed soon after the conception of using NMR for radiological imaging. In 1973 Lauterbur used Mn^{2+} to shorten T_1 in a pure water sample. As T_1-mapping techniques were developed, the field of MEMRI started to take advantages of their quantitative nature. Experiments to measure tissue T_1 and T_2 relaxation times were conducted as early as 1971, where discriminations between normal tissue and malignant tumor specimens were discerned from their relaxation times (104). Mansfield et al. extended these techniques to imaging biological structures. In 1970, a commonly used method to calculate T_1 values was conceived by Look and Locker (143,144). Using this technique, T_1 relaxation times can be estimated using a periodic train of excitation pulses following an inversion pulse, sampling multiple time points during signal recovery. This method can significantly reduce the scanning time without sacrificing accuracy, and has been shown to have almost the same

efficiency as spin-echo IR methods in terms of the SNR per unit time (145,146). The first published biological T_1-maps were by Pykett et al. (147) in 1978. These images provided anatomical insight into a tumerous rat leg.

Quantitative MEMRI T_1-mapping has been applied to numerous fields. The quantitatively derived results using such techniques provide an insight into altered Ca^{2+} handling dynamics, and may prove useful in determining potentially salvageable tissue in the diseased heart. Elemental analysis, a process where a sample of the blood or tissue material is analyzed for the elemental and sometimes isotopic composition, can be used to obtain the *ex vivo* Mn^{2+} content for a given tissue sample. The analysis can be qualitative (determining what elements are present), and it can be quantitative (determining how much of each are present). By correlating regional T_1 values to elemental analysis sample data, estimates of the absolute regional Mn content can be made *in vivo* using Equation 1.31, which can be of particular importance under diseased conditions where alterations in Mn^{2+} and Ca^{2+} handling are expected.

One application of MEMRI T_1-mapping has been to improve neuronal tract tracing techniques (145). In neuronal tract tracing, Mn^{2+} causes a wide range of T_1 changes, varying from short T_1 values at the injection site to longer values in more distant regions. This particular study used a Look Locker T_1 mapping protocol enabling sufficient sensitivity to detect the full range of T_1 values with full brain coverage in a reasonable time. It was concluded that the use of quantitative techniques in MEMRI should allow for the study of more extensive pathways and should also allow for lower Mn^{2+} doses administrations.

T_1-mapping has also been applied to studying the common neuropsychiatric condition hepatic encephalopathy (HE) (148). Within clinically relevant acquisition times significant correlations between the change in T_1 and HE severity have been shown in the globus pallidus, the caudate nucleus, and the posterior limb of the internal capsule.

MRI has been used as a modality to track cellular migration. A majority of this work to date has been performed using ultra-small iron oxide particle. However, recently $MnCl_2$ has been shown to be a potential alternative to iron oxide in cell labeling studies (149). One of the limitations of cell labeling with iron oxide particles is that a decrease in signal is observed for the T_2^* effects which requires homogeneous images. In an ideal experimental system, all nuclei in a given chemical environment within a magnetic field possess the same spin frequency. However, in a real system, there are minor differences in chemical environment which can lead to a distribution of resonance frequencies around the ideal system. Over time, this distribution can lead to a dispersion of the tight distribution of magnetic spin vectors, and loss of signal coherence leading to the corresponding transverse relaxation time constant, T_2^*, which is usually much smaller than T_2. Mn^{2+} enhancement causes signal enhancement and alleviates some of these drawbacks. In addition, only a relatively short amount of time is required to achieve labeling of cells with $MnCl_2$. Within this study by Aoki et al., T_1-maps were calculated following a 1 hour period of human lymphocytes incubation with 0.05-1.0 mM $MnCl_2$. Significant signal enhancement was observed. This suggests that $MnCl_2$ might be an alternative to iron oxide cell labeling for MRI-based cell migration studies.

1.7.1 Look Locker T_1-Mapping

One potential goal of using a quantitative technique for cardiac MEMRI studies is to estimate the delivery of Mn^{2+} to viable myocardium *in vivo*, with applications to assess regional Mn^{2+} handling alterations in a myocardial infarction model. One such technique used to quantify T_1 values, developed by Look and Locker, was previously introduced. Following the description of Look-Locker (LL) T_1-mapping presented by Chuang et al. (145), multiple time points are sampled during the relaxation following an inversion pulse separated by the interexcitation interval τ. This sampling is achieved using $N \times \mathrm{RF}$ pulses of the same flip angle (FA), α. Both Look and Locker (144) and Brix et. al (150) derive an expression for the signal evolution in the above LL T_1-mapping protocol. The partially relaxed longitudinal magnetization, $M(n)$, before each excitation pulse, can be described by an exponential recovery with time constant T_1^*.

$$M(n) = M(\infty) - \left[M(\infty) - M(0)\right]e^{-n\tau/T_1^*}, n = 0,1,\cdots,N-1 \qquad \text{Equation 1.32}$$

where, $M(\infty) = M_{eq}\dfrac{1-e^{-\tau/T_1}}{1-e^{-\tau/T_1^*}}$. M_{eq} is the equilibrium longitudinal magnetization and the effective longitudinal relaxation time constant, T_1^* is related to the actual T_1, α and τ by:

$$\frac{1}{T_1^*} = \frac{1}{T_1} - \frac{\ln\cos(\alpha)}{\tau} \qquad \text{Equation 1.33}$$

The T_1 value for each pixel can be calculated by obtaining T_1^* from a three-parameter fit to Equation 1.32, and substituting this value into Equation 1.33. However, this assumes that the exact FA is known for each pixel, which is a poor assumption. Due to inhomogeneities in the B_1 field caused by imperfect excitation pulses and the RF coil

profile, the FA differs from the intended value. This can be overcome by taking the relationship between $M(\infty)$ and $M(0)$, with T_1 being simplified to $T_1^* M(0)/M(\infty)$ when $\tau << T_1^*$, as shown by Steinhoff et. al (151). Chuang et al. (145) demonstrate how $M(\infty)/M(0)$, T_1^*, and therefore T_1, can be obtained independent of knowing the precise FA, and without the requirement that τ and T_d, the delay time between the inversion and the first excitation pulse of a slice, are short. This is achieved under the assumption that the longitudinal magnetization before each inversion pulse has reached steady state.

Estimates of T_1 acquired by the imaging techniques both prior to and following Mn^{2+} administration can be applied to Equation 1.31 to obtain *in vivo* estimates of the regional Mn content, potentially containing information regarding the Ca^{2+} content in that tissue.

1.8 Clinical Manganese Based Contrast Agents

1.8.1 Development of MnDPDP

Manganese dipyridoxyl diphosphate (MnDPDP) is approved as an i.v. contrast agent for MR imaging of the liver. MnDPDP is a chelate consisting of the organic ligand dipyridoxyl diphosphate (DPDP) and Mn^{2+}. Following i.v. injection, MnDPDP is metabolized by a process involving dephosphorylation of MnDPDP to MnPLED (manganese dipyridoxyl ethyliamine), and exchange of Mn^{2+} for Zn^{2+} (152) with the consequent release of manganese ions. In humans the rate of total manganese plasma

clearance is multiphasic (152). The initial clearance half-life lasts for less than 20 minutes, with the longer terminal elimination phase occurring between 5 and 11 hours. Following i.v. injection of MnDPDP, the released manganese accumulates in the liver, bile, pancreas, kidneys and cardiac muscle (153). Following oral intake the manganese accumulation occurs only in the liver and bile (154). Due to its T_1 relaxation effect, the released Mn^{2+} ions act as an MR contrast agent (94,95), which allows MnDPDP to be used as an MR contrast agent.

With a wide range of application in both humans and animals, MnDPDP has been shown as a gradual or slow-release complex for Mn^{2+} uptake in hepatocytes (153,155,156). Similarly, animal studies have shown that Mn^{2+} release from MnDPDP can be used to demarcate infarcted (136,157) and stunned (158) myocardium.

One clinical concern over the use of MnDPDP is the potential neurotoxic effects caused by manganese overexposure. The brain is a major target organ for Mn toxicity and retains Mn much longer that other tissues. Mn neurotoxicity results in progressive neurodegenerative disorders of the extrapyrimidal system, similar to Parkinson's disease (119,126). Such a disorder is the result of chronic overexposure to Mn, with limited treatment options and no cure. However, no cases of Mn intoxication have been reported following singular low doses of MnDPDP, even after several years of clinical use (119). It is unlikely that a single dose of MnDPDP would lead to any neurological consequences, but care should be taken to avoid repeated exposure to Mn. Studies in rodents and dogs (159) have indicated that a single i.v. injection of MnDPDP is tolerated at doses of approximately 400 times the clinical dose, up to 2000 μmol kg^{-1}. Combinations of clinical and non-

clinical studies demonstrate that MnDPDP has a good safety profile for clinical use as an i.v. hepatobiliary MR contrast agent.

1.8.2 MnDPDP in the Liver

MnDPDP is clinically approved for MR imaging of the liver, and is available in two preparations; one for a 1-2 min injection (USA) at a concentration of 0.05 mol L^{-1}, and one for 10-15 min infusion (Europe) with a concentration of 0.01 mol L^{-1} (160). Primarily developed for imaging of the hetatobiliary system (161), MnDPDP causes homogeneous liver enhancement following injection in healthy patients (156). The liver signal enhancement begins within 1-2 minutes following injection, with the maximum enhancement seen within 5-10 minutes after infusion. The enhancement then persists for several hours.

Hepatocellular carcinoma (HCC) is curable by liver transplantation if the tumor is small (<3 cm) and solitary (162). Therefore the accurate and timely diagnosis and characterization of liver tumors is important for a successful prognosis. In 1997, Kane et al. conducted a study comparing the lesion detection and characteristic predicted by MnDPDP-enhanced MR imaging to surgical excision and pathological examination (163). As part of a phase III clinical trial, 90 patients under consideration for surgical treatment of the neoplastic hepatic disease were infused with 5 μmol kg^{-1} MnDPDP. Comparisons were made between both spin-echo and gradient-echo T_1-weighted MR images pre- and post-contrast. These pre-operative findings were compared to intra-operative ultrasonography and histology of the resected liver specimens. Eleven out of 14 patients with liver metastases showed a good correlation between the MR images and the hepatic disease. For

patients with primary liver tumors, 5 out of 6 MR findings correlated to the hepatic disease. The authors concluded that it is possible to characterize liver lesions using MnDPDP-enhanced MRI. MnDPDP is considered important to the assessment of patients with liver disease where accurate decisions for surgical planning are imperative.

More recent research has been into the detection of colorectal hepatic metastases using MnDPDP (164). Colorectal hepatic metastases show high signal restricted diffusion on diffusion-weighted MRI (DWI), as compared to the healthy liver tissue. The diagnostic accuracy of three different MR imaging protocols were compared: MnDPDP, DWI and combined MnDPDP and DWI. It was found that the combination of DWI and MnDPDP-enhanced MR imaging resulted in the highest diagnostic accuracy and increased the sensitivity without loss in specificity.

In a European phase III clinical trial, MnDPDP was shown to be a safe contrast agent at the approved dose of 5 μmol kg^{-1}, and at a slow infusion rate of 2-3 ml min^{-1} (165). This study showed MnDPDP to be effective and safe in enhanced MR imaging of the liver, with adverse effects reported in only 7% of the 624 patients involved. A majority of the reported adverse effects were nausea, headache and pruritus.

1.8.3 MnDPDP in Cardiac Research

Manganese-enhanced MRI (MEMRI) has a number of applications to cardiac studies. As discussed previously, Mn^{2+} is an excellent cardiac contrast agent candidate due to its similarity to Ca^{2+}. Initial studies using manganese contrast demonstrated the ability to demarcate infarcted regions in animal hearts, both *ex vivo* (166,167) and *in vivo* (136,157,168). The effect of MnDPDP-enhanced MRI on different animal models has been

studied, with myocardial R_1 $(= 1/T_1)$ increasing steadily with i.v. doses of MnDPDP up to 20 μmol kg^{-1} in pigs (169) and up to 100 μmol kg^{-1} in rats (136,157).

The latter two studies looked at the effect of MnDPDP in rat MI models. The necrosed myocardium showed a higher rise in R_1 than the viable myocardium over the first 5-10 minutes. However, while the viable myocardial R_1 values continued to rise with time, the necrosed tissue R_1 values decreased. This trend continued over several hours, with the necrosed regions being clearly discernable, even at low doses of MnDPDP.

More recently the relaxation enhancing properties of MnDPDP in the human myocardium has been studied (170). In this particular investigation, R_1 measurements were calculated for the myocardium of fifteen healthy patients using an inversion recovery (IR) turbo fast low-angle shot (FLASH) sequence, both before and at various time points post i.v. MnDPDP injection. Left ventricular (LV) wall R_1 values increased on average 37% one hour following a MnDPDP dose of 5 μmol kg^{-1}, the clinical liver dose. This elevation remained for approximately two hours, before a gradual decline lasting over 24 hours. Varying the dose of MnDPDP injections did not cause the R_1 values to increase linearly.

Following this work, Skjold et al. performed a study on patients with recent myocardial infarction (11). The aim was to see if regions of the affected LV wall would show signs of reduced R_1 compared to healthy, viable myocardial tissue after a low dose of MnDPDP. The results showed that reduced wall thickening at the infarction site was associated with reduced contrast enhancement. On the other hand, the remote regions showed larger increases in R_1. This is most likely due to the selective and slow Mn accumulation in viable myocytes. Conclusions drawn from this work suggest that the demarcation of infarcted myocardial regions is possible with manganese-based MRI

contrast. The combination of low doses of MnDPDP with R_1 mapping techniques can reliably identify infarcted regions.

Studies using clinical MnDPDP have demonstrated that Mn^{2+} is released slowly from DPDP (171,172). These findings helped to more fully evaluate those mechanisms which enhance myocardial signal intensity due to MnDPDP (173-176). MnDPDP has also been found to be retained in non-ischemic myocardial tissue (136). Encouragingly, MnDPDP (170) and EVP-1001 (a newer developed Mn^{2+} -based contrast agent in Phase II trial) have both been used to image human myocardium.

One concern with the administration of MnDPDP is the potential cardiac side effect caused by the reaction of the released Mn^{2+} with the myocardial processing of Ca^{2+}. However, it has been shown that MnDPDP is well tolerated in the rat heart up to concentrations of 250 μmol L^{-1} and is approximately 10 times less cardiotoxic than $MnCl_2$ (129).

1.8.4 Further MnDPDP Applications

In addition to liver and heart studies, pancreatic and neuronal manganese accumulation has opened avenues for MEMRI research. MEMRI has been used to develop techniques for improving anatomical and functional imaging of the rat brain (142,145). As discussed previously, toxicity is a concern that needs to be addressed when applying MEMRI to the CNS. Use of a Mn^{2+} releasing contrast agent, such as MnDPDP, could avoid the high initial Mn^{2+} concentrations following local injections into the CNS. Olsen et al. establish that MnDPDP gives sufficient Mn enhancement compared to $MnCl_2$ in the CNS (177). The group injected both MnDPDP and $MnCl_2$ intravenously into a rat model to

produce functional visual pathway images. Significant contrast enhancement of the retina and optic nerve on T_1-weighted FLASH MR images were produced 12-24 hours post-MnDPDP injection. The signal enhancement was similar to that of the $MnCl_2$ injection. The conclusion drawn from this study was that Mn^{2+} was released from MnDPDP in sufficient amounts to obtain functional tracing of the adult rat primary visual pathway.

There are a wealth of studies, both completed and ongoing, into the use of MnDPDP as a pancreas-specific contrast agent (178). A 20 min infusion of 10 μmol kg^{-1} BW MnDPDP in healthy volunteers resulted in an increase in gradient-echo T_1-weighted image signal-to-noise of 98±13% in the pancreatic parenchyma (179). The use of MnDPDP-enhanced imaging of pancreatic ductal adenocarcinoma was assessed in a phase II trial (180). The tumor contrast-to-noise was increased 209% in gradient-echo T_1-weighted images after MnDPDP injection. In contrast, the tumors showed no significant increase in signal intensity following injection. The fact that MnDPDP is only taken up by the normal pancreatic parenchyma gives this contrast agent a theoretical advantage over Gd. Further work on MnDPDP pancreatic mass detection has shown that MnDPDP facilitates staging of pancreatic tumors by detection of metastatic lesions in the liver. Here it was suggested that MnDPDP could be useful in the differential diagnosis of patients with pancreatitis. The degree of uptake homogeneity could help diagnoses between focal pancreatitis and malignant tumors.

1.9 Pharmaceutical Alterations of Ca^{2+} Handling

1.9.1 Positive Inotropic Agents

Heart failure is primarily caused by a defect in cardiac contractility, and as such drugs that increase the inotropy and contractility (positive inotropes) have long been used a pharmacologic agents (181). Classical inotropes, such as beta-agonists (dobutamine, dopamine) and phosphodiesterase inhibitors (milrinone) have been shown to improve clinical symptoms and hemodynamics of acutely decompensated chronic heart failure (ADHF) patients (182). However, these classical inotropes can promote and accelerate some pathophysiologic mechanisms causing further myocardial injury leading to increased short- and long-term mortality (183,184). This has lead to the introduction of more clinically cardioprotective inotropes, such as levosimedan (185,186).

Classical inotropic agent dobutamine, one of the most potent inotropes currently available in the clinic (187), exists as a racemic mixture of dextroisomers and levoisomers, which are potent β- and α-adrenergic agonists, respectively (188). Dobutamine increases contractility by inducing an increase in calcium released from the SR by increasing the intracellular cyclic adenylate monophosphate (cAMP) levels (181). Dobutamine is known to increase intracellular Ca^{2+} while also increasing the stroke volume. However, increased contractility is achieved at the expense of increased myocardial oxygen demand, potentially exacerbating the myocardial ischemia and leading to increased myocardial apoptosis in the presence of hibernating myocardium (189).

As discussed in §1.6, dobutamine has been used concurrently with MEMRI studies in mice to demonstrate the effect of altering Ca^{2+} influx on Mn^{2+} handling. Increases in the

steady-state signal enhancement in the left ventricular free wall (LV Wall) of mice following dobutamine administration were observed, relative to mice receiving no dobutamine (99). This is in agreement with the fact that Mn^{2+} is transported via the L-Type Ca^{2+} channel, and that the rate of Mn^{2+} enhancement is proportional to changes in Ca^{2+} influx.

1.9.2 Sodium-Calcium Exchange Inhibitors

Protocols that selectively inhibit the NCX are useful for investigating the roles of the NCX and PMCA, and have been shown to have potential therapeutic effects during myocardial ischemic-reperfusion injuries (190). During Ca-dependent arrhythmias NCX inhibitors will change the degree of cellular Ca^{2+} overloading and will also change the membrane current. When the NCX is functioning to pump Ca^{2+} from the cell, the NCX inhibitor is expected to increase the intracellular Ca^{2+} concentration, inducing cardiotonic and hypertensive effects in the circulatory system (191). When the NCX works as a pathway for Ca^{2+} entry - as it does during ischemia/reperfusion injury and digitalism - the NCX inhibitor is expected to guard against Ca^{2+} overloading.

In 1984 the first NCX inhibitor drug, an amiloride analogue 3',4'-dichlorobenzamil (DCB) (192), was reported. The first potent and relatively selective inhibitor of the NCX (193) was KB-R7943 (194). New benzyloxyphenyl analogues have more recently been developed and are both selective and potent NCX inhibitors. These include SEA0400 (195), SN-6 (196) and YM244769 (197). These newer inhibitors are trypsin-insensitive drugs that act from extracallular or intramembrane sites. Amongst the three, SEA0400 is the most potent and selective inhibitor (190).

Given the potential clinical benefits of inhibiting the NCX during states of myocardial ischemia reperfusion, studies have been conducted to clarify the importance of this efflux mechanism. SEA0400, 2-[4-[(2,5-difluorophenyl)methoxy]phenoxy]-5-ethoxyaniline, has been shown to provide protection from cardiac ischemia/reperfusion injury and digitalis induced arrhythmia (190,198,199) and from myocardial stunning (200). The drug inhibits salt-dependent hypertension induced in transgenic mice with vascular expression of NCX1.3, commonly referred to as the kidney variant. SEA0400 also prevents hypertension associated secondary organ injury in the kidney and heart (201).

Despite the number of techniques available for determining myocardial viability, a majority of the contrast agents and techniques currently under clinical use only provide indirect viability estimates via extracellular perfusion, metabolism or contraction measurements. This dissertation applies the technique of cardiac MEMRI to indirectly study cellular ionic Ca^{2+} changes that are known to exhibit changes under ischemic conditions. The ability to monitor changes in the intracellular handling of these ions could provide a more direct assessment of viability that is not available to perfusion agents.

Cardiac MEMRI studies have previously been used to assess myocardial viability, however the true quantitative potential of this technique is yet to be realized. This dissertation also attempts to address this current gap by performing quantitative MEMRI studies in order to better understand Mn^{2+} handling in the myocardium and its relationship to Ca^{2+} handling, and to study alterations in handling post-MI. This information could allow for more accurate diagnosis and therapeutic treatment monitoring in the diseased myocardium.

CHAPTER 2: PURPOSE OF DOCTORAL DISSERTATION

Intracellular calcium is a central regulator of cardiac contractility and viability (202); despite its importance, methods to assess calcium dynamics during myocardial infarction are currently limited. In recent years MEMRI has emerged as a non-invasive technique to monitor Ca^{2+} in cardiovascular disease, both diagnostically and prognostically. However, the full potential of this technique, and the interpretability of its results, are limited by the lack of a thorough understanding of the Mn^{2+} transport mechanisms involved. For example, reduced perfusion in the diseased heart may lead to a reduction in the accumulation of Mn^{2+} due to the relatively small extracellular Mn^{2+} concentration, $[Mn^{2+}]_e$, irrespective of Ca^{2+} transport kinetics (203). In addition to the perfusion required to deliver Mn^{2+} ions to the viable myocytes, Mn^{2+} accumulation also depends on the Gibbs free energy and the sarcolemmal Ca^{2+}-transporters.

The work contained within this dissertation attempts to investigate the feasibility of using an *in vivo* T_1-mapping MEMRI technique to assess and model Mn^{2+} dynamics in the mouse myocardium for both healthy mice and mice following myocardial infarction. Due to the biochemical similarities between Ca^{2+} and Mn^{2+}, the results of this study could provide an innovative and effective technique to monitor the progression of calcium dependent heart disease. Such knowledge could be applied to the development of preclinical and clinical protocols, such as in the detection of potentially salvageable myocardium *in vivo* for future treatment or evaluation of disease progression.

2.1 Background – Quantitative Cardiac Manganese-Enhanced MRI

2.1.1 Introduction

In spite of the established importance of calcium regulation in the heart both prior to, and following, myocardial injury, monitoring strategies to assess calcium homeostasis in affected cardiac tissue are limited. Mn^{2+} infusion in mice has been shown to lead to significant signal enhancement in T_1-weighted cardiac MRI (99). It has also been demonstrated that MEMRI is sensitive to changes in inotropy (99), consistent with the model that Mn^{2+}-induced enhancement of cardiac signal is indicative of the rate of calcium influx into the heart. In order to more accurately assess manganese fluxes *in vivo* and to assess changes in Mn^{2+} uptake due to myocardial infarction, a quantitative imaging technique is required. The goal of using a quantitative technique is to be able to estimate absolute regional Mn^{2+} content *in vivo*, with applications to assess regional Mn^{2+} handling alterations in a myocardial infarction model.

The following background studies were conducted in order to assess the feasibility of combining quantitative imaging protocols to the field of cardiac MEMRI. Results from these background studies could then lay the foundations for a more thorough investigation into the Mn^{2+} handling properties of myocytes, the goal of this dissertation.

2.1.2 Myocardial Manganese Influx

As a background study (204), a T_1-mapping protocol was implemented to determine the relationship between the Mn^{2+} infusion dose and the calculated absolute tissue relaxation times due to Mn^{2+} uptake in murine cardiac myocytes. T_1-mapping MEMRI

experiments were performed in adult male C57Bl/6 mice anesthetized with a mixture of medical air, oxygen (1:1), and 2.5% isoflurane, and maintained at a heart rate of 460±30 bpm with 1.25±0.32% isoflurane throughout the MRI session. $MnCl_2$ doses ranging from 25 to 297 nmoles g^{-1} total body weight (BW) (prepared from a 60mM stock solution) were infused into healthy mice via the tail vein at a rate of 0.6 ml h^{-1}. This dose range had previously been shown not to cause cardiac depressive effects (99).

Short-axis T_1-weighted images and T_1-maps were acquired both prior to and following $MnCl_2$ infusion on a 7.0-T 20-cm horizontal bore BioSpec MRI spectrometer (Bruker Instruments, Billerica, MA, USA), as described by Waghorn et al. (204). Sample ECG gated short-axis cardiac MRI images are shown in Figure 2.1. Figures 2.1a and 2.1b show the T_1-weighted signal intensity enhancements pre- and post-Mn^{2+} infusion, respectively, while Figures 2.1c and 2.1d show the corresponding T_1-maps pre- and post-Mn^{2+} infusion, respectively. At this manganese dose of 280 nmoles g^{-1} BW there is significant signal intensity enhancement in the myocardium following Mn^{2+} infusion. Region-of-interest (ROI) analysis was performed on the 2D T_1-maps using AMIDE (205) to calculate the average regional T_1 value. A ROI was created within the left ventricular free wall (LV Wall), Figure 2.1b. T_1 values were obtained from both pre-Mn^{2+} infusion T_1-map ROIs and post-Mn^{2+} infusion T_1-map ROIs. *In vivo* ΔR_1 [s^{-1}] values were calculated as (post-$MnCl_2$ infusion R_1) – (pre-$MnCl_2$ infusion R_1), Equation 1.31, where the relaxation rate, R_1, is defined as $1/T_1$.

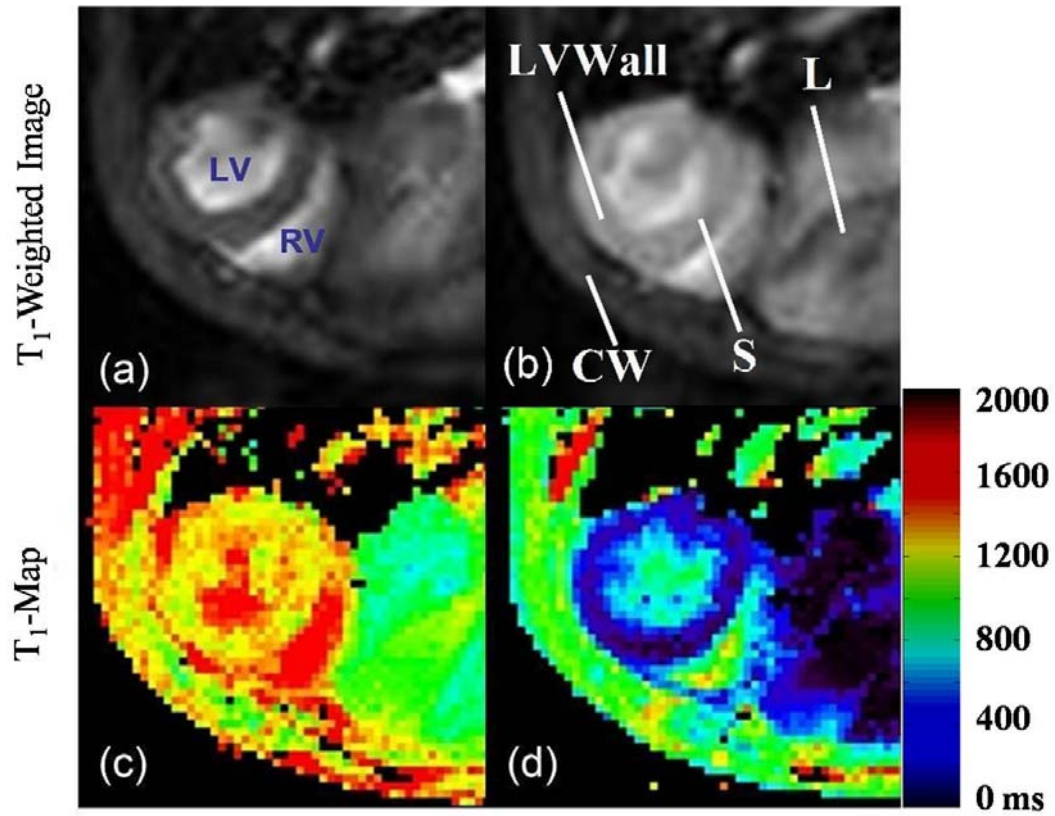

Figure 2.1

Figure 2.1 Example short-axis heart images for a control mouse. (a) T_1-weighted pre-$MnCl_2$ infusion image; (b)T_1-weighted post- $MnCl_2$ infusion image; (c) pre- $MnCl_2$ infusion T_1-map; (d) post-$MnCl_2$ infusion T_1-map. (b) shows the locations of the interventricular septum (S), left ventricular free wall (LVWall), liver (L) and chest wall (CW).

In order to acquire *in vivo* Mn content data, two pieces of information are needed. One is the dependence of $MnCl_2$ infusion dose on LV Wall relaxivity, and the other is the absolute tissue Mn content following $MnCl_2$ infusion. Absolute manganese content data for heart and blood samples acquired from mice sacrificed immediately after imaging were measured by inductively coupled plasma-mass spectrometry (ICP-MS) analysis (CANTEST Ltd., North Vancouver, BC, Canada). These *ex vivo* absolute manganese

content values were then correlated to *in vivo* ΔR_1 values, allowing for an estimate of the absolute Mn content in the heart.

The effect of altering the infusion dose on LV Wall ΔR_1 is shown Figure 2.2, with the data summarized in Table 2.1. Here, the post-$MnCl_2$ infusion T_1-map sequence was initiated approximately 5 minutes post-infusion. The summarized T_1-map data points are shown as triangles in Figure 2.2, with the sample size and uncertainty (±1 SD) shown. The first two columns in Table 2.1 display the grouped Mn^{2+} infusion doses and corresponding LV Wall ΔR_1 values. The sample sizes are displayed in parentheses. ΔR_1 values ranged from 0.16 s^{-1} for the lowest dose regime, up to an average of 4.61 s^{-1} for doses above 197 nmoles g^{-1} BW.

Also shown in Figure 2.2 and Table 2.1 are the elemental analysis results for the heart tissue and blood sample absolute manganese content. These absolute manganese content values were quantified using ICP-MS, and are shown in columns 3-5 of Table 2.1.

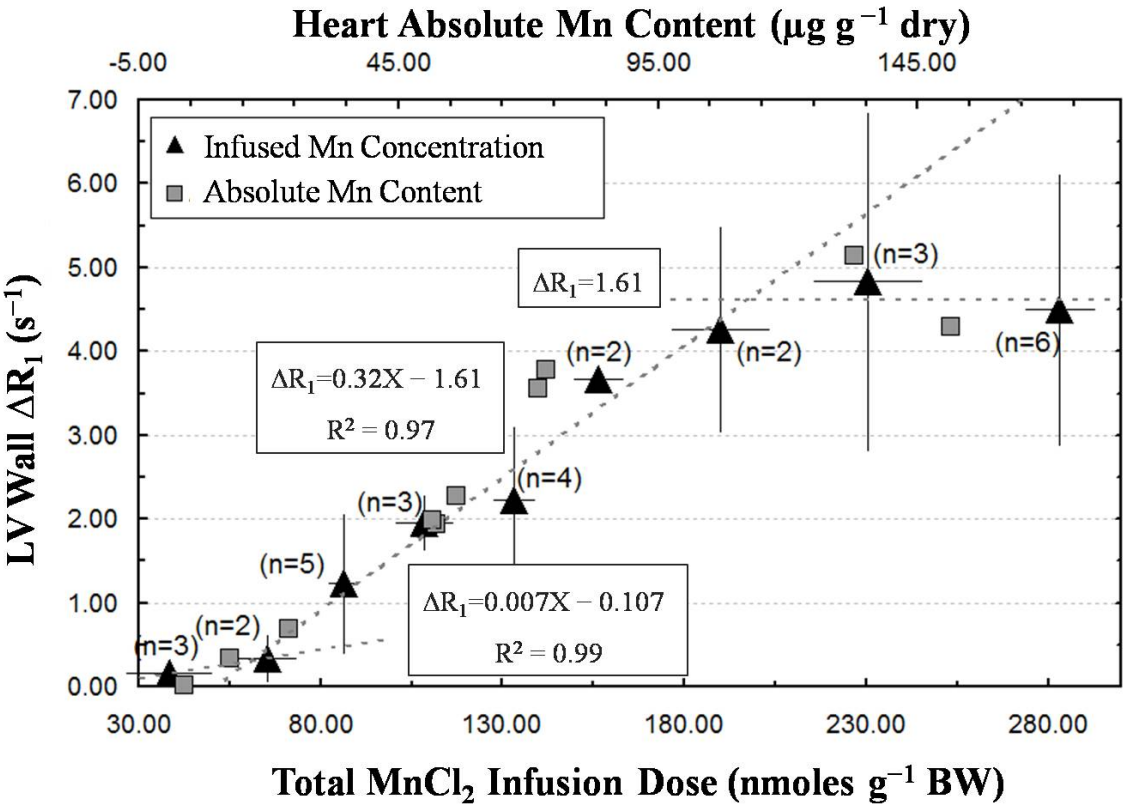

Figure 2.2

Figure 2.2 Effect of altering the dose of infused Mn^{2+} on left ventricular free wall relaxivity (triangles). The x-axis shows the total dose of infused $MnCl_2$, normalized to the mouse BW. The y-axis shows the change in relaxation rate, ΔR_1, pre- vs. post- $MnCl_2$ infusion. As a function of dose, two linear dose uptake regions were noted, along with a plateau region above 197 nmoles g^{-1} BW. The least square fits are shown with total Mn^{2+} infusion dose, X [nmoles g^{-1} BW]. Comparison of this data to the total heart manganese content [μg g^{-1} dry], as determined by ICP-MS (squares) is also shown. This plot can be used to estimate the Mn content *in vivo*.

Table 2.1 Dose dependent T_1-map ΔR_1 values for the LV Wall are shown in columns 1 and 2. ICP-MS absolute blood and heart Mn values from mouse samples are displayed in columns 3-5. LV Wall ROI absolute Mn content from the calculated content maps are given in the final column.

Mn^{2+} Infusion Dose (nmoles g^{-1} BW)	**LV Wall ΔR_1 (s^{-1})**	**Mn^{2+} Infusion Dose for Elemental Analysis (nmoles g^{-1} BW)**	**Heart Absolute Mn Concentration (µg g^{-1} dry weight)**	**Blood Absolute Mn Concentration (µg ml^{-1})**	**Concentration Map LV Wall ROI Data (nmoles g^{-1})**
38.34±11.98 (n=3)	0.16±0.17	37.55±16.82 (n=2)	8.15±6.04	0.22±0.04	6.48±7.78
65.46±8.16 (n=2)	0.33±0.29	-	-	-	12.22±8.87
86.21±4.37 (n=5)	1.23±0.84	83.85	23.78	0.41	36.05±23.91
108.33±8.09 (n=3)	1.96±0.34	108.87±11.36 (n=2)	53.87±3.31	0.41±0.03	63.16±10.65
132.98±5.92 (n=4)	2.23±0.87	130.38	52.32	0.53	80.04±35.68
156.17±7.01 (n=2)	3.67±0.15	156.17±7.01 (n=2)	72.72±1.03	0.55±0.09	114.52±13.04
189.89±13.59 (n=2)	4.26±1.24	199.50	132.74	0.61	139.74±77.11
230.40±15.10 (n=3)	4.83±2.02	243.17	151.35	0.69	166.41±77.11
283.13±9.73 (n=6)	4.49±1.63	-	-	-	221.97±131.13

Values are expressed as mean ± SD, with sample size in parentheses

Three regions are shown in Figure 2.2. At $MnCl_2$ infusion doses, X [nmoles g^{-1} BW], below 197 nmoles g^{-1} BW two linear uptake regimes can potentially be fit to the data, intercepting at 61 nmoles g^{-1} BW. Above 197 nmoles g^{-1} BW, the relaxivity enhancement reaches a plateau. Within this physiological steady state any further increase in Mn^{2+} dose does not result in an increase of ΔR_1. The plateau occurs at ΔR_1 = 4.61±1.64 s^{-1}. The best fit for the two phases below 197 nmoles g^{-1} BW have the form $\Delta R_{1,low}$ = 0.007X-0.107 (r^2 = 0.99) and $\Delta R_{1,high}$ = 0.032X-1.613 (r^2 = 0.97) for the doses below and above 61 nmoles g^{-1} BW, respectively. The lower curve is fit under the assumption that ΔR_1 = 0 below 16.3 nmoles g^{-1} BW. This is deduced visually from Figure 2.2 and is consistent with the fact that there is initially a non-zero volume of saline infused into the tail vein prior to Mn^{2+} entering the mice, inherent in the infusion line setup. For the average mouse weight of 22.6±2.2 g, the average dose of saline present in the infusion line is 16.3±0.7 nmoles g^{-1}.

This dose dependent relationship can be used to optimize current manganese infusion protocols by minimizing the potential toxic effects of Mn^{2+} while still achieving adequate signal enhancement. Also, fitting this dose dependent data to *ex vivo* absolute Mn content values provides the ability to produce Mn concentration maps and to quantify the *in vivo* manganese content.

The correlation between the infused Mn^{2+} dose, X [nmoles g^{-1} BW], and absolute heart Mn content, Y [μg g^{-1} dry weight], can be fit linearly with Y = 0.70X-25.9 (r^2 = 0.94, Figure 2.3a). Similarly, the effect of altering the dose of infused Mn^{2+} on absolute blood sample Mn content, Z [μg ml^{-1}], yields a linear relationship of Z = 0.002X+0.16 (r^2 = 0.93, Figure 2.3b).

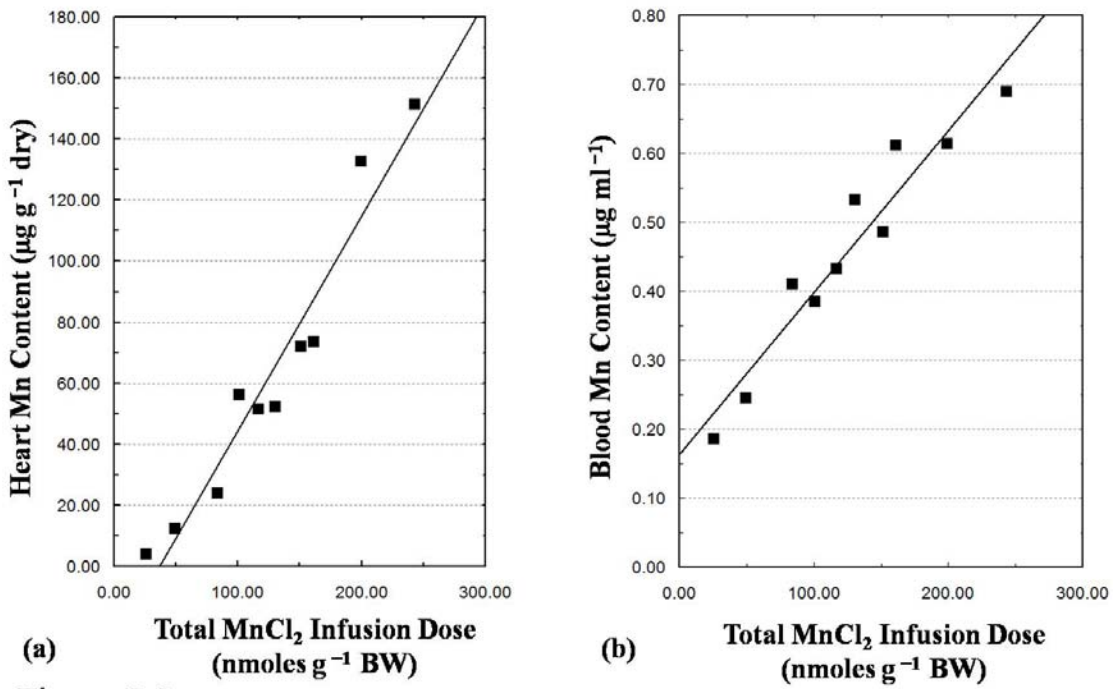

Figure 2.3

Figure 2.3 Effect of $MnCl_2$ infusion dose on the total Mn content determined by ICP-MS for (a) the heart and (b) blood. The x-axis shows the total dose of $MnCl_2$ infused. The y-axis shows the absolute Mn content in μg g^{-1} dry weight for the heart and μg ml^{-1} for the blood. Both plots show the linear least square best fit to the data.

One of the primary goals for this background study was to apply quantitative techniques to cardiac MEMRI studies in order to quantitatively estimate the absolute manganese map for the heart, *in vivo*. The data presented in Figure 2.2 shows the relationship between ΔR_1 and the absolute heart manganese concentration, where the elemental analysis data points (square data point) are overlaid onto the dose dependent plot (triangular data points). Using the data obtained from this dose dependent study a myocardial relaxivity of 5.17 $mM^{-1}s^{-1}$ was estimated, based on the measured R_1 values in the myocardium and from the elemental analysis measurements. Using this relaxivity, *in*

vivo absolute Mn concentration maps [nmoles g^{-1}] were produced. The LV Wall ROI data for these maps are shown in the final column of Table 2.1.

T_1-mapping of cardiac MEMRI has proved sensitive enough to provide quantitative information over a range of Mn^{2+} doses. By demonstrating the dynamic range of relaxation rate changes over a range of Mn^{2+} infusion doses this method can provide a means of optimizing Mn^{2+} infusion protocols. Mn^{2+} is known to be cardiotoxic at high doses (129). However, this study has demonstrated a large range of signal enhancement at subtoxic levels. Due to this fact, lower doses of Mn^{2+} can be used while still producing significant relaxivity changes.

Results of the dose dependent study (Figure 2.2) not only allow for the design of contrast agent optimal doses to minimize toxicity concerns, but also allow for *in vivo* estimates of absolute Mn content to be made following LV Wall ΔR_1 calculations. This technique can therefore be used to monitor the *in vivo* Mn levels non-invasively. One interesting observation is the non-linear relationship between the total $MnCl_2$ infusion dose and the LV Wall ΔR_1. Instead of a purely linear increase in signal intensity enhancement a plateau region occurs at a dose above 197 nmoles g^{-1} BW, likely due to physiological effects. This is in good agreement with previously reported results (99). Following the same non-linear form as the total infusion dose, it is seen that above approximately 100 μg g^{-1} dry heart weight, the absolute Mn content also reaches a plateau. Within this plateau there is no increase in ΔR_1 following an increase in absolute heart Mn content. As the infusion of $MnCl_2$ increases, the absolute Mn content of the heart also increases (Figure 2.3a), but ΔR_1 reaches a plateau at 4.61 s^{-1}.

The plateau effect can be potentially explained in a number of ways, either due to the limitations of Ca^{2+} uptake, or due to limited compartmentalization. The cellular binding sites could become saturated at a certain dose, limiting the uptake of Mn^{2+}. Another explanation for the plateau phenomena could be due to a gradient effect whereby the cells become saturated and are unable to uptake more Mn^{2+}. Similarly, Mn^{2+} could have an inhibitory effect on the Ca^{2+} channels, limiting the scope for Mn^{2+} uptake.

The non-zero intercept in Figure 2.2 is in part due to the finite length of infusion tubing attached to the tail vein needle. A short, 9.9±0.4 cm, length of PE10 tubing containing saline solution connects the infusion needle to the $MnCl_2$ infusion line. This length of tubing corresponds to an equivalent infusion dose of 16.3±0.7 nmoles g^{-1} BW $MnCl_2$. This helps to validate our assumption for the low dose linear fit, where at doses below 16.3 nmoles g^{-1} BW there is assumed to be no manganese infusion and $\Delta R_1 = 0$.

2.1.3 Preliminary Myocardial Manganese Efflux Studies

A second preliminary study was performed to test the feasibility of using the T_1-mapping MEMRI technique to study the Mn^{2+} efflux phenomena temporally. This is important because it could provide a quantitative means of measuring the rate of manganese efflux from the myocardium, and could also potentially provide information regarding the Mn^{2+} efflux rates from individual compartments. Within this study temporal signal washout curves were produced from T_1-maps acquired at multiple time points post-infusion. The form of this curve could provide interesting information about the manganese efflux mechanisms, and could allow for useful *in vivo* examinations of the sodium-calcium exchanger (NCX) as a potential efflux pathway.

For this Mn^{2+} efflux study, a single dose of 282.57±5.96 nmoles g^{-1} BW was infused into the healthy mice at a constant rate of 0.6 ml h^{-1}. A temporal ΔR_1 washout curve was produced from T_1-maps acquired both prior to and at multiple time points post-infusion. The washout period was examined from 0.2 – 99.2 h. Values of ΔR_1 were calculated by subtracting the average baseline ROI R_1 ($R_{1,baseline,LVWall}$ = 0.78±0.04 s^{-1} from 33 control mice) from the post-Mn^{2+} infusion ROI R_1 value. Figure 2.4 shows the temporal relationship of the Mn^{2+} washout curve in the LV Wall, while Table 2.2 summarizes the washout data for the LV Wall. The LV Wall ΔR_1 signal had been attenuated by 50% in the first 2.5 hours post-infusion. In comparison, it has been shown in a rat model that manganese is cleared from all the major organs within 24 hours (206). Despite this initially rapid attenuation of the ΔR_1 signal, there is a non-zero ΔR_1 value remaining until a few days post-infusion suggesting retention of the remaining Mn^{2+}. During the first 9 hours post-infusion the washout data for this infusion dose can be fit exponentially with LV Wall $\Delta R_1 = (5.24\ s^{-1})e^{-0.40 \cdot t}$ (r^2 = 0.93, with t given in units of hours). This information provides a better imaging timeframe for the cardiovascular disease model in the current study, while containing information on the potential extrudability of Mn^{2+} from the myocardium.

Table 2.2 Temporal ΔR_1 signal attenuation post-$MnCl_2$ infusion in the LV Wall.

Time Post-Mn^{2+} Infusion (h)	**LV Wall ΔR_1 (s^{-1})**
0.31±0.11 (n=7)	4.44±1.48
1.35±0.30 (n=3)	3.65±1.08
2.41±0.37 (n=5)	2.23±0.75
3.33±0.04 (n=2)	1.04±0.29
4.25±0.41 (n=3)	0.70±0.16
6.33±0.08 (n=2)	0.63±0.36
7.34±0.37 (n=5)	0.45±0.35
9.22±1.11 (n=2)	0.59±0.39
11.40±0.54 (n=5)	0.64±0.16
13.19±0.62 (n=2)	0.36±0.03
21.11 (n=1)	0.14
46.07±3.30 (n=3)	0.07±0.04
99.19 (n=1)	0.08

Values are expressed as mean ± SD, with sample size in parentheses

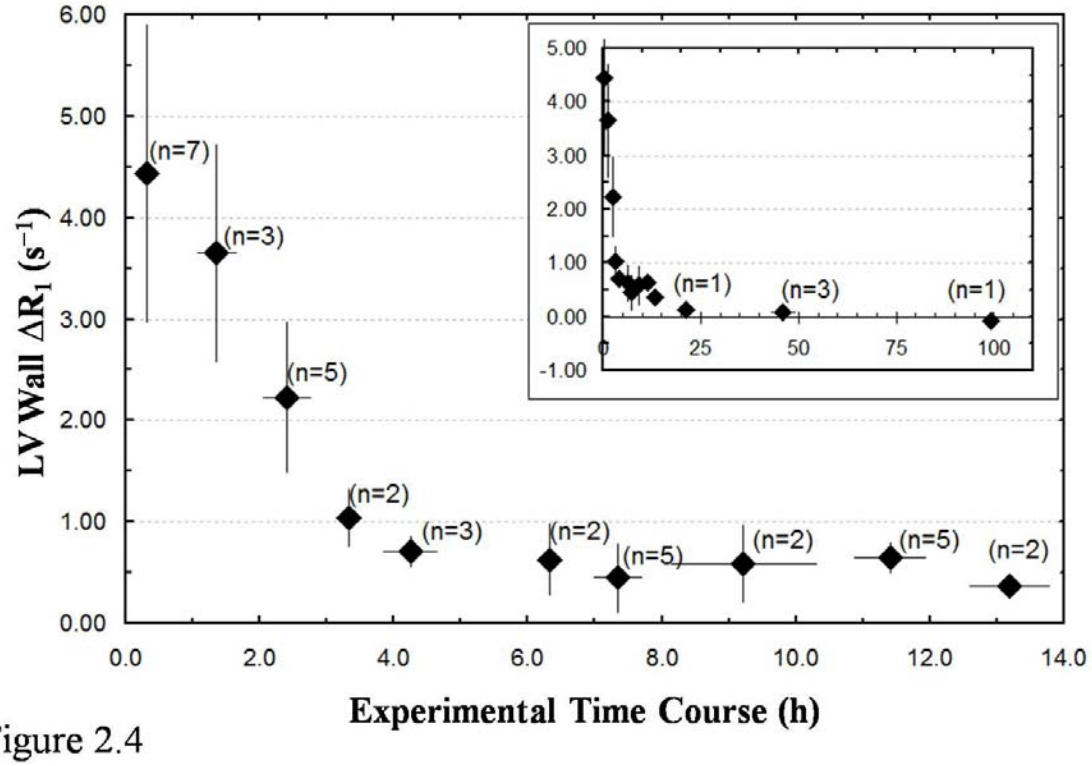

Figure 2.4

Figure 2.4 Temporal Mn^{2+} washout curve. The x-axis shows experimental time course post- $MnCl_2$ infusion, in hours. The y-axis shows the difference of relaxation rate, ΔR_1, pre- vs. post- $MnCl_2$ infusion. The insert plot shows the complete washout curve over an extended period of time.

The form of the Mn^{2+} washout curve is still uncertain and numerical modeling of Mn transport may provide additional insight. The complicated form of this curve could contain information about the Mn^{2+} efflux mechanisms within the myocardium. Accumulation of Mn^{2+} in various compartments within the myocytes could explain the variations between the initially rapid washout and the sustained signal enhancement over a few days. Differences in individual compartment efflux rates would contribute to the washout curve. One potential efflux mechanism for Mn^{2+} is via the sodium-calcium exchanger (NCX). The NCX is an important transporter for the regulation of intracellular

Ca^{2+} concentration (207). By altering the characteristics of different efflux mechanisms, such as the NCX channel, it might be possible to further interrogate the form of the curve and the underlying physiology. This information, along with the use of physiological modulators such as pharmaceutical agents, could be critical for examining potential Mn^{2+} extrudability pathways. This technique could also provide a means of identifying Mn^{2+} efflux modulation due to myocardial injury.

2.1.4 Manganese Influx in a Myocardial Infarction Model

It has previously been shown (137) that T_1-weighted MEMRI in a murine MI model provides clear delineation of the myocardial infarction site. The final background study for this dissertation was designed to characterize the efficacy of applying a quantitative MEMRI T_1-mapping technique to assess the dynamic features of calcium response due to myocardial injury in a murine model. Results from this study could then be used to further address Mn^{2+} handling dynamics, including alterations following MI, which could ultimately lead to a better understanding of the relationship between Mn^{2+} and Ca^{2+}.

For this study mice were divided into three experimental groups: control (n = 6, average weight = 22.57±3.24 g), sham-operated (n = 21, 23.06±2.48 g) and myocardial infarction (MI) (n = 6, 23.24±1.02 g). The control group underwent no surgical procedures, while the sham-operated and MI groups both underwent thoracotomy with the MI group receiving permanent MI via left anterior descending coronary artery (LAD) ligation. The aim of this study was to characterize the efficacy of MEMRI T_1-mapping for assessing alterations in calcium homeostasis. To accomplish this aim, cardiac images

were acquired both pre- and post-MI, in a murine model. The post-MI time point was chosen to emphasize calcium alteration after MI, while avoiding the pathological complexity of heart failure at later times. Imaging was therefore performed 13±4 days and 12±6 days post-surgery for the MI and sham-operated groups, respectively.

For Mn^{2+} administration, a tail-vein infusion line was placed and all three groups of mice were infused with 282.5±4.0 nmoles g^{-1} BW at a constant rate of 0.6 ml h^{-1}. Short axis images were acquired for the control and sham-operated mice midway through the left ventricle and perpendicular to the long axis of the heart. In the myocardial infarction group the short axis was again defined perpendicular to the long axis of the heart, but located at the area with the greatest LV wall-thinning due to the injury, typically within 1 mm of the center of the ventricle. In the case of the control and sham-operated mice, ROI tools were used to select a region of interest within the left ventricular free wall (LV Wall). To quantitatively assess the dynamic features of the calcium response due to the myocardial injury additional regions of interest were defined for the MI group. The peri-infarcted zone ROIs were defined in the regions of the LV Wall immediately surrounding the injury site, starting at the outer boundary of the left ventricular thinning and extending approximately 1.5mm into the viable tissue. An additional ROI, the necrosed tissue ROI, was created within the injury site of the left ventricular free wall. *In vivo* ΔR_1 values were calculated as before, with post-$MnCl_2$ T_1-maps being acquired 0.25±0.05 h after the initial $MnCl_2$ infusion.

Figure 2.5 shows sample post-Mn^{2+} infusion T_1-maps for (a) sham-operated and (b) MI mice. The sham-operated mouse shows a well defined LV Wall and interventricular septum with relatively uniform Mn^{2+} uptake throughout. In the MI model

there is substantial LV Wall thinning at the injury site, accompanied by higher T_1 values due to reduced uptake of Mn^{2+}.

The results of this study are shown in Figure 2.6, where the data is presented as the average ROI ΔR_1 (solid horizontal line) ± SD (shaded box), with the data range (solid vertical line). Table 2.3 also shows theses results, along with the statistical test results. Twenty-one sham-operated surgeries were performed to ensure consistency in the surgical technique before performing MI surgery in the MI group. Imaging results for all of the sham operations were found to be self-consistent (i.e., there was no image-based trend between the time of surgery and the value of LV Wall ΔR_1).

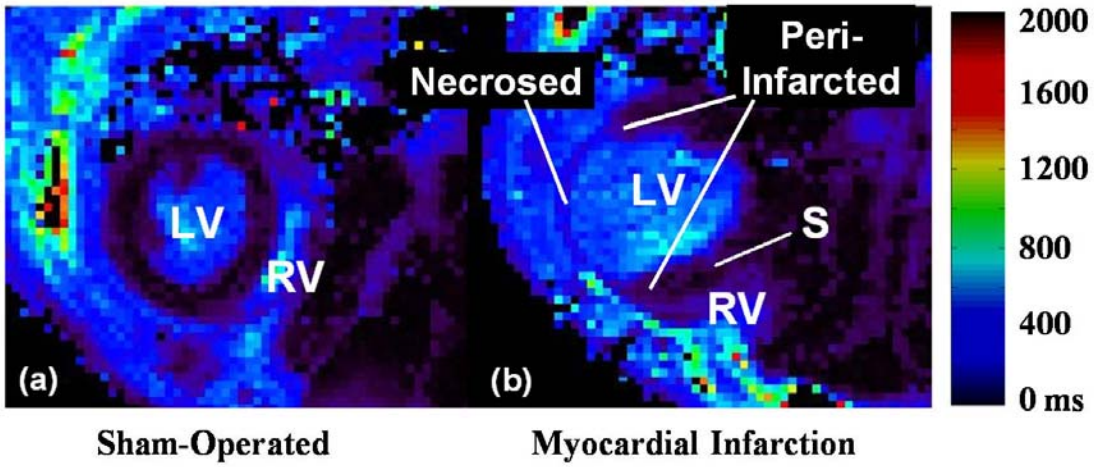

Figure 2.5

Figure 2.5 Example short-axis post- $MnCl_2$ infusion T_1-map cardiac images for; (a) a sham-operated mouse, and (b) a myocardial infarction mouse. Significant LV Wall thinning can be seen for the MI mouse with a longer T_1 relaxation time relative to healthy myocardial tissue. (b) shows the interventricular septum (S), myocardial infarction peri-infarcted zone and myocardial infarction necrosed tissue site.

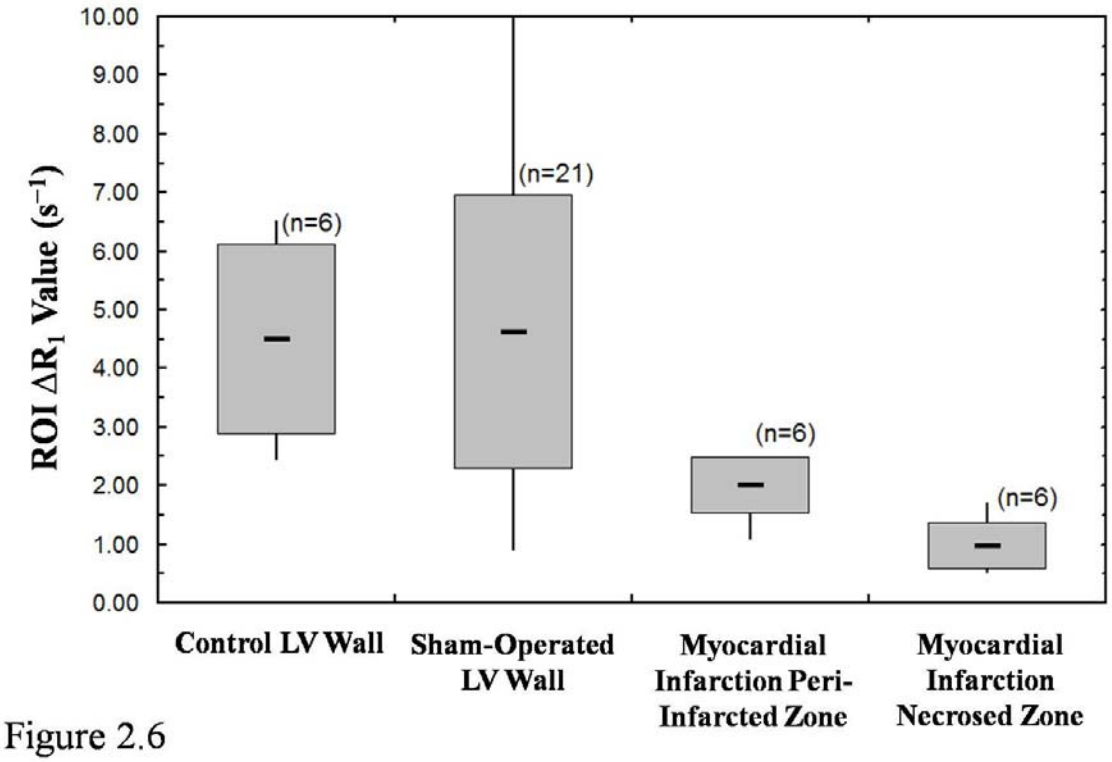

Figure 2.6

Figure 2.6 The effect of myocardial injury on the uptake of Mn^{2+}. Regions of interest were defined for the LV Wall in the control and sham-operated groups. ROIs for the MI model were also defined at the injury site contained within the LV Wall and in the peri-infarcted zone, immediately surrounding the injury site. Data is presented as the average ROI ΔR_1 (solid horizontal line, $\mathbf{s^{-1}}$) ± SD (shaded box), with the data range shown (solid vertical line).

There is no statistically significant difference between the LV Wall ΔR_1 values of the control (4.49±1.63 s^{-1}) and sham-operated (4.62±2.34 s^{-1}) mice ($p = 0.91$) suggesting that the procedure of opening the chest does not affect Mn^{2+} uptake within the heart. Comparing the control and sham-operated LV Wall ΔR_1 values with the MI group peri-infarcted zone ΔR_1 values using ANOVA, however, shows that there is a significant difference in relaxivity between the groups ($p = 0.03$). Cross-comparison of all of the groups individually with t-tests demonstrates that the MI group peri-infarcted zone ΔR_1

(2.00±0.49 s^{-1}) is significantly less than the control and sham-operated groups ($p < 0.05$), with the MI injury site ΔR_1 (0.97±0.39 s^{-1}) being significantly less ($p < 0.05$) than all of the groups.

Table 2.3 Average ΔR_1 signal enhancement post-Mn^{2+} infusion for control, sham-operated and myocardial infarction groups. For the myocardial infarction group ROIs were defined both for the myocardial infarction peri-infarcted zone, surrounding the infarction site, and the infarcted site (MI).

Group - Region of Interest (ROI)	ROI ΔR_1 (s^{-1})
Control – LV Wall	4.49±1.63 (n=6)$^{\dagger *\ddagger}$
Sham-Operated – LV Wall	4.62±2.34 (n=21)
Myocardial Infarction – Peri-infarcted Zone	2.00±0.49 (n=6)
Myocardial Infarction – MI Site	0.97±0.39 (n=6)

Values are expressed as mean ± SD, with sample size in parentheses
$^{\dagger}p = 0.03$ between all LV Wall groups (ANOVA, single factor)
$^{*}p = 0.91$ between control and sham-operated LV Wall groups (unpaired two-tailed t-test)
$^{\ddagger}p < 0.05$ between every two group combination except the control and sham-operated LV Wall combination (unpaired two-tailed t-test)

This final background study has demonstrated the quantitative ability of MEMRI T_1-mapping in the murine heart to determine cellular viability in the vicinity of the myocardial infarction site. This could ultimately lead to an early *in vivo* indicator of viable treatment options depending on the state of the myocytes and their potential salvageability.

The myocardial infarction study utilized the optimal dose and timing properties acquired from the previous sections of this background study. Statistically significant differences between healthy myocardial tissue, in the control and sham-operated groups,

and the MI peri-infarcted zone in the MI group were demonstrated. Mn^{2+} had previously been shown to provide functional, pathological and viability data in myocardial tissue using T_1-weighted imaging techniques in mice (137) and dogs (10). Manganese-dipyridoxyl diphosphate (MnDPDP), a Mn^{2+} releasing contrast agent (172), is currently approved for clinical liver imaging. MnDPDP-enhanced images have demonstrated manganese retention in viable pig myocardium (208) with clearance of manganese from infarcted myocytes in a rat model (136). This behavior is consistent with MEMRI contrast. Recently, MnDPDP has been used as a viability marker in patients with myocardial infarction (11). However, more quantitative information was required to be able to assess the extent of damage to the myocardium, which has been demonstrated here through the T_1-mapping protocol.

Myocardial infarction causes physiological remodeling leading to potential Ca^{2+} handling alterations. This remodeling process can potentially be observed and monitored using MEMRI T_1-mapping as shown by the sensitivity of our data. The injury site of the LV Wall showed a ΔR_1 almost 5 times less than the healthy LV Wall of the control mouse. More interestingly, with respect to recovery of the injured tissue, this technique is sensitive to the reduced uptake of Mn^{2+} in the peri-infarcted zone. During myocardial ischemia intracellular calcium concentrations increase due to increased Ca^{2+} influx and reduced efflux (2). However, our results show reduced Mn^{2+} uptake in both the MI site and peri-infarcted zone.

The phenomena of reduced Mn^{2+} uptake in both the MI region and the peri-infarcted zone are complex to address. To date, conflicting results have also been reported in other studies. *In vivo* manganese-enhanced MRI has observed signal attenuations in mice

(137), rat (138) and larger mammalian species (139). However, *in vitro* studies have shown enhanced Ca^{2+} influx as a compensatory process (140).

Camelliti, et al. (141) have shown *ex vivo* results which demonstrate small islands of viable myocytes in ischemic regions. These islands could potentially explain the non-zero Mn^{2+} uptake in the ischemic regions. In the peri-infarcted area this background study suggests that the volume of viable tissue is still reduced as compared to healthy LV Wall tissue of the control and sham operated mice. This could potentially explain the reduction of Mn^{2+} uptake in this area. Temporal responses to myocardial infarction could now be predicted in mice using this preclinical model, looking at the alterations in calcium handing with recovery.

These results demonstrate the sensitivity of this technique to determine altered manganese uptake, not only at the necrotic site but also within the peri-infarcted zone. Calculating the *in vivo* Mn content map could allow for potentially salvageable myocardium to be identified for future therapeutic treatment or prevention, in preclinical models.

2.1.5 Conclusion

These background studies have demonstrated that T_1-mapping of cardiac MEMRI can be used to quantify Mn concentrations *in vivo* and to define regions of potentially altered Ca^{2+} homeostasis in a myocardial infarction model. The effect of the manganese infusion dose has been studied up to approximately 297 nmoles g^{-1} BW, with an initial slow uptake occurring below 61 nmoles g^{-1} BW, and a more rapid uptake until 197 nmoles g^{-1} BW. At this dose the physiological steady state was achieved.

Mn^{2+} washout has also been investigated in the LV Wall. The ΔR_1 signal has attenuated to 50% of the steady state signal by approximately 2.5 hours post-infusion. There is still a ΔR_1 effect remaining after a few days suggesting potential Mn^{2+} retention at the site. The overall washout progression warrants further investigation, but this technique could provide a potential way to examine the extrudability of Mn^{2+} from the myocardium.

One motivation for these background studies was that myocardial infarction causes physiological remodeling leading to potential Ca^{2+} handling alteration. With the potential of using T_1-mapping and ICP-MS analysis to quantify the *in vivo* concentration of Mn, more insight into myocardial infarction peri-infarcted zones may be provided. This technique could provide additional information such as: (1) optimization of the Mn^{2+} dose to minimize the study dose; (2) quantification of Mn content *in vivo*; (3) temporal response of myocardial infarction or ischemic-reperfusion model(s); (4) pharmacological efficacy; and (5) potential preclinical and translational models to monitor disease treatment.

Overall, these background studies have demonstrated the quantitative potential of MEMRI studies to study Mn^{2+} fluxes in healthy and diseased myocardium. This dissertation builds upon these preliminary findings in an attempt to further understand Mn^{2+} handling dynamics and the relationship between Mn^{2+} and Ca^{2+} handling in the mouse myocardium. The following three sections, §2.2, 2.3 and 2.4, outline the goals of the subsequent studies in this dissertation.

2.2 Part I – Mn^{2+} Dose Dependent Cardiac Efflux

The first section of this dissertation attempts to determine the feasibility of monitoring Mn^{2+} efflux *in vivo* using T_1-mapping MEMRI. It has been shown (§2.1.3) that MEMRI T_1-mapping protocols are sensitive enough to detect alterations in ΔR_1 in the mouse myocardium post-$MnCl_2$ infusion. However, the relationship between ΔR_1 and the absolute Mn content has not been determined, and may be variable with increasing time post-$MnCl_2$ infusion. Here, a $MnCl_2$ dose dependent study was used to observe the effect of altered $MnCl_2$ infusion doses on the temporal rate of change of ΔR_1 in the left ventricular free wall (LV Wall). To ascertain whether the temporal changes in ΔR_1 were caused by true Mn^{2+} efflux from the myocardium, *in vivo* data was then correlated to the acquired absolute Mn content, obtained *ex vivo* via elemental analysis results from sample mice hearts. Results from this study could be used to determine whether ΔR_1 washout curves can predict changes in Mn^{2+} content, and also to determine the effect of altered Mn^{2+} concentrations on Mn^{2+} efflux in the healthy myocardium, providing early information regarding Mn^{2+} efflux under healthy conditions.

2.3 Part II – Pharmacologically and MI altered Mn^{2+} Efflux

In order to further probe potential Mn^{2+} efflux mechanisms, ΔR_1 washout curves were produced following pharmaceutical alterations of the known Ca^{2+} efflux mechanisms, either by inhibiting the NCX with varying doses of SEA0400, or by using

inotropic agent dobutamine, known to increase calcium influx and assumedly calcium efflux. The form of these efflux curves could indirectly contain information concerning the relative contribution of the Ca^{2+} transport mechanism.

Having previously studied Mn^{2+} dynamics in the unaltered healthy myocardium in §2.2, the MEMRI T_1-mapping efflux technique was then applied to a myocardial infarction model to detect potential regional variations in the Mn^{2+} efflux properties. Alterations in Ca^{2+} handling following MI can exacerbate myocardial injury. Of particular interest is the peri-infarcted zone, which could potentially undergo therapeutic intervention to aid remodeling of the myocardium post-infarction. By studying Mn^{2+} efflux as a function of position in the myocardium, it could be possible to determine alterations in Mn^{2+} flux owing to the injury. In order to provide this dynamic, position-dependent data, novel in-house software was devised and written in order to automatically isolate myocardial tissue from the T_1 maps with minimal user input and bias. The isolated myocardium was then radially segmented, allowing for position-dependent Mn^{2+} efflux curves to be produced. Observed dynamic variations in Mn^{2+} efflux within the myocardium could provide information regarding alterations in Ca^{2+} handling.

2.4 Part III – Pharmacokinetic Modeling of Mn^{2+} Fluxes

In the final part of this dissertation, data from both previous studies (§2.2 and §2.3) were applied to a series of pharmacokinetic models to estimate the various Mn^{2+}

flux rate parameters (including myocardial Mn^{2+} influx and efflux), studying Mn^{2+} in the blood and heart systems. With knowledge of the Mn^{2+} infusion rate and dose, as well as absolute Mn content in the blood and heart at various time-points post-$MnCl_2$ infusion, *in vivo* ΔR_1 values could potentially be used to model the temporal Mn^{2+} content in the blood and heart as a function of time. Additionally, it should be possible to predict the transfer rates of Mn^{2+} from initial infusion into the blood stream, to myocardial uptake, efflux and the potential compartmentalization within the myocytes. This dissertation attempts to model both control (healthy myocardium) and MI transfer rates in an attempt to further understand the Mn^{2+} dynamics post-infusion and also the dynamic alterations due to the physiological processes involved with Mn^{2+} transport in the diseased heart.

CHAPTER 3: PART I - MN^{2+} DOSE DEPENDENT CARDIAC EFFLUX

3.1 Introduction

Calcium (Ca^{2+}) is a major regulator of cardiac contractility (202). When a myocyte is depolarized by an action potential, Ca^{2+} enters the cell primarily via L-type voltage-gated Ca^{2+} channels with a smaller contribution occurring via the reverse mode of the sodium-calcium exchanger (NCX) (4). This Ca^{2+} influx in the cytosol acts to trigger a subsequent release of Ca^{2+} stored in the sarcoplasmic reticulum through Ca^{2+}-release channels ultimately leading to myocardial contraction.

The efflux of Ca^{2+} occurs via the forward mode of the NCX and via the plasma membrane Ca^{2+}-ATPase mechanism (22). The net Ca^{2+} flux through the NCX occurs in the outward direction. Previous studies estimating the relative contributions to Ca^{2+} efflux showed that the NCX is the dominant mechanism with 9–32% of the efflux occurring from non-NCX mechanisms in rats (23,24) and 19% in mice (25).

Alterations in myocyte Ca^{2+} handling are essential to the dysfunctional characteristics of the failing heart (46). Although research has established that diminished cardiac performance in heart failure is due to abnormal intracellular Ca^{2+} handling, to the best of the author's knowledge no technique exists to directly observe *in vivo* intracellular Ca^{2+} flux fluctuations across the plasma membrane (47,48).

As demonstrated in §2, one potential technique for indirectly assessing intracellular Ca^{2+} movement *in vivo* is to use a surrogate marker such as manganese (Mn^{2+}) as a molecular contrast agent. The hypothesis is that the ability to measure Mn^{2+}

efflux *in vivo* using MEMRI as a quantitative imaging approach should reflect information concerning myocardial Ca^{2+} efflux, if retention of Mn^{2+} due to compartmentalization is relatively small compared to the total intracellular Mn^{2+} concentration.

The application of a T_1-mapping technique during MEMRI provides valuable quantitative information, while minimizing the effects of repositioning the animal between MEMRI sessions. The background study (§2.1.2) demonstrated that a MEMRI T_1-mapping protocol in a murine model exhibited a linear relationship between the amount of Mn^{2+} infused (in the range 25 – 197 nmoles g^{-1} body weight (BW) $MnCl_2$ infusion) and change in absolute ^1H_2O relaxation rates (ΔR_1) in heart tissue (204). This linear relationship suggested that the initial Mn^{2+} compartmentalization, such as in the mitochondria, is either linear and/or small compared to changes in the cystolic free Mn^{2+} concentration. Furthermore, §2.1.3 demonstrated that *in vivo* ΔR_1 washout curves could be produced and analyzed by acquiring T_1-maps at multiple time points post-$MnCl_2$ infusion.

3.1.1 Purpose

The purpose of this study was to use MEMRI in a murine heart model with a T_1-mapping technique to assess the dependence on $MnCl_2$ infusion doses on Mn^{2+} washout. In order to achieve this goal, it is necessary not only to produce dose dependent efflux curves, but also to ascertain the relationship between ΔR_1 efflux and Mn^{2+} content efflux post-$MnCl_2$ infusion. Therefore, this study was designed to 1) determine whether it was possible to monitor Mn^{2+} efflux in the heart using a T_1-mapping pulse sequence in order

to estimate the absolute Mn^{2+} content *in vivo* and 2) to study the dependence on $MnCl_2$ infusion, and therefore myocyte Mn^{2+} content, on the efflux properties of Mn^{2+}.

3.2 Materials and Methods

3.2.1 Experimental Protocol

MEMRI experiments were performed in a total of 62 healthy adult male C57Bl/6 mice (6-14 weeks old, 24.0±1.9 g) following the guidelines of the Institutional Animal Care and Use Committee at the Medical College of Georgia, Augusta, GA, USA. For all experimental procedures, the animals were anesthetized with a mixture of medical air, oxygen (1:1) and 2.5-3.0% isoflurane. The heart rate (HR) was maintained at 444±8 beats per minute (bpm) throughout the experiment by carefully adjusting the level of isoflurane. A custom-made water bed set at 38°C maintained a constant animal body temperature in the cradle throughout the MEMRI procedure.

Of the 62 mice, 40 were randomized into four $MnCl_2$ dose dependent experimental groups to, receiving single $MnCl_2$ infusion of:

1) 283±6 nmoles g^{-1} BW (number of mice, $n_{mice} = 15$; total number of T_1-maps post-$MnCl_2$ infusion, $n_{maps} = 41$);
2) 190±2 nmoles g^{-1} (Control, $n_{mice} = 14$, $n_{maps} = 36$)
3) 119±3 nmoles g^{-1} ($n_{mice} = 7$, $n_{maps} = 21$);
4) 65±0.2 nmoles g^{-1} ($n_{mice} = 4$, $n_{maps} = 14$)

All of the $MnCl_2$ doses were previously shown not to cause measurable cardiotoxic effects (99), with the Control, 190 nmoles g^{-1} $MnCl_2$ dose, found to lie at the high dose end of the linear Mn^{2+} uptake region, §2.1.2 (204). After the proper level of anesthesia was achieved in each animal, $MnCl_2$ infusions (prepared from a 60 mM stock solution; Sigma-Aldrich, St. Louis, MO) were administered intravenously via the tail vein. All $MnCl_2$ infusions were completed at a constant rate of 0.6 ml h^{-1} with the aid of a syringe pump (KD Scientific Inc., Holliston, MA, USA).

For the remaining mice not selected for one of the four dose-dependent efflux groups, as well as for select mice included in the efflux study (n = 33), T_1-maps were acquired prior to $MnCl_2$ infusion to determine the baseline (pre-$MnCl_2$ infusion) R_1 values required for calculation of ΔR_1. T_1-maps were then acquired for the four efflux groups at various post-infusion time points, ranging from 0.2 hrs to 12 hrs. T_1 mapping was not performed during the first 0.2 hrs following $MnCl_2$ infusion, to allow for assumed blood pool clearance (10).

As previously stated, all mice were anesthetized during the experimental procedures (contrast agent infusion, drug administration, and imaging sessions). The mice were allowed to recover between procedures so that the maximum time under anesthesia was 2.5 hrs for each mouse, followed by a recovery period of at least 2.5 hrs. These timeframes reduced the NCX inhibitory effect known to be caused by isoflurane (209); imaging time points selected for each mouse therefore followed these guidelines. In addition, efforts were made to vary the time interval between successive data points so as not to bias the results with potential anesthesia effects. The ΔR_1 washout curves were

produced for each group by calculating T_1 values in the left ventricular free wall from T_1-maps acquired at the various time points post-$MnCl_2$ infusion.

A subgroup of randomly selected animals (n = 14) was sacrificed immediately after imaging to measure the absolute Mn content in the heart tissue (n = 12) and/or blood samples (n = 11) by inductively coupled plasma-mass spectrometry (ICP-MS) analysis (CANTEST Ltd., North Vancouver, BC, Canada). To maintain a consistent harvest time, the tissue and blood samples were obtained approximately one hour after initiation of the final T_1-map to allow sufficient time to acquire the T_1-map (~43 minutes) and to harvest the individual samples.

3.2.2 Manganese-Enhanced Magnetic Resonance Imaging

MEMRI data for this, and subsequent studies, were acquired on a 7.0-T 20-cm horizontal bore Bruker BioSpec MRI spectrometer (Bruker Instruments, Billerica, MA, USA) equipped with a micro-imaging gradient insert (950 mT m^{-1}). Animal setup procedures followed those previously described (99). A standard Bruker volume coil (35 mm inner diameter) was used to transmit and receive at ^1H frequency (300 MHz). Electrocardiographic (ECG) and respiratory signals were monitored by a physiological monitoring system (SA Instruments, INC., Stony Brook, NY) with the ECG signal used to gate the images. All images were gated using the R wave of the ECG. Short axis images were acquired midway through the left ventricle and perpendicular to the long axis of the heart. A T_1-weighted MRI Gradient Echo Flow Compensation (GEFC) pulse sequence (210) was used for slice localization and to visualize Mn^{2+} uptake in the myocardium with the imaging parameters as follows:

Matrix = 128 x 128; TE/TR = 3.5/35 ms; slice thickness = 1.0 mm; FOV = 3.0 x 3.0 cm; flip angle = 60° and NA = 6.

TR was purposely set at a shorter time than the average R-R period detected on the ECG (138±1.5 ms) to ensure the true repetition time for the imaging sequence was the R-R period.

Both pre- and post-$MnCl_2$ infusion T_1-maps were acquired with an ECG-gated, flow-compensated Look-Locker MRI pulse sequence (§1.7.1) as previously described (145), using the following parameters:

Matrix = 128 x 128; TE/TR = 2.5 ms/10 s; slice thickness = 1.0 mm; FOV = 3.0 x 3.0 cm; NA = 2; inversion time = 9 ms; average echo interval = 138 ms (determined by the average R-R period before acquisition); number of echo images = 50; average flip angle = 11±1°

The echo interval was set as the approximate mean R-R period observed prior to the execution of each T_1-map sequence. The initial inversion pulse per repetition was gated, with the subsequent echo pulses separated by the constant echo interval. The T_1 value estimation was therefore not affected by R-R period fluctuations occurring during TR. The total imaging time per T_1-map was approximately 43 minutes.

3.2.3 Data Analysis

T_1-mapping

The T_1 value of each pixel was calculated using a custom-written C^{++} program (145). The signal recovery of each pixel was fit from the 50 echo images by the three-

parameter Levenburg-Marquardt non-linear curve-fitting algorithm. Region-of-interest (ROI) analysis was performed on the 2D T_1-maps using AMIDE (205) to calculate the average regional T_1 value. ROIs were selected within the left ventricular free wall (LV Wall) area. As previously stated, *in vivo* ΔR_1 values were calculated as (post-$MnCl_2$ infusion $1/T_1$) – (pre-$MnCl_2$ infusion $1/T_1$). The ΔR_1 values were stated as a mean ± standard deviation in units of [s^{-1}].

Statistics

Individual ΔR_1 data points for all of the $MnCl_2$ dose dependent groups were fit with a least-square first-order exponential decay using GraphPad Prism statistics software (GraphPad, San Diego, CA, USA). The 95% confidence intervals (CI) for the extrapolated ΔR_1 at the time of infusion, t = 0, ($\Delta R_{1,0}$) and half-life values were calculated from the exponential fit. The $\Delta R_{1,0}$ and half-life values were compared between groups using an extra sum-of-squares F test, comparing the ratio of the difference between the least-square fit from the washout curves to the residual sum of squares within each curve. Comparisons between the four experimental groups were assessed using ANOVA with a Tukey post hoc test to determine differences between sub-groups. The level of significance was set at 0.05.

3.3 Results

Figure 3.1 shows sample cardiac short axis T_1-maps; pre-$MnCl_2$ infusion (Figure 3.1a), 0.2 hrs (Figure 3.1b), and 5 hrs (Figure 3.1c) post-$MnCl_2$ infusion. The average LV Wall ROI size was 22±5 voxels (Figure 3.1b).

3.3.1 Dose Dependent Efflux

For all of the dose dependent groups, ΔR_1 values were calculated by subtracting the average baseline R_1 value (0.78±0.04 s^{-1}) from the post-$MnCl_2$ infusion ROI R_1 values. Figure 3.2a shows the LV Wall ΔR_1 washout curves for the four $MnCl_2$ infusion doses; Figure 3.2b shows the corresponding half-life values.

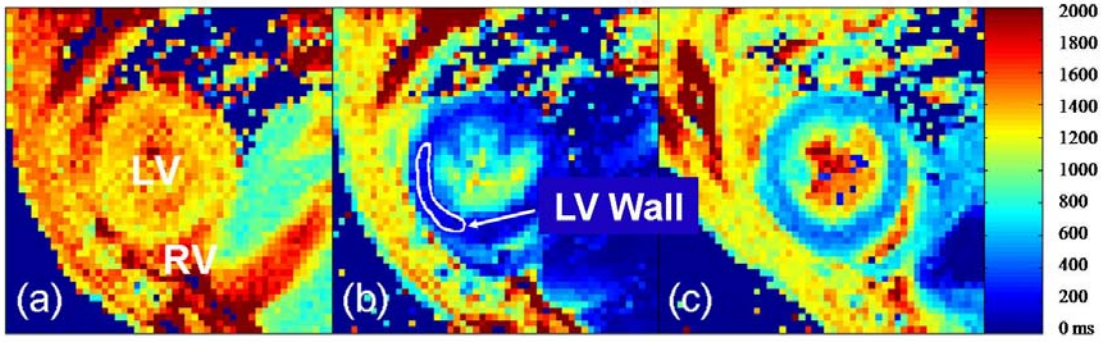

Figure 3.1

Figure 3.1 Example short-axis mouse heart T_1-maps (a) pre-$MnCl_2$ infusion (b) 0.2 hrs and (c) 5 hrs post-$MnCl_2$ infusion. Left and right ventricles are labeled as LV and RV respectively, with a sample LV Wall ROI also shown.

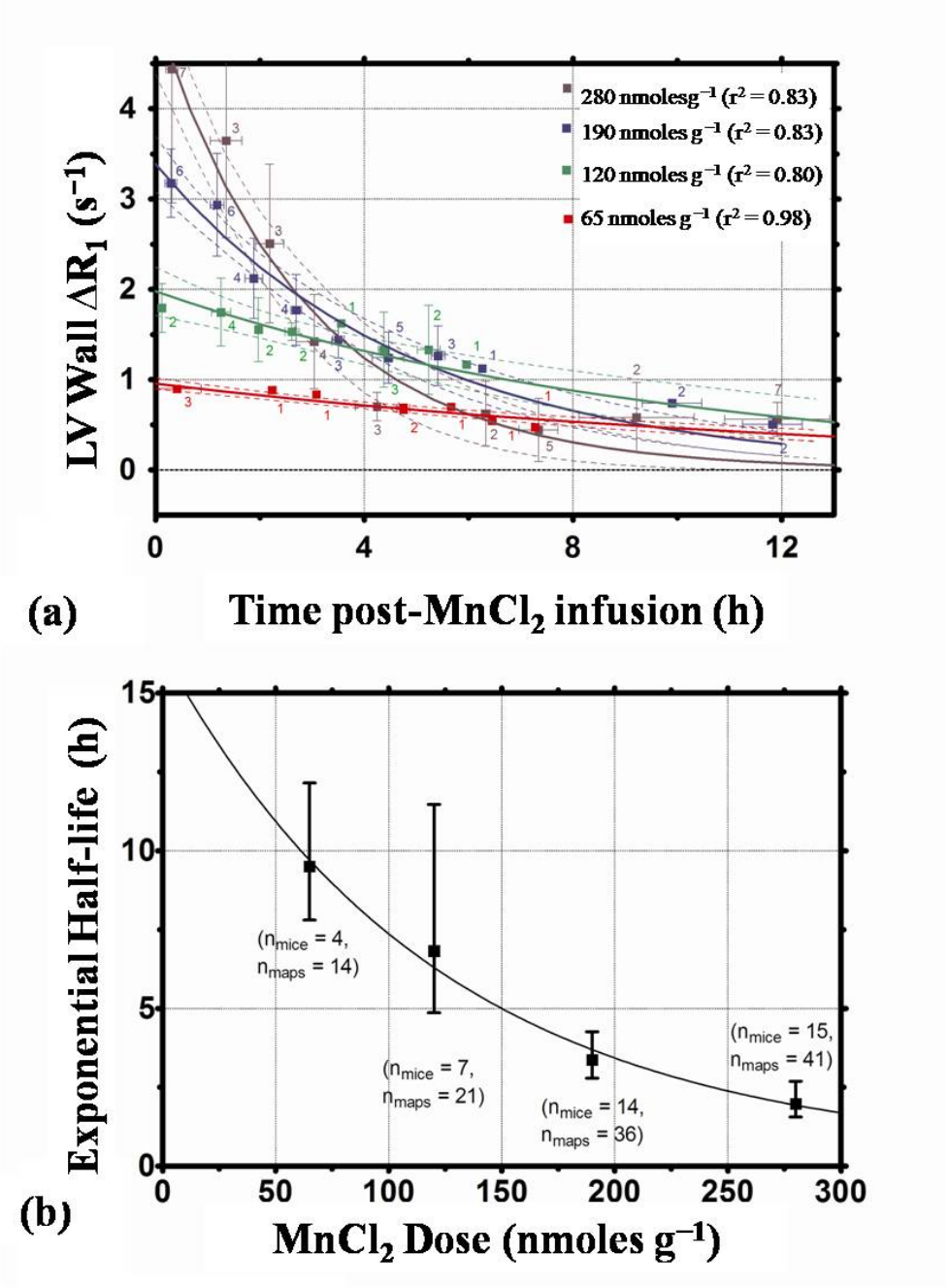

Figure 3.2

Figure 3.2 Dependence of the temporal changes in LV Wall ΔR_1 on the $MnCl_2$ infusion dose. (a) Binned data ± 1 standard deviation and first-order exponential fits using individual data points with 95% confidence intervals. (b) Corresponding dependence of the temporal LV Wall ΔR_1 washout half-life on the dose of $MnCl_2$. A first-order exponential was used to fit the half-life data. Sample sizes are shown for the mice (n_{mice}) and T_1 maps (n_{maps}). LV = left ventricle.

As shown in Figure 3.2a, the first-order exponential decay curves provided a good fit for the *in vivo* efflux data (r^2 = 0.86±0.08). As the $MnCl_2$ infusion dose increased, uptake of Mn^{2+} in the heart also increased, as did the rate of Mn^{2+} efflux.

Figure 3.2b shows the specific correlation between the infusion dose and the exponential efflux properties. Mathematical equations describing the total dependence of the efflux half-life and $\Delta R_{1,0}$ values on the $MnCl_2$ infusion dose are shown in Equation 3.1 and Equation 3.2, respectively. The curve associated with Equation 3.1 is shown in Figure 3.2b, which illustrates that the Mn^{2+} efflux half life is exponentially dependent on the dose (r^2 = 0.70) whereas Mn^{2+} uptake (proportional to $\Delta R_{1,0}$) is linearly correlated to the dose (r^2 = 0.99).

$$t_{1/2}\left[\text{hrs}\right] = 16.3e^{-0.082 \times \text{Dose}\left[\text{nmoles/g}\right]} + 0.33 \qquad \text{Equation 3.1}$$

$$\Delta R_{1,0}\left[s^{-1}\right] = 0.019 \times \text{Dose}\left[\text{nmoles/g}\right] - 0.21 \qquad \text{Equation 3.2}$$

Using the 190 nmoles g^{-1} $MnCl_2$ group as the control, all other $MnCl_2$ dose groups were found to have significantly different half-life and $\Delta R_{1,0}$ values ($p < 0.05$).

3.3.2 Absolute Manganese Content Efflux

Figure 3.3 shows the temporal response of the absolute cardiac Mn content post-infusion for the Control group (n = 12). A first-order exponential curve was fit to the absolute Mn content data, as shown. The Control group yielded an absolute Mn content efflux half-life of 4.5±3.4 hrs (r^2 = 0.58) with a corresponding extrapolated Mn content at time zero of 22.2±6.5 μg g^{-1} wet weight. There was no significant difference between the *in vivo* LV Wall ΔR_1 half-life and the absolute cardiac Mn content half-life obtained via elemental analysis (*p = 0.64)*.

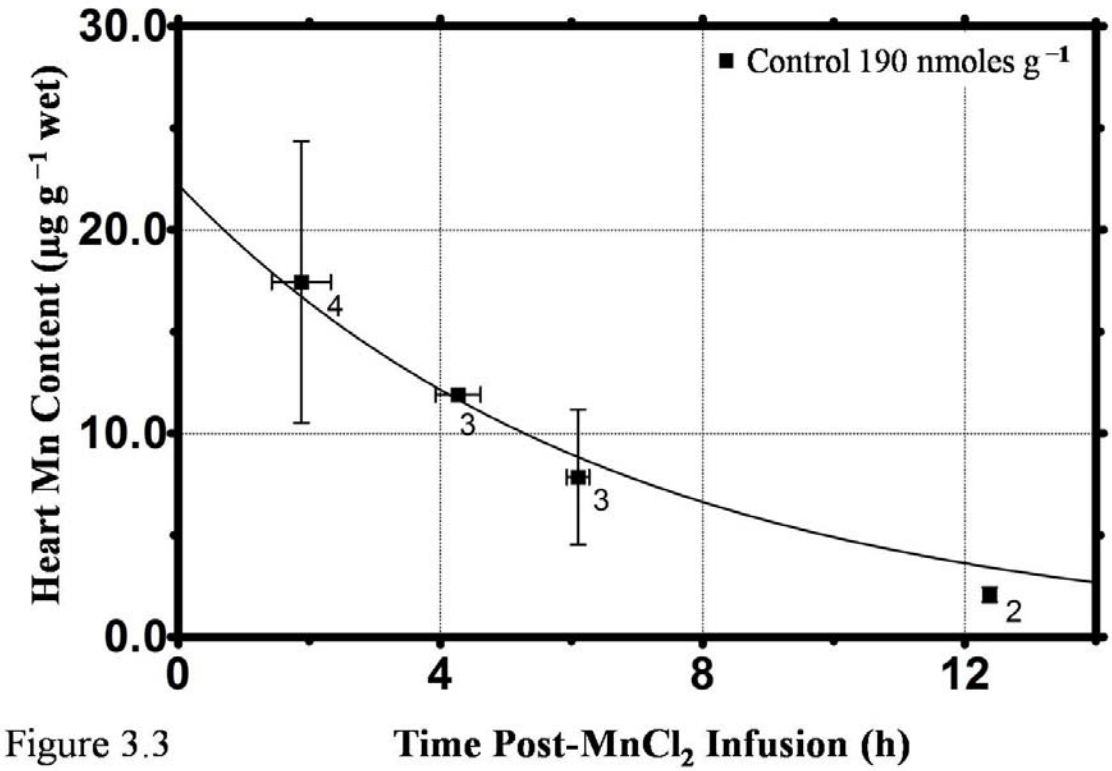

Figure 3.3

Figure 3.3 Elemental analysis data showing the temporal changes in Mn content for the control, 190 nmoles g^{-1} group, along with the first order exponential fit. Sample size (n) is also shown.

3.4 Discussion

The T_1-mapping MEMRI technique used in this study demonstrated its sensitivity to detect temporal changes in ^1H_2O relaxation rates in the LV Wall following infusion of $MnCl_2$ in healthy adult male mice. No significant difference was found between the *in vivo* LV Wall ΔR_1 half-life and the absolute cardiac Mn content half-life obtained via elemental analysis. This correlation between *in vivo* ΔR_1 efflux and the efflux of absolute cardiac Mn content post-$MnCl_2$ infusion suggested that the observed ΔR_1 changes reflect

changes in Mn^{2+} content, making this technique appropriate for the evaluation of Mn^{2+} efflux *in vivo*.

Additionally, this study found that increased $MnCl_2$ infusion doses lead to an increase in $\Delta R_{1,0}$ and the ΔR_1 efflux rate in the healthy mouse myocardium. The finding of a linear dose dependent increase of $\Delta R_{1,0}$ is in agreement with previous Mn^{2+} influx studies, §2.1.2 (99,204). Within the $MnCl_2$ dose-dependent groups, Mn^{2+} efflux occurred with a half-life dependent on the initial Mn^{2+} content such that an increase in the Mn^{2+} uptake caused an increase in the Mn^{2+} efflux rate.

This study demonstrated that cardiac MEMRI T_1-mapping in mice provided a non-invasive technique to monitor changes in ΔR_1 from which Mn^{2+} efflux could be inferred. The temporal change in LV Wall ΔR_1 after a 190 nmoles g^{-1} BW $MnCl_2$ infusion followed an exponential decay, thus allowing for inferred determinations of Mn^{2+} efflux half-lives. The half-life for the control curve was 3.4 hrs. The relatively rapid blood pool clearance, with a half-life of approximately 12 minutes, compared to the cardiac Mn^{2+} clearance (10), suggested that during the imaging time course there was negligible Mn^{2+} influx, allowing for Mn^{2+} efflux to be approximated with first-order exponential curves. Nevertheless, this first-order exponential fit is not without drawbacks. If Mn^{2+} efflux is multi-compartmental and occurs via multiple mechanisms, a more complicated washout form would be warranted with multiple exponential parameters.

Elemental analysis of heart tissue samples collected over the first 8 hrs post-$MnCl_2$ infusion demonstrated that the reduction in LV Wall ΔR_1 was linearly proportional to the myocardial Mn content (Figure 3.2). The linearity of the temporal

data, suggest that 1) observed temporal changes in ΔR_1 are linearly proportional to changes in Mn content and 2) Mn^{2+} efflux could be estimated from the ΔR_1 washout curves. If significant changes in the amount of intracellular versus extracellular Mn^{2+} occurred during the experimental timeframe, the observed Mn^{2+} longitudinal relaxivity would not be constant, since intracellular and extracellular Mn^{2+} have different relaxivities (211). In addition, the longitudinal relaxivity of intracellular Mn^{2+} would be expected to be much higher due to protein binding. However, the finding of a linear correlation between *in vivo* ΔR_1 and absolute heart Mn content over several hours suggests that the longitudinal relaxivity does not change over time. Similar to results shown by Waghorn et al. (204), this linear relationship suggests that the initial Mn^{2+} compartmentalization, such as in the mitochondria, is either linear and/or small compared to changes in the cystolic free Mn^{2+} concentration. If the latter were true, the degree of compartmentalization would have a relatively minor impact on Mn^{2+} fluxes compared to the effect of the NCX efflux mechanism during the current experimental protocol. Indeed, Figures 3.2a and 3.3 display non-zero exponential plateaus of ΔR_1 and heart Mn content respectively for times much longer than the efflux half-life. This residual increase above the baseline is relatively small and could be due to Mn compartmentalization.

3.4.1 Study Limitations

There are a number of factors that could potentially complicate the relationship between Mn^{2+} and Ca^{2+} transport. Differences between the binding constants of Mn^{2+} and Ca^{2+} may alter the relative contributions of the NCX as an efflux mechanism. Similarly, low extracellular Mn^{2+} concentrations create a concentration gradient potentially

allowing Mn^{2+} extrusion to occur via the Ca^{2+} channels. Compartmentalization of Mn^{2+} and the effect of mitochondrial Mn^{2+} on the MEMRI signal could also affect the interpretation of Mn^{2+} washout measurements. The compartmentalization effect involves compartments that are both extracellular (vascular and interstitial) and intracellular (cytoplasmic and mitochondrial). The following sections, §4 and §5, attempts to address these limitations.

3.5 Conclusions

The MEMRI T_1-mapping protocol provides a quantitative means of measuring temporal changes in LV Wall ^1H_2O longitudinal relaxation rates, allowing for the inferred, non-invasive investigation of Mn^{2+} efflux mechanisms. The findings from this study suggest that the half-life of Mn^{2+} efflux is approximately 3.4 hrs following an infusion dose of 190 nmoles g^{-1} $MnCl_2$. Using *in vivo* T_1-mapping data, myocardial Mn^{2+} content could be estimated using the correlation between *in vivo* ΔR_1 and elemental analysis of Mn content.

These findings, along with the biochemical similarities between Ca^{2+} and Mn^{2+}, strongly suggest that under appropriate conditions changes in Mn^{2+} efflux may reflect changes in Ca^{2+} efflux, such that MEMRI T_1 mapping could be an innovative and effective technique to monitor an important factor associated with the progression of heart disease.

CHAPTER 4: PART II – PHARMACOLOGICALLY AND MYOCARDIAL INFARCTION ALTERED MN^{2+} EFFLUX

4.1 Introduction

Myocardial infarction (MI) is defined as the presence of necrosis (cell death of cardiac myocytes) resulting from prolonged ischemia due to a coronary perfusion imbalance between blood supply and demand (40). Along with the rise and fall of cardiac serum biomarkers, the clinical criteria for diagnosing a MI includes images showing acute loss of viable myocardium. Imaging methods such as nuclear medicine (58), computerized tomography (59) and magnetic resonance imaging (MRI) (61) are useful for detecting the location and size of newly infarcted tissue. Kim et al. (62) demonstrated that MRI delayed enhancement methods using gadolinium (Gd) contrast could delineate regions of irreversible injury and viable tissue after a myocardial injury. Mechanisms underlying Gd concentration in the necrotic myocardium are most likely due to abnormal coronary perfusion and increased tissue edema (63). However, use of an intracellular viability tracer would allow for improved identification, quantification and evaluation of the potentially salvageable peri-infarcted tissue. Such an improved imaging technique may assist in developing new therapies for treating damaged tissue in the heart and ultimately enhance clinical outcomes for the post-MI patient (56).

During myocardial ischemia, a reduced calcium (Ca^{2+}) efflux and/or an increased Ca^{2+} influx via the sodium-calcium exchanger (NCX) results in an elevated Ca^{2+} concentration in the myocytes (4). This intracellular Ca^{2+} overload causes cellular

necrosis via protease activation, membrane rupture, cell contracture, and/or gap junction dysfunction (5).

The final background study, §2.1.4 (204) demonstrated that T_1-mapping MEMRI was able to detect and quantify regional variations of Mn^{2+} uptake in the infarcted mouse heart, which indirectly reflected altered intracellular Ca^{2+} fluctuations in the necrosed versus ischemic myocardium. Thus, the T_1-mapping MEMRI technique has the potential for improving the evaluation of necrosed and peri-infarcted tissue zones in a post-MI model.

Biochemical similarities and indirect correlations between Mn^{2+} and Ca^{2+} dynamics suggest that Mn^{2+} influx, §2.1.2 (99), and efflux, §2.1.3 (212), data could be used to predict altered Ca^{2+} handling. While differences in Mn^{2+} influx have previously been used to delineate MI regions (11,137), complexities of these approaches (e.g., myocardial perfusion, Mn^{2+} dissociation from the chelating agents) limit the interpretability of study results. The kinetics underlying Mn^{2+} efflux are not well understood, particularly since Ca^{2+} efflux (and presumably Mn^{2+} efflux) occurs via both the NCX and the plasma membrane calcium pump ATPase (PMCA).

Pharmacologic agents that selectively inhibit the NCX mechanism should be useful for investigating how the NCX influences cardiac function, particularly since these drugs exhibit potential therapeutic effects after myocardial injury (190). During the early phase of reperfusion following myocardial ischemia, the trans-sarcolemmal ion gradients driving flux via the NCX cause Ca^{2+} to enter the cell producing intracellular Ca^{2+} overload (213,214). NCX inhibitors reduce intracellular Ca^{2+} concentration in these situations, which minimizes the amount of myocardial injury and lessens the detrimental

remodeling effects promoting heart failure (215). SEA0400, the most selective and potent NCX inhibitor to date (190,195), has been shown to protect against cardiac ischemia-reperfusion injury, digitalis-induced arrhythmias, and myocardial stunning.

4.1.1 Purpose

The first part of this study was designed to test the sensitivity of the T_1-mapping MEMRI technique in a murine heart model to detect changes in ΔR_1 following treatment with NCX inhibitor SEA0400. The goal was to determine whether changes in ΔR_1 were correlated to changes in the absolute Mn^{2+} content in the myocardium. The hypothesis was that Mn^{2+} will be extruded from cells via the NCX, with changes in Mn^{2+} efflux reflecting changes in Ca^{2+} efflux.

Furthermore, this study examined the potential of implementing T_1-mapping MEMRI to monitor potential changes in Mn^{2+} efflux rates following inhibition of the NCX with various doses of SEA0400 as well as with the inotropic agent dobutamine and post-MI. Observed temporal changes could potentially be used for inferring Mn^{2+} efflux as a tool for monitoring changes in Ca^{2+} efflux, a technique which could be used to monitor cardiac disease progression.

Therefore, the purpose of this study was to characterize myocardial Mn^{2+} efflux properties in both healthy male adult mice and ones experiencing surgically induced MI. The goals for this section of the dissertation were therefore:

1. To determine whether the MEMRI T_1 mapping technique was sensitive to changes in Mn^{2+} efflux following SEA0400 administration, and whether alterations in ΔR_1 reflected changes in Mn^{2+} handling

2. To study and quantify the changes in Mn^{2+} efflux in healthy male mice, using T_1-mapping MEMRI, for different conditions (various NCX antagonist pharmacologic agent doses and a β-adrenergic agonist pharmacologic agent)
3. To quantitatively define the peri-infarcted zone in post-MI male adult mice
4. To study difference in Mn^{2+} efflux properties between healthy and MI murine hearts, as well as between the necrosed and peri-infarct regions in the MI murine hearts.

4.2 Methods

4.2.1 Experimental Protocol

MEMRI experiments were performed on adult male C57Bl/6 mice (6-14 weeks old, 23.9±2.3 g) following the guidelines of the Institutional Animal Care and Use Committee at the Medical College of Georgia, Augusta, GA. MEMRI efflux studies were conducted in n = 60 mice, as described in §3.2.1. The mice were randomized into four groups:

1. SEA0400 (10 – 50 mg kg^{-1} SEA0400 following 190 nmoles g^{-1} $MnCl_2$; n = 30);
2. Dobutamine (15 μg g^{-1} dobutamine following 190 nmoles g^{-1} $MnCl_2$; n = 6);
3. Sham (sham-operation / thoracotomy only with 190 nmoles g^{-1} $MnCl_2$; n = 7);
4. MI (surgically induced MI with either 190 or 280 nmoles g^{-1} $MnCl_2$; n = 17)

Table 4.1 shows the number of mice in, and total number of T_1 maps generated for, each of these groups (as well as the dose dependent groups from §3) and their

associated pharmacologic dose/procedure subgroups. Both $MnCl_2$ doses used in this study (i.e. 190 and 280 nmoles g^{-1}) have been shown not to cause cardiotoxic effects in rodents (99,204). The reference $MnCl_2$ dose of 190 nmoles g^{-1} was found to lie at the high level end of the linear Mn^{2+} uptake region, §2.1.2 (204). The pharmacologic agents SEA0400 (Taisho Pharmaceutical, Tokyo, Japan) and dobutamine (MP Biomedicals, Irvine, CA) were used to manipulate Mn^{2+} efflux via alteration of intracellular Ca^{2+} concentration. A selective NCX inhibitor, SEA0400, was given to a group of healthy mice in order to attenuate Ca^{2+} efflux in the myocardium and thereby reduce Mn^{2+} efflux (190,198,212). A β-adrenergic agonist, dobutamine, was given to a separate group of healthy mice to increase contractility while minimally affecting heart rate (216). This positive inotropic effect was expected to increase Ca^{2+} efflux and thereby increase Mn^{2+} efflux in the healthy murine myocardium. Both SEA0400 and dobutamine were administered as a bolus intraperitoneal injection one hour after the $MnCl_2$ infusion.

4.2.2 Myocardial Infarction Model

Mice randomized into both the Sham and MI groups underwent a thoracotomy to expose the heart. As previously described (204), the Sham mice then had their chests immediately sutured closed and the MI mice had their left anterior descending coronary artery permanently ligated to produce an acute infarction in the left ventricular (LV) myocardium. These mice were then allowed to recover from the surgery for 8±1 days before beginning the MEMRI sessions. Previous research demonstrated that the mice recovered from surgery without complications during this time period, providing an observable differentiation between the infarcted and remote viable tissue during imaging

(204). Additionally, waiting for 8-days minimized any potential complications that would confound the data results owing to the early inflammatory processes occurring after surgery since inflammatory cells such as macrophages are known to uptake Mn^{2+} (149).

4.2.3 Manganese-Enhanced Magnetic Resonance Imaging

MEMRI data were again acquired on a 7.0-T 20-cm horizontal bore Bruker BioSpec MRI spectrometer (Bruker Instruments, Billerica, MA) equipped with a micro-imaging gradient insert (950 mT/m) (204), as described in §3.2.2. Short-axis images were acquired midway through the LV and perpendicular to the long axis of the heart for the healthy and sham-operated mice. For the MI group, the short-axis slice contained the area with the thinnest portion of the LV wall (typically located within 1 mm of the LV center).

4.2.4 Data Analysis

T_1 Mapping

Mn^{2+} efflux properties were characterized via T_1 maps generated from pre-contrast MRI as well as MEMRI, as described in §3.2.3. T_1 values were estimated by fitting the signal recovery of each pixel with a three-parameter Levenburg-Marquardt non-linear curve-fitting algorithm using the 50 echo images acquired via the Look-Locker sequence (145). Region-of-interest (ROI) analysis was performed on the 2D T_1 maps for the SEA0400, and Dobutamine groups using the AMIDE (205) software to calculate the mean T_1 value in the LV free wall area.

T_1 maps were generated from MRI performed prior to $MnCl_2$ infusion for the non-surgical SEA0400 and Dobutamine (n = 33), Sham (n = 21) and MI (n = 9) groups, and at various times post-$MnCl_2$ infusion. These T_1 maps assessed residual Mn^{2+} retention and changes in absolute ^1H_2O relaxation rate, ΔR_1, in the LV free wall. *In vivo* ΔR_1 values were again calculated as (post-$MnCl_2$ infusion $1/T_1$) – (pre-$MnCl_2$ infusion $1/T_1$), whereby the relaxation rate (R_1) equaled $1/T_1$ in units of [s^{-1}] (212). T_1 mapping was not performed during the first 0.2 hours following $MnCl_2$ infusion to allow for an assumed blood pool clearance (10).

Myocardial Isolation and Segmentation Software

Using the created T_1 maps, a custom Matlab® (Math Works, Natick, MA) program was run to automatically and objectively isolate the myocardium area for the Control (190 nmoles g^{-1} $MnCl_2$ dose, §4), Sham and MI groups (see Appendix A, Figure A.1 and Figure A.2). T_1 map data for the myocardium were segmented automatically using a program developed in our lab by Dr. Nathan Yanasak, and adapted for use within this study. The program required a T_1-weighted (T_1W) image and a T_1 map as input, using the high contrast difference between tissue and blood on the T_1W image to define the interior wall of the LV via segmentation of blood using a histogram of image intensities. The program user was also required to provide a point graphically to represent the approximate center of the heart and another to locate the approximate center of the necrosed tissue within the MI site, or the center of the RV for the healthy or sham-operated mice. The line subtended between these two points allows the angular segments from each myocardium to be aligned for statistical comparison (using a line between the

LV center and the right ventricle as a reference for 0^o, the line between LV center and MI is approximately 135^o).

Isolation of the myocardium proceeds by determining an initial guess for the middle position of myocardium tissue and corresponding T_1 at this position as a function of angle of rotation around the LV. At each angular position around the myocardium, final isolation used the guessed mean value of T_1 to define a range of T_1 values around that mean, within which pixels are included in the myocardium. The function that defined this range varies inversely with mean T_1, to prevent contamination of the MI tissue with adjacent chest wall of similar T_1 value. Isolated pixels were organized into 360 regions, or "sectors", by angular position (i.e. 360 × 1° radial segments, with approximately 4 voxels per sector), and the mean and standard deviation of T_1 and R_1 values were calculated in each sector.

To determine the initial guess for the middle myocardial position and T_1 value, blood was segmented using the T_1W image and a mask was created. Blood in the LV defined the approximate inner boundary of the search volume containing the myocardium. Blood from the RV was used to define the approximate outer boundary of the search volume containing the myocardium, which included a region slightly larger than the RV location. Next, the approximate position of middle of the myocardial wall at a given angle of rotation around the LV was determined. Within the search volume, the pixel with the minimum T_1 value in the myocardium at a particular angle was considered to be located at the middle of the myocardial wall. These locations over all angles formed a distorted ellipse. As the myocardium can be considered to be well-approximated by an elliptical shape, the function defining the middle position of the myocardium at a given

angle was smoothed spatially. Smoothing occurred in three stages: an initial boxcar smoothing procedure, followed by convolution of the function with a gaussian kernel. A final stage involving frequency-domain filtering eliminated components with a spatial periodicity < 60^o. Using this smoothed function, the T_1 value in the middle of the myocardium was determined as a function of angle, and this was smoothed as well using the same frequency-domain filtering process.

Region Defining MI Curve Fitting Algorithm

From the 360 one-degree sectors calculated for the isolated myocardium, radial position-dependent ΔR_1 values were calculated for each sector. For the Control and Sham groups, the ΔR_1 values were calculated from the average T_1 value across the isolated myocardium. For the MI mice, an algorithm was applied to the radial data to delineate between the 1) viable [healthy, unaffected remote tissue; Region A], 2) necrosed [infarcted tissue; Region B] and 3) peri-infarcted [ischemic with an admixture of viable and necrotic tissue] zones. Regions A and B were defined as constant ΔR_1 values with $\Delta R_1(A) > \Delta R_1(B)$. The peri-infarcted zone was defined as the region between the viable and necrosed zones such that ΔR_1 varied linearly with the specific radial position. Using these definitions, an algorithm using a non-linear least-square fitting technique produced a curve locating the viable, necrosed, and peri-infarcted regions. The 180° location defined the middle of the necrosed zone.

Using these average ΔR_1 values, efflux curves were produced for the Control, Sham and MI (Regions A and B) groups. Then individual ΔR_1 values from each radial

sector of the MI hearts were used to generate 360 ΔR_1 first-order exponential efflux curves.

Statistics

With the exception of the Dobutamine group, the ΔR_1 efflux data were fitted to a least-square first-order exponential decay curve using GraphPad Prism statistics software (GraphPad, San Diego, CA). The Dobutamine group ΔR_1 efflux data were fitted to a second-order exponential decay curve along with the 190 nmoles g^{-1} $MnCl_2$ (Control dose, §3) and 50 mg kg^{-1} SEA0400 data. The second-order exponential decay curves were generated to account for the relatively short elimination half-life of dobutamine in the myocardium. The extrapolated ΔR_1 at the time of infusion (t = 0; $\Delta R_{1,0}$) and half-life values were calculated from these exponential decay curves. The $\Delta R_{1,0}$ and half-life values were compared between groups using an extra sum-of-squares F test (0.05 level of significance), which compared the ratio of the difference between the least-square fit from the washout curves to the residual sum of squares within each decay curve.

Histology

Three post-MI mice were randomly selected for histological analysis following MEMRI to provide preliminary data for correlating the *in vivo* segmented region-defining MI curve locating the viable, necrosed and peri-infarcted regions to histological evidence. While heavily anesthetized with isoflurane, the animals were sacrificed by exsanguination when the hearts were excised from the chest. The hearts were then sliced along the short-axis for hematoxylin and eosin (H&E) staining. Histologic sections

corresponding to individual MEMRI images of each animal were qualitatively compared to the associated *in vivo* ΔR_1 data.

4.3 Results

4.3.1 Detecting Pharmacologically Altered Mn^{2+} Efflux Rates *in vivo*

Figure 4.1 shows an example of four cardiac short-axis T_1 maps generated over time from mice in the Control group. Following infusion of 190 nmoles g^{-1} $MnCl_2$, the myocardial tissue becomes darker in the T_1 maps, representing a reduction in the T_1 values due to an increase in Mn^{2+} content. The T_1 values gradually return to the pre-infusion T_1 values with increasing time, shown as a yellow color.

Absolute Mn content was measured from the heart tissue and blood samples of randomly selected mice to establish the relationship between temporal changes in the LV Wall ΔR_1 and absolute cardiac Mn content, following SEA0400 administration. Figure 4.2 shows the elemental analysis results for the heart tissue samples obtained from the control, 20 mg kg^{-1} and 50 mg kg^{-1} SEA0400 experimental groups, with Figure 4.2a showing the relationship between the LV Wall ΔR_1 and absolute heart Mn content, including data from §2.1.2. No statistically significant differences were found between the groups following linear least-square fitting to the data. A common fit with a slope of 0.10 ($p = 0.38$) and y-intercept of 0.48 ($p = 0.08$) was found. The absence of statistically significant differences in the slopes of the ΔR_1 / Mn content curves between the control and SEA0400 groups suggests that myocardial ^1H_2O relaxivities were not influenced by

administration of SEA0400. A linear fit to all of the data groups was demonstrated with the 95% confidence band in Figure 4.2a. This corresponding relaxivity in the myocardium was 6.92 $mM^{-1}s^{-1}$ using an assumed myocardial tissue density of 1.055 g ml^{-1} (217).

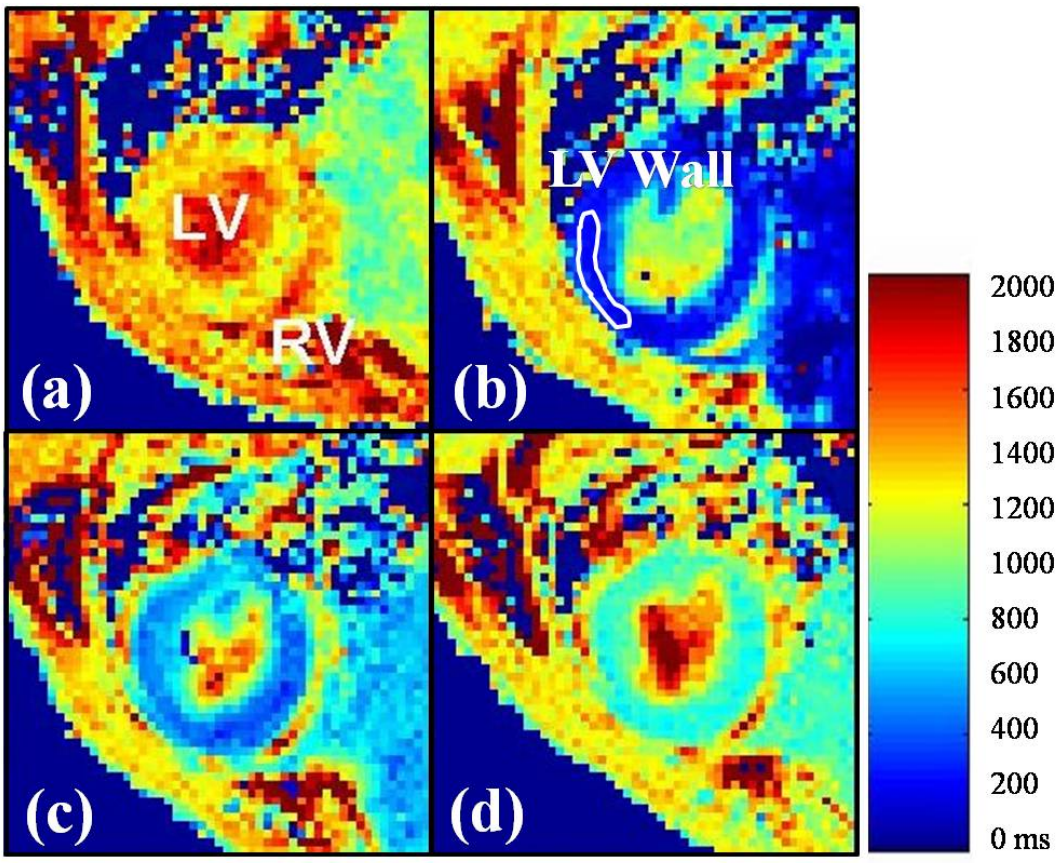

Figure 4.1

Figure 4.1 Sample short-axis mouse heart T_1 maps from a healthy myocardium, acquired (a) pre-$MnCl_2$ infusion, (b) 1.3 h, (c) 4.1 h, and (d) 11.4 h post-190 nmoles g^{-1} $MnCl_2$ infusion. Left and right ventricles are labeled as LV and RV, respectively. A sample LV Wall region of interest (ROI) is also shown in (b).

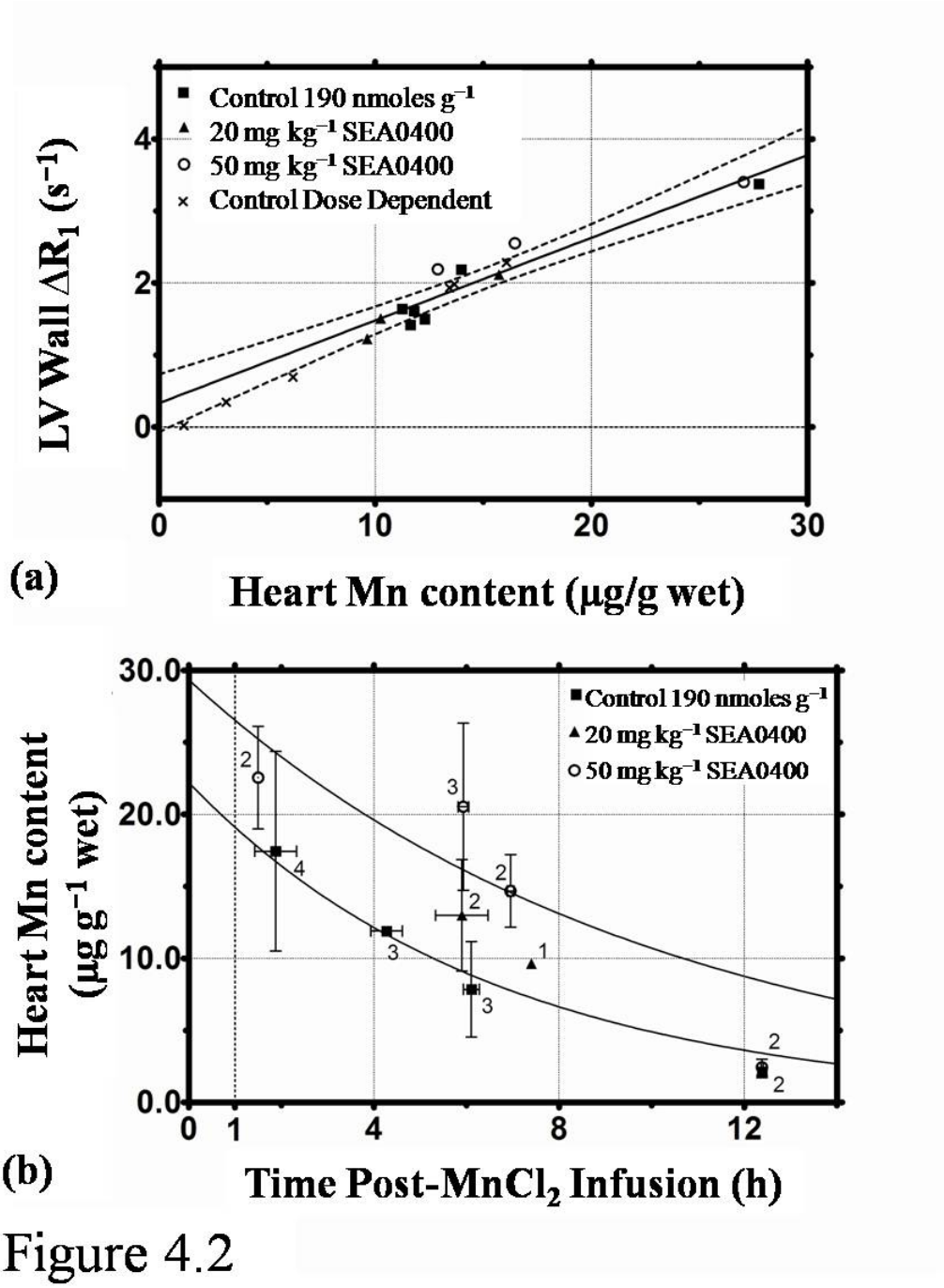

Figure 4.2

Figure 4.2 Elemental analysis data showing; (a) the effect of the absolute heart Mn content on the *in vivo* LV Wall ΔR_1 for three experimental groups; control (square), 20 mg kg^{-1} (triangle) and 50mg kg^{-1} (open circle) SEA0400. A linear fit to all of the data, along with the 95% confidence band, is shown. Also shown is dose dependent data (x) from Waghorn et al, 2008, §2.1.2. Temporal changes in Mn content for each group are shown in (b), along with first order exponential fits for the control and 50 mg kg^{-1} SEA0400. Sample size (n) is also shown.

Figure 4.2b shows the temporal response of the absolute cardiac Mn content post-infusion. First-order exponential curves were fit to both the control (n = 12, squares) and 50 mg kg^{-1} SEA0400 groups (n = 9, open circles), as shown. The control group yielded a half-life of 4.5±3.4 hrs (r^2 = 0.58, as shown in §3.3.2) while the half-life for the 50 mg kg^{-1} SEA0400 was 6.87±5.2 hrs (r^2 = 0.63). The corresponding extrapolated Mn contents at time zero were 22.2±6.5 and 29.3±7.1 μg g^{-1} wet weight for the control and 50 mg kg^{-1} SEA0440 groups respectively. Exponential curves for the control and 50 mg kg^{-1} SEA0400 groups were significantly different ($p < 0.05$). At 6 hrs post-$MnCl_2$, the 50 mg kg^{-1} SEA0400 group exhibited a Mn content of 16.0 μg g^{-1} that was approximately twice the content of the control group for the same time point.

T_1 values were acquired from blood samples taken from 16 mice (n = 3, pre-$MnCl_2$ (baseline); n = 6, control; n = 4, SEA0400 20 mg kg^{-1}; n = 3, SEA0400 50 mg kg^{-1}). $\Delta R_{1,blood}$ values were calculated by subtracting the average baseline (pre-$MnCl_2$) R_1 value ($R_{1,blood,baseline}$ = 1.28±0.17 s^{-1}) from the individual R_1 values post-$MnCl_2$ infusion. The average $\Delta R_{1,blood}$ for the control, 20 mg kg^{-1} and 50 mg kg^{-1} SEA0400 experimental groups over the time range of 1.5 – 12.4 hrs post-infusion was 0.17±0.48 s^{-1} ($\Delta R_{1,blood}$ = 0.13±0.20, 0.20±0.17 and 0.23±0.35 for the control, 20 mg kg^{-1} and 50 mg kg^{-1} SEA0400 groups respectively).

In addition to the $\Delta R_{1,blood}$ calculations, elemental analysis was performed on the blood samples from 18 mice (n = 2, baseline; n = 8, control; n = 8, SEA0400 50mg kg^{-1}). The average baseline Mn content was 0.09±0.01 μg ml^{-1} with the corresponding contents for the control and SEA0400 groups being 0.16±0.04 and 0.19±0.05 μg ml^{-1}, respectively, both in the time range of 1.5 to 12.4 hrs post-infusion. The increase in blood

Mn content for both groups, although non-zero, was minute compared to the infused content and could not be detected as an increase in $\Delta R_{1,blood}$. Using a linear least-square best fit, no temporal trend for the blood Mn content was observed for either the control (slope = −0.01±0.01 μg ml^{-1} $hour^{-1}$, r^2= 0.55), or 50 mg kg^{-1} SEA0400 (slope = −0.01±0.01 μg ml^{-1} $hour^{-1}$, r^2= 0.20) groups over the time range of sample acquisition (t = 1.5 – 12.4 hrs).

For the *in vivo* data, values of ΔR_1 for the healthy mice were calculated by subtracting the average baseline ROI R_1 ($R_{1,baseline,LVWall}$ = 0.78±0.04 s^{-1} from 33 mice) from the post-$MnCl_2$ infusion ROI R_1 value. Infusion of 190 nmoles g^{-1} BW $MnCl_2$ solution into the control group produced a LV Wall ΔR_1 washout curve as shown in Figure 4.3 (squares, also shown in §3). Fitting a least-square first-order exponential to the individual, unbinned data points (r^2 = 0.83) gave ΔR_1 (at zero time post-infusion), $\Delta R_{1,0}$ = 3.4±0.3 s^{-1}. The T_1 shortening effect was rapidly attenuated, with a ΔR_1 half-life of 3.4±0.6 hrs (n = 14; total number of T_1-maps = 36). There was no significant difference between the *in vivo* LV Wall ΔR_1 half-life and the absolute cardiac Mn content half-life obtained via elemental analysis (*p = 0.64)*.

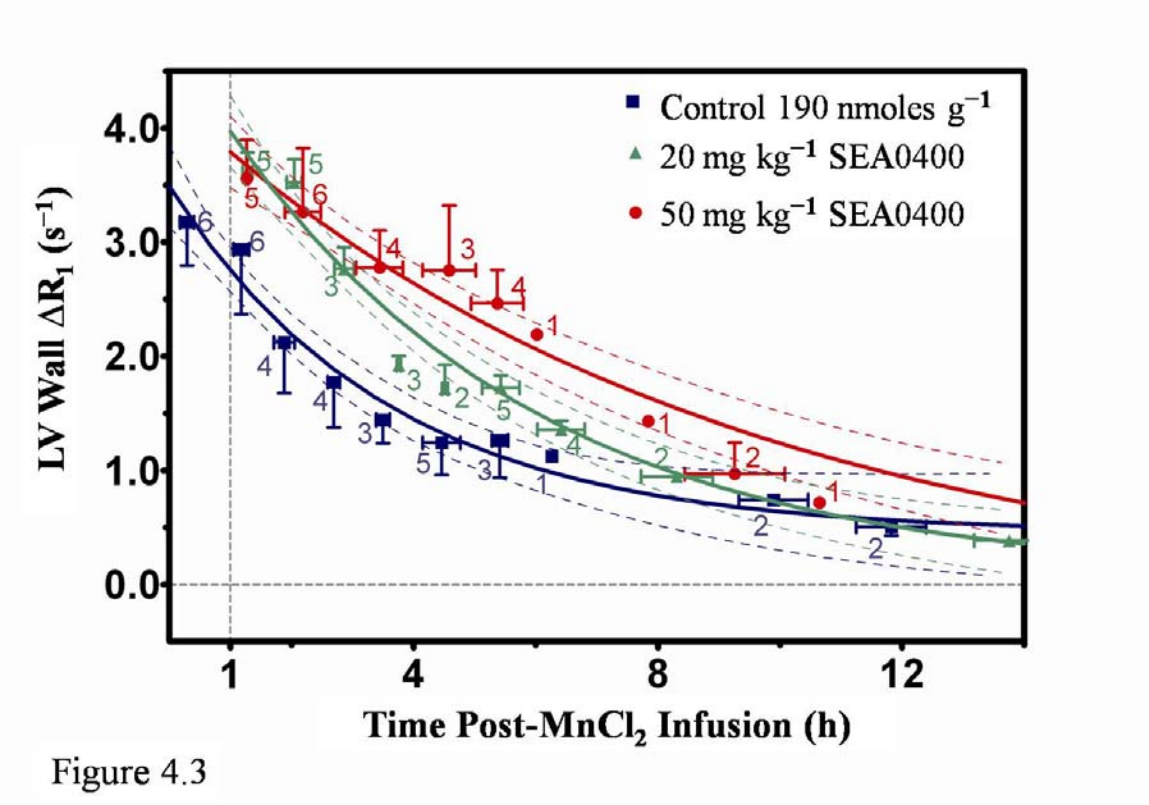

Figure 4.3

Figure 4.3 The effect of the NCX channel inhibitor SEA0400 on the temporal changes in ΔR_1, measured in the LV Wall. First order exponential fits using individual data points are shown along with the binned data ± 1SD and the 95% CI envelopes. Sample size, n, is also shown.

The effects of the NCX inhibitor SEA0400 on the temporal changes in LV Wall ΔR_1 are also shown in Figure 4.3. The washout curves displayed in Figure 4.3 were obtained following a single intraperitoneal injection of either 20 mg kg^{-1} or 50 mg kg^{-1} SEA0400 one hour post-$MnCl_2$ infusion. Least-square first-order exponential curves were fit to the temporal LV Wall ΔR_1 data beginning at one hour post-$MnCl_2$ infusion (t = 1 hour). For the 50 mg kg^{-1} SEA0400 group (open circles) (n = 7, total number of T_1-maps = 29), the exponential curve was extended, with a ΔR_1 reduction half-life of 5.6±1.1 hrs and a $\Delta R_{1,0}$ = 4.3±0.4 s^{-1} (r^2 = 0.87). The 20 mg kg^{-1} SEA0400 group (triangles)

displayed a half-life of 3.6±0.5 hrs and a $\Delta R_{1,0}$ = 4.8±0.2 s^{-1} (n = 8, total number of T_1-maps = 33, r^2 = 0.91). For comparison, the control group was also fit to a least-square first-order exponential curve excluding data for t < 1 hour. This fit yielded a half-life of 3.2±0.5 hrs and a $\Delta R_{1,0}$ = 3.5±0.8 s^{-1} (r^2 = 0.77). All three washout curves in Figure 4.3 include the 95% CI envelopes, where regions with no overlap between groups demonstrated significance at that particular time.

In the time range of 4.9 – 5.9 hrs post-$MnCl_2$ infusion, the average ΔR_1 values for the SEA0400 groups were 2.46±0.29 s^{-1} (n = 4) and 1.72±0.24 s^{-1} (n = 5) for 50 mg kg^{-1} and 20 mg kg^{-1} doses respectively, as compared to the control group of 1.27±0.28 s^{-1} (n = 4). This range was selected to ensure that sufficient time had elapsed after SEA0400 administration, to allow for the observation of any potential drug effects. An ANOVA test comparing the LV Wall ΔR_1 values for the three groups within this time interval showed a significant difference in LV Wall ΔR_1 between the groups ($p < 0.05$). Further Tukey post hoc comparisons revealed significant differences between all group combinations ($p < 0.05$).

Figure 4.4 illustrates the dependence of the exponential temporal response of the LV Wall ΔR_1 washout curves on the SEA0400 dose. Figure 4.4a shows the dependence of half-life on the dose; Figure 4.4b shows the dependence of $\Delta R_{1,0}$. For both curves, SEA0400 dose was plotted against the relevant exponential fit parameters of the washout data (t ≥ 1 hour) with the 95% CI shown. An extra sum-of-squares F test showed that the washout half-life was significantly different between these three groups ($p < 0.01$). The 50 mg kg^{-1} group had a half-life significantly different from the control group ($p < 0.01$), although the half-life for the 20 mg kg^{-1} group was not statistically different from the

control group ($p = 0.54$). No statistical difference was found between $\Delta R_{1,0}$ measured in the two SEA0400 groups ($p = 0.12$), although a statistical difference existed between $\Delta R_{1,0}$ when comparing all three groups ($p < 0.01$). These findings suggest that SEA0400 caused an initial increase in ΔR_1 that was independent of dose, while a higher dose of SEA0400 was required to reduce the rate of ΔR_1 change.

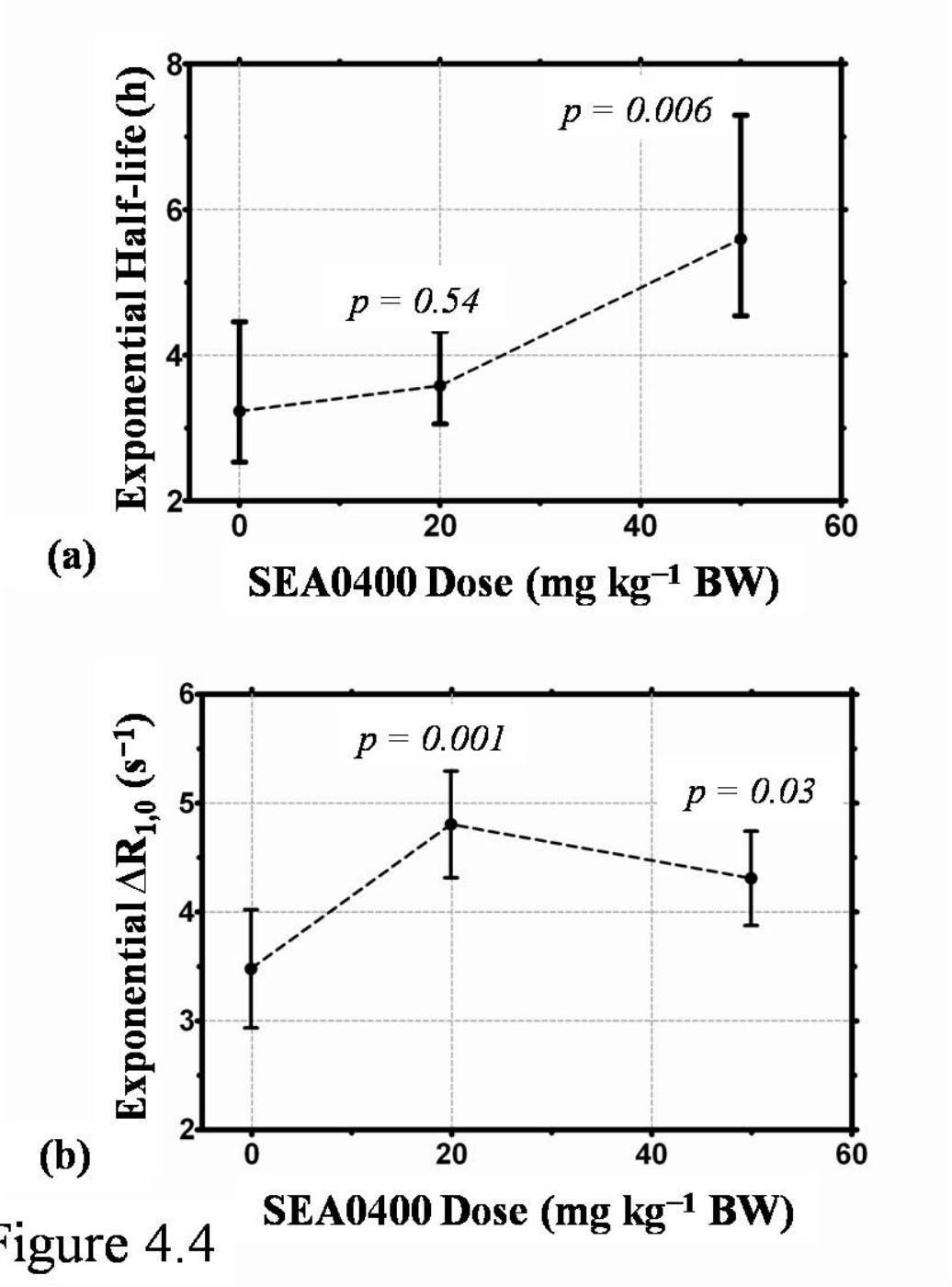

Figure 4.4

Figure 4.4 The dependence of the temporal LV Wall ΔR_1 washout half-life (a) and extrapolated ΔR_1 at the time of $MnCl_2$ infusion ($\Delta R_{1,0}$) (b) on the dose of NCX inhibitor SEA0400. Both values result from a first order exponential fit to the temporal ΔR_1 washout, starting at one hour post-Mn^{2+} infusion. Shown are the 95% CI values and resulting extra sum-of-squares F test comparing the individual SEA0400 groups to the control group.

4.3.2 The Effect of SEA0400 and Dobutamine on Mn^{2+} Efflux

Having demonstrated the ability of MEMRI T_1-mapping to detect pharmacologically altered Mn^{2+} efflux rates (§4.3.1), additional studies were performed to further assess the Mn^{2+} efflux mechanisms. Combining data from Part I (§3) and Part II (§4), Figure 3.2, Table 4.1, Figure 4.1, and Figure 4.3 all provide evidence that T_1-mapping MEMRI detected and quantified Mn^{2+} efflux in healthy male mice under different conditions. Table 4.1 summarizes the heart rate, half-life and $\Delta R_{1,0}$ values for the different group conditions and their associated pharmacologic/procedural subgroups. A one-way ANOVA test showed a significant difference in heart rate among the groups ($p = 0.028$); the Tukey post-hoc test found that heart rate was only significantly different between the 35 mg kg^{-1} SEA0400 and Dobutamine groups ($p = 0.02$). The 34 and 50 mg kg^{-1} SEA0400 dose group half-life values were significantly different from the $MnCl_2$ Control (190 nmoles g^{-1}) group, as were the Dobutamine and Region B (Necrosed) groups ($p < 0.05$). Half-life values normalized to the Control group are shown in the final column of Table 4.1. Normalized values < 1 represent an increase in the efflux rate relative to the control group and values > 1 an increase in Mn^{2+} efflux rate.

For the healthy mice not undergoing surgery (SEA0400, and Dobutamine groups), ΔR_1 values were calculated by subtracting the average baseline R_1 value (0.78±0.04 s^{-1}) from the post-$MnCl_2$ infusion ROI R_1 values. Figure 4.5a shows the LV Wall ΔR_1 washout curves for the four SEA0400 doses; Figure 4.5b shows the corresponding half-life and $\Delta R_{1,0}$ values. A small increase in ΔR_1 was observed after SEA0400 administration relative to the control group. The first-order exponential curves provided a reasonable fit to the SEA0400 efflux data ($r^2 = 0.91\pm0.05$) with increasing doses of

SEA0400 reducing the efflux rate following longer retention of Mn^{2+}. In Figure 4.5b, a significant increase in the efflux half-life was observed for the 35 and 50 mg kg^{-1} SEA0400 groups (p = 0.04 and 0.02, respectively) compared to the $MnCl_2$ Control group. While a significant increase in $\Delta R_{1,0}$ was observed for all SEA0400 groups compared to the $MnCl_2$ Control group ($p < 0.05$), the $\Delta R_{1,0}$ values among the SEA0400 groups were not significantly different (p = 0.30).

Figure 4.6a shows the second-order exponential decay curves for the Dobutamine group in comparison to the $MnCl_2$ Control and 50 mg kg^{-1} SEA0400 groups; Figure 4.6b shows the corresponding exponential half-life values. The Dobutamine efflux curve was found to be significantly different from the Control and SEA0400 curves ($p < 0.001$). Figure 4.6b shows how the Dobutamine group's Initial (fast efflux rate) and Delayed (slow efflux rate) half-life values compared to the other two groups. The Dobutamine group had an initial efflux rate significantly faster than the Control and 50 mg kg^{-1} SEA0400 groups with a slower associated delayed rate. This finding suggests an apparent increase in Mn^{2+} efflux following increases in the inotropic rate, which decreased with a reduced drug effect.

Figures 4.7 and 4.8 both provide evidence that T_1-mapping MEMRI quantitatively defined the peri-infarcted zone. Figure 4.7 shows examples of the segmentation output for post-$MnCl_2$ infusion T_1 maps in post-MI mice; the radial orientation is shown in Figure 4.7b. Figures 4.7c, 4.7d, and 4.7e illustrate the temporal changes in T_1 values due to Mn^{2+} efflux at 1.6 h, 3.6 h, and 6.3 h post-$MnCl_2$ Control infusion dose, respectively.

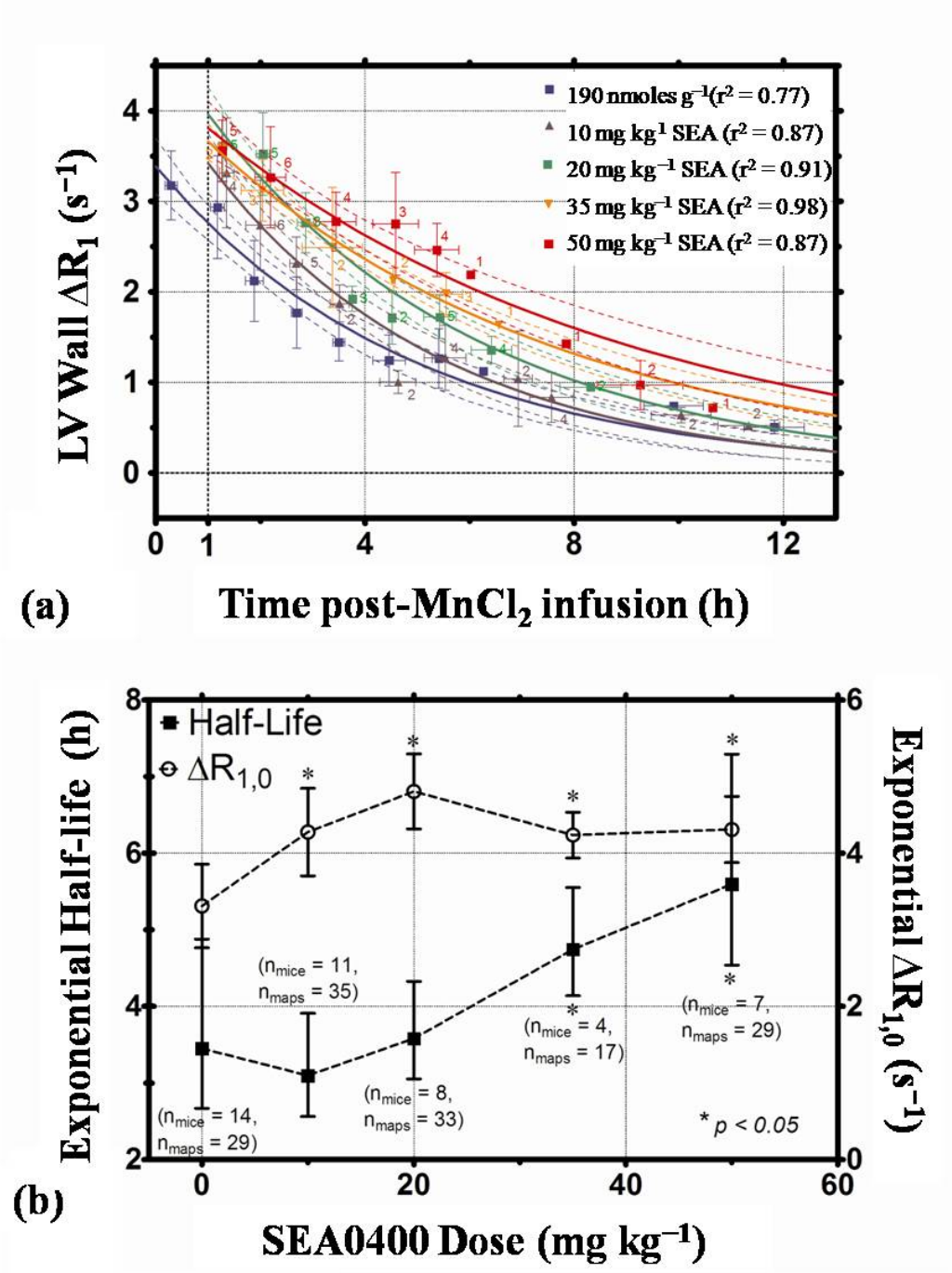

Figure 4.5

Figure 4.5 Effect of altering the SEA0400 dose (sodium calcium exchanger inhibitor) on the temporal changes in LV Wall ΔR_1. (a) Binned data ± 1standard deviation and first-order exponential fits using individual data points with 95% confidence intervals. (b) Corresponding dependence of the temporal LV Wall ΔR_1 washout half-life (solid squares) and extrapolated $\Delta R_{1,0}$ (open circles) on the SEA0400 dose. LV = left ventricle.

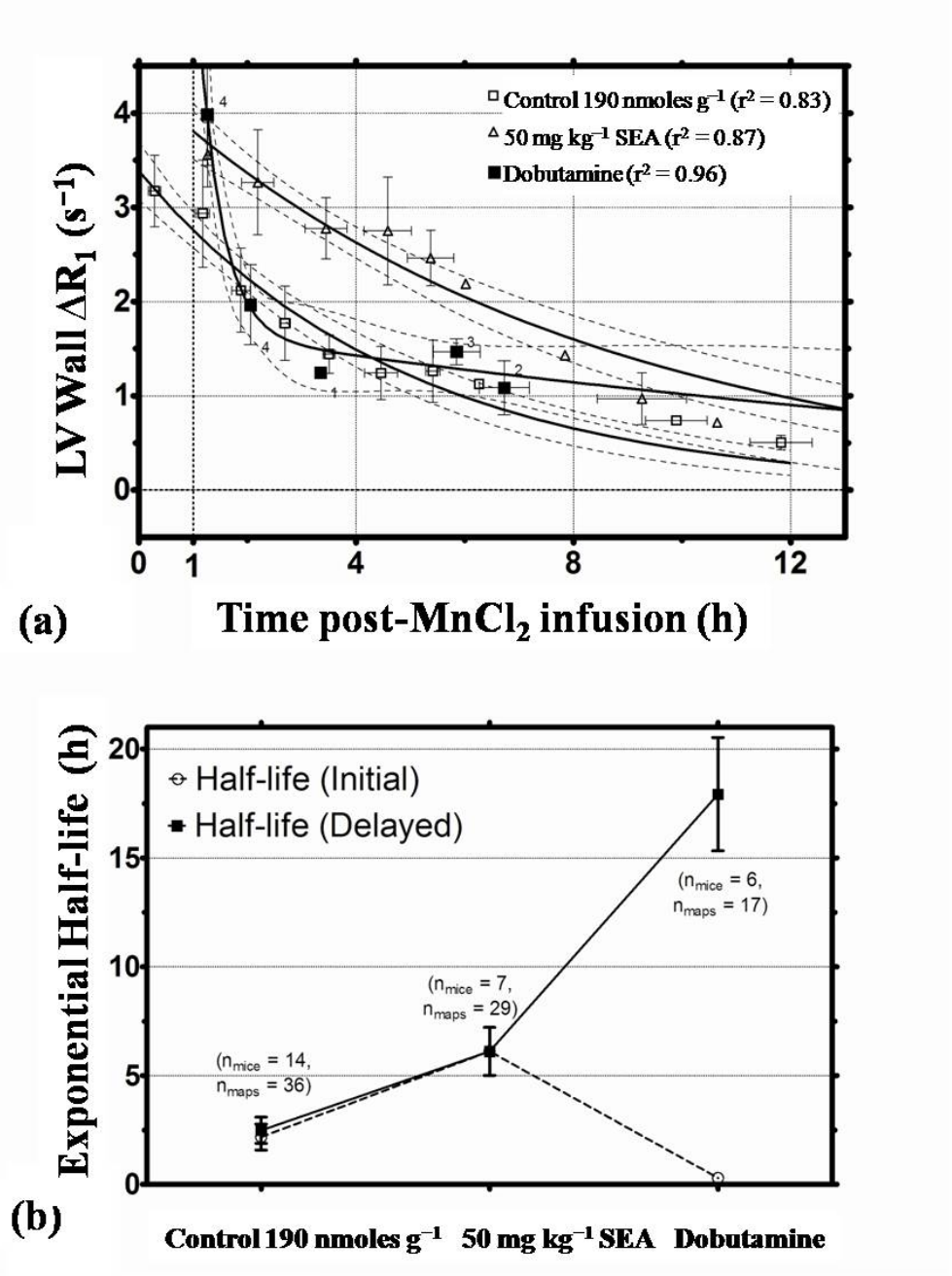

Figure 4.6

Figure 4.6 The effect of dobutamine on the temporal changes in LV Wall ΔR_1 compared to the Control (190 nmoles g^{-1}) and 50 mg kg^{-1} SEA0400 groups. (a) Binned data ± 1standard deviation and first-order exponential fits using individual data points with 95% confidence intervals. (b) A comparison between the second-order fast (open circle) and slow (solid square) half-lives for the 190 nmoles g^{-1}, 50 mg kg^{-1} SEA0400 and Dobutamine groups. LV = left ventricle.

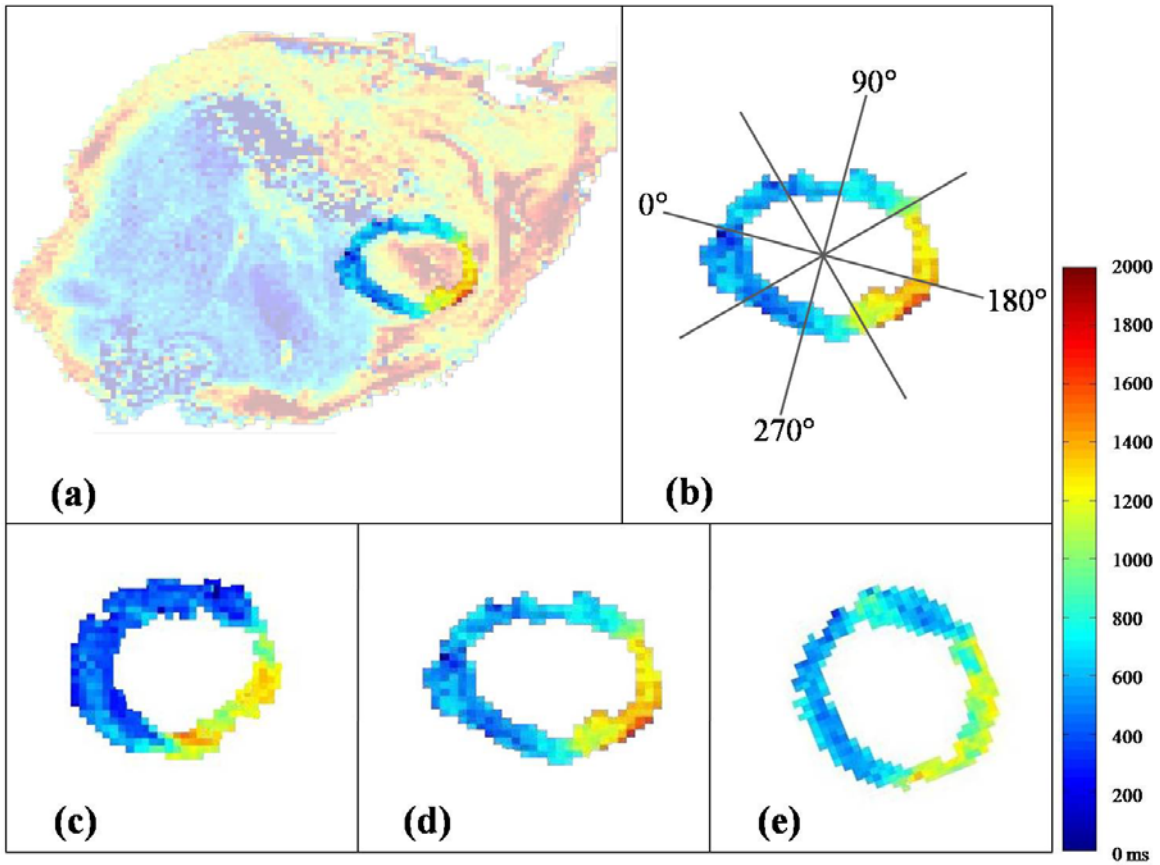

Figure 4.7

Figure 4.7 (a) Sample cardiac short-axis T_1 map for a myocardial infarction mouse after infusion of the manganese contrast agent ($MnCl_2$). The segmented myocardium is shown with the remaining tissue illustrated with increased opacity. (b) Demonstration of the sectoring orientation on the isolated myocardium. Temporal manganese ion efflux is demonstrated at (c) 1.6 h (d) 3.6 h and (e) 6.3 h post-190 nmoles g^{-1} $MnCl_2$ infusion.

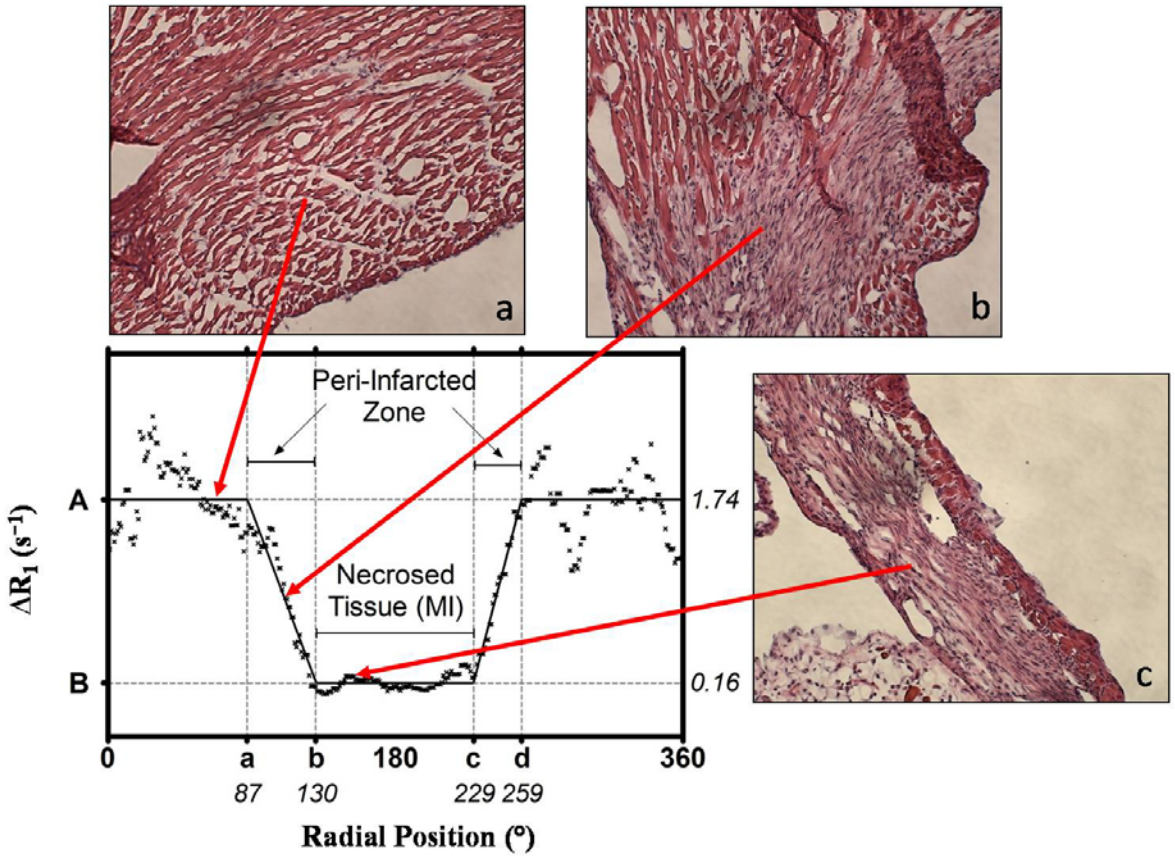

Figure 4.8

Figure 4.8 Sample radial fitting for an infarcted myocardium at 1.6 h after infusion of the manganese contrast agent. The fitting algorithm optimizes average ΔR_1 values for the viable zone (A), and the necrosed zone (B), with the peri-infarcted zone linearly connecting these two regions. Also shown is a comparison of the *in vivo* ΔR_1 radial profile to histological staining, along with the correlating histological slice locations.

Figure 4.8 illustrates how the sectored ΔR_1 values fitted to a region-defining MI curve to delineate Region A (viable zone), Region B (necrosed zone) and the peri-infarcted zone boundaries (radial positions a, b, c and d). Three histological H&E stained images are also shown that correspond to the defined viable (Figure 4.8a), peri-infarcted (Figure 4.8b), and necrosed (Figure 4.8c) zones on the curve.

Figure 4.9 and Figure 4.10 both showed that Mn^{2+} efflux properties differed between healthy and MI murine hearts, as well as between the necrosed and peri-infarct regions. For the Sham group, Figure 4.9a illustrates the dependence of ΔR_1 on position in the segmented myocardium (allowing for calculation of the average ΔR_1 value) as well as on time. A similar trend was observed for the Control group (data not shown). As $MnCl_2$ post-infusion time increased, the average ΔR_1 values were reduced due to Mn^{2+} efflux from the myocardium. Figure 4.9b shows a similar temporal trend for the MI group data with the segmented region-defining MI curves overlaid on the regional ΔR_1 data. As before, the ΔR_1 values decreased as time post-infusion increased, with the rate dependent on the defined tissue type (viable, peri-infarcted or necrosed).

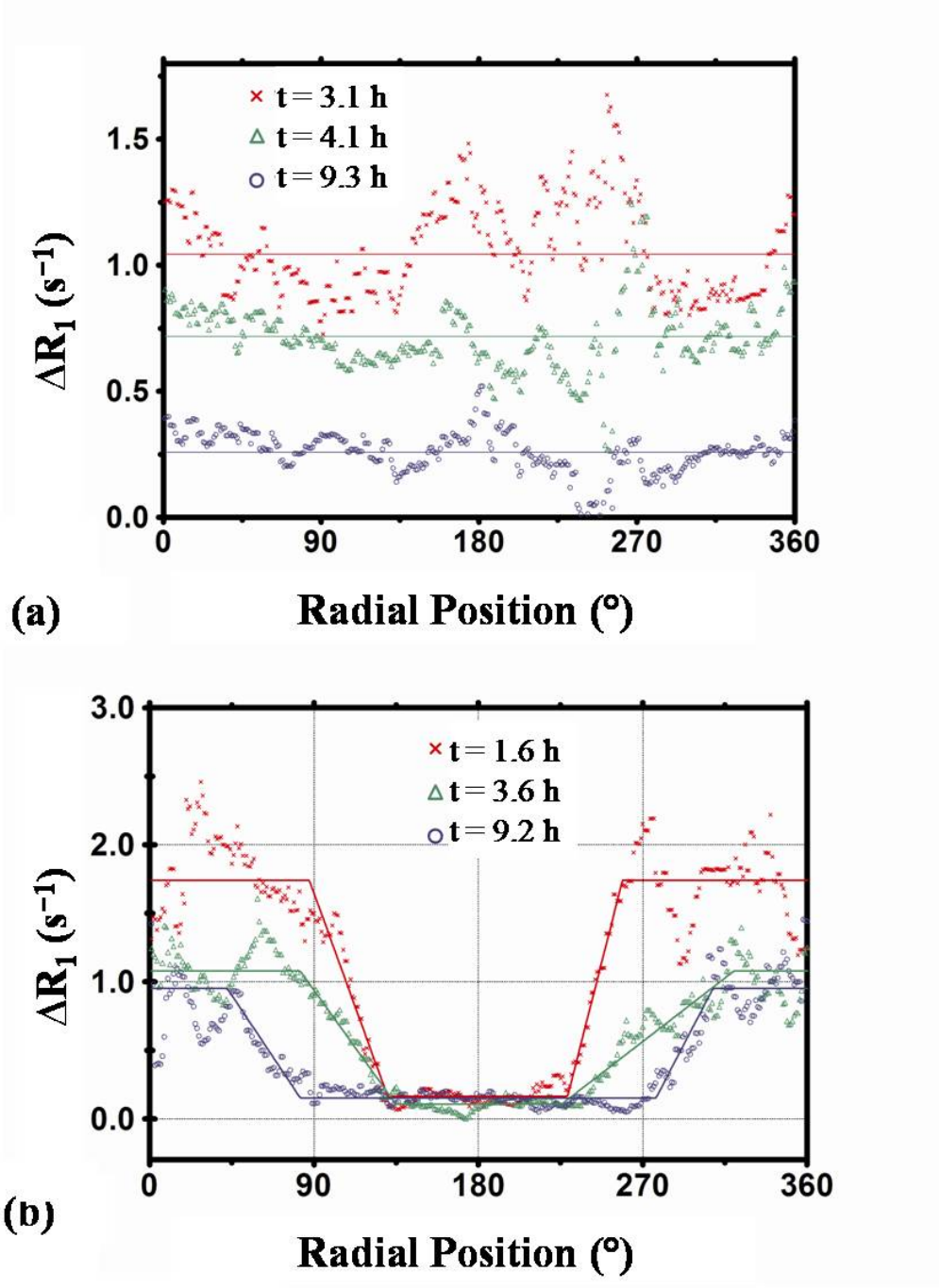

Figure 4.9

Figure 4.9 Sample temporal radial fitting of the segmented myocardium for the (a) Sham (thoracotomy only) and (b) MI (thoracotomy and coronary artery occlusion) groups.

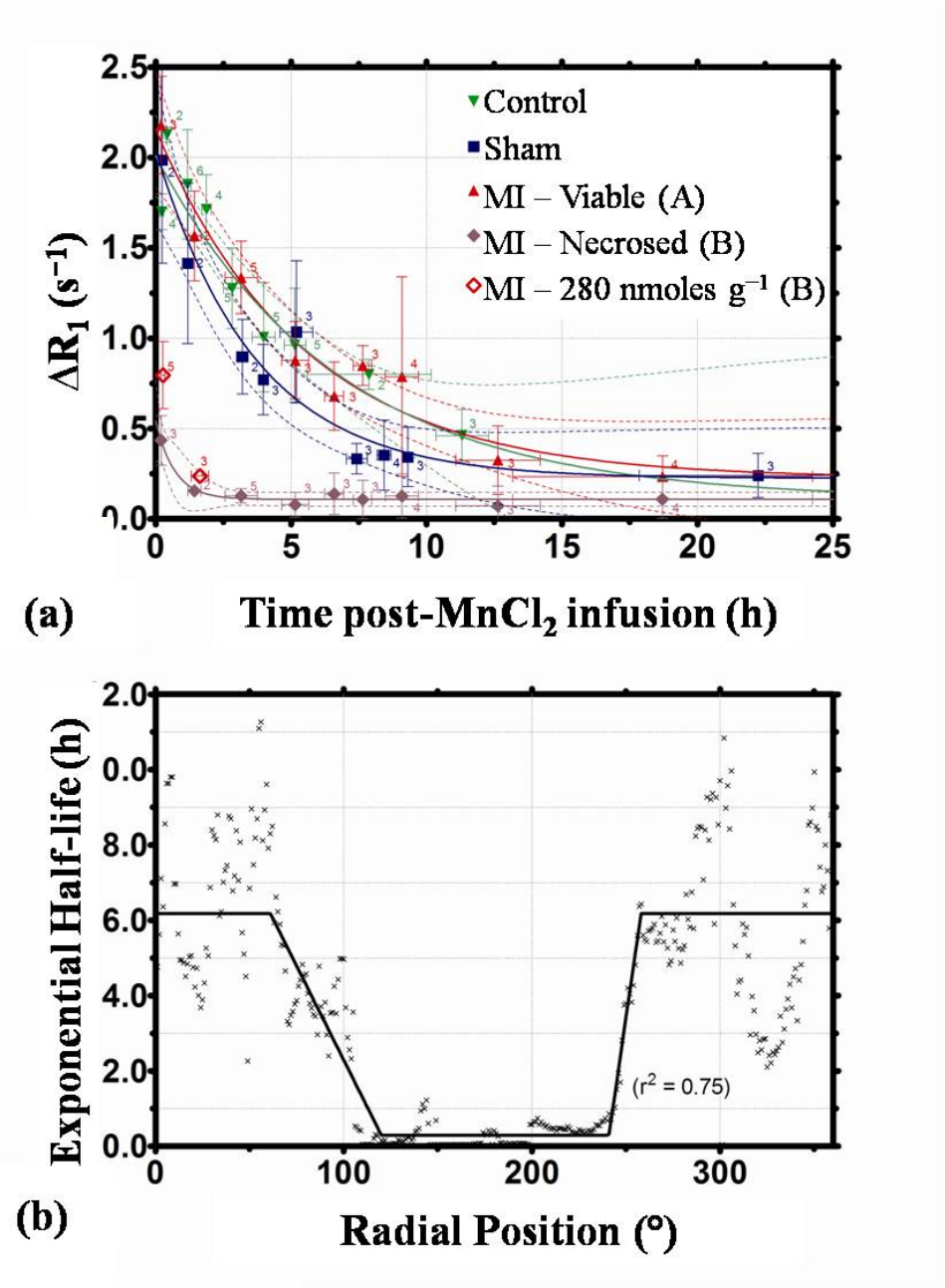

Figure 4.10

Figure 4.10 (a) First-order exponential efflux curves for the Control (no surgery; 190 nmoles g^{-1} $MnCl_2$), Sham (thoracotomy only) and MI (thoracotomy and coronary artery occlusion) groups. Sample sizes are shown with corresponding 95% confidence intervals. (b) Radial Mn^{2+} efflux half-life data points calculated from first-order exponential curves on each sector of the myocardium. A radial fit is overlaid of the calculated average half-life values for the viable and necrosed zones. A line depicting the peri-infarcted zone linearly connects these two regions. A = Region A; B = Region B.

Efflux curves for the Control and Sham groups, as well as MI Regions A and B (with the 190 nmoles g^{-1} $MnCl_2$ infusion), are shown in Figure 4.10a. For the Control group, no significant difference was found when comparing the efflux half-life obtained using the isolation/segmentation software versus the ROI technique (p = 0.19). No significant difference was found between the first-order exponential fits of the Control, Sham and MI Region A groups (p = 0.39). However, a significant difference was found in both the half-life and $\Delta R_{1,0}$ for MI Region B ($p < 0.05$). Additionally, the MI Region B group with the 280 nmoles g^{-1} $MnCl_2$ infusion was initially significantly different than MI Region B group with 190 nmoles g^{-1} $MnCl_2$ (t = 0.3±0.1 h), but no significant difference was observed by t = 1.6±0.1 h. Finally, efflux curves were produced for the MI group by calculating ΔR_1 for each radial sector. These values were then fitted to a first-order exponential curve, with the position-dependent half-life results shown in Figure 4.10b. Furthermore, Figure 4.10b shows that the regional rate of Mn^{2+} efflux exhibited a position-dependent pattern similar to the ΔR_1 region-defining MI curve shown in Figure 4.8 ($r^2 = 0.75$).

4.4 Discussion

Results from this study demonstrated the sensitivity of the T_1-mapping MEMRI technique for detecting and measuring Mn^{2+} efflux in the myocardium of both healthy and post-MI mice under various conditions. Changes in ΔR_1 over time may be used to quantify changes in Mn^{2+} content *in vivo* under control conditions (§3) and/or when

modulating NCX kinetics with the NCX inhibitor SEA0400. This information could be useful for indirectly assessing and understanding Ca^{2+} efflux properties as Mn^{2+} is considered its biochemical analogue. Most importantly, however, this study demonstrated a novel technique for identifying and quantifying specific regional differences in tissue characteristics that occur after a MI in the murine model. The region-defining MI curve not only eliminates user bias in determining the location of the infarcted, peri-infarcted, and viable myocardium, but also indirectly allows for the assessment of Ca^{2+} handling alterations in the salvageable peri-infarcted zone. Using the segmentation and curve fitting methodology derived from T_1-mapping MEMRI, the salvageable peri-infarcted tissue adjacent to the necrosed area can be specifically located, the extent of which is known to be a predictor of post-MI mortality (56). Thus, this innovative imaging technique could ultimately enhance clinical outcomes for post-MI patients.

4.4.1 Pharmacologically Altered Mn^{2+} Efflux

This study found that varying doses of SEA0400 and a single dose of dobutamine affected Mn^{2+} efflux in the healthy murine heart. Inhibition of the NCX with SEA0400 extended the ΔR_1 washout curve due to an assumed inhibition of the Mn^{2+} efflux. Treating mice with 50 mg kg^{-1} SEA0400 extended the ΔR_1 half-life from 3.4 to 5.6 hrs. Several hours after inhibition of the NCX with 50 mg kg^{-1} SEA0400, the absolute cardiac Mn content was greater in the treatment group mice than in the control mice (Figure 4.2b). These results suggest that a greater retention of Mn^{2+} occurred following $MnCl_2$ infusion. This effect was also observed with *in vivo* T_1-mapping (Figure 4.3 and Figure 4.5). Therefore, the inhibition of Mn^{2+} efflux using a known NCX inhibitor, in

conjunction with the previous establishment of Mn^{2+} as a Ca^{2+} analogue during influx (99), indicated that changes in Mn^{2+} efflux most likely reflected changes in Ca^{2+} efflux. The 34 and 50 mg kg^{-1} SEA0400 doses increased $\Delta R_{1,0}$ following NCX inhibition, which reduced net Mn^{2+} efflux without affecting Mn^{2+} influx via the L-type Ca^{2+} channels. Altered Mn^{2+} efflux rates were not seen with the lower SEA0400 doses, probably because SEA0400 has a biological half-life shorter than the current imaging temporal resolution.

The positive inotropic state following administration of dobutamine caused a biphasic Mn^{2+} efflux curve in the healthy myocardium. This finding was exhibited by an initial rapid increase in the Mn^{2+} efflux rate followed by a gradual decrease as a slower Mn^{2+}efflux rate reduced the Mn^{2+} content. These results suggest that alterations in Ca^{2+} handling caused by changes in the inotropic state of the heart are also observed for Mn^{2+}, and that the T_1 mapping MEMRI efflux technique is sensitive enough to detect these effects.

The 50 mg kg^{-1} SEA0400 efflux curve in Figure 4.3 and Figure 4.5 suggested that a gradual de-inhibition of the NCX occurred over time. At approximately 6 hrs post-$MnCl_2$ infusion, the temporal rate of change of ΔR_1 appeared to increase, suggesting a reduction in the inhibitory effects of the NCX inhibitor. This study demonstrated that a first-order exponential fit provided a relatively good approximation for detecting Mn^{2+} efflux rates and modulations. A thorough modeling of the washout data is essential to fully understand the inhibitory effects of SEA0400 and Mn^{2+} efflux rates, and such modeling is studied in §5.

The SEA0400 doses used in the current study were selected based on previous studies conducted *in vivo* in cerebral models, due to a lack of *in vivo* cardiac studies using

SEA0400. Previously, SEA0400 was found to be an extremely potent and selective inhibitor of the NCX in neurons, astrocytes, and microglia, with IC_{50} values of 5 to 33 nM when 1 and 3 mg kg^{-1} doses were administered intravenously, respectively (195). The precise mechanism of SEA0400 in NCX inhibition remains to be determined. Nevertheless, significant interactions are seen between SEA0400 and the intrinsic ionic regulatory mechanisms of NCX1.1 (218). For example, in this study Lee et al. suggested that SEA0400 acted to inhibit the reverse mode of the NCX more effectively than the forward mode (~90% vs. ~30% following application of 300 nm SEA0400). These investigators concluded that the potency of SEA0400 depended on the experimental conditions, with the greatest potency observed for the conditions approaching unidirectional transport in the Ca^{2+} entry mode.

An increase in $\Delta R_{1,0}$ relative to the control group was observed following SEA0400 administration, independent of the dose (Figure 4.5). There are two potential explanations for this phenomenon. Firstly, when net Mn^{2+} efflux is inhibited by SEA0400 and the influx of Mn^{2+} via Ca^{2+} channels is unchanged, a resultant increase in Mn^{2+} accumulation could occur. The net Mn^{2+} efflux is defined as the unidirectional efflux – unidirectional influx, where the unidirectional influx approaches zero for a majority of the experiment conditions as extracellular Mn^{2+} is shown to be near zero. Ultimately, this effect would be expected to increase the Mn^{2+} content in the LV wall of a treated mouse heart compared to an untreated one. The results of the current study showed a small increase in blood Mn content above the baseline level between 1.5 and 12.4 hrs post-$MnCl_2$ infusion. Therefore, one can assume that the blood Mn content was also above the

pre-$MnCl_2$ infusion baseline level at one hour post-$MnCl_2$ infusion when SEA0400 was administered.

Also, increased $\Delta R_{1,0}$ may be due to an increase in the longitudinal relaxivity following binding of Mn^{2+} with larger molecules within the cell. This effect could potentially be caused by the introduction of SEA0400 to the system. These potential mechanisms warrant further study.

One concern with using SEA0400 was the potential positive inotropic effect in the mouse myocardium, which was previously reported in rats but not rabbits (219). As demonstrated by Hu et al. (99), positive inotropic and chronotropic effects altered Mn^{2+} influx. While the current study found no chronotropic changes (i.e., no change in heart rate) associated with administration of SEA0400, this pharmacologic agent may still cause an increase in inotropy (i.e., contractility measured via left ventricular pressure) of the mouse heart. The apparent independence of $\Delta R_{1,0}$ on the SEA0400 dose found in this study suggests that SEA0400 doses between 20 and 50 mg kg^{-1} may not considerably alter the myocardial inotropic state. However, further research is required to fully understand these changes in Mn^{2+} uptake following treatment with SEA0400.

Overall, this aspect of the study using a healthy murine myocardium found that the T_1-mapping MEMRI technique detected and quantified:

1) increased Mn^{2+} uptake associated with an increased Mn^{2+} efflux rate due to increased Mn^{2+} infusion doses
2) decreased Mn^{2+} efflux rates following NCX inhibition with SEA0400
3) increased Mn^{2+} efflux rates due to the positive inotropic effect of dobutamine

This information concerning Mn^{2+} efflux dynamics could potentially enhance understanding of Ca^{2+} dynamics, particularly when investigating pathophysiological phenomena and/or developing new therapeutic pharmaceutical agents.

4.4.2 MI Altered Mn^{2+} Efflux

As previously mentioned, this study introduced a novel quantitative method for objectively identifying the locations of necrosed, peri-infarcted and viable tissue in the post-MI myocardium. This innovative methodology isolates and segments the MEMRI T_1 maps and then fits the calculated ΔR_1 values into a region-defining MI curve that shows the location (in radial degrees) of the infarcted (necrosed), peri-infarcted (ischemic) and viable remote tissue.

This information would be clinically useful not only for treating the precise areas of salvageable tissue, but also for monitoring progression of the remodeling process during healing. Thus, patient outcomes would be enhanced as improved treatment modalities target specific tissue areas and ultimately prevent the adverse remodeling that promotes heart failure development in post-MI patients.

Results from this study further showed Mn^{2+} handling within the viable region of the MI group and the Sham group were unaltered after surgery. However, decreases in both $\Delta R_{1,0}$ and efflux half-life were observed in both the necrosed and peri-infarcted zones of the MI group.

Within the $MnCl_2$ dose-dependent groups, Mn^{2+} efflux occurred with a half-life dependent on the initial Mn^{2+} content such that an increasing Mn^{2+} uptake caused an increase in the Mn^{2+} efflux rate. Therefore, the regional Mn^{2+} uptake in viable cells

within the peri-infarcted zones could potentially be estimated by examining the Mn^{2+} efflux properties. Mn^{2+} efflux from the necrosed region (MI Region B) occurred with a significantly faster half-life than in the Control group with the same $MnCl_2$ infusion dose. Using Equation 3.1, the inferred equivalent infusion dose for the infarcted (necrosed) and peri-infarcted regions was found to be larger than the 280 nmoles g^{-1} $MnCl_2$ infusion dose. This finding suggests that both the necrosed and peri-infarcted regions experience increased Mn^{2+} uptake, and therefore potentially Ca^{2+} uptake.

A limitation of this assumption is that the rapid ΔR_1 efflux rate from the necrosed and/or peri-infarcted tissue could be caused in part by the dissociation of Mn^{2+} from larger molecules and proteins, reducing T_1 values independent of intracellular Mn^{2+} content handling. However, the initial efflux rate in the necrosed region was shown to be dose-dependent, which is an effect that would likely be caused by altered intracellular Mn^{2+} concentration rather than molecular dissociation. Although Mn^{2+} has potential cardiotoxic effects, the subtoxic $MnCl_2$ doses used in this study provided sufficient signal enhancement and contrast. Additionally, Mn-based contrast agent MnDPDP has been successfully used in a number of cardiac human studies (11).

Although Mn^{2+} handling data may mimic alterations in Ca^{2+} handling, the precise relationship between these two ions is still unknown. Ca^{2+} and Mn^{2+} extrusion rates are not equal due to their different binding constants and maximal rates for efflux transporters (NCX and PMCA). Furthermore, Mn^{2+} can be extruded via the reverse mode of Ca^{2+} channels due to low extracellular Mn^{2+} concentration. These conditions make the precise relationship between Mn^{2+} and Ca^{2+} transport complicated, and studies to address this are reserved for future work.

In summary, this study showed that T_1-mapping MEMRI quantified Mn^{2+} dynamics in both healthy and post-MI mice under various conditions. A novel technique was also introduced for identifying and quantifying specific regional differences of tissue characteristics in the post-MI mouse heart that could potentially be translated into the clinical environment. This information from healthy and post-MI mice may be used to evaluate Mn^{2+} efflux dynamics, which would broaden the understanding of Ca^{2+} dynamics as well as locate specific tissue areas needing therapeutic intervention.

Table 4.1 Group Characteristics

Types	Size*		Heart Rate	Exponential Fit†		Normalized
	n_{mice}	n_{maps}	(bpm)	$t_{1/2}$ (h)	$\Delta R_{1,0}$ (s^{-1})	$t_{1/2}$ ‡
$MnCl_2$ Dose (nmoles g^{-1})						
283±6	15	41	444±21	2.0±0.6§	5.0±0.6§	0.6
190±2 (Control)	14	36	456±30	3.4±0.6	3.4±0.3	1.0
119±3	7	21	438±54	6.8±3.3§	2.0±0.3§	2.0
65±0.2	4	14	438±32	9.5±2.2§	0.96±0.1§	2.8
SEA0400 Dose (mg kg^{-1})						
10±0.2	11	35	455±27	3.1±0.7	4.3±0.6§	0.9
20±0.2	8	33	449±30	3.6±0.5	4.8±0.2§	1.0
34±0.8	4	17	427±24#	4.7±0.7§	4.2±0.3§	1.4
50±0.2	7	29	439±32	5.6±1.1§	4.3±0.4§	1.6
Dobutamine Dose (µg g^{-1})‖						
15.0±0.3	6	17	478±37#			
Initial				0.29±0.14§	–	0.1
Delayed				17.9±2.6§	–	5.3
Sham						
190±1 nmoles g^{-1}	7	25	447±31	2.5±2.0	2.0±0.4	
MI						
190±1 nmoles g^{-1}	9	30	444±35			
Region A (Viable)				3.8±2.7	2.2±0.3	
Region B (Necrosed)				0.49±0.2§	0.54±0.3§	
282±2 nmoles g^{-1}	8	8	430±33	–	–	

Table 4.1 (continued).
* n_{mice} is the number of mice in each group; n_{maps} is the number of T_1 maps generated for each group.
† Exponential half-life and $\Delta R_{1,0}$ values (mean ± standard deviation) for each group.
‡ Half-life value of $MnCl_2$, SEA0400 and Dobutamine groups normalized to $MnCl_2$ Control group.
§ Significantly different from $MnCl_2$ Control group ($p < 0.05$).
‖ Second-order exponential data.
Significant difference between groups ($p < 0.05$)

CHAPTER 5: PART III – PHARMACOKINETIC MODELING OF MN^{2+} FLUXES

5.1 Introduction

A majority of Ca^{2+} ions entering cardiac cells via L-type calcium channels induce calcium release from the sarcoplasmic reticulum (SR) (3). The resultant increase in intracellular free calcium, $[Ca^{2+}]_i$, boosts the amount of Ca^{2+} binding to the thin-filament protein troponin C, ultimately resulting in contraction. During relaxation, Ca^{2+} is removed from the cytosol via one of four transporters: two extracellular transporters (the sodium-calcium exchanger, NCX, and plasma membrane Ca^{2+}-ATPase, PMCA), and two intracellular transporters (SR Ca^{2+}-ATPase and mitochondrial Ca^{2+} uniporter). Previous attempts to estimate the relative contributions to Ca^{2+} efflux have shown that the NCX is the dominant efflux mechanism, with non-NCX mechanisms contributing between 9 and 32% (23,24) of the efflux in rats and 19% in mice (25).

In addition to the important role of Ca^{2+} in the function of viable myocytes, alterations in Ca^{2+} handling, primarily via increases in $[Ca^{2+}]_i$ (2), provide a major contribution to irreversible ischemic damage (46-48). Cell death can result from one of several mechanisms following elevations in $[Ca^{2+}]_i$. Protocols that selectively inhibit the NCX are useful for investigating the roles of the NCX and PMCA, and have been shown to have potential therapeutic effects during myocardial ischemic-reperfusion injuries (190). When the NCX works as a pathway for Ca^{2+} entry, as it does during ischemia/reperfusion injury, the NCX inhibitor is expected to guard against Ca^{2+}

overloading. SEA0400, a selective and potent NCX inhibitor, has been shown to provide protection from cardiac ischemia/reperfusion injury (190,198,199) and from myocardial stunning (200).

Despite the established importance of Ca^{2+} for myocardial viability, no *in vivo* imaging technique exists to assess the Ca^{2+} content or changes in Ca^{2+} handling post-MI in the heart. As shown in §3 and §4, MEMRI studies have demonstrated the ability to detect Mn^{2+} efflux *in vivo* (212), with Mn^{2+} efflux occurring, at least in part, via the NCX. It has also been shown that T_1-weighted MEMRI provides clear delineation of the myocardial infarction site in both murine (137,204) and canine (10) MI models, with similar application in humans (11).

Application of pharmacokinetic models to biological data can provide an insight into physiologic processes, allowing for the determination of pharmaceutical efficacy and handling properties. One commonly employed approach to characterize the pharmacokinetic properties of external agents (such as pharmaceuticals and contrast agents) is to represent the body as a system of homogeneous compartments (220). Transfer rates between compartments, as well as elimination rates of the agent from the system, are assumed to follow first-order linear kinetics. Agents that are introduced into the body require a finite amount of time to distribute throughout the system of available compartments. Therefore, following intravenous administration of a given contrast agent or pharmaceutical, such as I.V. $MnCl_2$ infusions, at least two compartments are required to model the disposition of the agent, transported from the blood compartment to other organs of interest.

Purpose

This final part of the dissertation aims to model the cardiac transport properties of Mn^{2+}, using *in vivo* cardiac MEMRI efflux data collected in §3 and §4 in combination with a number of pharmacokinetic models. Such a model would allow future predictions of functional cardiac behavior in the laboratory, in preparation for future translational studies. Complimentary to data describing ordinary efflux (§3), additional data from *in vivo* MEMRI efflux studies was acquired using mice following inhibition of the NCX with SEA0400 (§4), with the pharmacokinetic properties of SEA0400 as well as the efflux properties of Mn^{2+} serving as the processes under investigation. Knowledge of the properties of SEA0400, such as the rates of drug absorption from the peritoneum and clearance (likely by the liver) are important to fully understand the Mn^{2+} and Ca^{2+} transport alterations. Finally, alterations in Ca^{2+} transport mechanisms following myocardial infarction (MI) were addressed by performing *in vivo* cardiac MEMRI efflux studies in mice following MI (§4). This data was then compared to the healthy transport data for assessment of Mn^{2+} handling alterations.

Ultimately, this study attempts to characterize Mn^{2+} transport mechanisms in the mouse heart using pharmacokinetic models, and by inference, to derive a descriptive framework for understanding cardiac Ca^{2+} flux data. This could provide useful information regarding pharmaceutical properties as well as allowing for better estimates of the Ca^{2+} content and handling alterations in the myocardium from *in vivo* MEMRI studies.

5.2 Methods and Materials

In vivo MEMRI T_1-mapping efflux studies were previously conducted (§3 and §4) in adult male C57Bl/6 mice (6-14 weeks old, 23.9±2.3 g) (212). All experiments followed the guidelines of the Institutional Animal Care and Use Committee at the Medical College of Georgia, Augusta, GA, USA, as previously described (204).

$MnCl_2$ infusions (prepared from a 60 mM stock solution) were administered intravenously via the tail vein, at a constant rate (k_0) of 0.6 ml h^{-1} (= 3.6×10^4 nmoles h^{-1}) with the aid of a syringe pump (KD Scientific Inc., Holliston, MA, USA). The total infusion time, T (h), was therefore dependent on the infusion dose and mouse body weight (BW) (Equation 5.1).

$$k_0(t) = \begin{cases} k_0 & 0 \le t \le \mathrm{T} \\ 0 & t > \mathrm{T} \end{cases} \qquad \text{Equation 5.1}$$

The mice, as previously described, were randomized into three groups for efflux studies:

1) $MnCl_2$ dose dependent (65±0.2, 119±2, 190±3 (Control) and 283±6 nmoles g^{-1} body weight $MnCl_2$, n = 40 mice)
2) SEA0400 dose dependent (190±1 nmoles g^{-1} BW $MnCl_2$ infusion, followed 1 hour later with an i.p. injection of 10±0.2, 20±0.2, 34±0.8 and 50±0.2 mg kg^{-1} SEA0400, n = 30)
3) Myocardial infarction (MI, 190±0.1 nmoles g^{-1} BW $MnCl_2$, n = 9)

Table 5.1 shows the total study sizes (number of mice and total number of T_1-maps post-$MnCl_2$ infusion), $MnCl_2$ infusion doses (nmoles g^{-1} BW), and pharmaceutical doses for each group.

Table 5.1 Summarized raw input data

Study Group	Infusion Time, T (h)	Number of mice	Number of T_1-Maps	Number of blood data points
Control (nmoles g^{-1} $MnCl_2$)				
283±6	0.18	14	41	3
190±2	0.12	14	36	9
119±3	0.08	7	21	1
65±0.2	0.05	4	14	1
SEA0400 (mg kg^{-1}) (1 h post-190 nmoles g^{-1} BW $MnCl_2$)				
10±0.2	0.13	11	35	1
20±0.2	0.13	8	33	1
34±0.8	0.14	4	17	1
50±0.2	0.13	7	29	9
Myocardial Infarction (nmoles g^{-1} $MnCl_2$)				
190±1	0.13	9	30	–

As previously presented, washout curves were obtained for each group, showing changes in left ventricular free wall (LV Wall) relaxation rate, $\Delta R_1 = 1/T_1$(post-) – $1/T_1$(pre-$MnCl_2$ infusion). From the duration of the T_1 map acquisition (~43 min), individual data points were defined to have been acquired at the center of k-space, approximately 21.5 min after initiation of the imaging sequence. Elemental analysis data, using inductively coupled plasma-mass spectrometry (ICP-MS) analysis (CANTEST Ltd., North Vancouver, BC, Canada), were acquired from select heart (n = 29) and blood (n = 26) samples to obtain the absolute sample Mn content. A correlational analysis was performed between the *ex vivo* data to *in vivo* ΔR_1 data, to obtain a relationship between the increase in Mn content and ΔR_1.

Pharmacokinetic Models

The $MnCl_2$ pharmacokinetic properties, with and without use of SEA0400, were modeled using three models: Model 1 (Figure 5.1a) was a two-compartment model, representing the blood and heart; Model 2 (Figure 5.1b) was a three-compartment model, consisting of blood, cytosolic free Mn^{2+} and cytosolic compartmentalized Mn^{2+}; Model 3 (Figure 5.1c) contained four compartments for the blood, cytosolic free Mn^{2+}, sarcoplasmic reticulum and mitochondria compartments. Appendix A, Figures A.3 and A.4 represent the modeling process in the form of a flow chart.

For each of the models, $MnCl_2$ was infused into the blood compartment at a rate of $k_0(t)$, as given in Equation 5.1, with the infusion duration, T, dependent on the mouse BW. First order rate parameters, k_{ab} [h^{-1}] (Figure 5.1), were used to describe the rate of transfer from compartment *a* to *b*, where k_{10} is defined as the rate parameter for Mn^{2+}

efflux from the blood to organs other than the heart (e.g. liver, kidney and other major organs).

For the SEA0400 group, the NCX inhibitor was administered one hour post-$MnCl_2$ infusion with the expected effect of reducing the cardiac efflux transfer rates, dependent on the drug's absorption and elimination rates. In order to model the drug pharmacokinetics of SEA0400, and therefore the Mn^{2+} transport mechanisms, an equation for the drug plasma concentration (C_p) was used (Equation 5.2), commonly applied to pharmaceutical modeling (221):

$$C_p(t) = \frac{\mathrm{FD}}{\mathrm{V_d}} \frac{k_{abs}}{\left(k_{abs} - k_{el}\right)} \left(\mathrm{e}^{-k_{el} \cdot t} - \mathrm{e}^{-k_{abs} \cdot t}\right) \qquad \text{Equation 5.2}$$

In Equation 5.2, F is the fraction of drug absorbed, V_p is the apparent volume of distribution of the drug and D is the drug dose administered. The rate parameters, k_{el} and k_{abs} represent the drug elimination and absorption rates respectively.

The form for the Mn^{2+} transfer rate parameter k_{21} was given by Equation 5.3, under the assumption that k_{21} decreases linearly with increasing SEA0400 plasma concentration, C_p, as in Equation 5.2:

$$k_{21}\left(t \geq 1\right) = k_{21,initial}\left(1 - \frac{k_{abs}}{\left(k_{abs} - k_{el}\right)} \left(\mathrm{e}^{-k_{el} \cdot (t-1)} - \mathrm{e}^{-k_{abs} \cdot (t-1)}\right)\right) \qquad \text{Equation 5.3}$$

Parameter $k_{21,intial}$ is defined as the pre-pharmaceutical administration transfer parameter, $k_{21}(t < 1$ h). Due the relatively fast blood pool clearance, on order to 12 minutes (212), and the fact that SEA0400 was administered one hours post-$MnCl_2$ infusion, k_{12} is not expected to change appreciably following SEA0400 administration. All the transfer rate and pharmaceutical parameters were therefore time-independent with the exception of k_0 and k_{21} following SEA0400 administration.

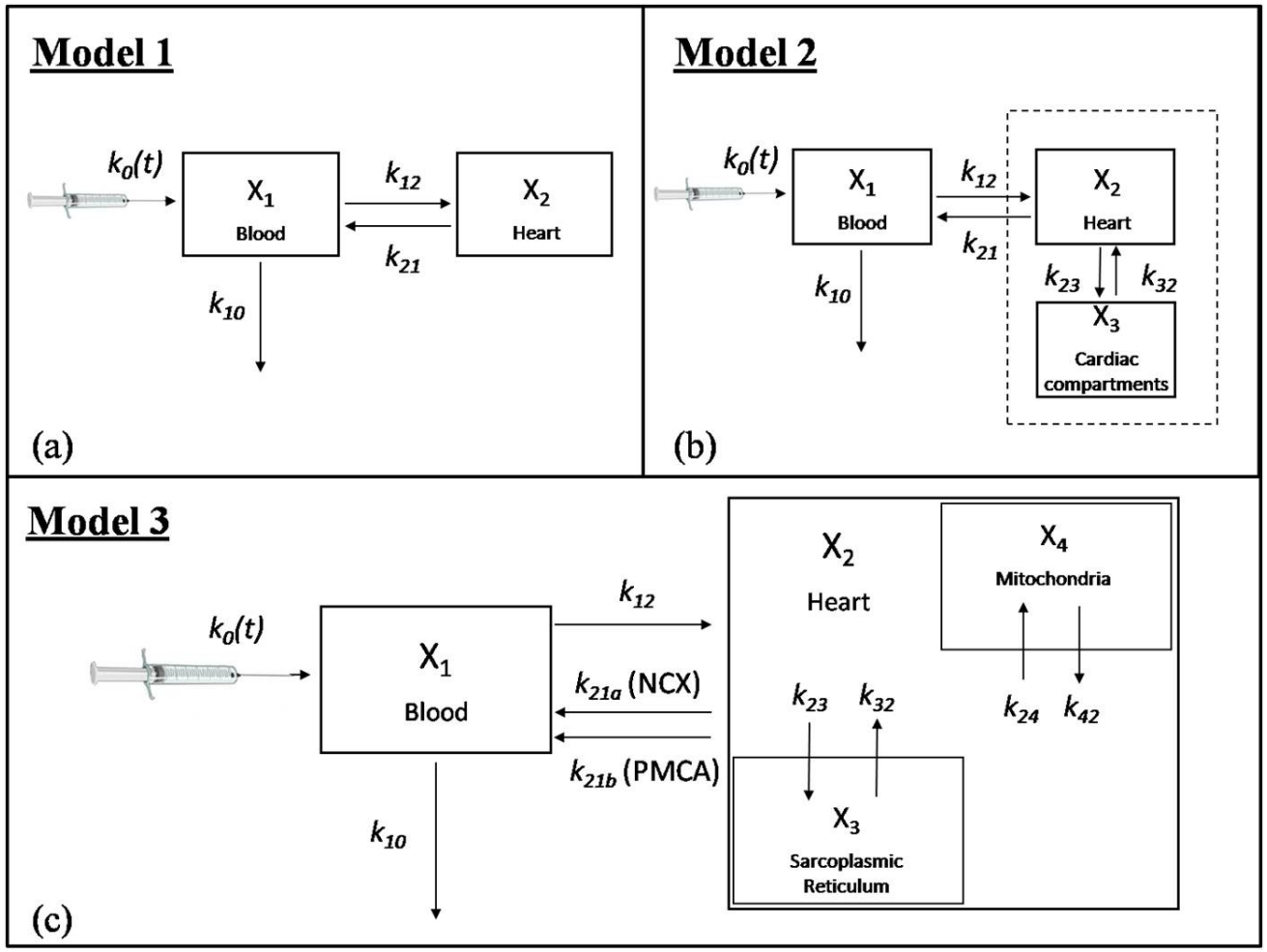

Figure 5.1

Figure 5.1 Schematic representations of pharmacokinetic Models 1 (a), 2 (b) and 3 (c).

The pharmaceutical absorption and elimination half-live ($t_{1/2abs}$ and $t_{1/2el}$ respectively) are given in Equation 5.4 and Equation 5.5.

$$t_{1/2abs} = \frac{\ln(2)}{k_{abs}} \qquad \text{Equation 5.4}$$

$$t_{1/2el} = \frac{\ln(2)}{k_{el}} \qquad \text{Equation 5.5}$$

For all of the models, a system of ordinary differential equations (ODEs) was obtained, dependent on the number of compartments and transfer rate parameters. The individual models and ODEs are described in more detail in the following subsections, and are summarized in Table 5.2.

Solutions to the ODEs were acquired using simultaneous 4th Order Runge-Kutta numerical methods in Matlab (Nantick, MA). Temporal *in vivo* cardiac Mn^{2+} content data and *ex vivo* blood Mn^{2+} content data were fit simultaneously to acquire least square fits for the first order rate parameters, k_{ab}. Least square fits of the pharmaceutical parameters, k_{abs} and k_{el} were also obtained using the SEA0400 groups, assuming that k_{ab} was unchanged from the control 190 nmoles g^{-1} group. Parameter $k_{21,intial}$ (Equation 5.3) was defined as the best fit k_{21} parameter using the control 190 nmoles g^{-1} BW group. The only constraint made by the least square fitting technique was that the transfer rate parameters and pharmaceutical parameters were ≥ 0.

Table 5.2 Summary of the pharmacokinetic models

Model	Compartment				Model Fit Parameters		
	1	2	3	4	Efflux Group	Parameter	Total Number
1	Blood	Total Myocardium	–	–	$MnCl_2$ SEA0400	k_{10}, k_{12}, k_{21} k_{abs}, k_{el}	5
2	Blood	Free Cytosol	Cytosolic Compartments	–	$MnCl_2$ SEA0400	k_{10}, k_{12}, k_{21}, k_{23}, k_{32} k_{abs}, k_{el}	7
3	Blood	Free Cytosol	Sarcoplasmic Reticulum	Mitochondria	$MnCl_2$ and SEA0400	k_{10}, k_{12}, $k_{21a,21b}$ (NCX, PMCA), $k_{23,24}$ $k_{32,}$ $k_{42,}$ a, b, k_{abs}, k_{el}	10

Least square curve fitting techniques are inherently sensitive to the initial estimates of k_{ab}. For a given initial estimate of k_{ab} the fit may converge on solutions at local minima, which may not be the global minimum. In order to minimize potential errors caused by this effect, all the models employed a global search over a wide range in parameter space to find the initial estimates of k_{ab} corresponding to lowest fit residuals. To use the most realistic initial estimates for the fitting function, simultaneous solutions were obtained for the control 190 nmoles g^{-1} heart and 50 mg kg^{-1} SEA0400 heart efflux data, as well as the corresponding blood efflux data. All models assume that the two efflux groups share the same transfer rate parameters, with only $k_{21}(t)$, characterized by k_{abs} and k_{el}, being affected by administration of SEA0400.

Model 1 – Two-Compartment Model

Model 1 contains components representing the blood and myocardium (Figure 5.1a) with the absolute Mn content for each given by $X_1(t)$ and $X_2(t)$ [nmoles] respectively.

A system of ordinary differential equations (ODEs) was setup with dependent variables X_1 and X_2, and independent variable t [h], as shown in Equation 5.6.

$$\frac{dX_1}{dt} = k_0(t) - (k_{10} + k_{12})X_1(t) + k_{21}X_2(t)$$
$$\frac{dX_2}{dt} = k_{12}X_1(t) - k_{21}X_2(t) \qquad \text{Equation 5.6}$$

For the SEA0400 groups, a similar set of simultaneous ODEs was used, with k_{21} modeled as a function of time (Equation 5.3). This function was also applied to the SEA0400 groups for the following models.

Model 2 – Three-Compartment Model

In order to address the kinetics of Mn^{2+} compartmentalization within the myocardium, a third compartment was added (Figure 5.1b). Free Mn^{2+} was assumed to reside in compartment 2, but a third compartment representing the compartments within the myocyte (e.g. mitochondria and SR) was assumed. Rate parameters k_{23} and k_{32} define the uptake and release rates respectively for the third compartment.

A system of ordinary differential equations (ODEs) was setup for this model as shown in Equation 5.7.

$$\begin{aligned} \frac{dX_1}{dt} &= k_0(t) - (k_{10} + k_{12})X_1(t) + k_{21}X_2(t) \\ \frac{dX_2}{dt} &= k_{12}X_1(t) - (k_{21} + k_{23})X_2(t) + k_{32}X_3(t) \\ \frac{dX_3}{dt} &= k_{23}X_2(t) - k_{32}X_3(t) \end{aligned} \qquad \text{Equation 5.7}$$

Least square best fit values for the rate parameters (k_{ab}) were acquired following simultaneous least square fitting for both the blood (X_1) and heart (X_2 + X_3) compartments.

Model 3 – Four-Compartment Model

The four-compartment model was designed for the most physiological and anatomical specificity. The model contains two cytosolic compartments, representing the SR (compartment 3) and mitochondria (compartment 4), in addition to the free cytosolic Mn^{2+} (compartment 2). Additionally, efflux from the myocardium was modeled using two efflux rates, k_{21a} and k_{21b}, representing the NCX and PMCA efflux mechanisms respectively. The ODEs for this model are shown in Equation 5.8.

$$\frac{dX_1}{dt} = k_0(t) - (k_{10} + k_{12})X_1(t) + (k_{21a} + k_{21b})X_2(t)$$
$$\frac{dX_2}{dt} = k_{12}X_1(t) - (k_{21a} + k_{21b} + k_{23} + k_{24})X_2(t) + k_{32}X_3(t) + k_{42}X_4(t)$$
$$\frac{dX_3}{dt} = k_{23}X_2(t) - k_{32}X_3(t)$$
$$\frac{dX_4}{dt} = k_{24}X_2(t) - k_{42}X_4(t)$$

Equation 5.8

It is possible that differences exist in the longitudinal relaxivity, r_1, between cytosolic Mn in compartment 2 and the compartmentalized Mn in compartments 3 and 4, possibly due to the binding of Mn^{2+} to larger molecules within the compartments or to potential chelation of the free Mn^{2+} ions. To model this phenomenon, an additional function was added. Equation 5.9 demonstrates the relationship between the changes in relaxation rates between the compartments.

$$\Delta R_{1,T} = \Delta R_{1,cytosolic} + \Delta R_{1,comp}$$
$$\Delta R_{1,T} = r_{1,T} \cdot X_T ; \Delta R_{1,cytosolic} = a \cdot X_2 ; \Delta R_{1,comp} = b \cdot (X_3 + X_4)$$
$$X_T = {}^{1}\!/_{r_{1,T}} (a \cdot X_{cytosolic} + b \cdot X_{comp})$$

Equation 5.9

From Equation 5.9, $r_{1,T}$, is defined as the ratio between in the *in vivo* cardiac ΔR_1 values and the increase in Mn content. $\Delta R_{1,T}$, $\Delta R_{1,cytosolic}$ and $\Delta R_{1,comp}$ represent the change in relaxation rates for the total heart (combined compartments 2, 3 and 4), cytosolic Mn (compartment 2) and compartmentalized Mn (compartments 3 and 4) respectively, with weighting constants *a* and *b* proportional to the relaxivities of compartment 2 and 3 respectively. The total cytosolic and compartmentalized Mn content was therefore $a/r_{1,T} \cdot X_{cytosolic}$ and $b/r_{1,T} \cdot X_{comp}$ respectively, using solutions to Equation 5.8, $X_{cytosolic}$ (= X_2) and X_{comp} (= X_3 + X_4).

To reduce the number of variables in Model 4 for better model behavior while maintaining realistic physiological constraints, the following relationships were used for the rate parameters (Equation 5.10 and Equation 5.11), all derived from literature regarding Ca^{2+} transfer rates (25,222-225):

$$k_{21a} = 0.8 \cdot k_{21total}, \quad k_{21b} = 0.2 \cdot k_{21total} \qquad \text{Equation 5.10}$$

$$k_{23} = 0.9 \cdot k_{2comp}, \quad k_{24} = 0.1 \cdot k_{2comp} \qquad \text{Equation 5.11}$$

$k_{21total}$ and k_{2comp} are the total transfer rates from compartment 2 to the blood, and from compartment 2 to compartments 3 and 4, respectively. These two parameters were estimated via the modeling technique. SEA0400 was assumed only to reduce the rate of Mn^{2+} efflux via the NCX (k_{21a}), with k_{21a} therefore being modeled as a function of time using Equation 5.3.

Statistics

For all the models, the residuals and coefficient of determination, R^2, were calculated. The models were then compared to each other using an F test, both for individual efflux study groups as well as an overall model comparison for all of the efflux groups combined. These tests were used to ascertain whether potential decreases in sum-of-squares for the more complicated models outweighed the loss of degrees of freedom following increased numbers of fit parameters. The level of significance was set at 0.05. For comparison, a first-order exponential fit was also made for the efflux data, corresponding to a simple one-compartment model with no physiological detail.

Myocardial Infarction

For each T_1 map in the MI group, *in house* software was used to isolate the myocardium from the remaining tissue. The isolated myocardium was then segmented into 360 × 1° radial segments, where each sector contained approximately 4 voxels. Within each segment (with the center of the necrotic region shifted to 180°), the average T_1 values were determined, and the associated regional ΔR_1 values calculated. Average ΔR_1 values were calculated for the observed plateaus of the remote viable tissue (Region A) and the necrotic tissue (region B). Temporal average ΔR_1 values for regions A and B were fit with first-order exponentials. The exponential efflux properties of these regions were compared to the model output for the healthy mice groups.

5.3 Results

The average pre-infusion Mn content in the heart and blood was found to be 1.13±0.01 and 2.02±0.37 nmoles respectively, assuming a total heart weight of 0.1g, and a total blood volume of 2.17 ml/ 25 g BW (226,227). Correlating the *ex vivo* elemental analysis data to *in vivo* ΔR_1 data allowed for a relationship between the increase in Mn content (above the pre-infusion baseline) and ΔR_1 to be obtained (Equation 5.12, r^2 = 0.91). Using this equation, estimates for the increase in absolute Mn content were made from *in vivo* ΔR_1 values.

$$\text{Increase in Mn content}\left[\text{nmoles}\right] = 11.56 \cdot \Delta R_1\left[\text{sec}^{-1}\right] \qquad \text{Equation 5.12}$$

From Equation 5.9, $r_{1,T}$ is therefore equal to 1/11.56 nmoles^{-1} s^{-1}.

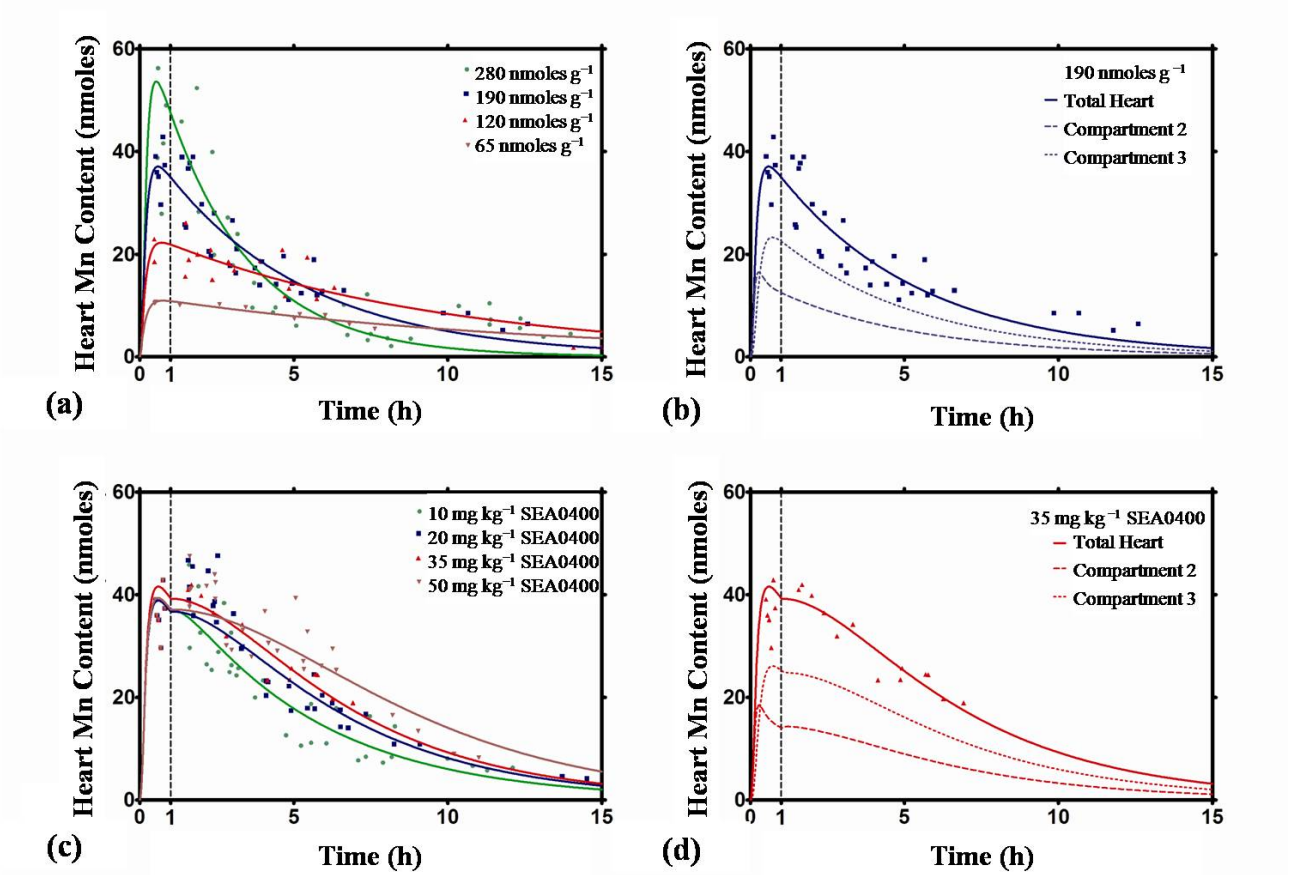

Figure 5.2

Figure 5.2 Cardiac Mn^{2+} efflux data for the $MnCl_2$ dose dependent infusion groups (a), and the SEA0400 dose dependent groups (c). Overlaid are the least square best fit total heart model results from Model 2. Mn^{2+} content in the heart (compartments 2 + 3, solid line), compartment 2 (dashed line) and compartment 3 (dotted line) for the 190 nmoles g^{-1} $MnCl_2$ and 35 mg kg^{-1} SEA0400 groups are shown in (b) and (d) respectively.

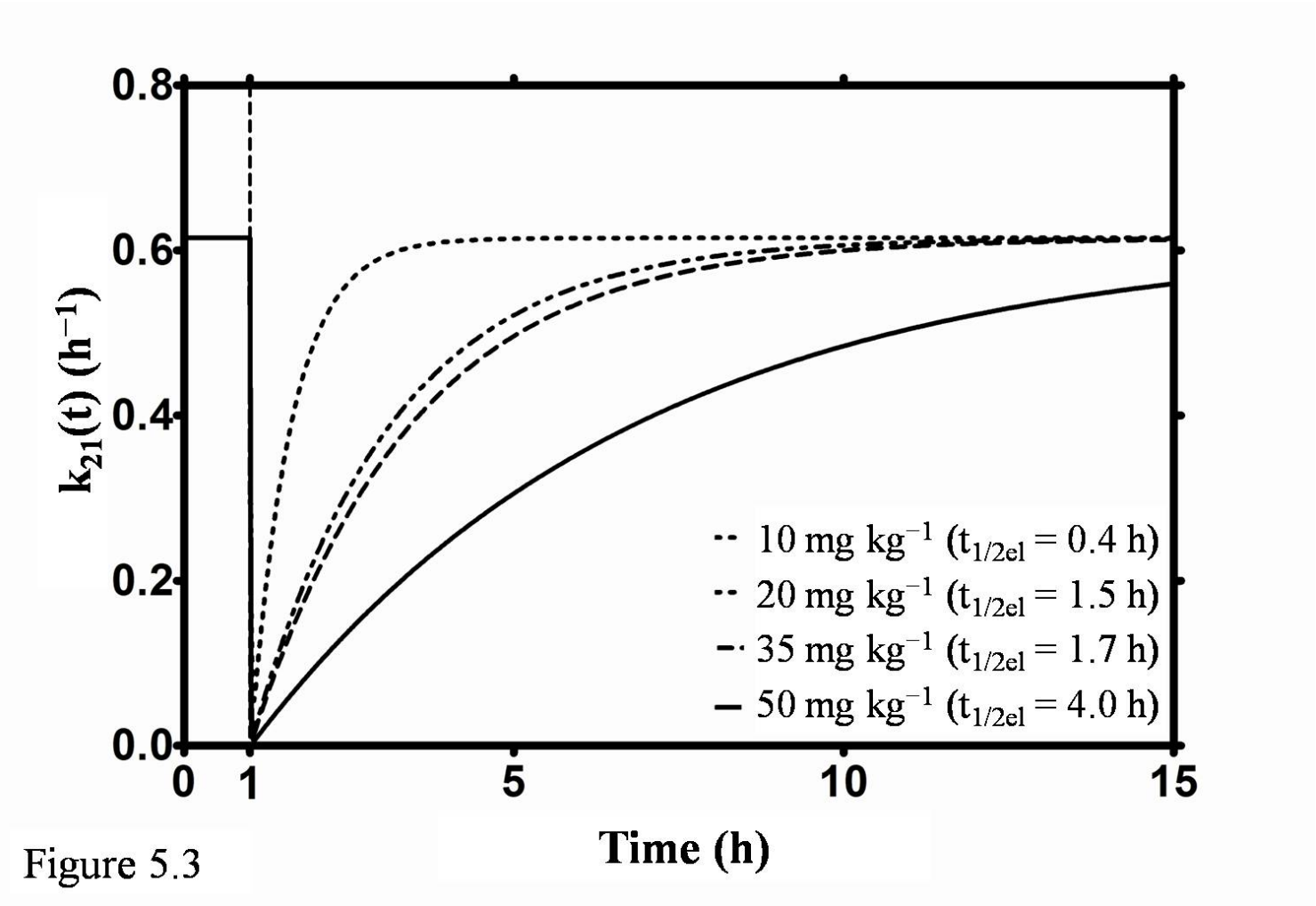

Figure 5.3

Figure 5.3 Temporal Mn^{2+} efflux transfer rate, $k_{21}(t)$, predicted by Model 2 following inhibition of the NCX with varying does of SEA0400, injected 1 hour post-$MnCl_2$ infusion. Also shown are the corresponding SEA00400 elimination half-lives.

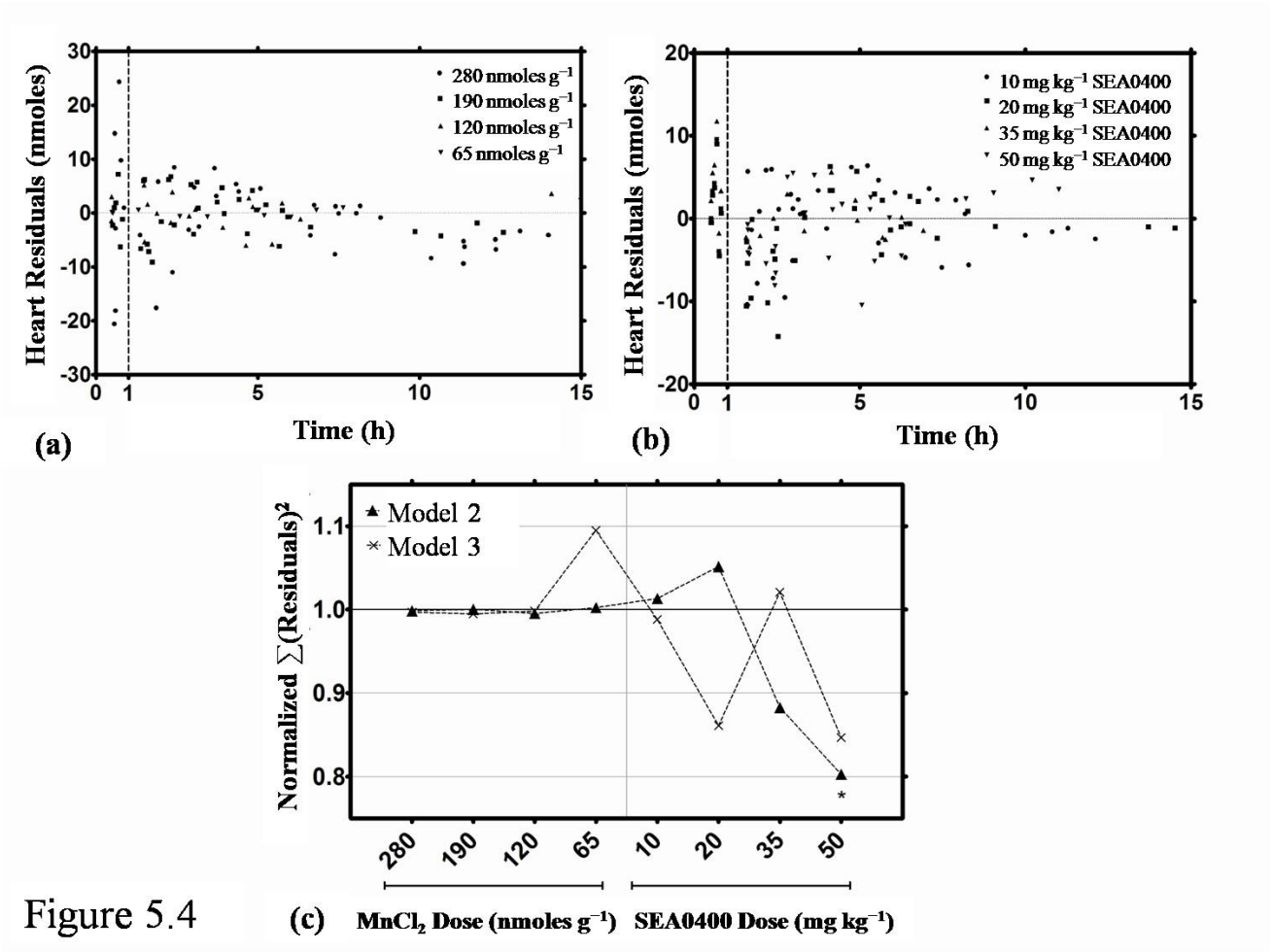

Figure 5.4

Figure 5.4 Model 2 total heart compartment (compartments 2 and 3) residuals for the control (a) and SEA0400 (b) dose dependent groups c) Model comparisons of the combined blood and heart sum of residuals squared for all the study groups, normalized to Model 1. * represents significance ($p < 0.05$)

Figure 5.2 shows the raw LV Wall Mn efflux data for the dose dependent (Figure 5.2a) and SEA0400 (Figure 5.2c) groups, along with the best fit solutions to Model 2 (solid lines). The total Mn^{2+} content in the heart (compartments 2 + 3, solid line), compartment 2 (dashed line) and compartment 3 (dotted line) for the 190 nmoles g^{-1} $MnCl_2$ and 35 mg kg^{-1} SEA0400 groups are shown in Figures 5.2b and 5.2d respectively. The SEA0400 dose dependent temporal fits for k_{21} are shown in Figure 5.3, with the temporal residuals for Model 2 displayed in Figures 5.4a and 5.4b. Output figures showing the least square best fits for all the three models for each efflux group are shown in Appendix B, Figure B.1.

Model Comparison

The least-square best-fit parameters from all three models are summarized in Table 5.3. By definition the SEA0400 groups have the same transfer rate parameters as the 190 nmoles g^{-1} $MnCl_2$ group, with the additional pharmaceutical parameters k_{abs} and k_{el} also shown in Table 5.3. Individual coefficients of determination, R^2, are shown in the lower right region of Table 5.3. For comparison between the three models, Figure 5.4c displays the sum of square residuals for the combined blood and heart data, normalized to Model 1, for each of the groups. Using an F test, there was no statistically significant benefit in increasing the number of model variables for each individual efflux group ($p > 0.05$), with the exception of the 50 mg kg^{-1} SEA0400 group where Model 2 provided a significant improvement over Model 1 ($p = 0.02$). Comparison of the three models for all of the efflux groups combined, demonstrated that no significant improvement was gained ($p = 0.62$) by adding additional compartments to Model 1. Considering this, Model 1

provided an adequate fit for all of the dose dependent efflux groups, as well as the 10, 20 and 35 mg kg^{-1} SEA0400 groups. The addition of a third compartment in Model 2 created a statistically significant improvement over the two-compartment model for the 50 mg kg^{-1} SEA0400 group. It is possible however that models with multi-cardiac compartments could provide more utility and realism in other pathological circumstances. Indeed, since the three-compartment model provided a better description for the 50 mg kg^{-1} SEA0400 group, and since there is virtually no difference between the models under other circumstances, use of a three-compartment model provides the most useful description.

Transfer Rate Parameters

The robustness of the different models can also be demonstrated from Table 5.3. The transfer rate parameters from the smaller, less complicated, models have demonstrated stability following addition of more compartments. Figure 5.5 displays the transfer rate parameters and pharmaceutical absorption and elimination half lives for the statistically best models. Applying a linear least square best-fit to the dose dependent transfer rate parameters yielded:

$$k_{10} = \left(3.9 \pm 1.4 \times 10^{-3}\right) \times \text{Dose} + \left(5.8 \pm 0.3\right) \quad \left(R^2 = 0.78\right) \qquad \text{Equation 5.13}$$

$$k_{12} = \left(1.2 \pm 0.3 \times 10^{-4}\right) \times \text{Dose} + \left(0.04 \pm 0.01\right) \quad \left(R^2 = 0.90\right) \qquad \text{Equation 5.14}$$

$$k_{21} = \left(1.4 \pm 0.2 \times 10^{-3}\right) \times \text{Dose} - \left(0.04 \pm 0.03\right) \quad \left(R^2 = 0.97\right) \qquad \text{Equation 5.15}$$

Table 5.3 Best fit parameters calculated by the three models

Dose	Model Fit Parameters (Model 1/ Model 2/ Model 3)							Model 3 ($s^{-1}nmoles^{-1}$)
	Transfer rate parameters (h^{-1})							
	k_{10}	k_{12}	$k_{21(a,)}$	k_{23}	k_{32}	k_{24}	k_{42}	a/b (× 11.56)
Control (nmoles g^{-1})								
280	6.9/6.9/6.9	0.07/0.07/0.07	0.37/0.91/0.79	−/5.9/0.41	−/4.5/0.57	−/−/0.05	−/−/0.87	1.1/2.3
190	6.4/6.7/6.6	0.06/0.06/0.06	0.22/0.62/0.71	−/7.4/0.48	−/4.3/0.37	−/−/0.05	−/−/0.75	1.1/2.4
119	6.5/6.1/6.5	0.06/0.05/0.05	0.11/0.54/0.58	−/11.8/0.61	−/3.1/0.28	−/−/0.07	−/−/0.37	1.0/2.5
65	5.9/6.0/6.0	0.04/0.04/0.04	0.08/0.51/0.60	−/12.4/0.60	−/2.4/0.19	−/−/0.07	−/−/0.31	0.9/2.3

	Drug Parameters (h^{-1})		Coefficient of Determination, R^2			
			Control (nmoles g^{-1})		SEA0400 (mg kg^{-1})	
	k_{abs}	k_{el}				
SEA0400 (mg kg^{-1})						
10	671/68/85	1.7/1.6/1.1	280	0.83/0.83/0.83	10	0.86/0.86/0.86
20	672/149/118	0.51/0.47/0.44	190	0.83/0.83/0.83	20	0.86/0.86/0.87
34	680/115/9.4	0.49/0.41/0.33	119	0.80/0.81/0.81	34	0.87/0.87/0.87
50	66/118/149	0.14/0.17/0.06	65	0.98/0.98/0.98	50	0.81/0.83/0.83

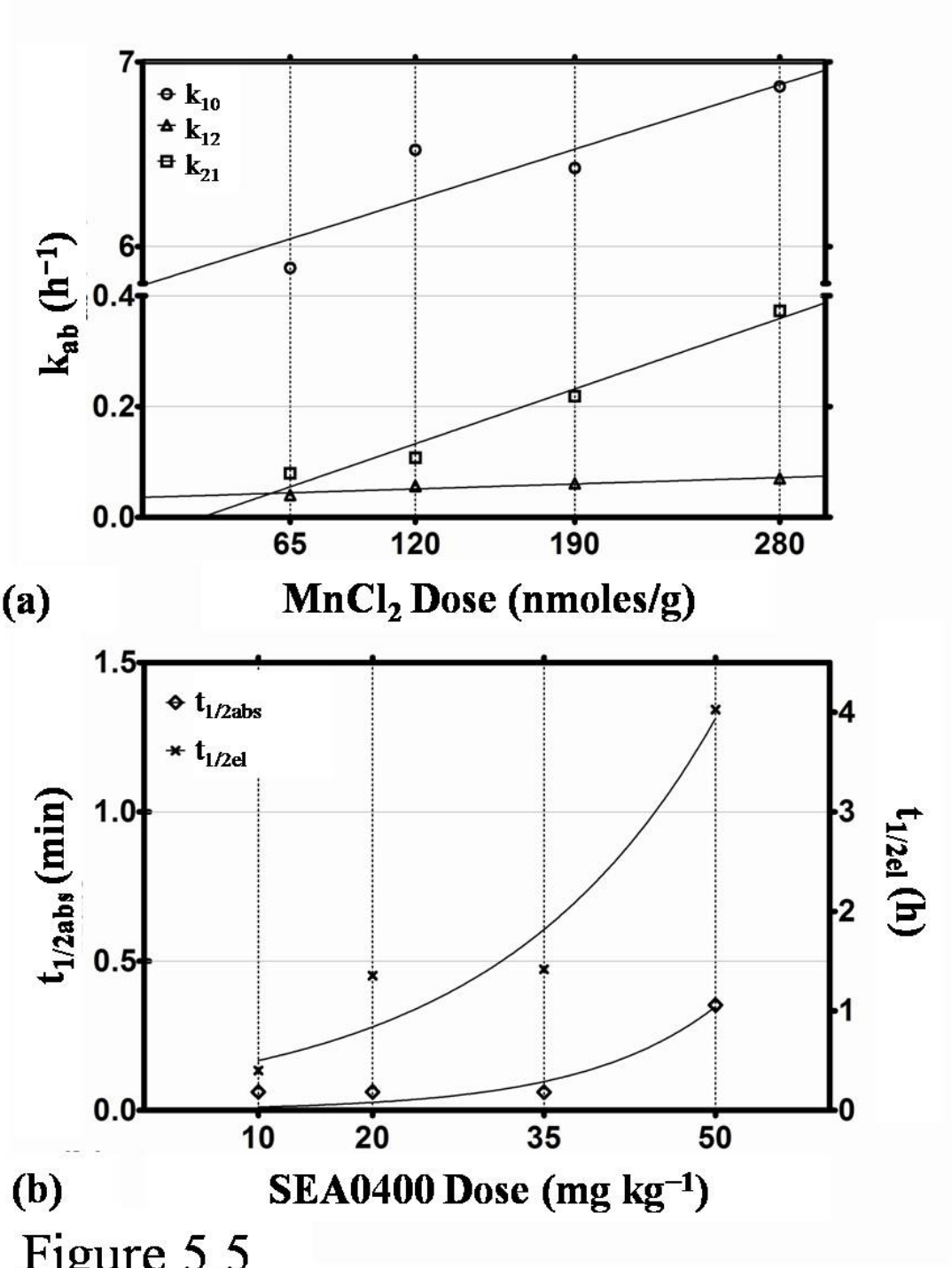

Figure 5.5

Figure 5.5 Dose dependent trends for the transfer rate parameters (a) and pharmaceutical absorption and efflux half-lives (b) predicted by the best model (Model 1 for all groups except the 50 mg kg^{-1} SEA0400 group, which is improved with Model 2). Also shown are linear least square and exponential best fits for the transfer rate parameters (a) and half-lives (b) respectively.

Similarly, first order exponential fits to the SEA0400 half lives yield:

$$t_{1/2abs}[\text{min}] = \left(4.9 \pm 7.2 \times 10^{-3}\right) \times \exp\left(\left(8.5 \pm 3.0 \times 10^{-2}\right) \times \text{Dose}\right) \quad \left(R^2 = 0.92\right) \quad \text{Equation 5.16}$$

$$t_{1/2el}[\text{hrs}] = \left(0.30 \pm 0.17\right) \times \exp\left(\left(5.2 \pm 1.2 \times 10^{-2}\right) \times \text{Dose}\right) \quad \left(R^2 = 0.94\right) \quad \text{Equation 5.17}$$

The best fits from Equation 5.13 through Equation 5.17 are displayed in Figures 5.5a and 5.5b.

Myocardial Infarction

Results from the MI study are displayed in Figure 5.6. Figure 5.6a represents, for one mouse, a sample regional plot of the remote (ΔR_1 = A) and necrosed (ΔR_1 = B) tissue, as well as the boundaries of the peri-infarcted zone. The range of peri-infarcted zone values is shaded in all the subplots of Figure 5.6. Figure 5.6b displays the temporal response of Mn^{2+} efflux in regions A and B, with first order exponential fits overlaid. In order to compare the infarcted efflux data to the control dose dependent data, a third plot, Figure 5.6c, is shown. This figure displays the efflux half lives of the dose dependent groups, as well as those for regions A and B. Following extrapolation of the exponential fit to the dose dependent half lives, the infarcted region is shown to correspond to a $MnCl_2$ infusion dose of approximately 400 nmoles g^{-1}. Using the linear fit for the predicted efflux transfer rate, k_{21} (Equation 5.15), shown in Figure 5.5a, the approximate efflux transfer rate for the infarcted region is 0.52 h^{-1}, an increase from 0.22 h^{-1} for the viable region of the same infusion dose. Thee efflux transfer rates for the peri-infarcted zone vary continuously between these limits.

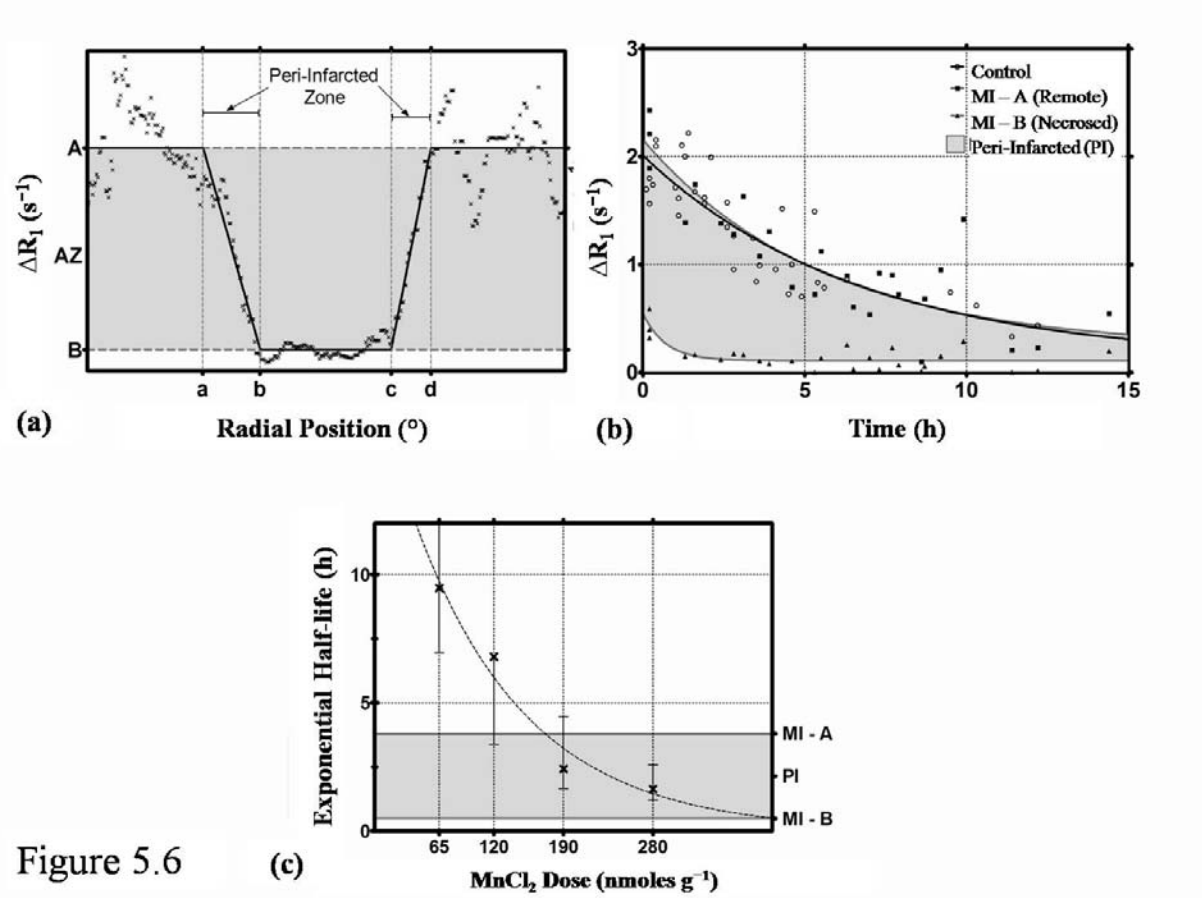

Figure 5.6

Figure 5.6 Comparison of the MI efflux data to the modeled healthy efflux data. (a) shows an example output from the radial MI fitting algorithm, fitting constant ΔR_1 values for the remote (A) and necrosed (B) tissue, and linearly changing ΔR_1 in peri-infarcted zone between. The temporal efflux of regions A and B are illustrated in (b). The exponential efflux half-lives for these regions are compared to the healthy, dose dependent efflux in (c). The potentially salvageable peri-infarcted zone tissue is shaded in all three subplots.

5.4 Discussion

The goals of this portion of the dissertation were to characterize the Mn^{2+} transport properties using pharmacokinetic modeling to gain an insight into the relationship between Mn^{2+} and Ca^{2+} transport in the healthy heart as well as alteration in Mn^{2+} handling following MI. The groups used to study the Mn^{2+} handling properties in the healthy heart were designed to test both the infusion dose dependence on Mn^{2+} influx and efflux, as well as to probe the efflux mechanisms by inhibiting the NCX with varying doses of SEA0400. It was found that, given the current sensitivity of the MEMRI technique, a two-compartment model incorporating compartments for the blood and heart (Model 1), was sufficient to describe the systems of Mn^{2+} transport. Only modeling of the 50 mg kg^{-1} SEA0400 group (Figure 5.4c), the most extreme case of NCX inhibition, gained a significant improvement with the addition of a third compartment representing cytosolic compartmentalization. These findings suggest that compartmentalization is not negligible; however, prolonged retention of Mn^{2+} is required in order for the models to be able to quantify this with certainty. Indeed, over the experimental timeframe Model 2 predicts that over half of the Mn^{2+} contained within the cytosol is retained within intracellular compartments (Figure 5.2).

Within this study, the transfer rate parameters k_{10}, k_{12} and k_{21}, were all shown to increase linearly with increasing $MnCl_2$ infusion doses (Figure 5.5a). The dose dependence of the linear uptake parameter, k_{12}, is in agreement with work previously conducted by Waghorn et al. (204), studying the relationship between Mn^{2+} infusion dose and myocardial Mn^{2+} uptake. While Mn^{2+} is known to act as a surrogate marker for Ca^{2+}

with respect to ionic uptake and efflux from the cytosol, the relationship between Ca^{2+} transport and Mn^{2+} transport is not well known. The relative contributions of the NCX and PMCA are likely to be different for Mn^{2+} and Ca^{2+} due to differences between their binding constants. Similarly, low extracellular Mn^{2+} concentrations create a concentration gradient potentially allowing Mn^{2+} extrusion to occur via the Ca^{2+} channels, while intracellular compartmentalization may also differ between the ions.

For Ca^{2+}, the NCX is known to account for approximately 80% of the total efflux in mice (25). Model 2 predicts that following inhibition of the NCX, the Mn^{2+} efflux rate is reduced to just 8.2, 1.8, 1.6 and 1.0 % of the initial, pre-SEA0400 administration, rate for the 10, 20, 35 and 50 mg kg^{-1} SEA0400 groups respectively. This maximum inhibition occurred on average 3 minutes post-SEA0400 administration. A possible cause of the difference between Ca^{2+} and Mn^{2+} efflux is due to the aforementioned differences in the extracellular concentrations of the respective ions. The relative contribution from the passive NCX is expected to increase with decreasing ion concentration gradients, with a consequent reduction in the contributions from the active PMCA. This effect is observed following inhibition of the NCX, where for the highest dose of SEA0400 the models predict that approximately 99% of Mn^{2+} efflux occurs via the NCX.

With respect to compartmentalization, it has been shown that Ca^{2+} uptake into the SR and mitochondria occurs at rates of 6.1×10^{-3} and 1.0×10^{-6} M s^{-1}, respectively (222,223), compared to an efflux rate of 3.0×10^{-2} M s^{-1} across the NCX. The efflux rate for Ca^{2+} is therefore approximately 5 times greater than for compartmentalization. In contrast, Model 2 predicts that the uptake of Mn^{2+} into the intracellular compartments occurs at a rate approximately 12 times greater than the efflux rate. Although further

studies are required to fully address this potential effect, if found to be significant, differences in Mn^{2+} and Ca^{2+} handling could potentially be explained by differences in the binding constants of the ions.

Model 3 attempts to address differences in relaxivity between free cytosolic Mn^{2+} and compartmentalized Mn^{2+}. For the dose dependent groups, the relaxivity of the compartments (SR and mitochondria) was found to be 2.3±0.1 times larger than for free cytosolic Mn^{2+}. This is most likely caused by the binding of Mn^{2+} to larger molecules within the compartments. An alternative hypothesis would be that, once compartmentalized, Mn^{2+} becomes chelated, thus reducing the relaxivity; however this effect was not predicted by the models. When considering the contribution of multiple compartments on the overall relaxation rate, a more thorough representation of the effective relaxation rate would be to consider the be the weighted average of the relaxation in the two compartments (228). If compartment i has a volume fraction f_i, an initial T_1 given by T_{1i} and a contrast agent concentration C_i, then the effective relaxation rate is given by Equation 5.18.

$$\frac{1}{T_1} = \sum_i f_i \left(\frac{1}{T_{1i}} + r_{1i} C_i \right) \qquad \text{Equation 5.18}$$

Model 3 incorporates a simplification of this equation (Equation 5.9), assuming that the volume fractions, f_i, for the free Mn^{2+} and compartmentalized Mn^{2+} are equal to each other. While a reasonable approximation for this study, the cytosol only constitutes approximately 11.5% of the myocardial cell volume, with the SR and mitochondria accounting for 36 % and 3.5% respectively (4,229).

The pharmacokinetic properties of SEA0400 were also addresses in this study, assuming that the plasma concentration was inversely proportional to the efflux rate, k_{21}

(Equation 5.3). The models all predict that the drug uptake occurs rapidly, with the maximum inhibition of the NCX occurring approximately 3 minutes post-administration. With respect to drug elimination, the predicted SEA0400 elimination half-lives are predicted to be of the same order of magnitude as unpublished SEA0400 data in rats. Although there is no published data for the kinetic properties of SEA0400, the assumptions and models presented in this current study appear to provide a good first order approximation for the pharmacokinetic transport properties of SEA0400, although further work is warranted to fully understand this.

It has previously been demonstrated that T_1-mapping MEMRI can be used to delineate different regions of the infarcted myocardium (204). This current study provides additional information with regards Mn^{2+} handling within different regions of the infarcted myocardium. Figure 5.6c demonstrates that the Mn^{2+} efflux half-life of the necrotic tissue within the MI site, as well as the peri-infarcted zone tissue, corresponds to efflux half-lives observed following increased Mn^{2+} infusion doses in healthy mice. The affected tissue also has Mn^{2+} handling properties associated with increased Mn^{2+} efflux rates. Application of MEMRI techniques to detect increases in $[Ca^{2+}]_i$ in ischemic tissue are currently limited, in part due to reduced perfusion in the ischemic tissue. However, by modeling Mn^{2+} efflux data, this study has demonstrated the ability of MEMRI T_1-mapping to minimize the uncertainties caused by perfusion limitations. The technique has also indirectly predicted an increase in Mn^{2+} content and Mn^{2+} efflux rates in the viable cells within ischemic regions. This increase is consistent with *ex vivo* Ca^{2+} studies, with the MEMRI T_1-mapping efflux technique having the potential to be used to indirectly predict alterations in Ca^{2+} handling in the infarcted heart.

5.4 Conclusions

Implementation of three multi-compartment pharmacokinetic models to Mn^{2+} efflux data in healthy and infarcted mice hearts has been demonstrated to effectively model Mn^{2+} transport mechanisms. In order to address the difference in Mn^{2+} and Ca^{2+} handling in the myocardium, the model predicted that Mn^{2+} is more dependent on the NCX for ionic efflux than is Ca^{2+}. This is likely due to the difference in the concentration gradients between the ions, driving the passive NCX pump. Within the cytosol the model predicts that Mn^{2+} uptake into compartments occurs at a faster rate than for efflux, contrary to the effect observed for Ca^{2+}. This can potentially be explained by considering differences in the binding constants for Mn^{2+} and Ca^{2+}. Additionally, Mn^{2+} stored within intracellular compartments, for example the SR and mitochondria, exhibits an apparent increase in relaxivity, r_1, relative to free cytosolic Mn^{2+}, possibly due to Mn^{2+} binding with larger molecules.

Finally, there is an apparent increase in the Mn^{2+} efflux rate from ischemic tissue, commensurate with increased Mn^{2+} content in viable cells within these regions. This effect has been widely observed for *ex vivo* Ca^{2+} transport, but has thus far proved elusive for *in vivo* MEMRI studies. The predictions made by this modeling technique allow for a more thorough understanding of the relationship between Mn^{2+} and Ca^{2+} handling in the heart. This approach therefore has the potential to be applied as a diagnostic tool in the early detection of abnormal Ca^{2+} handling in the myocardium, and for monitoring disease progression.

CHAPTER 6: CONCLUSIONS AND FUTURE DIRECTIONS

6.1 Conclusions

Quantitative T_1-mapping MEMRI techniques were applied within this dissertation to study the handling properties of Mn^{2+} in the myocardium under healthy control, pharmaceutically altered and post-MI conditions. The technique demonstrated its sensitivity to detect temporal changes in the absolute Mn content in the myocardium for both healthy mice, and mice undergoing alterations in Mn^{2+} handling due to inhibition of the NCX with SEA0400. These changes in Mn content were calculated using the correlation between *in vivo* ΔR_1 efflux and the efflux of absolute cardiac Mn content post-$MnCl_2$ infusion. Elemental analysis of heart tissue samples collected at various time points post-$MnCl_2$ infusion demonstrated that the reduction in LV Wall ΔR_1 was linearly proportional to the myocardial Mn content. The linearity of the temporal data, suggest that 1) observed temporal changes in ΔR_1 are linearly proportional to changes in Mn content and 2) Mn^{2+} efflux could be estimated from the ΔR_1 washout curves. This technique is therefore appropriate for the evaluation of Mn^{2+} efflux *in vivo*.

For healthy mice not undergoing any pharmaceutical intervention, the temporal change in LV Wall ΔR_1, and therefore Mn content, followed an exponential decay. This allowed for inferred determinations of Mn^{2+} efflux half-lives. For example, the half-life for the control, 190 nmoles g^{-1} BW $MnCl_2$, curve was 3.4 hrs. Increasing the absolute Mn content in the myocardium by infusing the mouse with increasing $MnCl_2$ infusion doses lead to an increase in the ΔR_1 efflux rate. Mn^{2+} efflux occurred with a half-life dependent

on the initial Mn^{2+} content such that an increase in the Mn^{2+} uptake caused an increase in the Mn^{2+} efflux rate.

It was also shown in this dissertation that changes in ΔR_1 over time may be used to quantify changes in Mn^{2+} content *in vivo* when modulating NCX kinetics with the NCX inhibitor SEA0400. This information could be useful for indirectly assessing and understanding Ca^{2+} efflux as Mn^{2+} is considered its biochemical analogue. By varying the intraperitoneal doses of SEA0400, as well as by using a single dose of dobutamine, Mn^{2+} efflux in the healthy murine heart was affected. Inhibition of the NCX with SEA0400 extended the ΔR_1 washout curve due to an assumed inhibition of the Mn^{2+} efflux. The inhibition of Mn^{2+} efflux using a known NCX inhibitor, in conjunction with the previous establishment of Mn^{2+} as a Ca^{2+} analogue during influx (99), indicates that changes in Mn^{2+} efflux most likely reflect changes in Ca^{2+} efflux.

The positive inotropic state following administration of dobutamine caused a biphasic Mn^{2+} efflux curve in the healthy myocardium. This finding was exhibited by an initial rapid increase in the Mn^{2+} efflux rate followed by a gradual decrease as a slower Mn^{2+}efflux rate reduced the Mn^{2+} content. These results suggest that alterations in Ca^{2+} handling caused by changes in the inotropic state of the heart are also observed for Mn^{2+}, and that the T_1 mapping MEMRI efflux technique is sensitive enough to detect these effects.

Overall, this study of Mn^{2+} efflux in the healthy murine myocardium found that the T_1-mapping MEMRI technique detected and quantified:

1) increased Mn^{2+} uptake associated with an increased Mn^{2+} efflux rate due to increased Mn^{2+} infusion doses

2) decreased Mn^{2+} efflux rates following NCX inhibition with SEA0400

3) increased Mn^{2+} efflux rates due to the positive inotropic effect of dobutamine

This information concerning Mn^{2+} efflux dynamics could potentially enhance understanding of Ca^{2+} dynamics, particularly when investigating pathophysiological phenomena and/or developing new therapeutic pharmaceutical agents.

One of the primary goals of this dissertation was to study alterations in Mn^{2+} handling in the post-MI murine heart. This dissertation has demonstrated a novel technique for identifying and quantifying specific regional differences in tissue characteristics that occur after a MI in the murine model. This innovative methodology isolates and segments the MEMRI T_1 maps and then fits the calculated ΔR_1 values into a region-defining MI curve that determines the location (in radial degrees) of the infarcted (necrosed), peri-infarcted (ischemic) and viable remote tissue. The region-defining MI curve introduced in this dissertation not only eliminates user bias in determining the location of the infarcted, peri-infarcted, and viable myocardium, but also has potential as a clinical tool to assist clinicians in diagnosing and treating post-MI patients.

Results from this study further showed that Mn^{2+} handling within the viable region of the MI group and the Sham group were unaltered after surgery. However, decreases in both the initial uptake of Mn^{2+} (represented by $\Delta R_{1,0}$) and efflux half-life were observed in both the necrosed and peri-infarcted zones of the MI group. As shown above, Mn^{2+} efflux occurred with a half-life dependent on the initial Mn^{2+} content such that an increasing Mn^{2+} uptake caused an increase in the Mn^{2+} efflux rate. Therefore, the regional Mn^{2+} uptake in viable cells within the peri-infarcted zones could potentially be

estimated by examining the Mn^{2+} efflux properties. Mn^{2+} efflux from the necrosed region (MI Region B) occurred with a significantly faster half-life than in the Control group with the same $MnCl_2$ infusion dose. The inferred equivalent infusion dose for the infarcted (necrosed) and peri-infarcted (ischemic) regions was found to be larger than the 280 nmoles g^{-1} $MnCl_2$ infusion dose. This finding suggests that both the necrosed and peri-infarcted regions experience increased Mn^{2+} uptake, and therefore potentially Ca^{2+} uptake.

The final section of the dissertation demonstrated the ability to characterize the Mn^{2+} transport properties using pharmacokinetic modeling. Implementation of three multi-compartment pharmacokinetic models to Mn^{2+} efflux data in healthy and infarcted mice hearts has been demonstrated to effectively model Mn^{2+} transport mechanisms. In order to address the difference in Mn^{2+} and Ca^{2+} handling in the myocardium, the model predicted that Mn^{2+} is more dependent on the NCX for ionic efflux than is Ca^{2+}. This is likely due to the difference in the concentration gradients between the ions, driving the passive NCX pump. Within the cytosol the model predicts that Mn^{2+} uptake into compartments occurs at a faster rate than for efflux, contrary to the effect observed for Ca^{2+}. This can potentially be explained by considering differences in the binding constants for Mn^{2+} and Ca^{2+}. Additionally, Mn^{2+} stored within intracellular compartments, for example the SR and mitochondria, exhibits an apparent increase in relaxivity, r_1, relative to free cytosolic Mn^{2+}, possibly due to Mn^{2+} binding with larger molecules.

Within this study, the transfer rate parameters k_{10}, k_{12} and k_{21}, were all shown to increase linearly with increasing $MnCl_2$ infusion. The dose dependence of the linear uptake parameter, k_{12}, is in agreement with the background work presented in §2.1 (204). While Mn^{2+} is known to act as a surrogate marker for Ca^{2+} with respect to ionic uptake and efflux from the cytosol, the relationship between Ca^{2+} transport and Mn^{2+} transport is not well known. The relative contributions of the NCX and PMCA are likely to be different for Mn^{2+} and Ca^{2+} due to differences between their binding constants. Similarly, low extracellular Mn^{2+} concentrations create a concentration gradient potentially allowing Mn^{2+} extrusion to occur via the Ca^{2+} channels, while intracellular compartmentalization may also differ between the ions.

For Ca^{2+}, the NCX is known to account for approximately 80% of the total efflux in mice (25). The relative contribution from the passive NCX is expected to increase with decreasing ion concentration gradients, with a consequent reduction in the contributions from the active PMCA. This effect is observed following inhibition of the NCX, where for the highest dose of SEA0400 the models predict that approximately 99% of Mn^{2+} efflux occurs via the NCX.

Model 3 attempts to address differences in relaxivity between free cytosolic Mn^{2+} and compartmentalized Mn^{2+}. For the dose dependent groups, the relaxivity of the compartments (SR and mitochondria) was found to be 2.3±0.1 times larger than for free cytosolic Mn^{2+}. This is most likely caused by the binding of Mn^{2+} to larger molecules within the compartments.

It has previously been demonstrated (§2.1 and §3) that T_1-mapping MEMRI can be used to delineate different regions of the infarcted myocardium (204). This current

study provides additional information with regards Mn^{2+} handling within different regions of the infarcted myocardium. Modeling conducted within this dissertation suggested that there is an apparent increase in the Mn^{2+} efflux rate from ischemic tissue, commensurate with increased Mn^{2+} content in viable cells within these regions. This effect has been widely observed for *ex vivo* Ca^{2+} transport, but has thus far proved elusive for *in vivo* MEMRI studies. The predictions made by this modeling technique allow for a more thorough understanding of the relationship between Mn^{2+} and Ca^{2+} handling in the heart. This approach therefore has the potential to be applied as a diagnostic tool in the early detection of abnormal Ca^{2+} handling in the myocardium, and for monitoring disease progression.

6.1.1 Summary

In summary, the findings presented in this dissertation, along with the biochemical similarities between Ca^{2+} and Mn^{2+}, strongly suggest that under appropriate conditions changes in Mn^{2+} efflux may reflect changes in Ca^{2+} efflux. As such, MEMRI T_1 mapping could be an innovative and effective technique to monitor an important factor associated with the progression of heart disease.

This study showed that T_1-mapping MEMRI quantified Mn^{2+} dynamics in both healthy and post-MI mice under various conditions. A novel technique was also introduced for identifying and quantifying specific regional differences of tissue characteristics in the post-MI mouse heart that could potentially be translated into the clinical environment. Using the segmentation and curve fitting methodology derived from T_1-mapping MEMRI, the salvageable ischemic tissue adjacent to the necrosed area

can be pinpointed for direct application of pharmacologic therapies. This information would be clinically useful not only for treating the precise areas of salvageable tissue, but also for monitoring progression of the remodeling process during healing. Thus, patient outcomes would be enhanced as improved treatment modalities target specific tissue areas and ultimately prevent the adverse remodeling that promotes heart failure development in post-MI patients.

6.2 Long-Term Goals

Although this dissertation suggests that Mn^{2+} handling data may mimic alterations in Ca^{2+} handling, the precise relationship between these two ions is still unknown. Ca^{2+} and Mn^{2+} extrusion rates are not equal due to their different binding constants and maximal rates for efflux transporters (NCX and PMCA). Furthermore, Mn^{2+} can be extruded via the reverse mode of Ca^{2+} channels due to low extracellular Mn^{2+} concentration. These conditions, although studied via pharmacokinetic modeling, make the precise relationship between Mn^{2+} and Ca^{2+} transport complicated, and studies to address this are required to address these long term goals.

In the study by Medina et al., 2007, (203), the authors speculate in their conclusions that knowledge of the relationship between Mn^{2+} and Ca^{2+} transport could allow for widespread repercussions in disciplines such as pharmacology and pathology. The current dissertation has attempted to answer many questions about the relationship between the flux of Mn^{2+}, as seen via *in vivo* MEMRI studies, and the true Ca^{2+} transport

properties. By using a known NCX inhibitor, SEA0400, alterations in Ca^{2+} flux can be estimated from the observed Mn^{2+} flux. However, the relationship between the two quantities will need to be further explored in order to fully determine Ca^{2+} fluxes *in vivo*.

One potential way of achieving this goal is by using diffuse reflectance and fluorescence techniques, as have been demonstrated by Du et al., 2005, (230). This study was shown to detect intracellular calcium changes during cerebral ischemia in a rat model. Despite the fact that calibrations between the Ca^{2+} fluxes detected using fluorescent and MEMRI techniques are potentially complicated, additional future studies applying this fluorescence technique to cardiac studies could add additional information to the *in vivo* MEMRI data that is presented in this dissertation.

Ultimately, this pre-clinical work has goals to be translated into the clinic, with the potential of being able to provide early diagnosis of cardiac disease, while offering *in vivo* insight into the dynamic Ca^{2+} alterations on a microscopic level. Such knowledge could be advantageous not only diagnostically, but also could help determine patient-specific treatment plans.

APPENDIX A: FLOW CHARTS

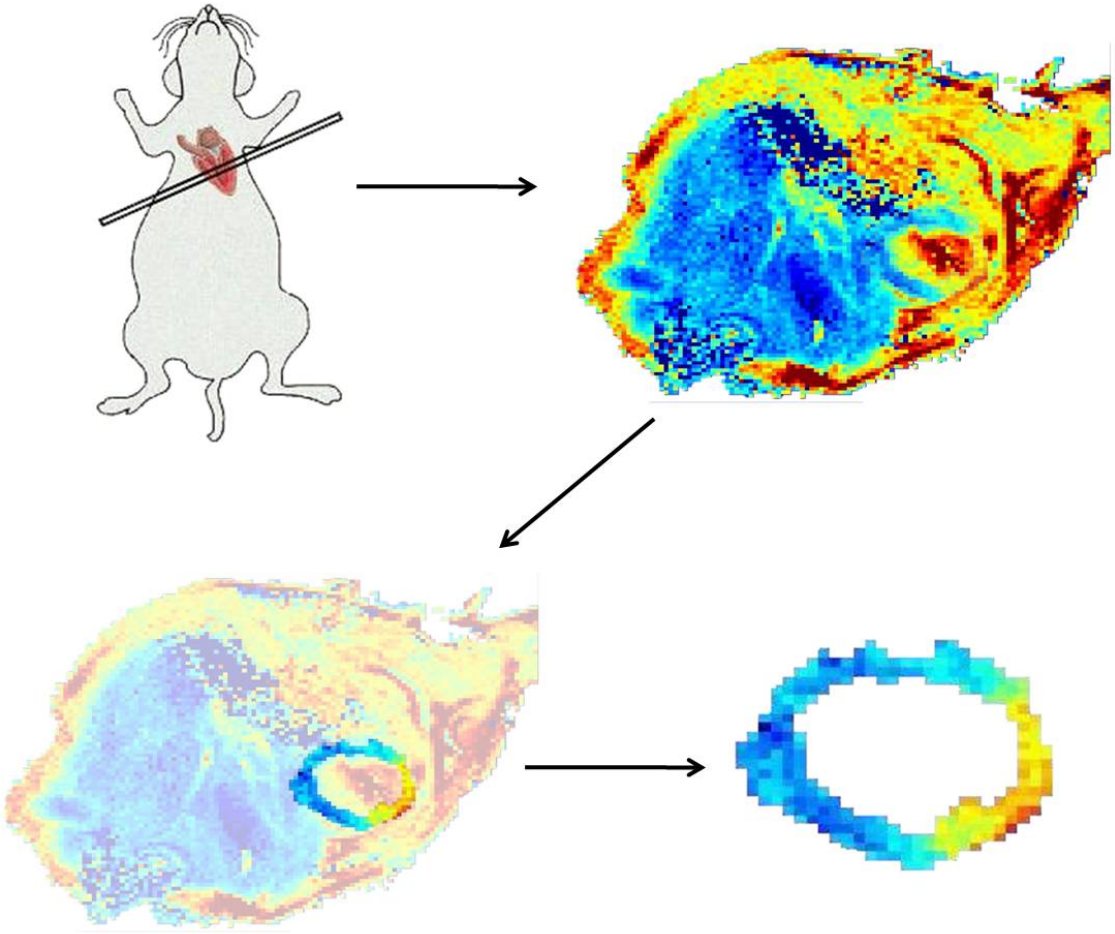

Figure A.1 Automated myocardial isolation flow chart. Representation of the short axis cardiac slice orientation (top left) used to acquire a short axis T_1-map of a MI mouse post-$MnCl_2$ infusion (top right). Input of this T_1 map with an associated T_1-weighted image (not shown), an unbiased isolation program was used to isolate the myocardial tissue from image (bottom left and right), as described in §4.

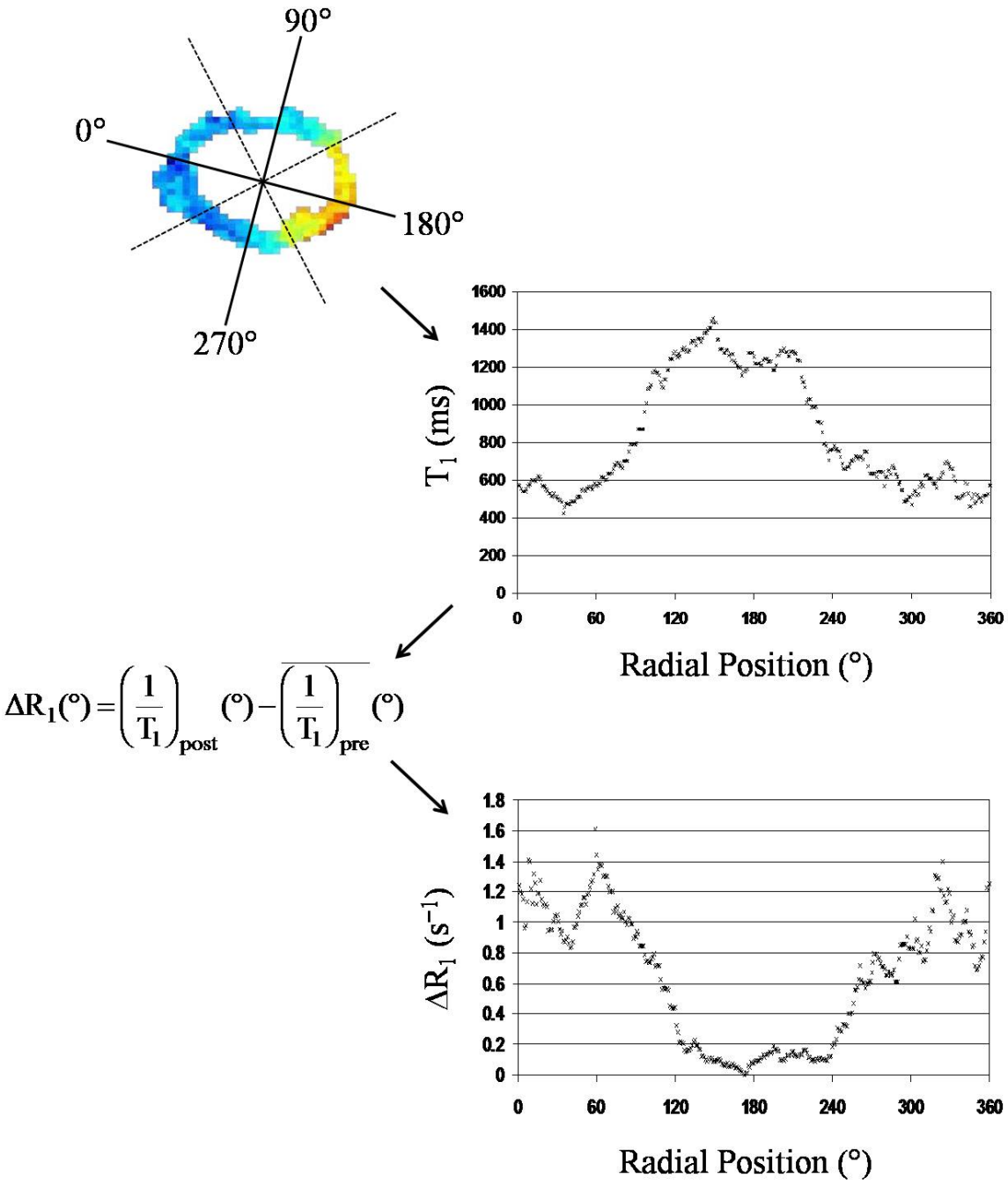

Figure A.2 Myocardium segmentation flow chart. The orientation definition (defined in the top image) is used to create a position dependent T_1 profile (top graph). Data from both pre- and post-$MnCl_2$ infusion T_1 maps are input into the shown equation, with a resultant output for the radial ΔR_1, at a given time, shown (bottom graph).

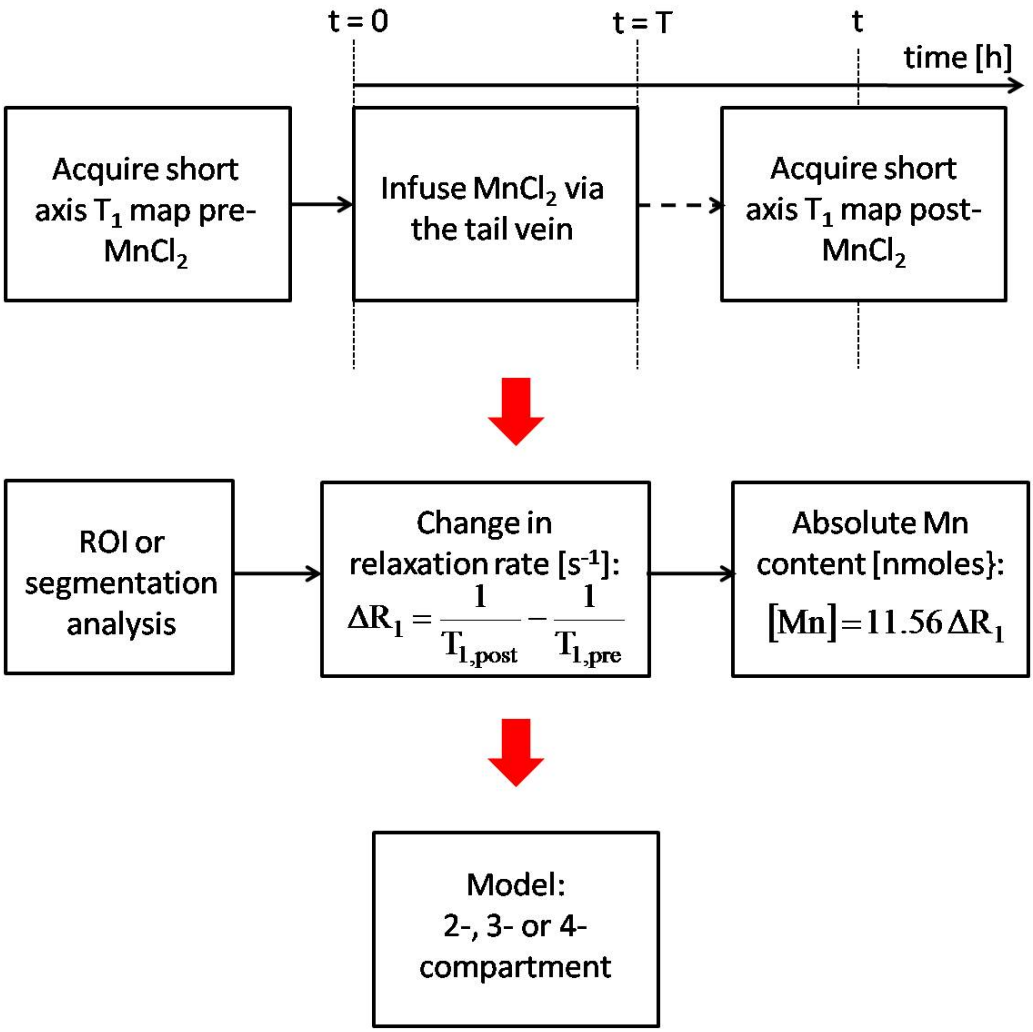

Figure A.3 Flow chart of the process of data acquisition and absolute Mn content calculation for the efflux studies, leading to the modeling of Mn transport with either 2- 3- or 4-compartment models.

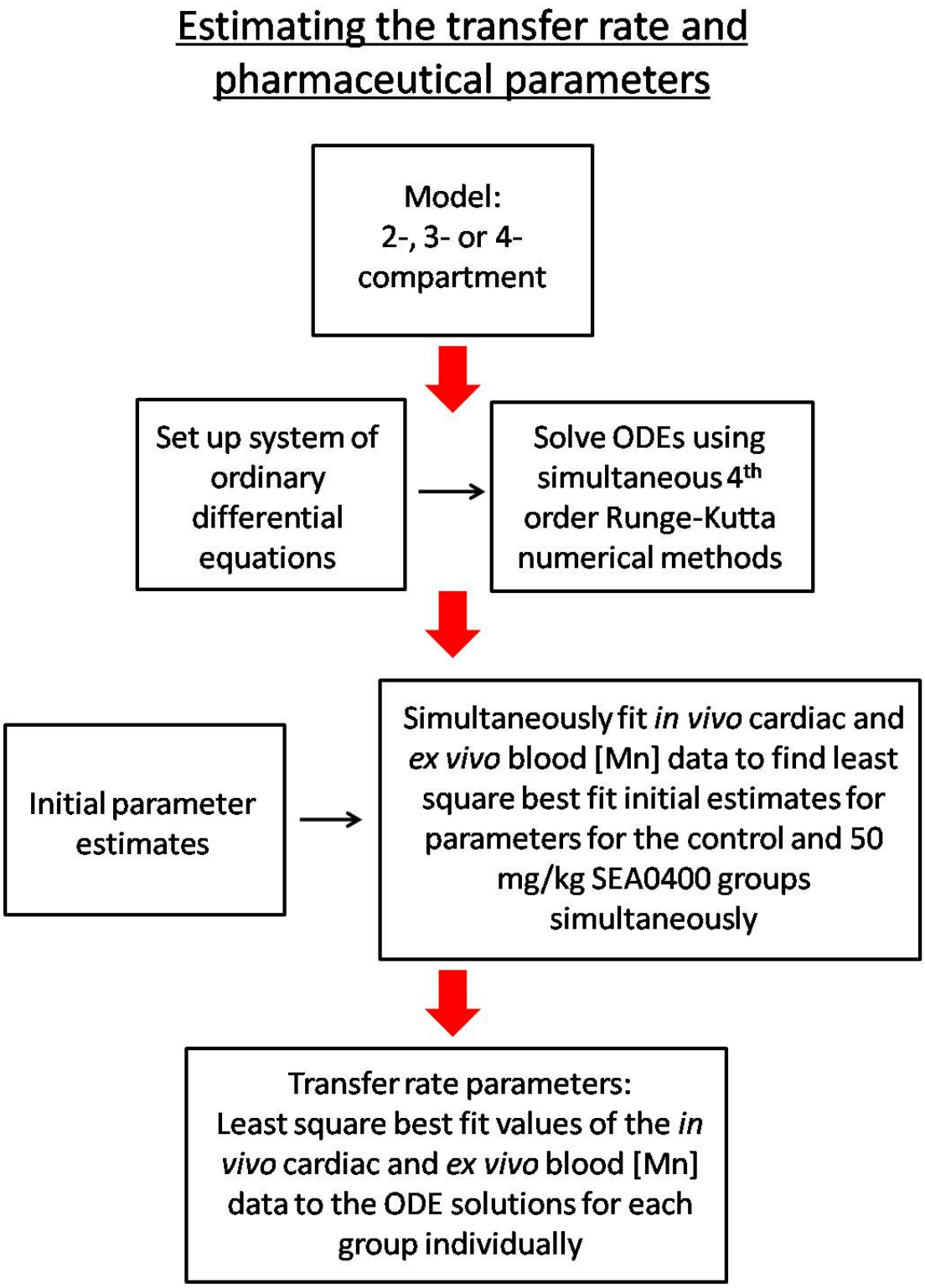

Figure A.4 Flow chart of the procedures involved with estimating the transfer rate and pharmaceutical parameters using pharmacokinetic modeling, as described in §5.

APPENDIX B: MODELING OUTPUT DATA

The following figures (Figure B.1) show the least square best fits for the three models described in §5. The model number and best fit parameters are shown in the top left panel of each figure, with the efflux group labeled above the plot in the top right panel.

For the control dose dependent figures there are a total of four panels. The raw cardiac Mn content data is shown in the top right panel along with the best fit to the model. The sum of residuals squared for each model fit are shown inside the axis. The same information for the blood is displayed in the bottom left panel, with the temporal heart residuals illustrated in the bottom right. For Model 2, the best fit Mn content for compartment 2 is illustrated by a dashed line, with compartment 3 shown as a dotted line. The fourth compartment in Model 3 is also shown with a dotted line; by definition at any given time the Mn content in compartment 4 is less than in compartment 3.

Due to the fact that the SEA0400 groups possess the same time independent transfer rate parameters as the Control 190 nmoles g^{-1} group for t < 1hr, the Control 190 nmoles g^{-1} and SEA0400 data is shown within the same figure for each SEA0400 model. For these SEA0400 groups the best fits cardiac data are shown for the control (top center; blue) and SEA0400 (top right, red) groups, with the corresponding blood data both shown in the bottom left panel. For reference, the total heart Mn content fit for the control group is overlaid on the SEA0400 plot as a dashed blue line. The cardiac residuals for the control and SEA0400 fits are displayed in the bottom center panel, with the temporal k_{21} fit shown in the bottom right panel.

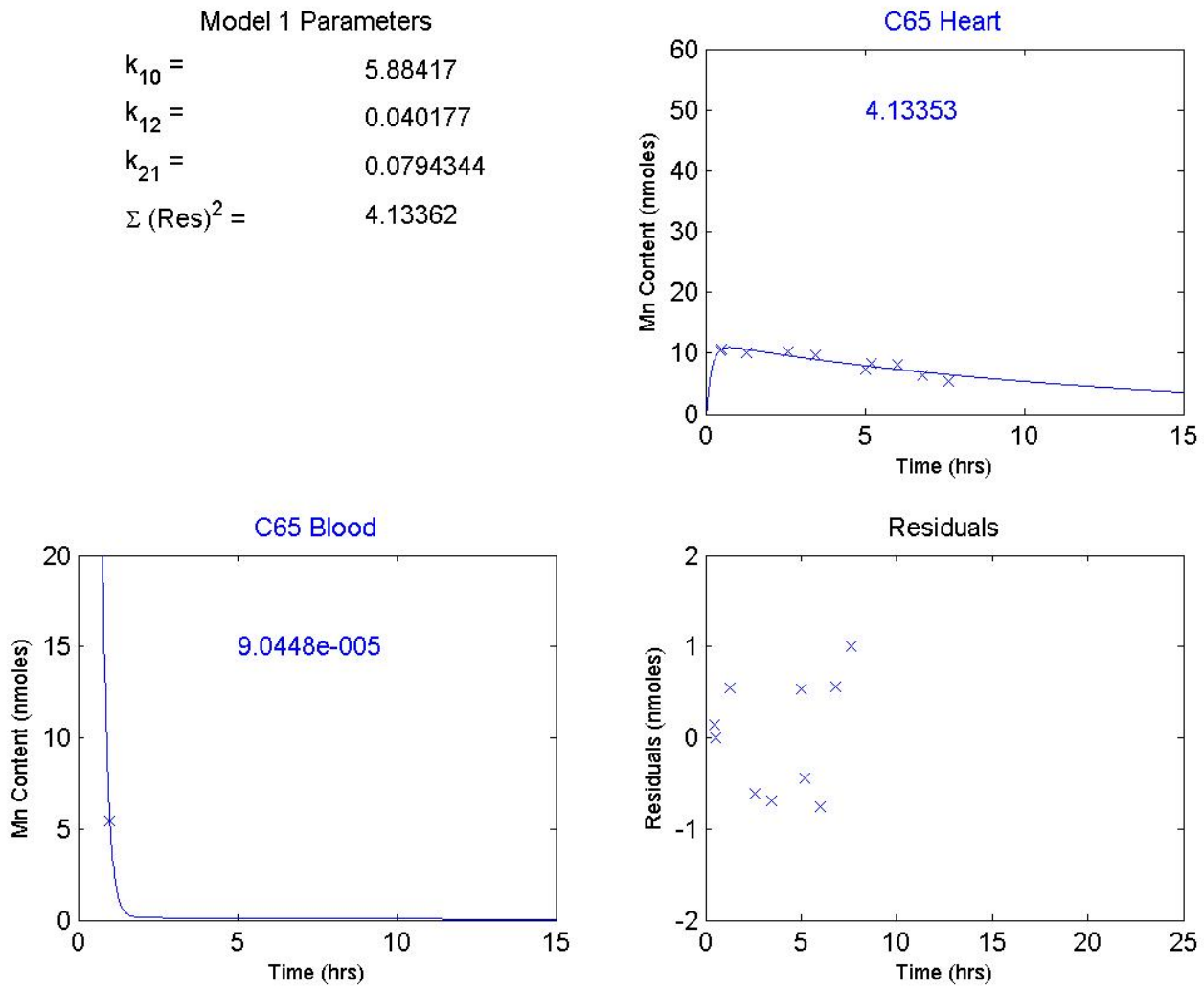

Figure B.1 Output model fits, residuals and parameters.

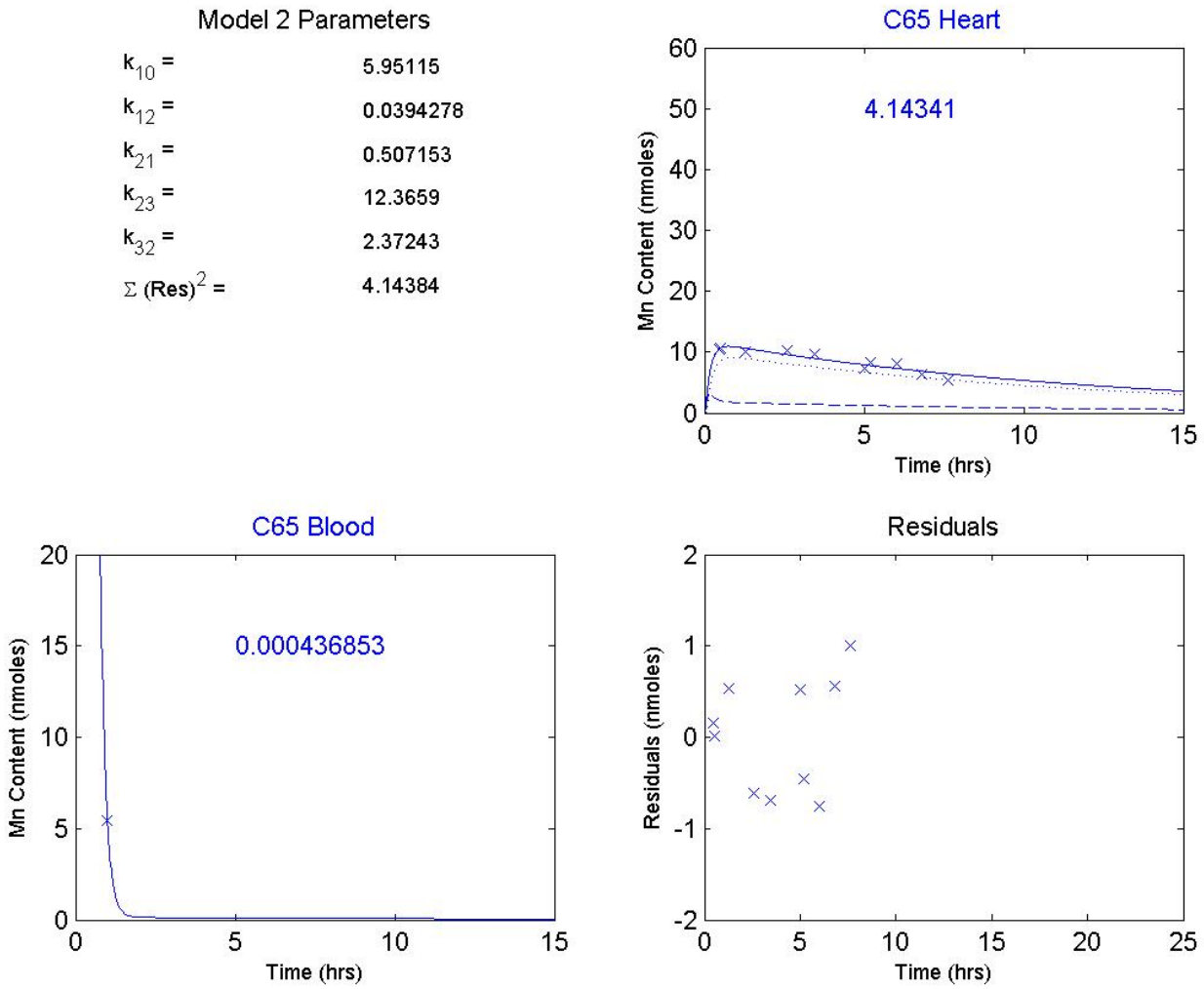

Figure B.1 continued

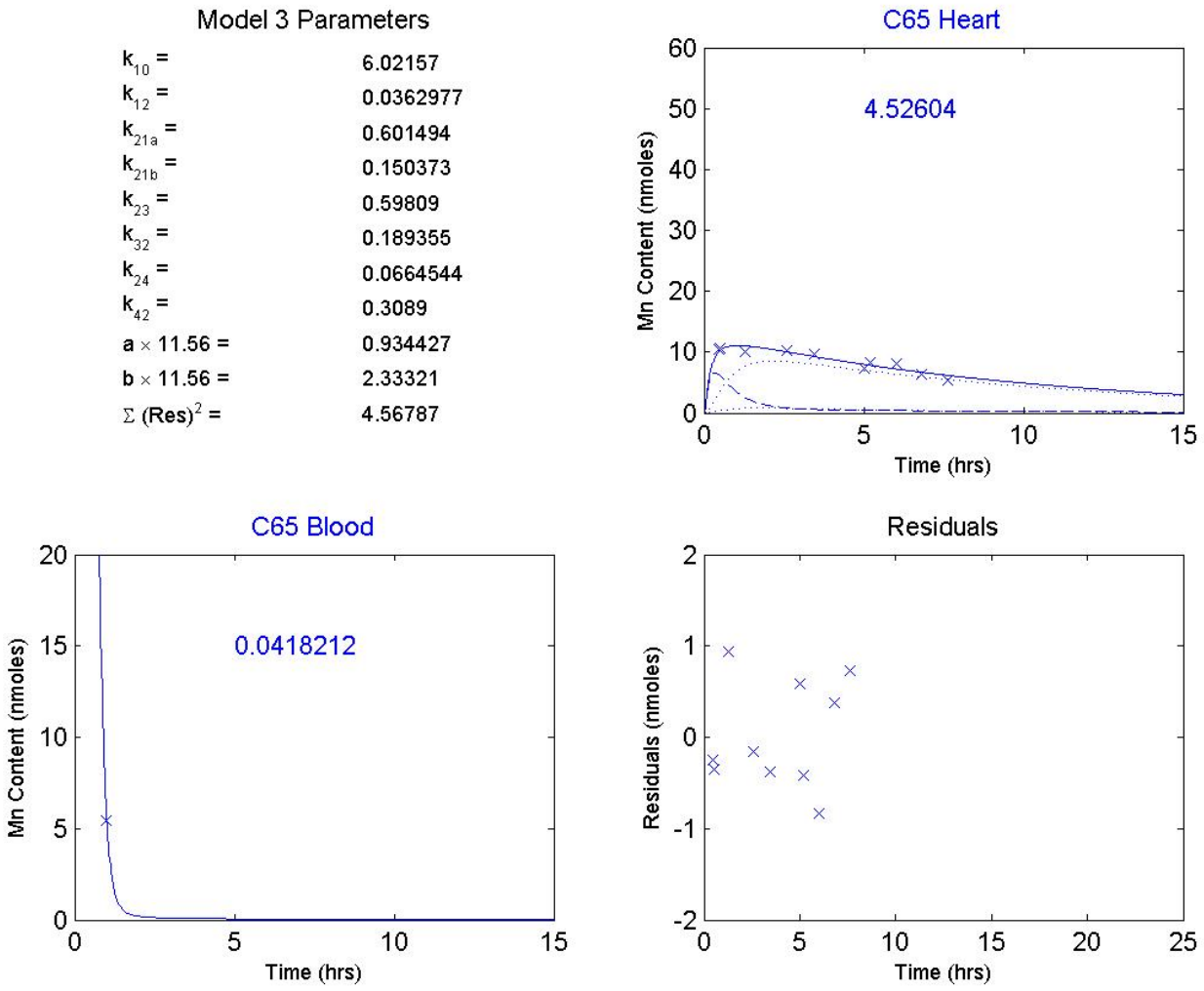

Figure B.1 continued

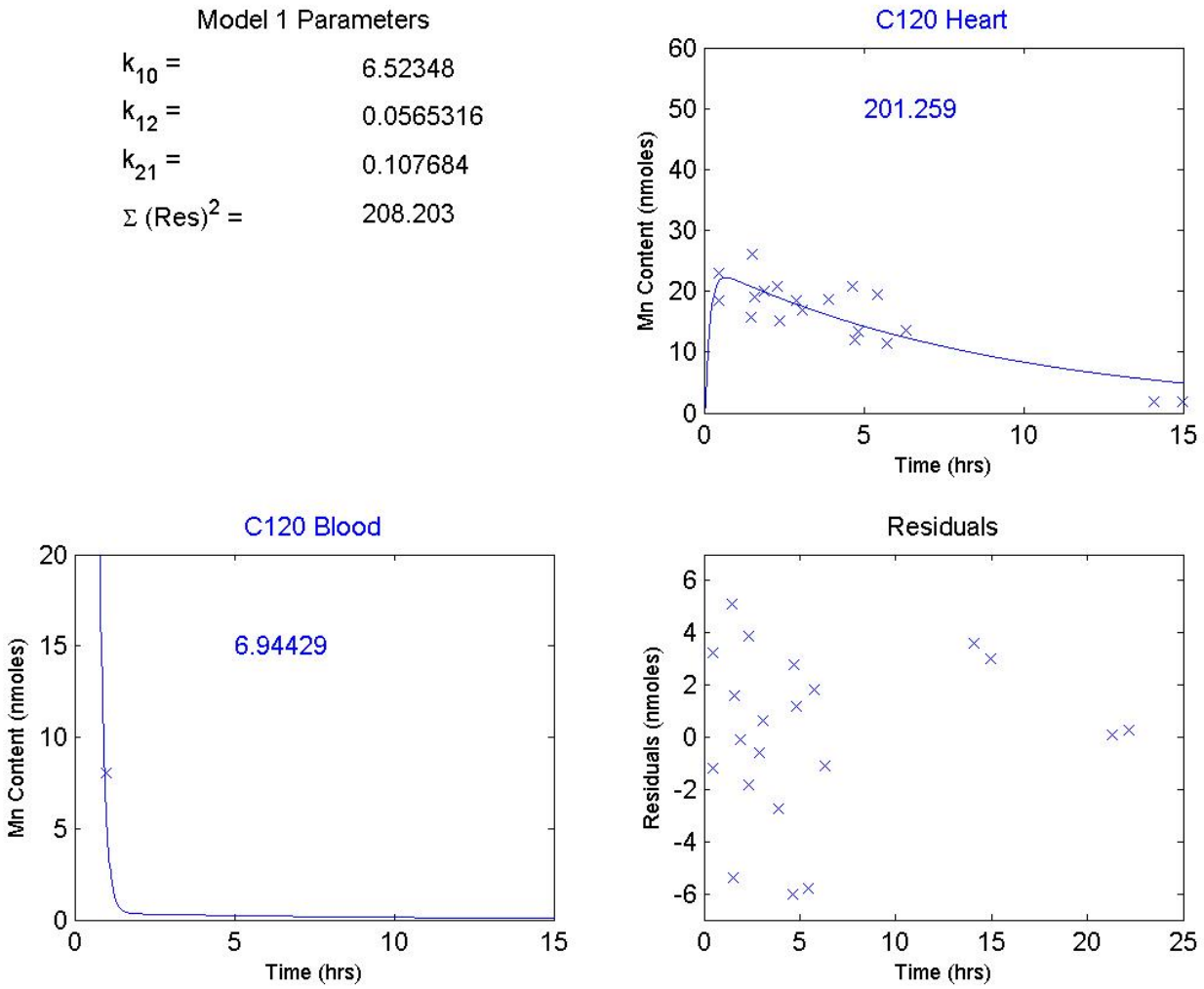

Figure B.1 continued

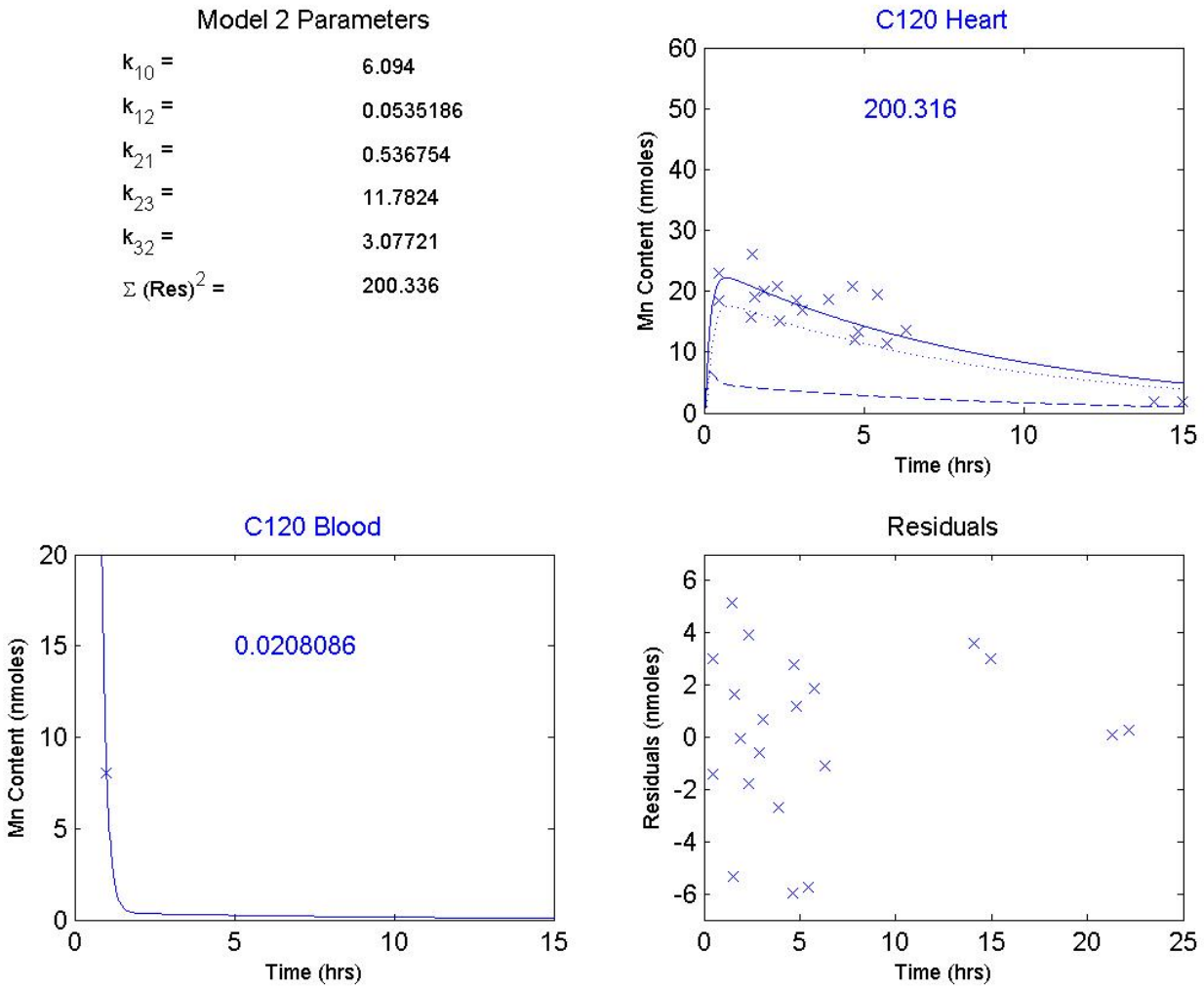

Figure B.1 continued

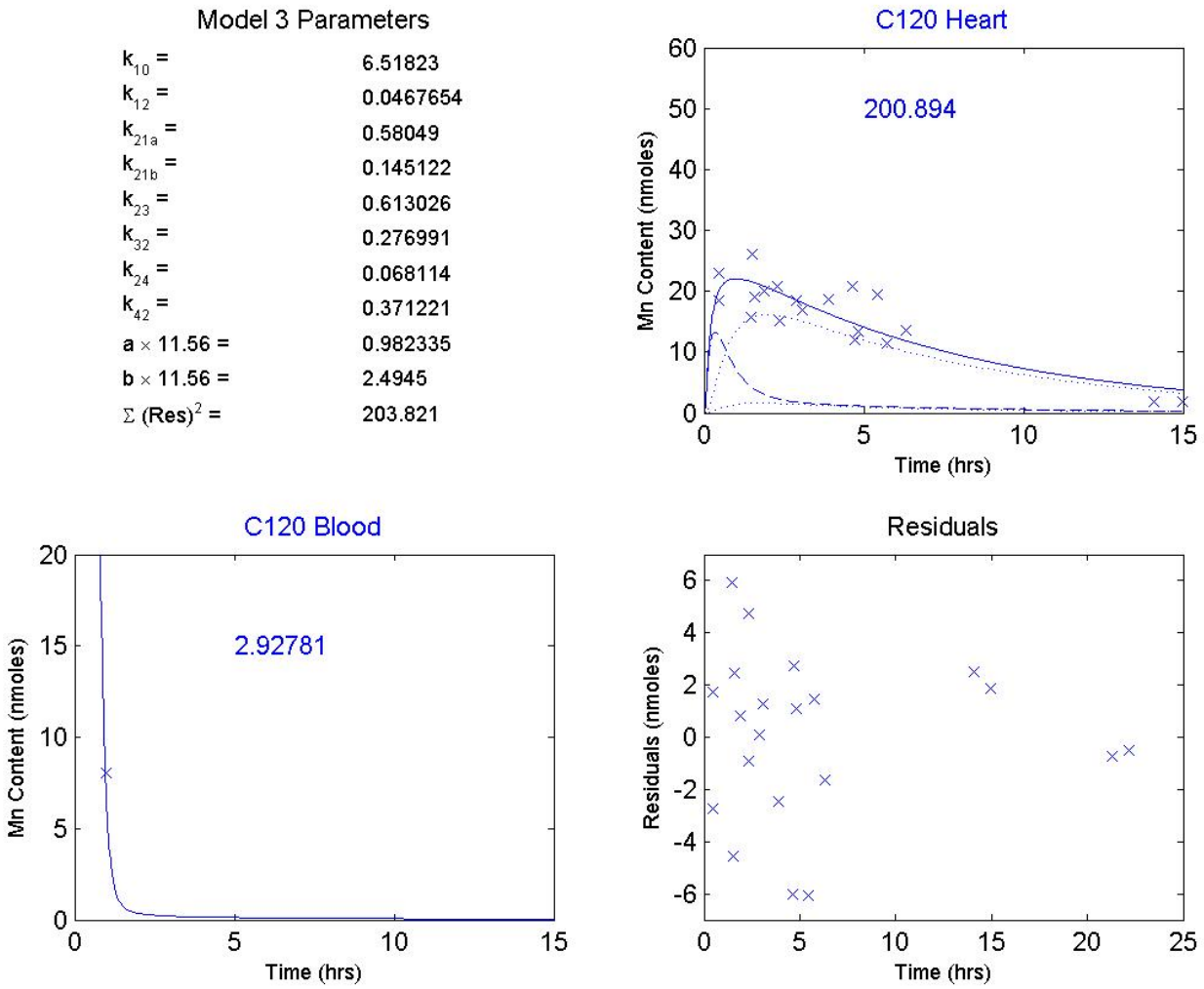

Figure B.1 continued

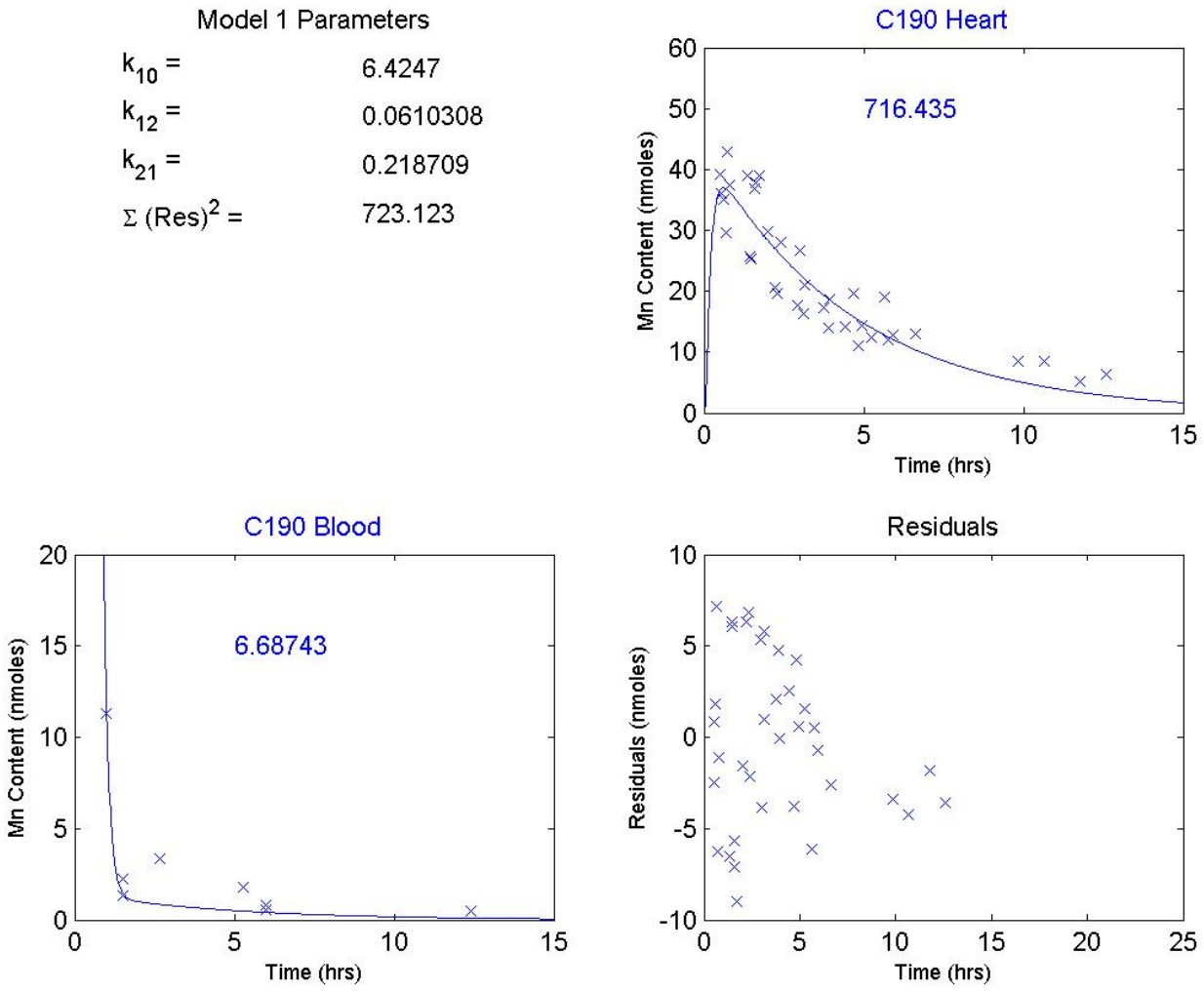

Figure B.1 continued

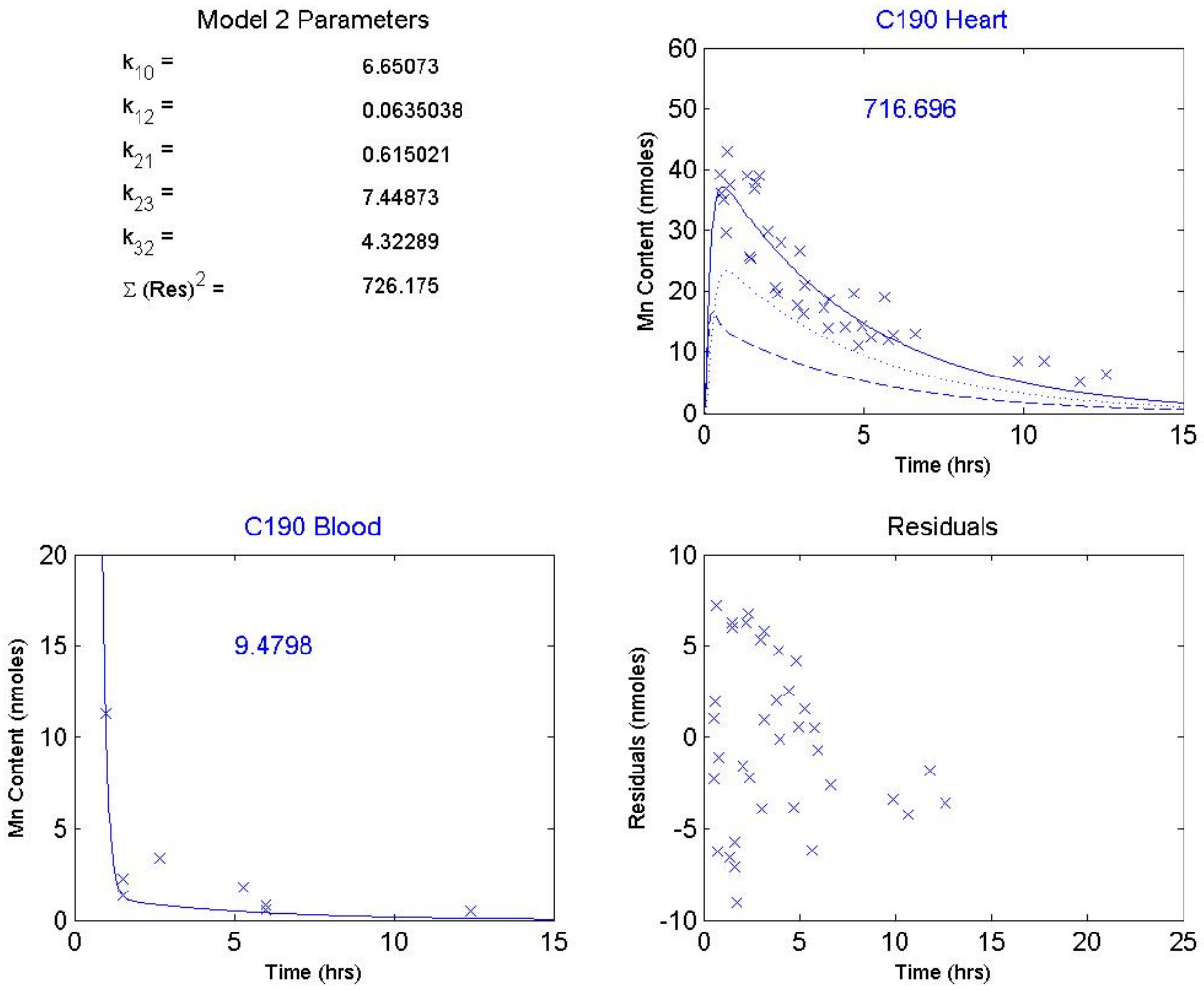

Figure B.1 continued

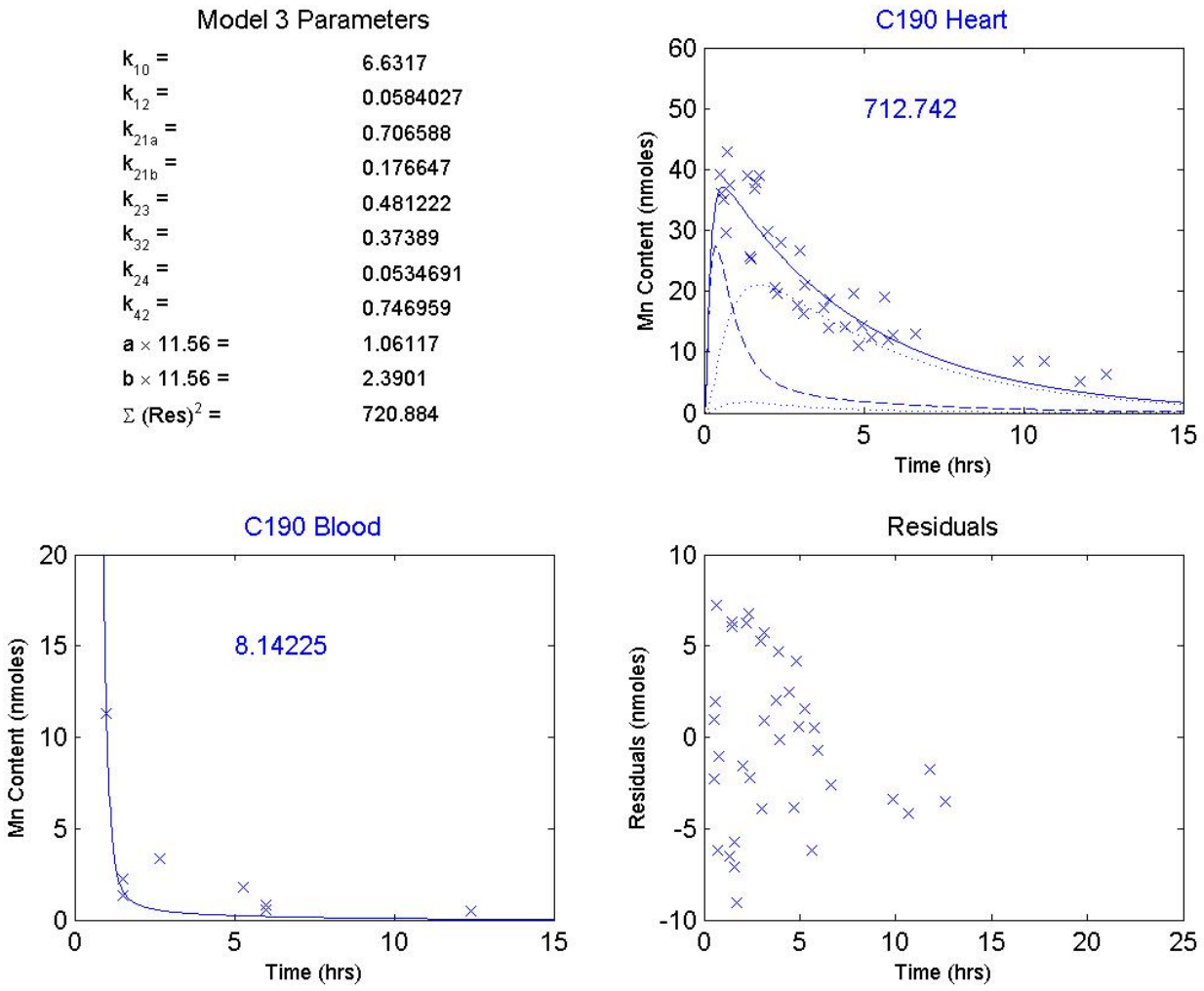

Figure B.1 continued

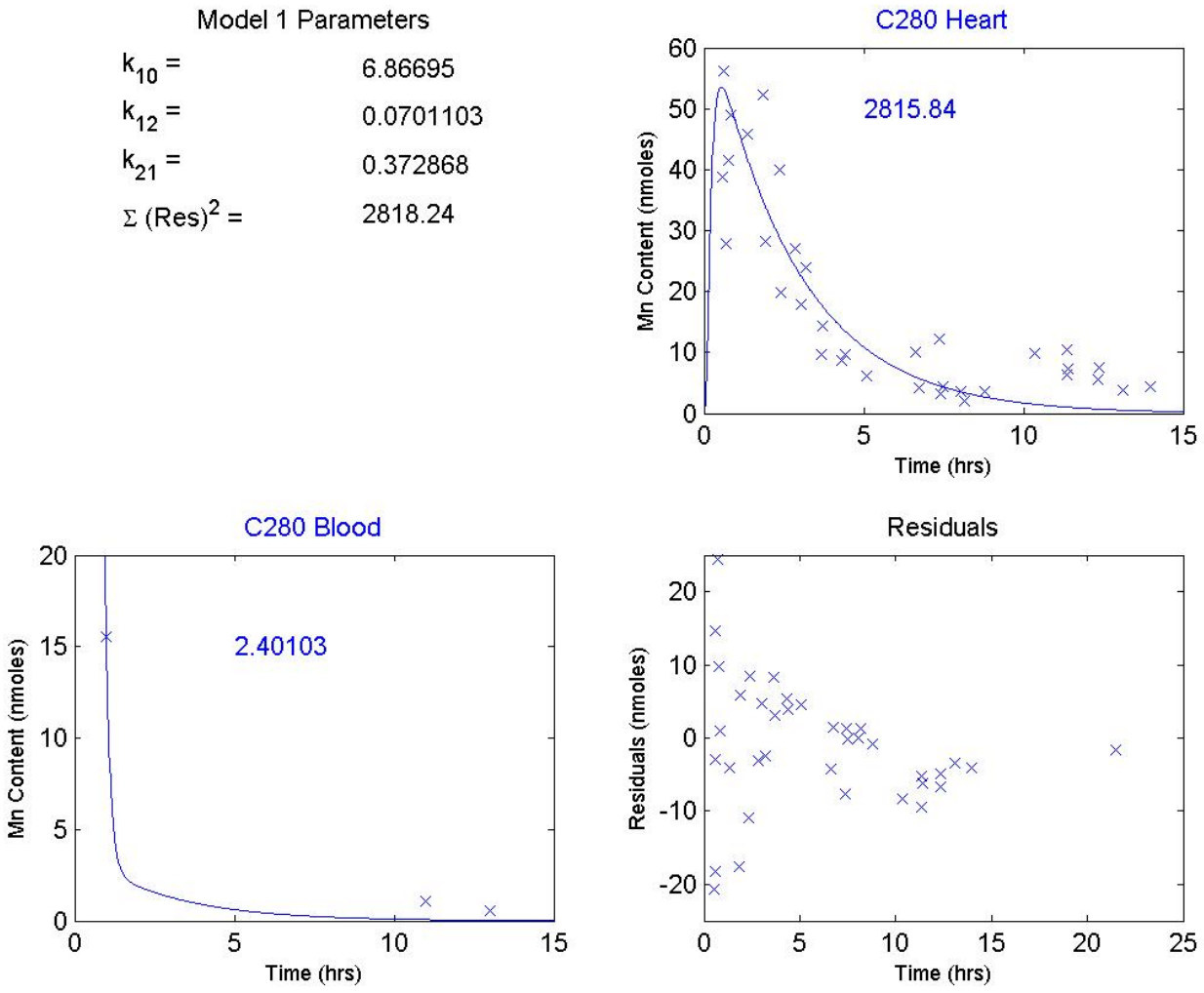

Figure B.1 continued

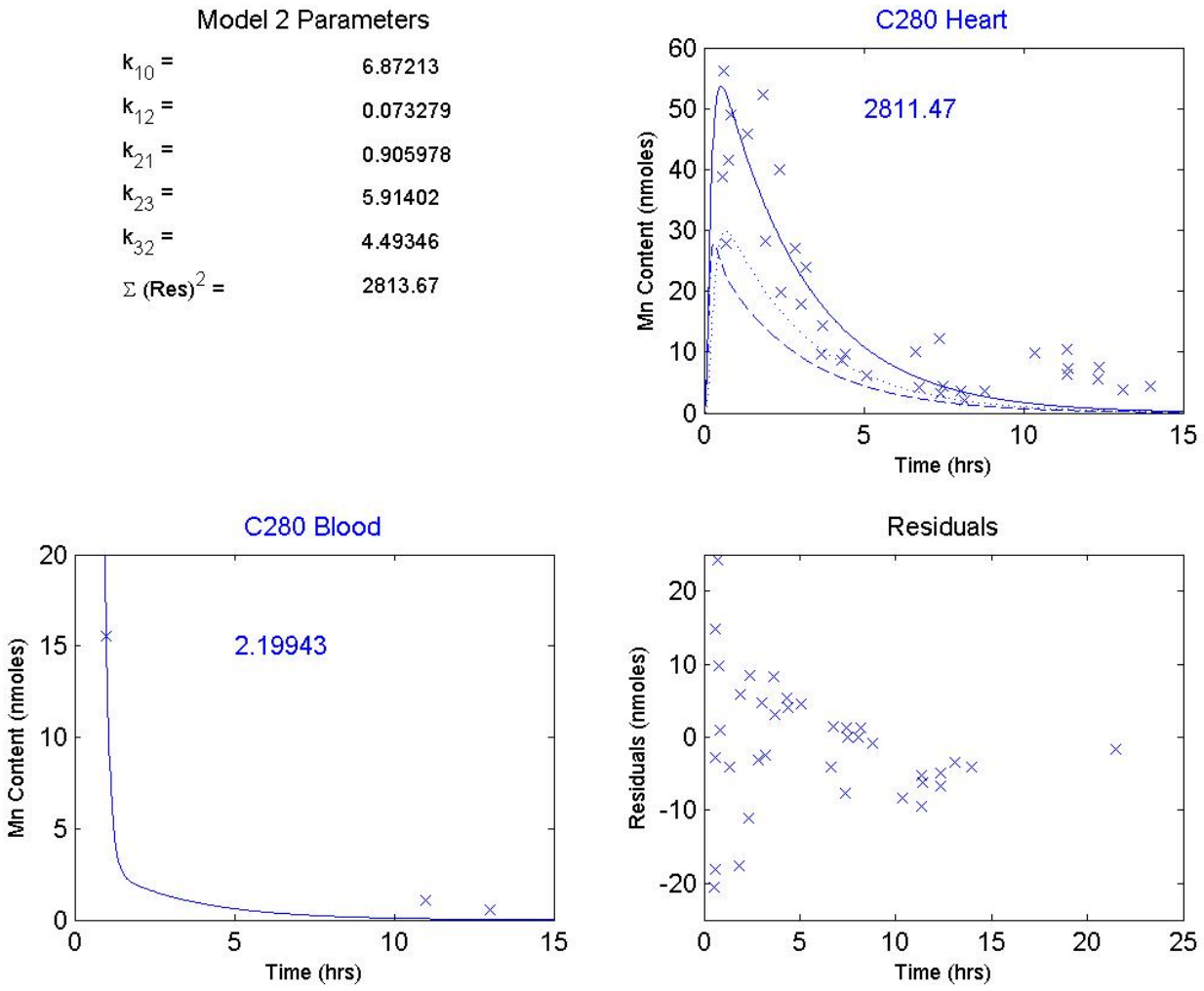

Figure B.1 continued

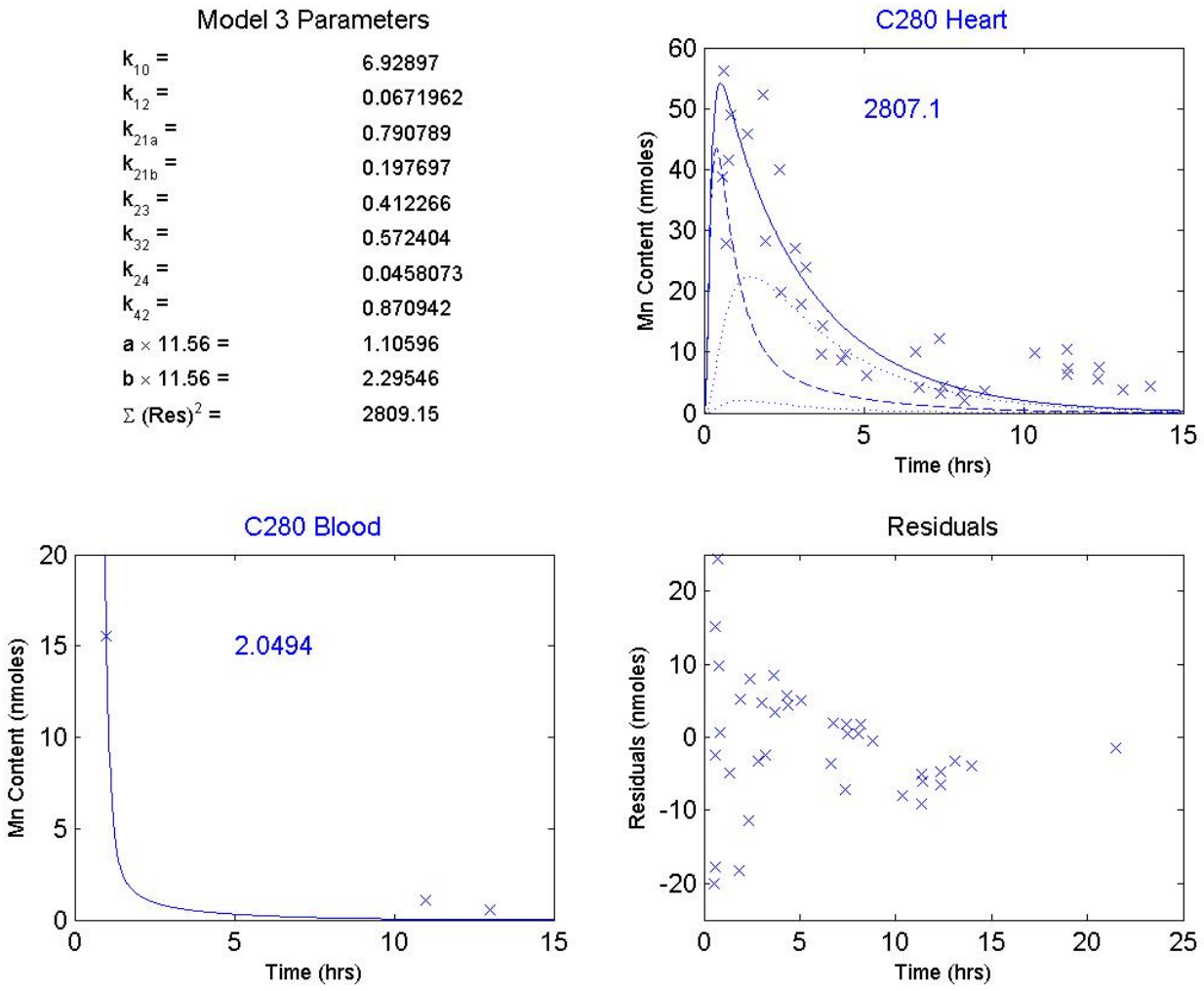

Figure B.1 continued

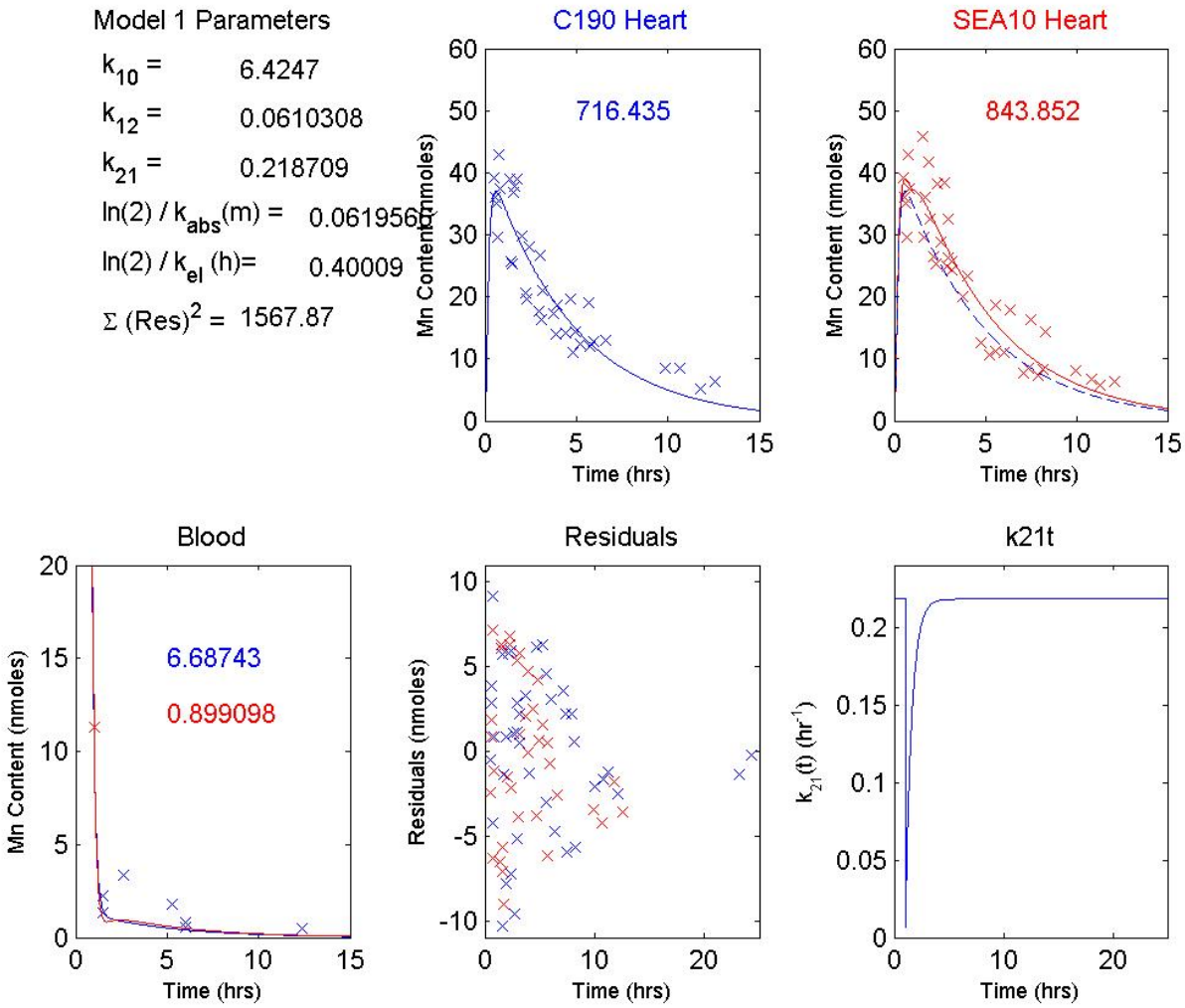

Figure B.1 continued

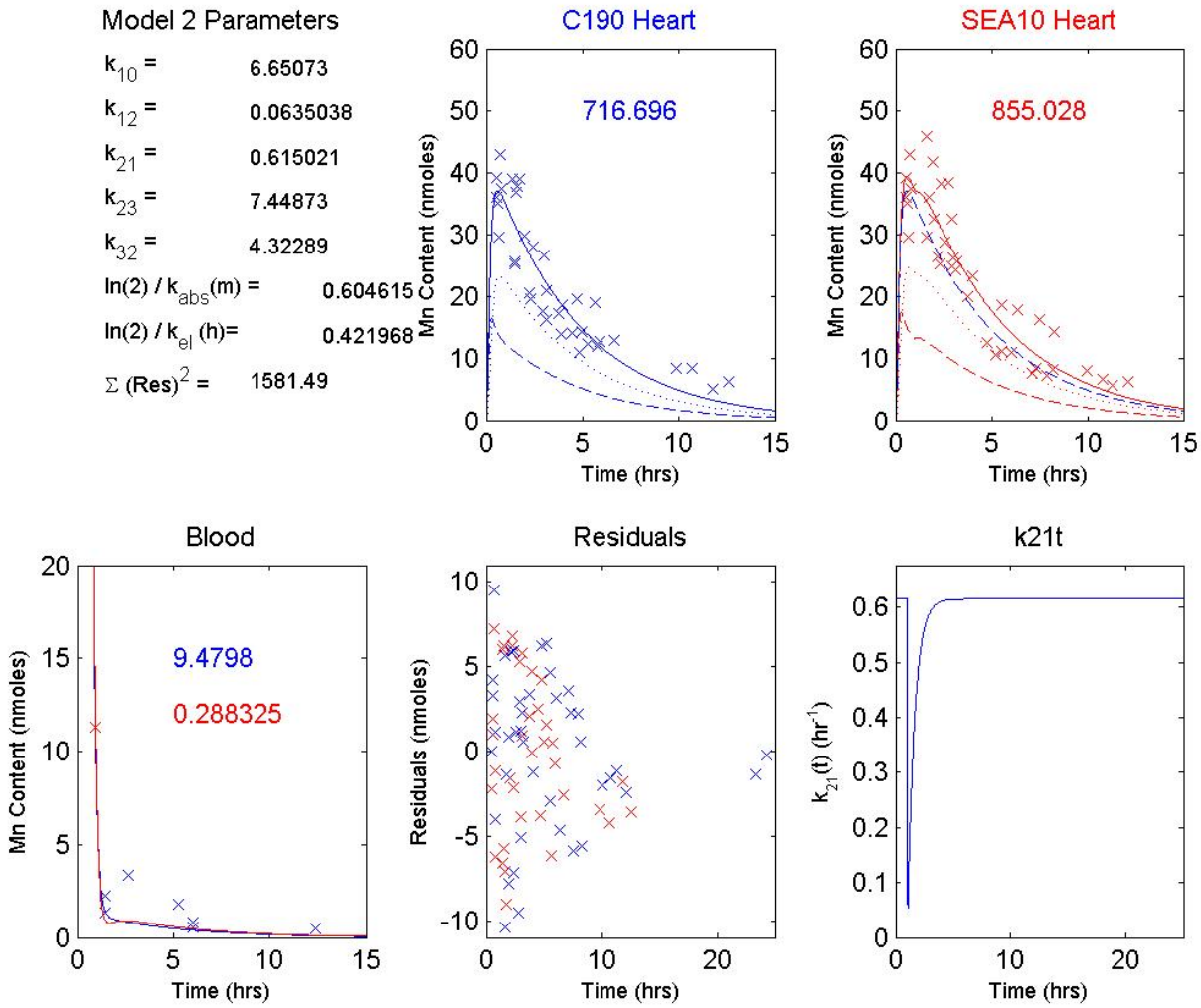

Figure B.1 continued

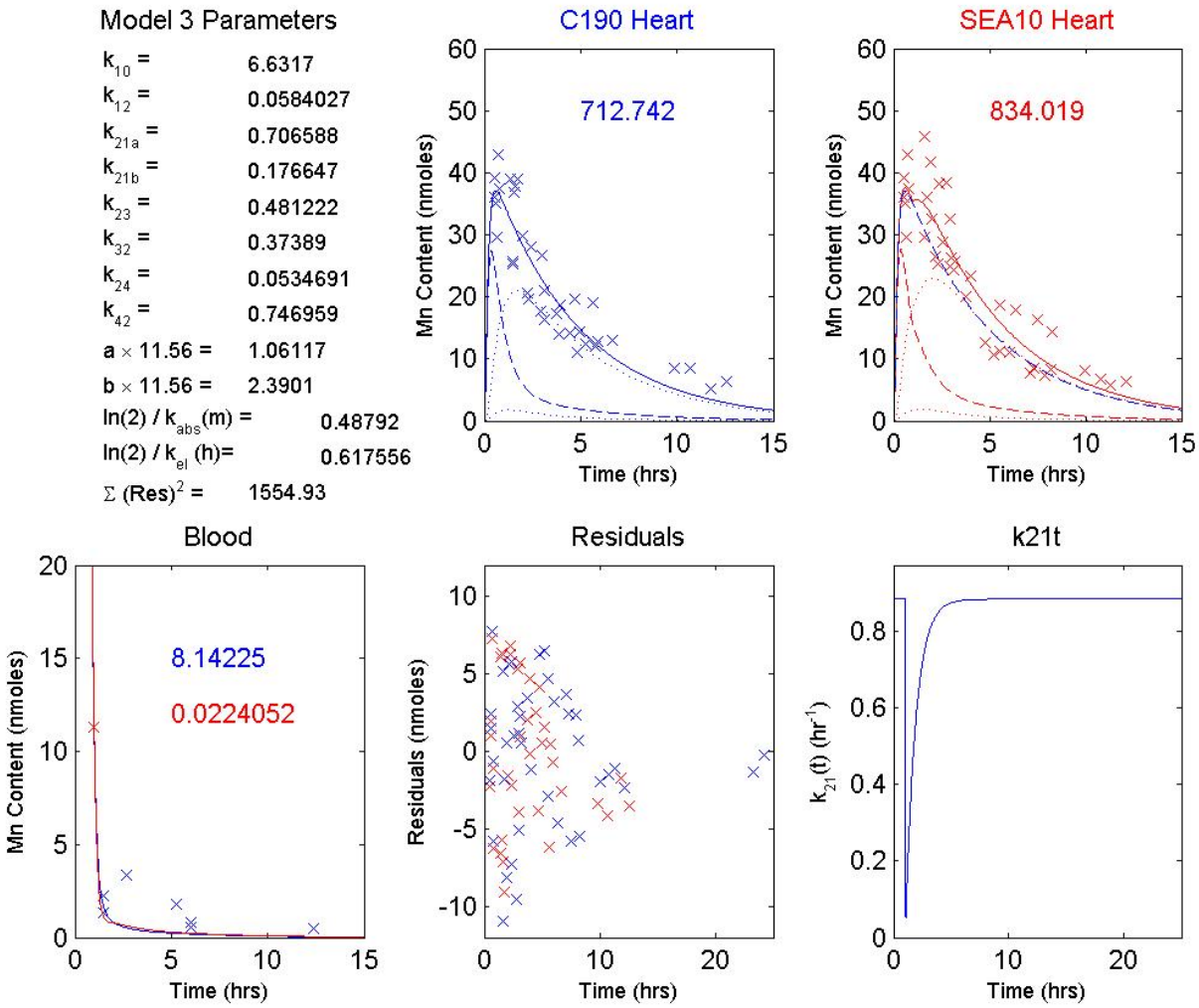

Figure B.1 continued

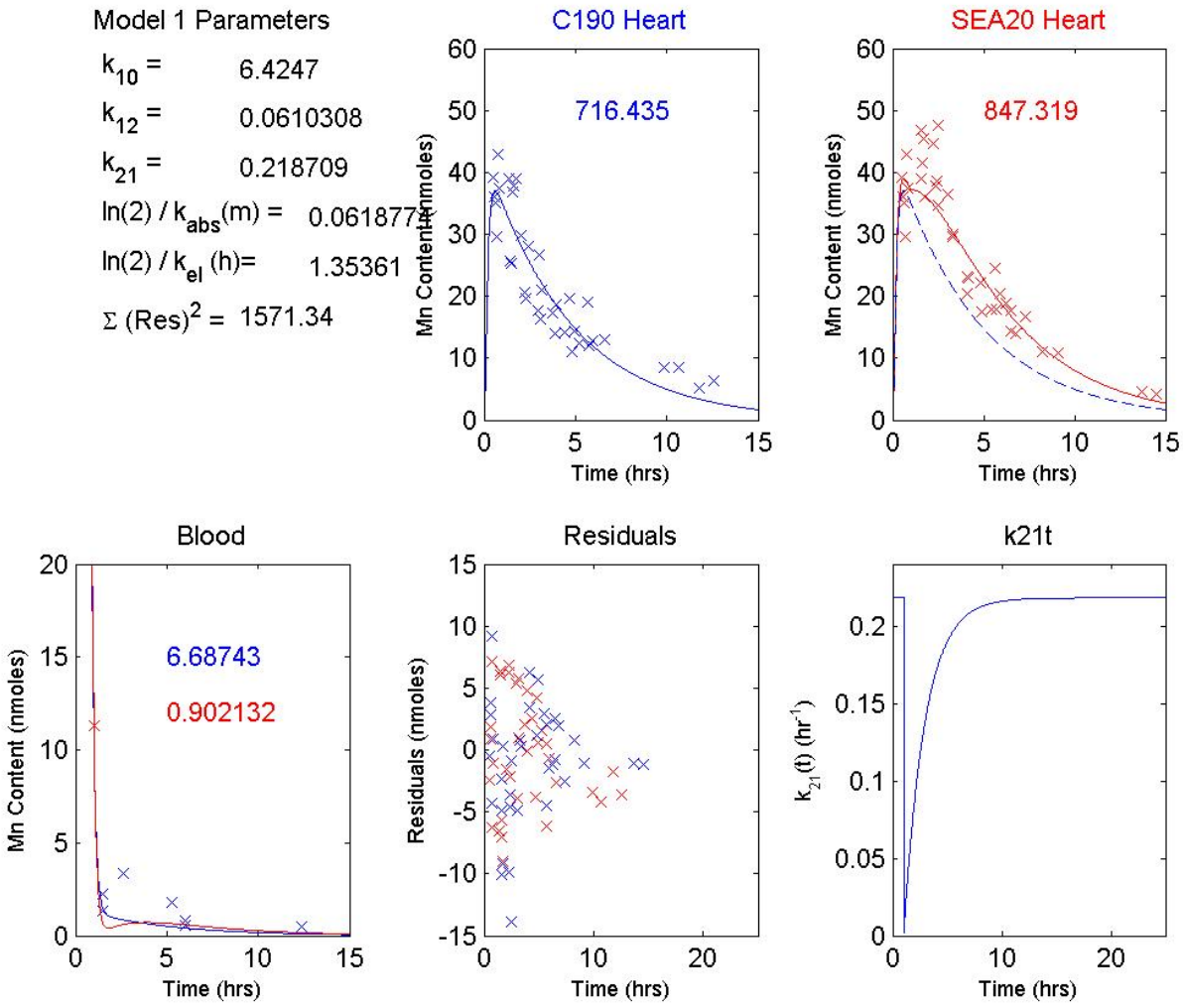

Figure B.1 continued

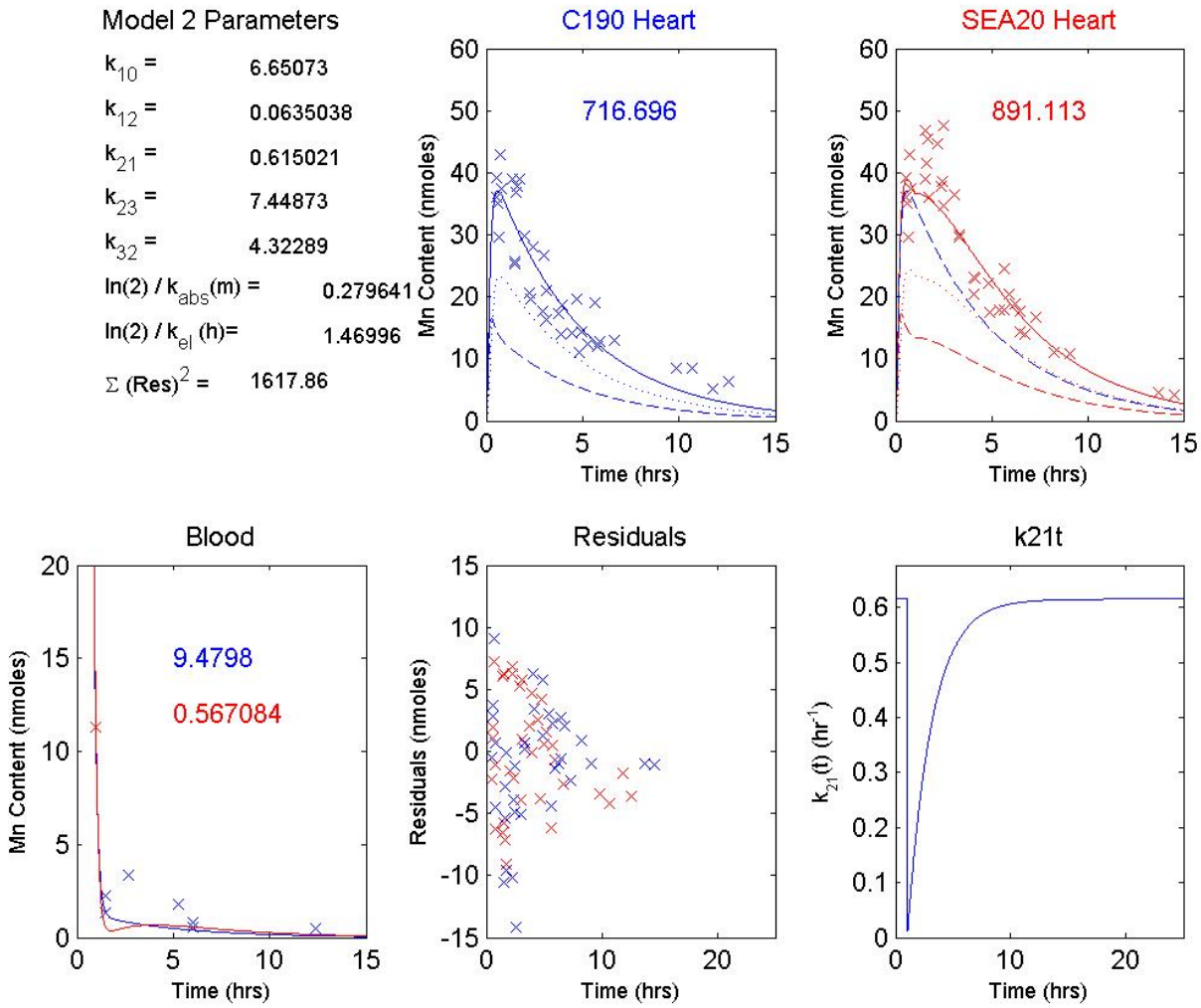

Figure B.1 continued

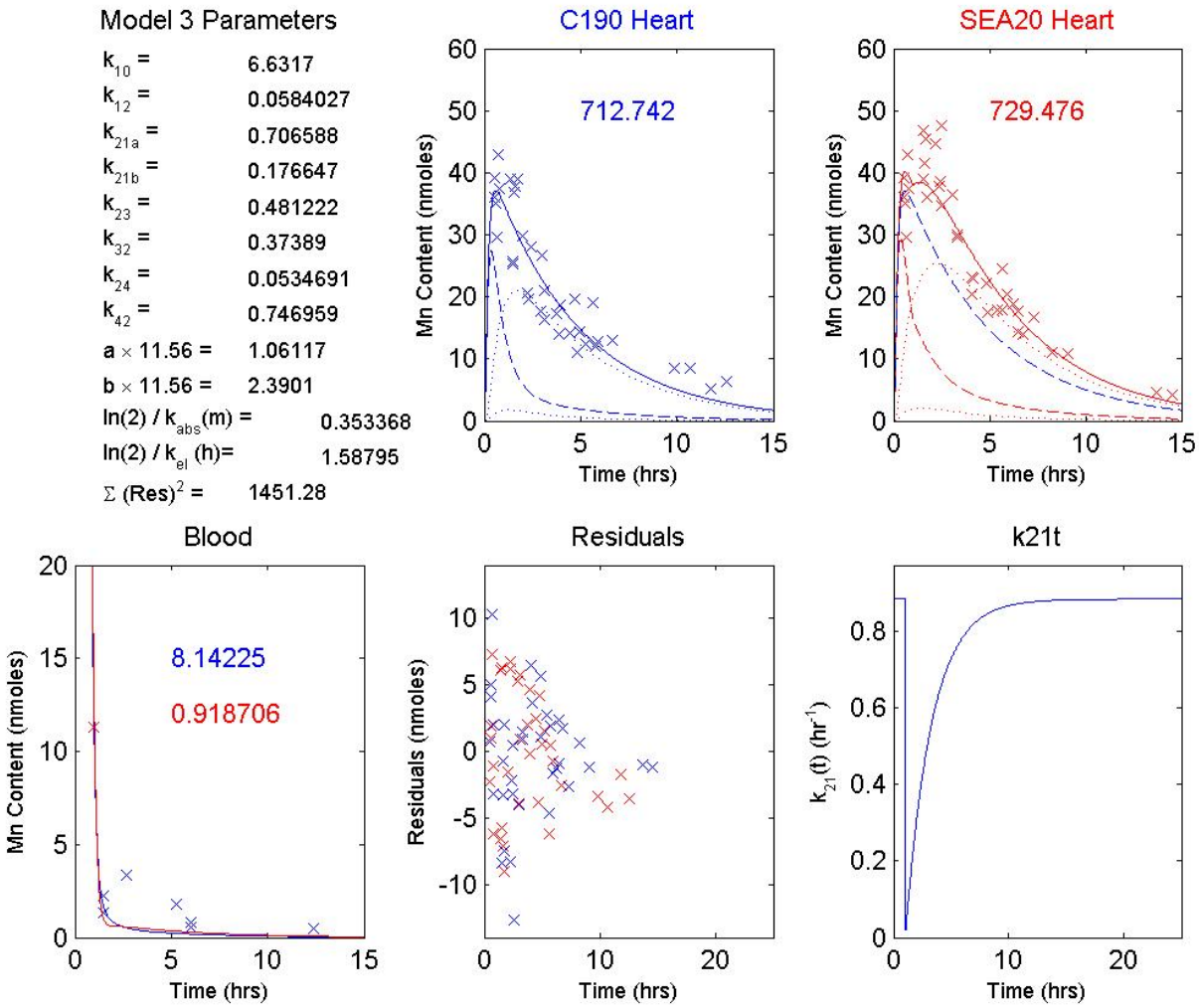

Figure B.1 continued

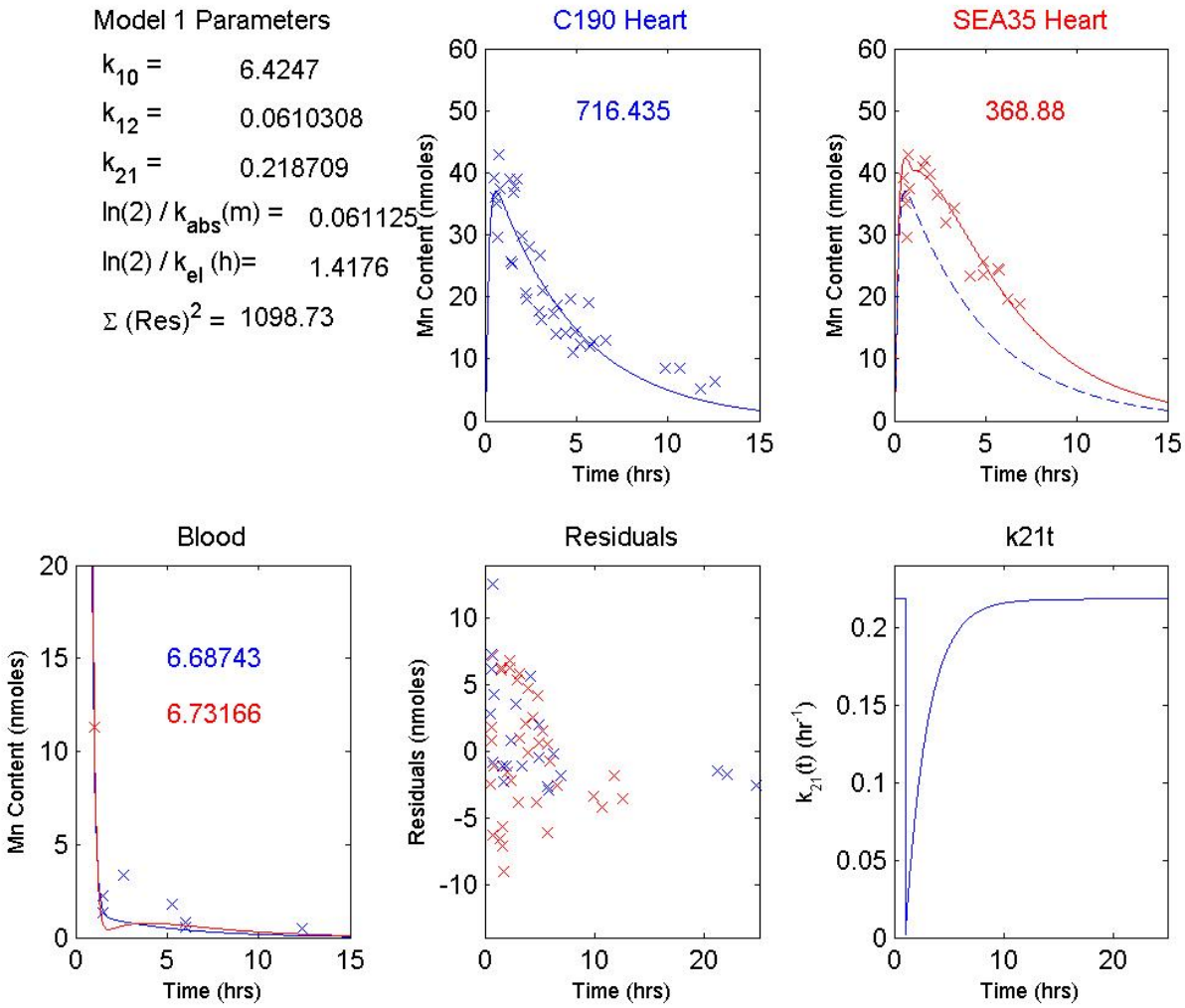

Figure B.1 continued

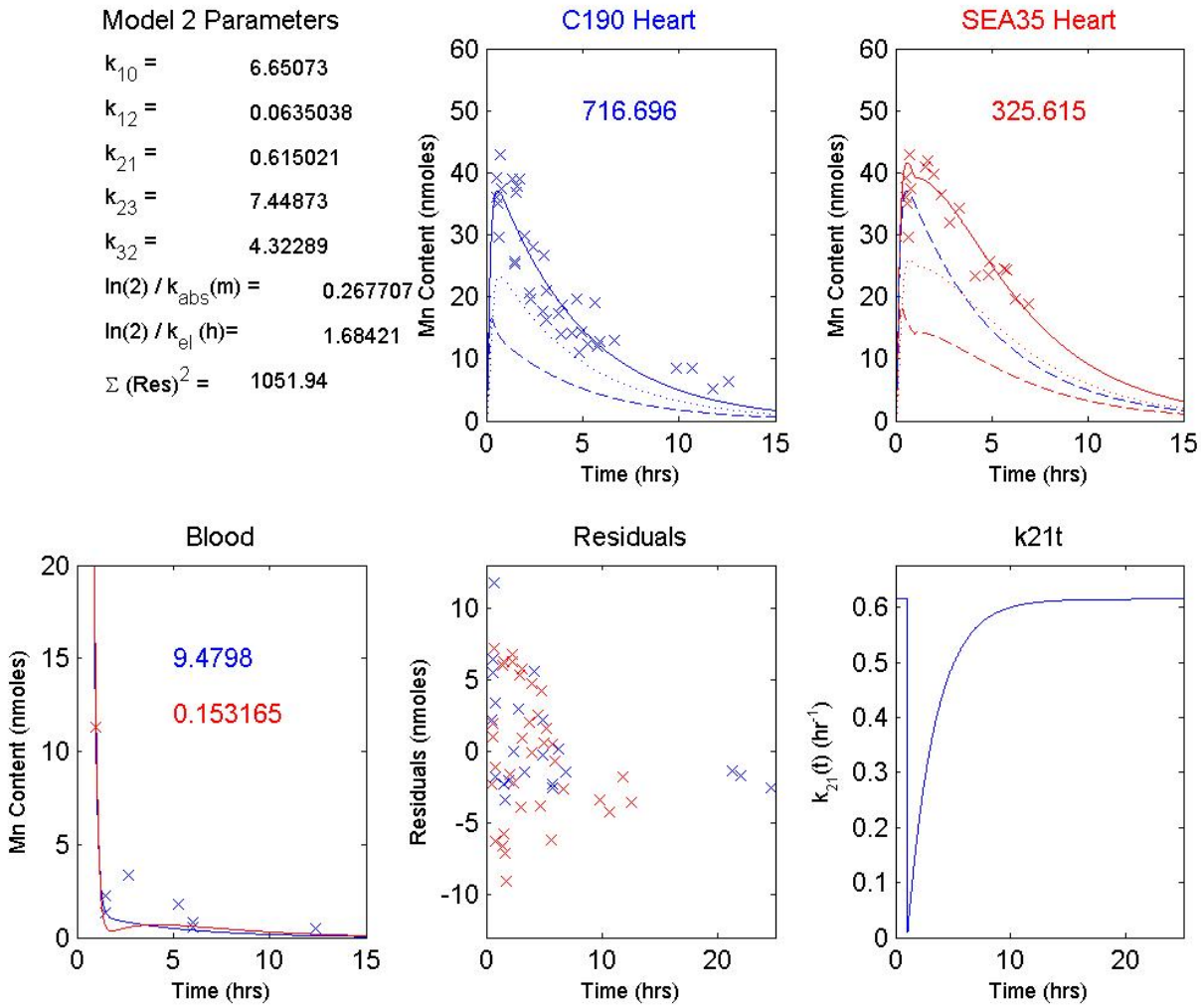

Figure B.1 continued

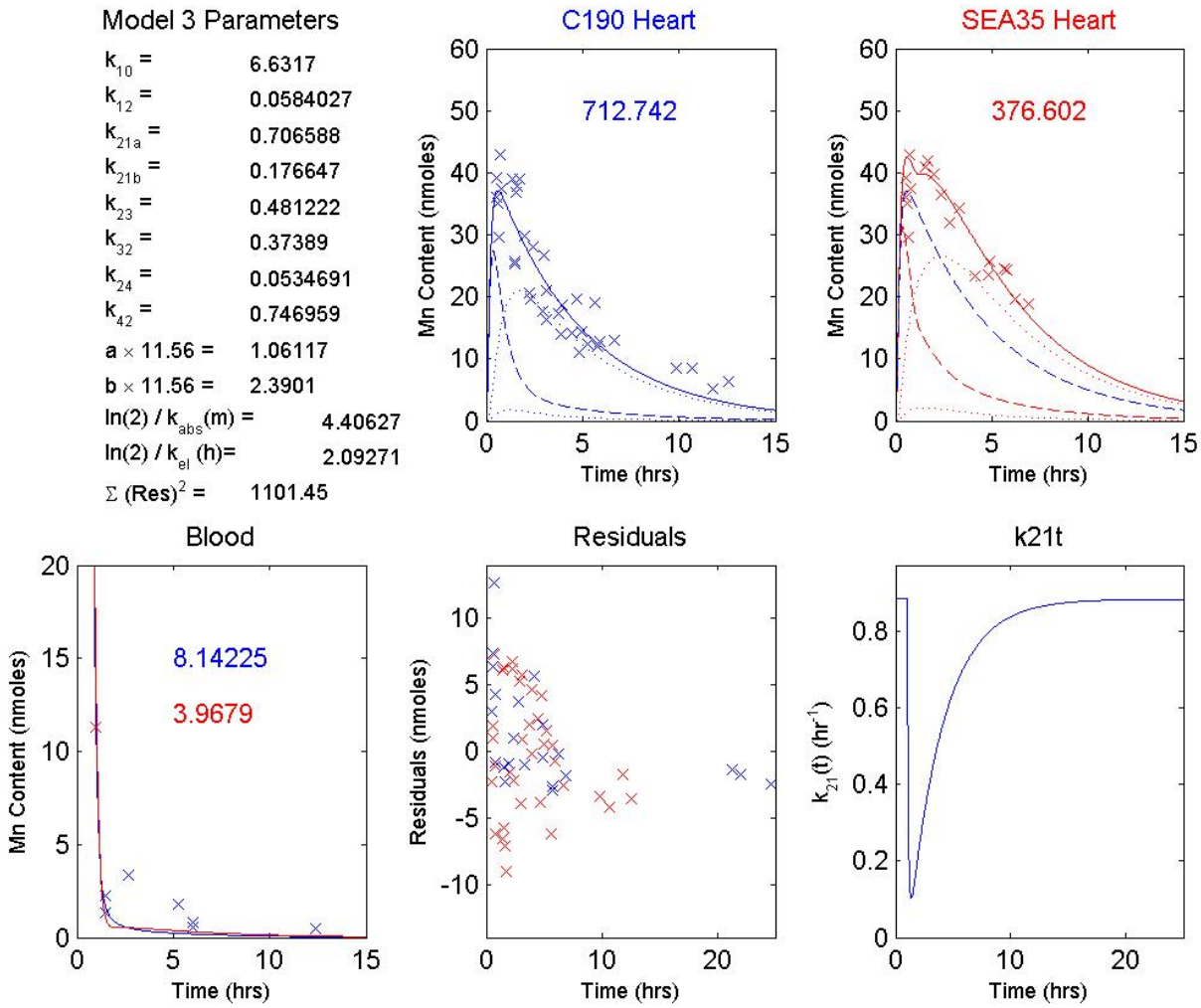

Figure B.1 continued

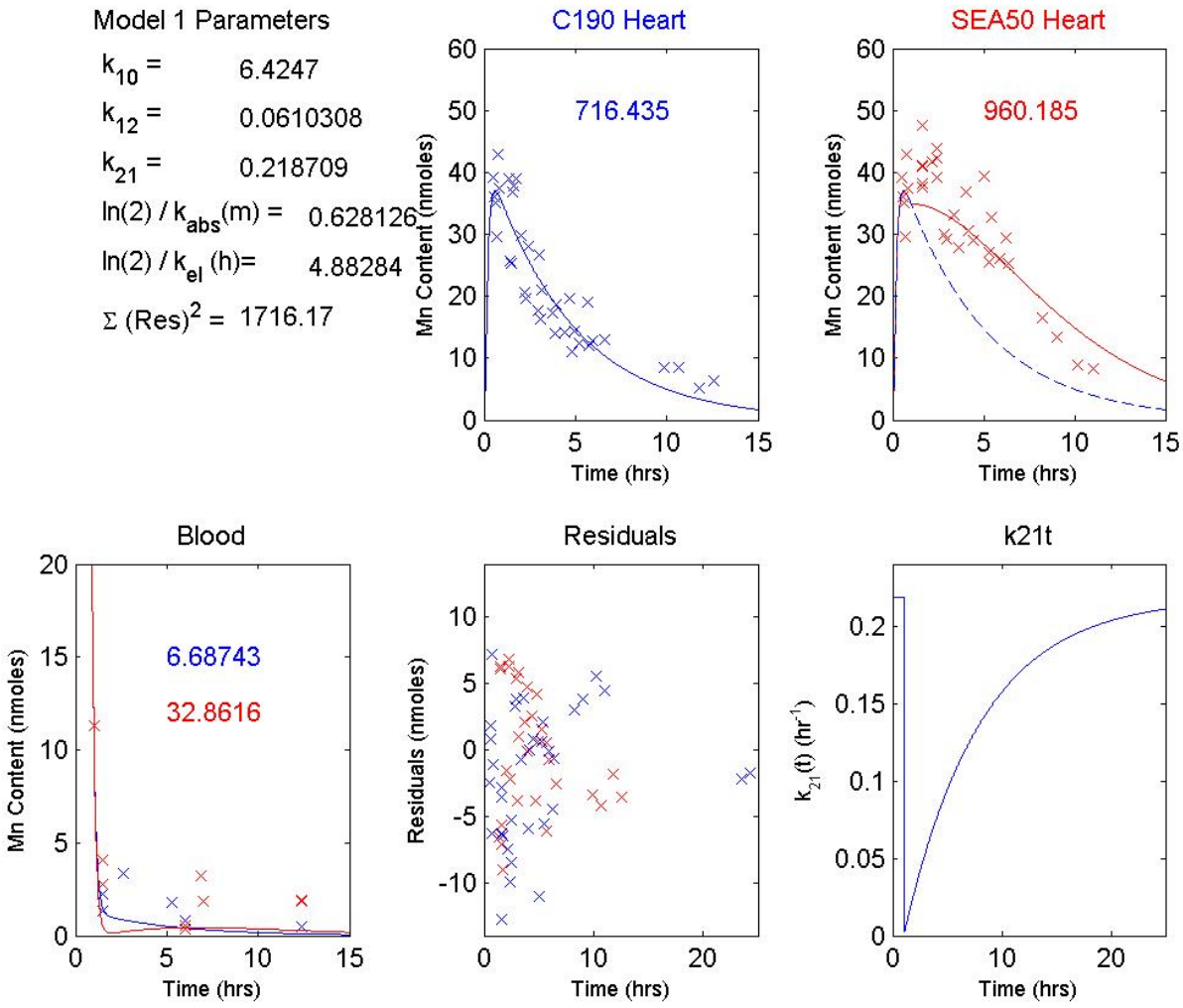

Figure B.1 continued

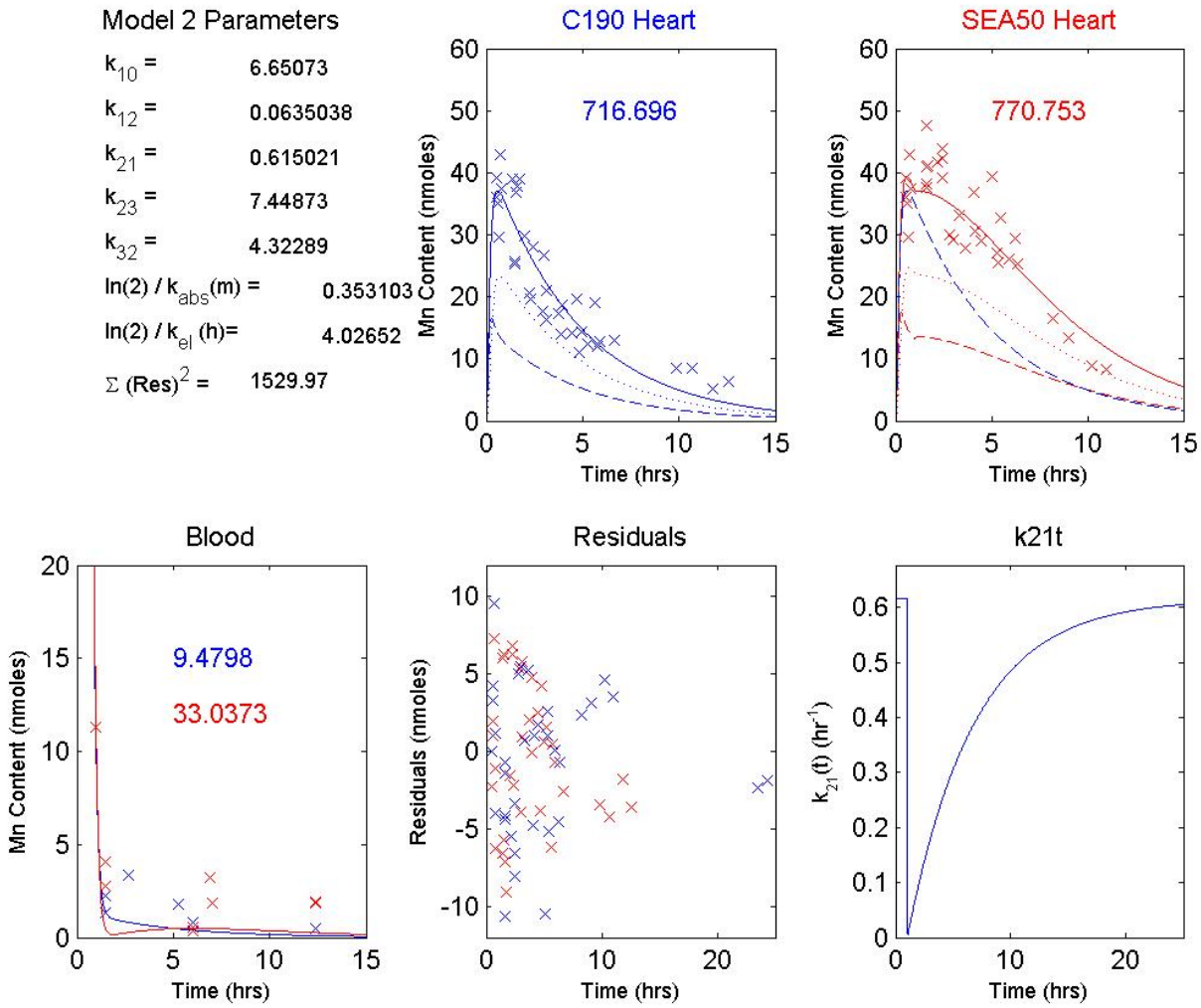

Figure B.1 continued

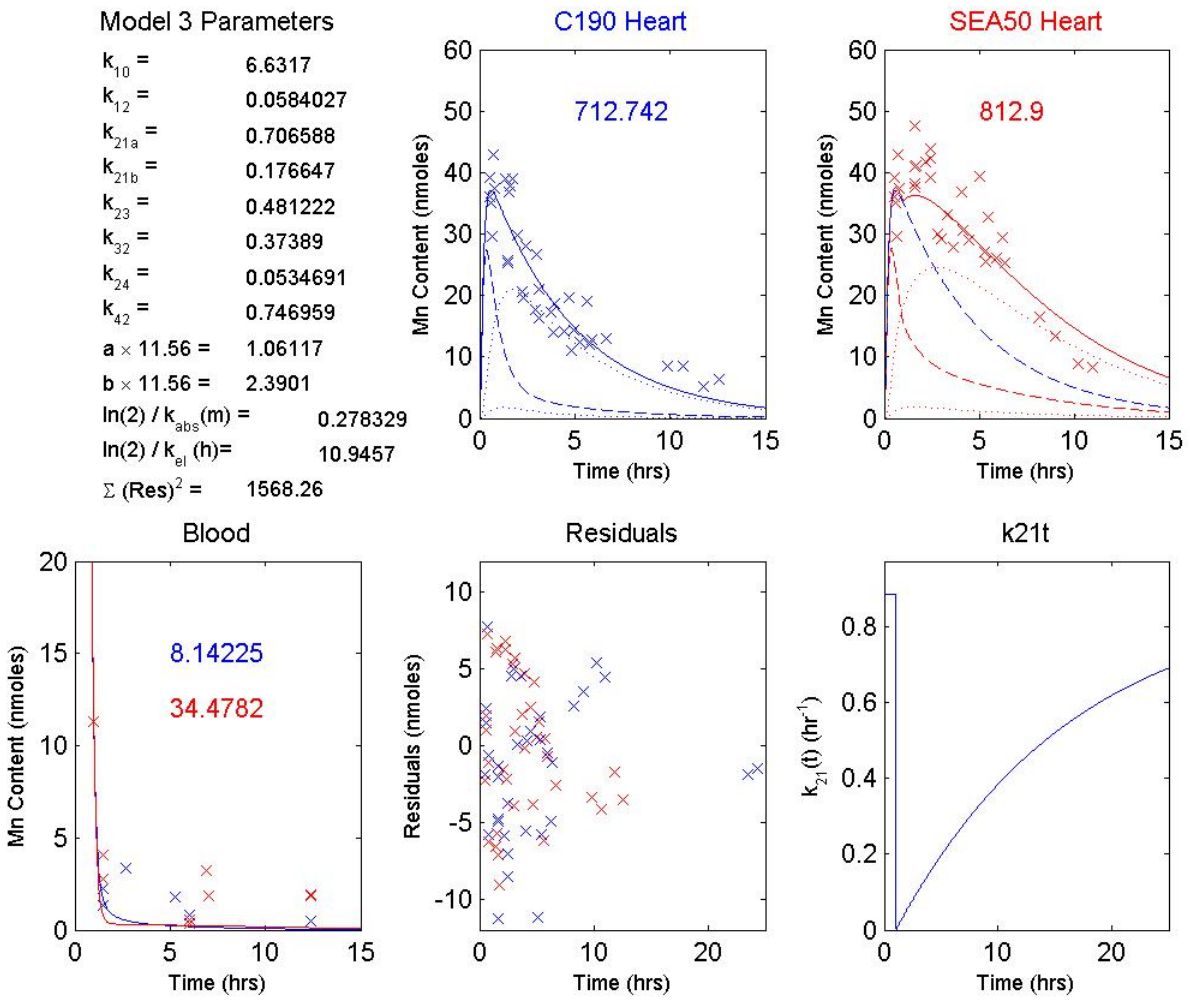

Figure B.1 continued

REFERENCES

1. Heron M, Hoyert DL, Murphy SL, Xu J, Kochanek KD, Tejada-Vera B. Deaths: Final Data for 2006. *Natl Vital Stat Rep* 2009; **57**; 14: 1-136.

2. Menown IB, Adgey AA. Cardioprotective therapy and sodium-hydrogen exchange inhibition: current concepts and future goals. *J Am Coll Cardiol* 2001; **38**; 6: 1651-1653.

3. Opie L. Heart Physiology, From Cell to Circulation: Lippincott Williams & Wilkins; 2004.

4. Katz AM. Physiology of the heart. Philadelphia: Lippincott Williams & Wilkins; 2006.

5. Orrenius S, Zhivotovsky B, Nicotera P. Regulation of cell death: the calcium-apoptosis link. *Nat Rev Mol Cell Biol* 2003; **4**; 7: 552-565.

6. Aoki I, Wu YJ, Silva AC, Lynch RM, Koretsky AP. In vivo detection of neuroarchitecture in the rodent brain using manganese-enhanced MRI. *Neuroimage* 2004; **22**; 3: 1046-1059.

7. Pautler RG, Koretsky AP. Tracing odor-induced activation in the olfactory bulbs of mice using manganese-enhanced magnetic resonance imaging. *Neuroimage* 2002; **16**; 2: 441-448.

8. Weng JC, Chen JH, Yang PF, Tseng WY. Functional mapping of rat barrel activation following whisker stimulation using activity-induced manganese-dependent contrast. *Neuroimage* 2007; **36**; 4: 1179-1188.

9. Puskin JS, Gunter TE. Ion and pH gradients across the transport membrane of mitochondria following Mn^{++} uptake in the presence of acetate. *Biochem Biophys Res Commun* 1973; **51**; 3: 797-803.

10. Hu TC, Christian TF, Aletras AH, Taylor JL, Koretsky AP, Arai AE. Manganese enhanced magnetic resonance imaging of normal and ischemic canine heart. *Magn Reson Med* 2005; **54**; 1: 196-200.

11. Skjold A, Amundsen BH, Wiseth R, Stoylen A, Haraldseth O, Larsson HB, Jynge P. Manganese dipyridoxyl-diphosphate (MnDPDP) as a viability marker in patients with myocardial infarction. *J Magn Reson Imaging* 2007; **26**; 3: 720-727.

12. Bers DM. Calcium fluxes involved in control of cardiac myocyte contraction. *Circ Res* 2000; **87**; 4: 275-281.

13. Bers DM. Cardiac excitation-contraction coupling. *Nature* 2002; **415**; 6868: 198-205.

14. Bers DM. Excitation-contraction coupling and cardiac contractile force: Kluwer Academic Publishers; 1991.

15. Catterall WA, Perez-Reyes E, Snutch TP, Striessnig J. International Union of Pharmacology. XLVIII. Nomenclature and structure-function relationships of voltage-gated calcium channels. *Pharmacol Rev* 2005; **57**; 4: 411-425.

16. Yamakage M, Namiki A. Calcium channels--basic aspects of their structure, function and gene encoding; anesthetic action on the channels--a review. *Can J Anaesth* 2002; **49**; 2: 151-164.

17. Wilson DP, Susnjar M, Kiss E, Sutherland C, Walsh MP. Thromboxane A2-induced contraction of rat caudal arterial smooth muscle involves activation of Ca^{2+} entry and Ca^{2+} sensitization: Rho-associated kinase-mediated phosphorylation of MYPT1 at Thr-855, but not Thr-697. *Biochem J* 2005; **389**; Pt 3: 763-774.

18. Dolphin AC. A short history of voltage-gated calcium channels. *Br J Pharmacol* 2006; **147 Suppl 1**: S56-62.

19. Wier WG. Intracellular calcium during excitation-contraction coupling in mammalian ventricle. *Med Sci Sports Exerc* 1991; **23**; 10: 1149-1156.

20. Mukherjee R, Spinale FG. L-type calcium channel abundance and function with cardiac hypertrophy and failure: a review. *J Mol Cell Cardiol* 1998; **30**; 10: 1899-1916.

21. Eisner DA, Sipido KR. Sodium calcium exchange in the heart: necessity or luxury? *Circ Res* 2004; **95**; 6: 549-551.

22. Caroni P, Carafoli E. An ATP-dependent Ca^{2+}-pumping system in dog heart sarcolemma. *Nature* 1980; **283**; 5749: 765-767.

23. Bassani JW, Bassani RA, Bers DM. Relaxation in rabbit and rat cardiac cells: species-dependent differences in cellular mechanisms. *J Physiol* 1994; **476**; 2: 279-293.

24. Varro A, Negretti N, Hester SB, Eisner DA. An estimate of the calcium content of the sarcoplasmic reticulum in rat ventricular myocytes. *Pflugers Arch* 1993; **423**; 1-2: 158-160.

25. Antoons G, Mubagwa K, Nevelsteen I, Sipido KR. Mechanisms underlying the frequency dependence of contraction and $[Ca^{2+}]_i$ transients in mouse ventricular myocytes. *J Physiol* 2002; **543**; Pt 3: 889-898.

26. Reuter H, Seitz N. The dependence of calcium efflux from cardiac muscle on temperature and external ion composition. *J Physiol* 1968; **195**; 2: 451-470.

27. Ehara T, Matsuoka S, Noma A. Measurement of reversal potential of Na^+-Ca^{2+} exchange current in single guinea-pig ventricular cells. *J Physiol* 1989; **410**: 227-249.

28. Fujioka Y, Komeda M, Matsuoka S. Stoichiometry of Na^+-Ca^{2+} exchange in inside-out patches excised from guinea-pig ventricular myocytes. *J Physiol* 2000; **523 Pt 2**: 339-351.

29. Kang TM, Hilgemann DW. Multiple transport modes of the cardiac Na^+/Ca^{2+} exchanger. *Nature* 2004; **427**; 6974: 544-548.

30. Sipido KR, Varro A, Eisner D. Sodium calcium exchange as a target for antiarrhythmic therapy. *Handb Exp Pharmacol* 2006; 171: 159-199.

31. Hryshko LV, Philipson KD. Sodium-calcium exchange: recent advances. *Basic Res Cardiol* 1997; **92 Suppl 1**: 45-51.

32. Levi AJ, Spitzer KW, Kohmoto O, Bridge JH. Depolarization-induced Ca entry via Na-Ca exchange triggers SR release in guinea pig cardiac myocytes. *Am J Physiol* 1994; **266**; 4 Pt 2: H1422-1433.

33. Eisner DA, Choi HS, Diaz ME, O'Neill SC, Trafford AW. Integrative analysis of calcium cycling in cardiac muscle. *Circ Res* 2000; **87**; 12: 1087-1094.

34. Leblanc N, Hume JR. Sodium current-induced release of calcium from cardiac sarcoplasmic reticulum. *Science* 1990; **248**; 4953: 372-376.

35. Eisner DA, Lederer WJ, Vaughan-Jones RD. The quantitative relationship between twitch tension and intracellular sodium activity in sheep cardiac Purkinje fibres. *J Physiol* 1984; **355**: 251-266.

36. Schwiening CJ, Kennedy HJ, Thomas RC. Calcium-Hydrogen Exchange by the Plasma Membrane Ca-ATPase of Voltage-Clamped Snail Neurons. *Proceedings: Biological Sciences* 1993; **253**; 1338: 285-289.

37. Thygesen K, Alpert JS, White HD, Jaffe AS, Apple FS, Galvani M, Katus HA, Newby LK, Ravkilde J, Chaitman B, Clemmensen PM, Dellborg M, Hod H, Porela P, Underwood R, Bax JJ, Beller GA, Bonow R, Van der Wall EE, Bassand JP, Wijns W, Ferguson TB, Steg PG, Uretsky BF, Williams DO, Armstrong PW, Antman EM, Fox KA, Hamm CW, Ohman EM, Simoons ML, Poole-Wilson PA, Gurfinkel EP, Lopez-Sendon JL, Pais P, Mendis S, Zhu JR, Wallentin LC, Fernandez-Aviles F, Fox KM, Parkhomenko AN, Priori SG, Tendera M, Voipio-Pulkki LM, Vahanian A, Camm AJ, De Caterina R, Dean V, Dickstein K, Filippatos G, Funck-Brentano C, Hellemans I, Kristensen SD, McGregor K, Sechtem U, Silber S, Widimsky P, Zamorano JL, Morais J, Brener S, Harrington R, Morrow D, Lim M, Martinez-Rios MA, Steinhubl S, Levine GN, Gibler WB, Goff D, Tubaro M, Dudek D, Al-Attar N. Universal definition of myocardial infarction. *Circulation* 2007; **116**; 22: 2634-2653.

38. Elliott MD, Kim RJ. Late gadolinium cardiovascular magnetic resonance in the assessment of myocardial viability. *Coron Artery Dis* 2005; **16**; 6: 365-372.

39. White HD, Chew DP. Acute myocardial infarction. *Lancet* 2008; **372**; 9638: 570-584.

40. Thygesen K, Alpert JS, White HD. Universal definition of myocardial infarction. *J Am Coll Cardiol* 2007; **50**; 22: 2173-2195.

41. Rosalki SB, Roberts R, Katus HA, Giannitsis E, Ladenson JH, Apple FS. Cardiac biomarkers for detection of myocardial infarction: perspectives from past to present. *Clin Chem* 2004; **50**; 11: 2205-2213.

42. Jaffe AS, Ravkilde J, Roberts R, Naslund U, Apple FS, Galvani M, Katus H. It's time for a change to a troponin standard. *Circulation* 2000; **102**; 11: 1216-1220.

43. Jaffe AS, Babuin L, Apple FS. Biomarkers in acute cardiac disease: the present and the future. *J Am Coll Cardiol* 2006; **48**; 1: 1-11.

44. Foo RS, Mani K, Kitsis RN. Death begets failure in the heart. *J Clin Invest* 2005; **115**; 3: 565-571.

45. Eefting F, Rensing B, Wigman J, Pannekoek WJ, Liu WM, Cramer MJ, Lips DJ, Doevendans PA. Role of apoptosis in reperfusion injury. *Cardiovasc Res* 2004; **61**; 3: 414-426.

46. Houser SR, Piacentino V, 3rd, Weisser J. Abnormalities of calcium cycling in the hypertrophied and failing heart. *J Mol Cell Cardiol* 2000; **32**; 9: 1595-1607.

47. Saini HK, Shao Q, Musat S, Takeda N, Tappia PS, Dhalla NS. Imidapril treatment improves the attenuated inotropic and intracellular calcium responses to ATP in heart failure due to myocardial infarction. *Br J Pharmacol* 2005; **144**; 2: 202-211.

48. Zhang XQ, Musch TI, Zelis R, Cheung JY. Effects of impaired Ca^{2+} homeostasis on contraction in postinfarction myocytes. *J Appl Physiol* 1999; **86**; 3: 943-950.

49. Sam F, Sawyer DB, Chang DL, Eberli FR, Ngoy S, Jain M, Amin J, Apstein CS, Colucci WS. Progressive left ventricular remodeling and apoptosis late after myocardial infarction in mouse heart. *Am J Physiol Heart Circ Physiol* 2000; **279**; 1: H422-428.

50. Lerman A, Zeiher AM. Endothelial function: cardiac events. *Circulation* 2005; **111**; 3: 363-368.

51. Jain AP, Mohan A, Gupta OP, Jajoo UN, Kalantri SP, Srivastava LM. Role of oxygen free radicals in causing endothelial damage in acute myocardial infarction. *J Assoc Physicians India* 2000; **48**; 5: 478-480.

52. van Dokkum RP, Eijkelkamp WB, Kluppel AC, Henning RH, van Goor H, Citgez M, Windt WA, van Veldhuisen DJ, de Graeff PA, de Zeeuw D. Myocardial

infarction enhances progressive renal damage in an experimental model for cardio-renal interaction. *J Am Soc Nephrol* 2004; **15**; 12: 3103-3110.

53. Roy D, Quiles J, Sinha M, Aldama G, Gaze D, Kaski JC. Effect of direct-current cardioversion on ischemia-modified albumin levels in patients with atrial fibrillation. *Am J Cardiol* 2004; **93**; 3: 366-368.

54. Tsutsui H, Ide T, Hayashidani S, Suematsu N, Shiomi T, Wen J, Nakamura K, Ichikawa K, Utsumi H, Takeshita A. Enhanced generation of reactive oxygen species in the limb skeletal muscles from a murine infarct model of heart failure. *Circulation* 2001; **104**; 2: 134-136.

55. Lindley TE, Doobay MF, Sharma RV, Davisson RL. Superoxide is involved in the central nervous system activation and sympathoexcitation of myocardial infarction-induced heart failure. *Circ Res* 2004; **94**; 3: 402-409.

56. Yan AT, Shayne AJ, Brown KA, Gupta SN, Chan CW, Luu TM, Di Carli MF, Reynolds HG, Stevenson WG, Kwong RY. Characterization of the peri-infarct zone by contrast-enhanced cardiac magnetic resonance imaging is a powerful predictor of post-myocardial infarction mortality. *Circulation* 2006; **114**; 1: 32-39.

57. Prisant LM. Management of hypertension in patients with cardiac disease: use of renin-angiotensin blocking agents. *Am J Med* 2008; **121**; 8 Suppl: S8-15.

58. Slart RH, Bax JJ, van Veldhuisen DJ, van der Wall EE, Dierckx RA, Jager PL. Imaging techniques in nuclear cardiology for the assessment of myocardial viability. *Int J Cardiovasc Imaging* 2006; **22**; 1: 63-80.

59. Blankstein R, Rogers IS, Cury RC. Practical tips and tricks in cardiovascular computed tomography: diagnosis of myocardial infarction. *J Cardiovasc Comput Tomogr* 2009; **3**; 2: 104-111.

60. Lim TH, Choi SI. MRI of myocardial infarction. *J Magn Reson Imaging* 1999; **10**; 5: 686-693.

61. Weinsaft JW, Klem I, Judd RM. MRI for the assessment of myocardial viability. *Cardiol Clin* 2007; **25**; 1: 35-56.

62. Kim RJ, Fieno DS, Parrish TB, Harris K, Chen EL, Simonetti O, Bundy J, Finn JP, Klocke FJ, Judd RM. Relationship of MRI delayed contrast enhancement to irreversible injury, infarct age, and contractile function. *Circulation* 1999; **100**; 19: 1992-2002.

63. Lloyd SG, Gupta H. Assessment of myocardial viability by cardiovascular magnetic resonance. *Echocardiography* 2005; **22**; 2: 179-193.

64. Di Carli MF, Davidson M, Little R, Khanna S, Mody FV, Brunken RC, Czernin J, Rokhsar S, Stevenson LW, Laks H, et al. Value of metabolic imaging with positron emission tomography for evaluating prognosis in patients with coronary artery disease and left ventricular dysfunction. *Am J Cardiol* 1994; **73**; 8: 527-533.

65. Rahimtoola SH. The hibernating myocardium. *Am Heart J* 1989; **117**; 1: 211-221.

66. Tillisch J, Brunken R, Marshall R, Schwaiger M, Mandelkern M, Phelps M, Schelbert H. Reversibility of cardiac wall-motion abnormalities predicted by positron tomography. *N Engl J Med* 1986; **314**; 14: 884-888.

67. Solomon SD, Zelenkofske S, McMurray JJ, Finn PV, Velazquez E, Ertl G, Harsanyi A, Rouleau JL, Maggioni A, Kober L, White H, Van de Werf F, Pieper K, Califf RM, Pfeffer MA. Sudden death in patients with myocardial infarction and left ventricular dysfunction, heart failure, or both. *N Engl J Med* 2005; **352**; 25: 2581-2588.

68. Buxton AE. Identifying the high risk patient with coronary artery disease--is ejection fraction all you need? *J Cardiovasc Electrophysiol* 2005; **16 Suppl 1**: S25-27.

69. Myocardial infarction redefined--a consensus document of The Joint European Society of Cardiology/American College of Cardiology Committee for the redefinition of myocardial infarction. *Eur Heart J* 2000; **21**; 18: 1502-1513.

70. Luepker RV, Apple FS, Christenson RH, Crow RS, Fortmann SP, Goff D, Goldberg RJ, Hand MM, Jaffe AS, Julian DG, Levy D, Manolio T, Mendis S, Mensah G, Pajak A, Prineas RJ, Reddy KS, Roger VL, Rosamond WD, Shahar E, Sharrett AR, Sorlie P, Tunstall-Pedoe H. Case definitions for acute coronary heart disease in epidemiology and clinical research studies: a statement from the AHA Council on Epidemiology and Prevention; AHA Statistics Committee; World Heart Federation Council on Epidemiology and Prevention; the European Society

of Cardiology Working Group on Epidemiology and Prevention; Centers for Disease Control and Prevention; and the National Heart, Lung, and Blood Institute. *Circulation* 2003; **108**; 20: 2543-2549.

71. Antman EM, Anbe DT, Armstrong PW, Bates ER, Green LA, Hand M, Hochman JS, Krumholz HM, Kushner FG, Lamas GA, Mullany CJ, Ornato JP, Pearle DL, Sloan MA, Smith SC, Jr. ACC/AHA guidelines for the management of patients with ST-elevation myocardial infarction--executive summary. A report of the American College of Cardiology/American Heart Association Task Force on Practice Guidelines (Writing Committee to revise the 1999 guidelines for the management of patients with acute myocardial infarction). *J Am Coll Cardiol* 2004; **44**; 3: 671-719.

72. Braunwald E, Antman EM, Beasley JW, Califf RM, Cheitlin MD, Hochman JS, Jones RH, Kereiakes D, Kupersmith J, Levin TN, Pepine CJ, Schaeffer JW, Smith EE, 3rd, Steward DE, Theroux P, Gibbons RJ, Alpert JS, Faxon DP, Fuster V, Gregoratos G, Hiratzka LF, Jacobs AK, Smith SC, Jr. ACC/AHA 2002 guideline update for the management of patients with unstable angina and non-ST-segment elevation myocardial infarction--summary article: a report of the American College of Cardiology/American Heart Association task force on practice guidelines (Committee on the Management of Patients With Unstable Angina). *J Am Coll Cardiol* 2002; **40**; 7: 1366-1374.

73. Dilsizian V, Rocco TP, Freedman NM, Leon MB, Bonow RO. Enhanced detection of ischemic but viable myocardium by the reinjection of thallium after stress-redistribution imaging. *N Engl J Med* 1990; **323**; 3: 141-146.

74. Ragosta M, Beller GA, Watson DD, Kaul S, Gimple LW. Quantitative planar rest-redistribution 201Tl imaging in detection of myocardial viability and prediction of improvement in left ventricular function after coronary bypass surgery in patients with severely depressed left ventricular function. *Circulation* 1993; **87**; 5: 1630-1641.

75. Tamaki N, Yonekura Y, Yamashita K, Saji H, Magata Y, Senda M, Konishi Y, Hirata K, Ban T, Konishi J. Positron emission tomography using fluorine-18 deoxyglucose in evaluation of coronary artery bypass grafting. *Am J Cardiol* 1989; **64**; 14: 860-865.

76. Senior R. Diagnostic and imaging considerations: role of viability. *Heart Fail Rev* 2006; **11**; 2: 125-134.

77. Marshall RC, Tillisch JH, Phelps ME, Huang SC, Carson R, Henze E, Schelbert HR. Identification and differentiation of resting myocardial ischemia and infarction in man with positron computed tomography, 18F-labeled fluorodeoxyglucose and N-13 ammonia. *Circulation* 1983; **67**; 4: 766-778.

78. Leppo JA. Myocardial uptake of thallium and rubidium during alterations in perfusion and oxygenation in isolated rabbit hearts. *J Nucl Med* 1987; **28**; 5: 878-885.

79. Ohtani H, Tamaki N, Yonekura Y, Mohiuddin IH, Hirata K, Ban T, Konishi J. Value of thallium-201 reinjection after delayed SPECT imaging for predicting reversible ischemia after coronary artery bypass grafting. *Am J Cardiol* 1990; **66**; 4: 394-399.

80. Kapur A, Latus KA, Davies G, Dhawan RT, Eastick S, Jarritt PH, Roussakis G, Young MC, Anagnostopoulos C, Bomanji J, Costa DC, Pennell DJ, Prvulovich EM, Ell PJ, Underwood SR. A comparison of three radionuclide myocardial perfusion tracers in clinical practice: the ROBUST study. *Eur J Nucl Med Mol Imaging* 2002; **29**; 12: 1608-1616.

81. Mahmarian JJ, Boyce TM, Goldberg RK, Cocanougher MK, Roberts R, Verani MS. Quantitative exercise thallium-201 single photon emission computed tomography for the enhanced diagnosis of ischemic heart disease. *J Am Coll Cardiol* 1990; **15**; 2: 318-329.

82. Van Train KF, Garcia EV, Maddahi J, Areeda J, Cooke CD, Kiat H, Silagan G, Folks R, Friedman J, Matzer L, et al. Multicenter trial validation for quantitative analysis of same-day rest-stress technetium-99^{m}-sestamibi myocardial tomograms. *J Nucl Med* 1994; **35**; 4: 609-618.

83. Gerber BL, Belge B, Legros GJ, Lim P, Poncelet A, Pasquet A, Gisellu G, Coche E, Vanoverschelde JL. Characterization of acute and chronic myocardial infarcts by multidetector computed tomography: comparison with contrast-enhanced magnetic resonance. *Circulation* 2006; **113**; 6: 823-833.

84. Gosalia A, Haramati LB, Sheth MP, Spindola-Franco H. CT detection of acute myocardial infarction. *AJR Am J Roentgenol* 2004; **182**; 6: 1563-1566.

85. Thomson LE, Kim RJ, Judd RM. Magnetic resonance imaging for the assessment of myocardial viability. *J Magn Reson Imaging* 2004; **19**; 6: 771-788.

86. Saeed M, Lund G, Wendland MF, Bremerich J, Weinmann H, Higgins CB. Magnetic resonance characterization of the peri-infarction zone of reperfused myocardial infarction with necrosis-specific and extracellular nonspecific contrast media. *Circulation* 2001; **103**; 6: 871-876.

87. Ni Y, Marchal G, Herijgers P, Flameng W, Petre C, Ebert W, Hilger CS, Pfefferer D, Semmler W, Baert AL. Paramagnetic metalloporphyrins: from enhancers of malignant tumors to markers of myocardial infarcts. *Acad Radiol* 1996; **3 Suppl 2**: S395-397.

88. Hedstrom E, Palmer J, Ugander M, Arheden H. Myocardial SPECT perfusion defect size compared to infarct size by delayed gadolinium-enhanced magnetic resonance imaging in patients with acute or chronic infarction. *Clin Physiol Funct Imaging* 2004; **24**; 6: 380-386.

89. Reichek N. MRI myocardial tagging. *J Magn Reson Imaging* 1999; **10**; 5: 609-616.

90. McVeigh E. Measuring mechanical function in the failing heart. *J Electrocardiol* 2006; **39**; 4 Suppl: S24-27.

91. Kraitchman DL, Young AA, Bloomgarden DC, Fayad ZA, Dougherty L, Ferrari VA, Boston RC, Axel L. Integrated MRI assessment of regional function and perfusion in canine myocardial infarction. *Magn Reson Med* 1998; **40**; 2: 311-326.

92. Kramer CM, Lima JA, Reichek N, Ferrari VA, Llaneras MR, Palmon LC, Yeh IT, Tallant B, Axel L. Regional differences in function within noninfarcted myocardium during left ventricular remodeling. *Circulation* 1993; **88**; 3: 1279-1288.

93. Geskin G, Kramer CM, Rogers WJ, Theobald TM, Pakstis D, Hu YL, Reichek N. Quantitative assessment of myocardial viability after infarction by dobutamine magnetic resonance tagging. *Circulation* 1998; **98**; 3: 217-223.

94. Mendonca-Dias MH, Gaggelli E, Lauterbur PC. Paramagnetic contrast agents in nuclear magnetic resonance medical imaging. *Semin Nucl Med* 1983; **13**; 4: 364-376.

95. Cory DA, Schwartzentruber DJ, Mock BH. Ingested manganese chloride as a contrast agent for magnetic resonance imaging. *Magn Reson Imaging* 1987; **5**; 1: 65-70.

96. Anderson M. Mn ions pass through calcium channels. A possible explanation. *J Gen Physiol* 1983; **81**; 6: 805-827.

97. Narita K, Kawasaki F, Kita H. Mn and Mg influxes through Ca channels of motor nerve terminals are prevented by verapamil in frogs. *Brain Res* 1990; **510**; 2: 289-295.

98. Shibuya I, Douglas WW. Indications from Mn-quenching of Fura-2 fluorescence in melanotrophs that dopamine and baclofen close Ca channels that are spontaneously open but not those opened by high $[K^+]O$; and that Cd preferentially blocks the latter. *Cell Calcium* 1993; **14**; 1: 33-44.

99. Hu TC, Pautler RG, MacGowan GA, Koretsky AP. Manganese-enhanced MRI of mouse heart during changes in inotropy. *Magn Reson Med* 2001; **46**; 5: 884-890.

100. Skjold A, Kristoffersen A, Vangberg TR, Haraldseth O, Jynge P, Larsson HB. An apparent unidirectional influx constant for manganese as a measure of myocardial calcium channel activity. *J Magn Reson Imaging* 2006; **24**; 5: 1047-1055.

101. Prince LP, Links JM. Medical imaging signals and systems: Pearson Prentice Hall; 2006.

102. Haacke EM, Brown RW, Thompson MR, Venkatesan R. Magnetic resonance imaging, physical principles and sequence design: John Wiley and Sons; 1999.

103. Webb AI. Introduction to biomedical imaging: John Wiley & Sons; 2003.

104. Damadian R. Tumor detection by nuclear magnetic resonance. *Science* 1971; **171**; 976: 1151-1153.

105. Lauterbur PC. The spontaneous development of biology from chemistry. *Astrobiology* 2008; **8**; 1: 3-8.

106. Stephens EM, Grisham CM. Lithium-7 nuclear magnetic resonance, water proton nuclear magnetic resonance, and gadolinium electron paramagnetic resonance studies of the sarcoplasmic reticulum calcium ion transport adenosine triphosphatase. *Biochemistry (Mosc)* 1979; **18**; 22: 4876-4885.

107. Wood ML, Hardy PA. Proton relaxation enhancement. *J Magn Reson Imaging* 1993; **3**; 1: 149-156.

108. Sobol WT. Magnetic resonance contrast agents. Physical basis of relaxation. *Neuroimaging Clin N Am* 1994; **4**; 1: 27-42.

109. Hendrick RE, Haacke EM. Basic physics of MR contrast agents and maximization of image contrast. *J Magn Reson Imaging* 1993; **3**; 1: 137-148.

110. MultiHance (gadobenate dimeglumine) injection 529 mg/mL full prescribing information. Bracco Diagnostics Inc. Princeton, NJ; May 2007.

111. Magnevist (brand of gedopentetate dimeglumine) injection full prescribing information. Bayer Healthcare Pharmaceuticals Inc. Wayne, NJ; June 2007.

112. Omniscan (gadodiamide) injection, full prescribing information. GE HealthCare Inc. Princeton, NJ; December 2007.

113. ProHance (gadoteridol) injection 279.3 mg/mL full prescribing information. Bracco Diagnostics Inc. Princeton, NJ; May 2007.

114. OptiMARK (gadoversetamide injection) full prescribing information. Mallinckrodt Inc. St. Louis, MO; October 2008.

115. TESLASCAN (mangafodipir trisodium) injection 50 µg/mL, prescribing information. Nycomed Inc. Princeton, NJ; April 1999.

116. Feridex I.V. (ferumoxides injectable solution) prescribing information. Bayer Healthcare Pharmaceuticals Inc. Wayne, NJ; May 2007.

117. Koretsky AP, Silva AC. Manganese-enhanced magnetic resonance imaging (MEMRI). *NMR Biomed* 2004; **17**; 8: 527-531.

118. Pautler RG. Biological applications of manganese-enhanced magnetic resonance imaging. *Methods Mol Med* 2006; **124**: 365-386.

119. Crossgrove J, Zheng W. Manganese toxicity upon overexposure. *NMR Biomed* 2004; **17**; 8: 544-553.

120. Takeda A. Manganese action in brain function. *Brain Res Brain Res Rev* 2003; **41**; 1: 79-87.

121. Sloot WN, Gramsbergen JB. Axonal transport of manganese and its relevance to selective neurotoxicity in the rat basal ganglia. *Brain Res* 1994; **657**; 1-2: 124-132.

122. Takeda A, Kodama Y, Ishiwatari S, Okada S. Manganese transport in the neural circuit of rat CNS. *Brain Res Bull* 1998; **45**; 2: 149-152.

123. Takeda A, Ishiwatari S, Okada S. In vivo stimulation-induced release of manganese in rat amygdala. *Brain Res* 1998; **811**; 1-2: 147-151.

124. Devenyi AG, Barron TF, Mamourian AC. Dystonia, hyperintense basal ganglia, and high whole blood manganese levels in Alagille's syndrome. *Gastroenterology* 1994; **106**; 4: 1068-1071.

125. Hsieh CT, Liang JS, Peng SS, Lee WT. Seizure associated with total parenteral nutrition-related hypermanganesemia. *Pediatr Neurol* 2007; **36**; 3: 181-183.

126. Dickerson RN. Manganese intoxication and parenteral nutrition. *Nutrition* 2001; **17**; 7-8: 689-693.

127. Josephs KA, Ahlskog JE, Klos KJ, Kumar N, Fealey RD, Trenerry MR, Cowl CT. Neurologic manifestations in welders with pallidal MRI T1 hyperintensity. *Neurology* 2005; **64**; 12: 2033-2039.

128. Ochi R. Manganese-dependent propagated action potentials and their depression by electrical stimulation in guinea-pig myocardium perfused by sodium-free media. *J Physiol* 1976; **263**; 2: 139-156.

129. Brurok H, Schjott J, Berg K, Karlsson JO, Jynge P. Effects of manganese dipyridoxyl diphosphate, dipyridoxyl diphosphate--, and manganese chloride on cardiac function. An experimental study in the Langendorff perfused rat heart. *Invest Radiol* 1995; **30**; 3: 159-167.

130. Pogwizd SM, Schlotthauer K, Li L, Yuan W, Bers DM. Arrhythmogenesis and contractile dysfunction in heart failure: Roles of sodium-calcium exchange, inward rectifier potassium current, and residual beta-adrenergic responsiveness. *Circ Res* 2001; **88**; 11: 1159-1167.

131. Saeed M. New concepts in characterization of ischemically injured myocardium by MRI. *Exp Biol Med (Maywood)* 2001; **226**; 5: 367-376.

132. Taylor AM, Panting JR, Keegan J, Gatehouse PD, Jhooti P, Yang GZ, McGill S, Francis JM, Burman ED, Firmin DN, Pennell DJ. Use of the intravascular contrast agent NC100150 injection in spin-echo and gradient-echo imaging of the heart. *J Cardiovasc Magn Reson* 1999; **1**; 1: 23-32.

133. Szolar DH, Saeed M, Wendland MF, Sakuma H, Roberts TP, Stiskal MA, Derugin N, Higgins CB. MR imaging characterization of postischemic myocardial dysfunction ("stunned myocardium"): relationship between functional and perfusion abnormalities. *J Magn Reson Imaging* 1996; **6**; 4: 615-624.

134. Saeed M, Higgins CB, Geschwind JF, Wendland MF. T_1-relaxation kinetics of extracellular, intracellular and intravascular MR contrast agents in normal and acutely reperfused infarcted myocardium using echo-planar MR imaging. *Eur Radiol* 2000; **10**; 2: 310-318.

135. Wendland MF, Saeed M, Lund G, Higgins CB. Contrast-enhanced MRI for quantification of myocardial viability. *J Magn Reson Imaging* 1999; **10**; 5: 694-702.

136. Bremerich J, Saeed M, Arheden H, Higgins CB, Wendland MF. Normal and infarcted myocardium: differentiation with cellular uptake of manganese at MR imaging in a rat model. *Radiology* 2000; **216**; 2: 524-530.

137. Hu TC, Bao W, Lenhard SC, Schaeffer TR, Yue TL, Willette RN, Jucker BM. Simultaneous assessment of left-ventricular infarction size, function and tissue viability in a murine model of myocardial infarction by cardiac manganese-enhanced magnetic resonance imaging (MEMRI). *NMR Biomed* 2004; **17**; 8: 620-626.

138. Krombach GA, Saeed M, Higgins CB, Novikov V, Wendland MF. Contrast-enhanced MR delineation of stunned myocardium with administration of $MnCl_2$ in rats. *Radiology* 2004; **230**; 1: 183-190.

139. Storey P, Chen Q, Li W, Seoane PR, Harnish PP, Fogelson L, Harris KR, Prasad PV. Magnetic resonance imaging of myocardial infarction using a manganese-based contrast agent (EVP 1001-1): preliminary results in a dog model. *J Magn Reson Imaging* 2006; **23**; 2: 228-234.

140. Corretti MC, Koretsune Y, Kusuoka H, Chacko VP, Zweier JL, Marban E. Glycolytic inhibition and calcium overload as consequences of exogenously generated free radicals in rabbit hearts. *J Clin Invest* 1991; **88**; 3: 1014-1025.

141. Camelliti P, Devlin GP, Matthews KG, Kohl P, Green CR. Spatially and temporally distinct expression of fibroblast connexins after sheep ventricular infarction. *Cardiovasc Res* 2004; **62**; 2: 415-425.

142. Lee JH, Silva AC, Merkle H, Koretsky AP. Manganese-enhanced magnetic resonance imaging of mouse brain after systemic administration of $MnCl_2$: dose-dependent and temporal evolution of T_1 contrast. *Magn Reson Med* 2005; **53**; 3: 640-648.

143. Look DC, Locker DR. Nuclear Spin-Lattice Relaxation Measurements by Tone-Burst Modulation. *Physical Review Letters* 1968; **20**; 18: 987-989.

144. Look DC, Locker DR. Time Saving in Measurement of NMR and EPR Relaxation Times. *The Review of Scientific Instruments* 1970; **41**; 2: 250-251.

145. Chuang KH, Koretsky A. Improved neuronal tract tracing using manganese enhanced magnetic resonance imaging with fast T_1 mapping. *Magn Reson Med* 2006; **55**; 3: 604-611.

146. Crawley AP, Henkelman RM. A comparison of one-shot and recovery methods in T_1 imaging. *Magn Reson Med* 1988; **7**; 1: 23-34.

147. Pykett IL, Mansfield P. A line scan image study of a tumorous rat leg by NMR. *Phys Med Biol* 1978; **23**; 5: 961-967.

148. Shah NJ, Neeb H, Zaitsev M, Steinhoff S, Kircheis G, Amunts K, Haussinger D, Zilles K. Quantitative T_1 mapping of hepatic encephalopathy using magnetic resonance imaging. *Hepatology* 2003; **38**; 5: 1219-1226.

149. Aoki I, Takahashi Y, Chuang KH, Silva AC, Igarashi T, Tanaka C, Childs RW, Koretsky AP. Cell labeling for magnetic resonance imaging with the T_1 agent manganese chloride. *NMR Biomed* 2006; **19**; 1: 50-59.

150. Brix G, Schad LR, Deimling M, Lorenz WJ. Fast and precise T_1 imaging using a TOMROP sequence. *Magn Reson Imaging* 1990; **8**; 4: 351-356.

151. Steinhoff S, Zaitsev M, Zilles K, Shah NJ. Fast T_1 mapping with volume coverage. *Magn Reson Med* 2001; **46**; 1: 131-140.

152. Toft KG, Hustvedt SO, Grant D, Martinsen I, Gordon PB, Friisk GA, Korsmo AJ, Skotland T. Metabolism and pharmacokinetics of MnDPDP in man. *Acta Radiol* 1997; **38**; 4 Pt 2: 677-689.

153. Hustvedt SO, Grant D, Southon TE, Zech K. Plasma pharmacokinetics, tissue distribution and excretion of MnDPDP in the rat and dog after intravenous administration. *Acta Radiol* 1997; **38**; 4 Pt 2: 690-699.

154. Thomsen HS, Loegager V, Noerrgaard H, Chabanova E, Moller J, Sonne J. Oral manganese for liver and bile imaging. *Acad Radiol* 2005; **12 Suppl 1**: S21-23.

155. Grant D, Zech K, Holtz E. Biodistribution and in vivo stability of manganese dipyridoxyl diphosphate in relation to imaging efficacy. *Invest Radiol* 1994; **29 Suppl 2**: S249-250.

156. Wang C, Gordon PB, Hustvedt SO, Grant D, Sterud AT, Martinsen I, Ahlstrom H, Hemmingsson A. MR imaging properties and pharmacokinetics of MnDPDP in healthy volunteers. *Acta Radiol* 1997; **38**; 4 Pt 2: 665-676.

157. Wendland MF, Saeed M, Bremerich J, Arheden H, Higgins CB. Thallium-like test for myocardial viability with MnDPDP-enhanced MRI. *Acad Radiol* 2002; **9 Suppl 1**: S82-83.

158. Kim TH, Yang DH, Choi JW, Kim ST, Yoon JH, Shin JH, Seo JB, Gong GY, Lim TH. Manganese dipyridoxyl diphosphate (MnDPDP)-enhanced magnetic

resonance imaging of acute reperfused myocardial injury in a cat model: part I: comparison with pathologic examination. *Invest Radiol* 2005; **40**; 1: 49-55.

159. Larsen LE, Grant D. General toxicology of MnDPDP. *Acta Radiol* 1997; **38**; 4 Pt 2: 770-779.

160. Bellin MF. MR contrast agents, the old and the new. *Eur J Radiol* 2006; **60**; 3: 314-323.

161. Rummeny EJ, Torres CG, Kurdziel JC, Nilsen G, Op de Beeck B, Lundby B. MnDPDP for MR imaging of the liver. Results of an independent image evaluation of the European phase III studies. *Acta Radiol* 1997; **38**; 4 Pt 2: 638-642.

162. McPeake JR, O'Grady JG, Zaman S, Portmann B, Wight DG, Tan KC, Calne RY, Williams R. Liver transplantation for primary hepatocellular carcinoma: tumor size and number determine outcome. *J Hepatol* 1993; **18**; 2: 226-234.

163. Kane PA, Ayton V, Walters HL, Benjamin I, Heaton ND, Williams R, Karani JB. MnDPDP-enhanced MR imaging of the liver. Correlation with surgical findings. *Acta Radiol* 1997; **38**; 4 Pt 2: 650-654.

164. Koh DM, Brown G, Riddell AM, Scurr E, Collins DJ, Allen SD, Chau I, Cunningham D, Desouza NM, Leach MO, Husband JE. Detection of colorectal hepatic metastases using MnDPDP MR imaging and diffusion-weighted imaging (DWI) alone and in combination. *Eur Radiol* 2008.

165. Torres CG, Lundby B, Sterud AT, McGill S, Gordon PB, Bjerknes HS. MnDPDP for MR imaging of the liver. Results from the European phase III studies. *Acta Radiol* 1997; **38**; 4 Pt 2: 631-637.

166. Brady TJ, Goldman MR, Pykett IL, Buonanno FS, Kistler JP, Newhouse JH, Burt CT, Hinshaw WS, Pohost GM. Proton nuclear magnetic resonance imaging of regionally ischemic canine hearts: effect of paramagnetic proton signal enhancement. *Radiology* 1982; **144**; 2: 343-347.

167. Goldman MR, Brady TJ, Pykett IL, Burt CT, Buonanno FS, Kistler JP, Newhouse JH, Hinshaw WS, Pohost GM. Quantification of experimental myocardial infarction using nuclear magnetic resonance imaging and paramagnetic ion

contrast enhancement in excised canine hearts. *Circulation* 1982; **66**; 5: 1012-1016.

168. Schaefer S, Lange RA, Kulkarni PV, Katz J, Parkey RW, Willerson JT, Peshock RM. In vivo nuclear magnetic resonance imaging of myocardial perfusion using the paramagnetic contrast agent manganese gluconate. *J Am Coll Cardiol* 1989; **14**; 2: 472-480.

169. Southon TE, Grant D, Bjornerud A, Moen OM, Spilling B, Martinsen I, Refsum H. NMR relaxation studies with MnDPDP. *Acta Radiol* 1997; **38**; 4 Pt 2: 708-716.

170. Skjold A, Vangberg TR, Kristoffersen A, Haraldseth O, Jynge P, Larsson HB. Relaxation enhancing properties of MnDPDP in human myocardium. *J Magn Reson Imaging* 2004; **20**; 6: 948-952.

171. Federle M, Chezmar J, Rubin DL, Weinreb J, Freeny P, Schmiedl UP, Brown JJ, Borrello JA, Lee JK, Semelka RC, Mattrey R, Dachman AH, Saini S, Harms SE, Mitchell DG, Anderson MW, Halford HH, 3rd, Bennett WF, Young SW, Rifkin M, Gay SB, Ballerini R, Sherwin PF, Robison RO. Efficacy and safety of mangafodipir trisodium (MnDPDP) injection for hepatic MRI in adults: results of the U.S. Multicenter phase III clinical trials. Efficacy of early imaging. *J Magn Reson Imaging* 2000; **12**; 5: 689-701.

172. Federle MP, Chezmar JL, Rubin DL, Weinreb JC, Freeny PC, Semelka RC, Brown JJ, Borello JA, Lee JK, Mattrey R, Dachman AH, Saini S, Harmon B, Fenstermacher M, Pelsang RE, Harms SE, Mitchell DG, Halford HH, Anderson MW, Johnson CD, Francis IR, Bova JG, Kenney PJ, Klippenstein DL, Foster GS, Turner DA. Safety and efficacy of mangafodipir trisodium (MnDPDP) injection for hepatic MRI in adults: results of the U.S. multicenter phase III clinical trials (safety). *J Magn Reson Imaging* 2000; **12**; 1: 186-197.

173. Brurok H, Schjott J, Berg K, Karlsson JO, Jynge P. Effects of manganese dipyridoxyl diphosphate, dipyridoxyl diphosphate--, and manganese chloride on cardiac function. An experimental study in the Langendorff perfused rat heart. *Invest Radiol* 1995; **30**; 3: 159-167.

174. Brurok H, Skoglund T, Berg K, Skarra S, Karlsson JO, Jynge P. Myocardial manganese elevation and proton relaxivity enhancement with manganese dipyridoxyl diphosphate. Ex vivo assessments in normally perfused and ischemic guinea pig hearts. *NMR Biomed* 1999; **12**; 6: 364-372.

175. Brurok H, Schjott J, Berg K, Karlsson JO, Jynge P. Effects of MnDPDP, DPDP--, and $MnCl_2$ on cardiac energy metabolism and manganese accumulation. An experimental study in the isolated perfused rat heart. *Invest Radiol* 1997; **32**; 4: 205-211.

176. Jynge P, Brurok H, Asplund A, Towart R, Refsum H, Karlsson JO. Cardiovascular safety of MnDPDP and $MnCl_2$. *Acta Radiol* 1997; **38**; 4 Pt 2: 740-749.

177. Olsen O, Thuen M, Berry M, Kovalev V, Petrou M, Goa PE, Sandvig A, Haraldseth O, Brekken C. Axon tracing in the adult rat optic nerve and tract after intravitreal injection of MnDPDP using a semiautomatic segmentation technique. *J Magn Reson Imaging* 2008; **27**; 1: 34-42.

178. Ahlstrom H, Gehl HB. Overview of MnDPDP as a pancreas-specific contrast agent for MR imaging. *Acta Radiol* 1997; **38**; 4 Pt 2: 660-664.

179. Gehl HB, Gunther RW, Klever P, Hauptmann S. [Manganese dipyridoxal diphosphate as a new contrast medium in the MRT of benign and malignant pancreatic tumors: initial clinical findings]. *Rofo* 1993; **159**; 3: 240-244.

180. Gehl HB, Urhahn R, Bohndorf K, Klever P, Hauptmann S, Lodemann KP, Matern S, Schumpelick V, Gunther RW. Mn-DPDP in MR imaging of pancreatic adenocarcinoma: initial clinical experience. *Radiology* 1993; **186**; 3: 795-798.

181. Felker GM, O'Connor CM. Inotropic therapy for heart failure: an evidence-based approach. *Am Heart J* 2001; **142**; 3: 393-401.

182. Parissis JT, Farmakis D, Nieminen M. Classical inotropes and new cardiac enhancers. *Heart Fail Rev* 2007; **12**; 2: 149-156.

183. Thackray S, Easthaugh J, Freemantle N, Cleland JG. The effectiveness and relative effectiveness of intravenous inotropic drugs acting through the adrenergic pathway in patients with heart failure-a meta-regression analysis. *Eur J Heart Fail* 2002; **4**; 4: 515-529.

184. Packer M. The search for the ideal positive inotropic agent. *N Engl J Med* 1993; **329**; 3: 201-202.

185. Papp Z, Csapo K, Pollesello P, Haikala H, Edes I. Pharmacological mechanisms contributing to the clinical efficacy of levosimendan. *Cardiovasc Drug Rev* 2005; **23**; 1: 71-98.

186. Mebazaa A, Barraud D, Welschbillig S. Randomized clinical trials with levosimendan. *Am J Cardiol* 2005; **96**; 6A: 74G-79G.

187. Pantos C, Mourouzis I, Tzeis S, Moraitis P, Malliopoulou V, Cokkinos DD, Carageorgiou H, Varonos D, Cokkinos D. Dobutamine administration exacerbates postischaemic myocardial dysfunction in isolated rat hearts: an effect reversed by thyroxine pretreatment. *Eur J Pharmacol* 2003; **460**; 2-3: 155-161.

188. Ruffolo RR, Jr., Spradlin TA, Pollock GD, Waddell JE, Murphy PJ. Alpha and beta adrenergic effects of the stereoisomers of dobutamine. *J Pharmacol Exp Ther* 1981; **219**; 2: 447-452.

189. Elsasser A, Schlepper M, Klovekorn WP, Cai WJ, Zimmermann R, Muller KD, Strasser R, Kostin S, Gagel C, Munkel B, Schaper W, Schaper J. Hibernating myocardium: an incomplete adaptation to ischemia. *Circulation* 1997; **96**; 9: 2920-2931.

190. Takahashi K, Takahashi T, Suzuki T, Onishi M, Tanaka Y, Hamano-Takahashi A, Ota T, Kameo K, Matsuda T, Baba A. Protective effects of SEA0400, a novel and selective inhibitor of the Na^+/Ca^{2+} exchanger, on myocardial ischemia-reperfusion injuries. *Eur J Pharmacol* 2003; **458**; 1-2: 155-162.

191. Iwamoto T. Forefront of Na^+/Ca^{2+} exchanger studies: molecular pharmacology of Na^+/Ca^{2+} exchange inhibitors. *J Pharmacol Sci* 2004; **96**; 1: 27-32.

192. Siegl PK, Cragoe EJ, Jr., Trumble MJ, Kaczorowski GJ. Inhibition of Na^+/Ca^{2+} exchange in membrane vesicle and papillary muscle preparations from guinea pig heart by analogs of amiloride. *Proc Natl Acad Sci U S A* 1984; **81**; 10: 3238-3242.

193. Watanabe Y, Koide Y, Kimura J. Topics on the Na^+/Ca^{2+} exchanger: pharmacological characterization of Na^+/Ca^{2+} exchanger inhibitors. *J Pharmacol Sci* 2006; **102**; 1: 7-16.

194. Watano T, Kimura J, Morita T, Nakanishi H. A novel antagonist, No. 7943, of the Na^+/Ca^{2+} exchange current in guinea-pig cardiac ventricular cells. *Br J Pharmacol* 1996; **119**; 3: 555-563.

195. Matsuda T, Arakawa N, Takuma K, Kishida Y, Kawasaki Y, Sakaue M, Takahashi K, Takahashi T, Suzuki T, Ota T, Hamano-Takahashi A, Onishi M, Tanaka Y, Kameo K, Baba A. SEA0400, a novel and selective inhibitor of the Na^+-Ca^{2+} exchanger, attenuates reperfusion injury in the in vitro and in vivo cerebral ischemic models. *J Pharmacol Exp Ther* 2001; **298**; 1: 249-256.

196. Iwamoto T, Inoue Y, Ito K, Sakaue T, Kita S, Katsuragi T. The exchanger inhibitory peptide region-dependent inhibition of Na^+/Ca^{2+} exchange by SN-6 [2-[4-(4-nitrobenzyloxy)benzyl]thiazolidine-4-carboxylic acid ethyl ester], a novel benzyloxyphenyl derivative. *Mol Pharmacol* 2004; **66**; 1: 45-55.

197. Kuramochi T, Kakefuda A, Sato I, Tsukamoto I, Taguchi T, Sakamoto S. Synthesis and structure-activity relationships of 6-{4-[(3-fluorobenzyl)oxy]phenoxy}nicotinamide derivatives as a novel class of NCX inhibitors: a QSAR study. *Bioorg Med Chem* 2005; **13**; 3: 717-724.

198. Wang J, Zhang Z, Hu Y, Hou X, Cui Q, Zang Y, Wang C. SEA0400, a novel Na^+/Ca^{2+} exchanger inhibitor, reduces calcium overload induced by ischemia and reperfusion in mouse ventricular myocytes. *Physiol Res* 2007; **56**; 1: 17-23.

199. Nagasawa Y, Zhu BM, Chen J, Kamiya K, Miyamoto S, Hashimoto K. Effects of SEA0400, a Na^+/Ca^{2+} exchange inhibitor, on ventricular arrhythmias in the in vivo dogs. *Eur J Pharmacol* 2005; **506**; 3: 249-255.

200. Takahashi T, Takahashi K, Onishi M, Suzuki T, Tanaka Y, Ota T, Yoshida S, Nakaike S, Matsuda T, Baba A. Effects of SEA0400, a novel inhibitor of the Na^+/Ca^{2+} exchanger, on myocardial stunning in anesthetized dogs. *Eur J Pharmacol* 2004; **505**; 1-3: 163-168.

201. Iwamoto T, Kita S, Zhang J, Blaustein MP, Arai Y, Yoshida S, Wakimoto K, Komuro I, Katsuragi T. Salt-sensitive hypertension is triggered by Ca^{2+} entry via Na^+/Ca^{2+} exchanger type-1 in vascular smooth muscle. *Nat Med* 2004; **10**; 11: 1193-1199.

202. Dhalla NS, Pierce GN, Panagia V, Singal PK, Beamish RE. Calcium movements in relation to heart function. *Basic Res Cardiol* 1982; **77**; 2: 117-139.

203. Medina DC, Kirkland DM, Tavazoie MF, Springer CS, Jr., Anderson SE. Na^+/Ca^{2+}-exchanger-mediated Mn^{2+}-enhanced ^1H_2O MRI in hypoxic, perfused rat myocardium. *Contrast Media Mol Imaging* 2007; **2**; 5: 248-257.

204. Waghorn BJ, Edwards T, Yang Y, Chuang KH, Yanasak N, Hu TC. Monitoring dynamic calcium homeostasis alterations by T_1-weighted and T_1-mapping cardiac manganese-enhanced MRI (MEMRI) in a murine myocardial infarction model. *NMR Biomed* 2008; **21**: 1102-1111.

205. Loening AM, Gambhir SS. AMIDE: a free software tool for multimodality medical image analysis. *Mol Imaging* 2003; **2**; 3: 131-137.

206. Ni Y, Petre C, Bosmans H, Miao Y, Grant D, Baert AL, Marchal G. Comparison of manganese biodistribution and MR contrast enhancement in rats after intravenous injection of MnDPDP and MnCl2. *Acta Radiol* 1997; **38**; 4 Pt 2: 700-707.

207. Shigekawa M, Iwamoto T. Cardiac Na^+-Ca^{2+} exchange: molecular and pharmacological aspects. *Circ Res* 2001; **88**; 9: 864-876.

208. Eriksson R, Johansson L, Bjerner T, Briley Saebo K, Ahlstrom H. Uptake of $MnCl_2$ and mangafodipir trisodium in the myocardium: a magnetic resonance imaging study in pigs. *J Magn Reson Imaging* 2004; **19**; 5: 564-569.

209. Haworth RA, Goknur AB. Inhibition of sodium/calcium exchange and calcium channels of heart cells by volatile anesthestics. *Anesthesiology* 1995; **82**; 5: 1255-1265.

210. Frahm J, Haase A, Matthaei D. Rapid NMR imaging of dynamic processes using the FLASH technique. *Magn Reson Med* 1986; **3**; 2: 321-327.

211. Nordhoy W, Anthonsen HW, Bruvold M, Brurok H, Skarra S, Krane J, Jynge P. Intracellular manganese ions provide strong T_1 relaxation in rat myocardium. *Magn Reson Med* 2004; **52**; 3: 506-514.

212. Waghorn B, Yang Y, Baba A, Matsuda T, Schumacher A, Yanasak N, Hu TC. Assessing manganese efflux using SEA0400 and cardiac T1-mapping manganese-enhanced MRI in a murine model. *NMR Biomed* 2009; **22**; 8: 874-881.

213. Tani M, Neely JR. Role of intracellular Na^+ in Ca^{2+} overload and depressed recovery of ventricular function of reperfused ischemic rat hearts. Possible involvement of H^+-Na^+ and Na^+-Ca^{2+} exchange. *Circ Res* 1989; **65**; 4: 1045-1056.

214. Kusuoka H, Camilion de Hurtado MC, Marban E. Role of sodium/calcium exchange in the mechanism of myocardial stunning: protective effect of reperfusion with high sodium solution. *J Am Coll Cardiol* 1993; **21**; 1: 240-248.

215. Yoshiyama M, Nakamura Y, Omura T, Hayashi T, Takagi Y, Hasegawa T, Nishioka H, Takeuchi K, Iwao H, Yoshikawa J. Cardioprotective effect of SEA0400, a selective inhibitor of the Na^+/Ca^{2+} exchanger, on myocardial ischemia-reperfusion injury in rats. *J Pharmacol Sci* 2004; **95**; 2: 196-202.

216. Westfall TC, Westfall DP. Adrenergic agonists and antagonists. In: Brunton LL, Lazo JS, Parker KL, editors. Goodman & Gilman's The Pharmacological Basis of Therapeutics. 11 ed. New York: McGraw-Hill; 2006.

217. Webb AI, Weaver BM. The density of equine tissue at 37 degrees C. *Res Vet Sci* 1979; **26**; 1: 71-75.

218. Lee C, Visen NS, Dhalla NS, Le HD, Isaac M, Choptiany P, Gross G, Omelchenko A, Matsuda T, Baba A, Takahashi K, Hnatowich M, Hryshko LV. Inhibitory profile of SEA0400 [2-[4-[(2,5-difluorophenyl)methoxy]phenoxy]-5-ethoxyaniline] assessed on the cardiac Na^+-Ca^{2+} exchanger, NCX1.1. *J Pharmacol Exp Ther* 2004; **311**; 2: 748-757.

219. Farkas AS, Acsai K, Nagy N, Toth A, Fulop F, Seprenyi G, Birinyi P, Nanasi PP, Forster T, Csanady M, Papp JG, Varro A, Farkas A. Na^+/Ca^{2+} exchanger inhibition exerts a positive inotropic effect in the rat heart, but fails to influence the contractility of the rabbit heart. *Br J Pharmacol* 2008; **154**; 1: 93-104.

220. Gibaldi M, Perrier D. Pharmacokinetics: Informa Healthcare USA, Inc; 2007.

221. Rukhadze MD, Okudzhava VM, Aleksishvili SK, Tsagereli SK, Makharadze TG. Determination of chlorpromazine in blood serum by ion-pair reversed-phase HPLC: Chlorpromazine pharmacokinetics in rabbits. *Pharma Chem J* 1999; **33**; 9: 502-504.

222. Seckin I, Sieck GC, Prakash YS. Volatile anaesthetic effects on Na^+-Ca^{2+} exchange in rat cardiac myocytes. *J Physiol* 2001; **532**; Pt 1: 91-104.

223. Sipido KR, Wier WG. Flux of Ca^{2+} across the sarcoplasmic reticulum of guinea-pig cardiac cells during excitation-contraction coupling. *J Physiol* 1991; **435**: 605-630.

224. Valeyev NV, Downing AK, Skorinkin AI, Campbell ID, Kotov NV. A calcium dependent de-adhesion mechanism regulates the direction and rate of cell migration: a mathematical model. *In Silico Biol* 2006; **6**; 6: 545-572.

225. Bassani JW, Bassani RA, Bers DM. A method to estimate mitochondrial Ca^{2+} uptake in intact cardiac myocytes. *Braz J Med Biol Res* 1996; **29**; 12: 1699-1707.

226. Cho YW, Park SA, Han TH, Son DH, Park JS, Oh SJ, Moon DH, Cho KJ, Ahn CH, Byun Y, Kim IS, Kwon IC, Kim SY. *In vivo* tumor targeting and radionuclide imaging with self-assembled nanoparticles: mechanisms, key factors, and their implications. *Biomaterials* 2007; **28**; 6: 1236-1247.

227. Seymour LW, Miyamoto Y, Maeda H, Brereton M, Strohalm J, Ulbrich K, Duncan R. Influence of molecular weight on passive tumour accumulation of a soluble macromolecular drug carrier. *Eur J Cancer* 1995; **31A**; 5: 766-770.

228. Modo M, Bulte J. Molecular and Cellular MR Imaging: CRC; 2007.

229. Page E. Quantitative ultrastructural analysis in cardiac membrane physiology. *Am J Physiol* 1978; **235**; 5: C147-158.

230. Du C, Koretsky AP, Izrailtyan I, Benveniste H. Simultaneous detection of blood volume, oxygenation, and intracellular calcium changes during cerebral ischemia and reperfusion in vivo using diffuse reflectance and fluorescence. *J Cereb Blood Flow Metab* 2005; **25**; 8: 1078-1092.